وزارة التعليم العالي والبحث العلمي
Ministère de l'Enseignement Supérieur et de la Recherche Scientifique
جامعة عبدالحميد ابن باديس - مستغانم
Université Abdelhamid Ibn Badis de Mostaganem
كلية العلوم و التكنولوجيا
Faculté des Sciences et de la Technologie

UNIVERSITE
ABDELHAMID IBN BADIS
MOSTAGANEM

N° D'ORDRE : D ...../2024

Thèse

Présentée pour obtenir le diplôme

DE DOCTORAT 3ème CYCLE

Filière : Génie des procédés

Spécialité : Génie des procédés des matériaux

Par

Melle BOUDJENANE Fatima Zohra

Contribution to the development of new organic materials for optoelectronics: characterization, structure and related properties

Soutenue le 25/04/2024 devant le jury composé de :

Président :	Nouredine **BENDERDOUCHE**	Pr	Université de Mostaganem
Examinateurs :	Kamel **ACEM**	Pr	Université de Tiaret
	Naima **BOUBEGRA**	MCA	Université de Mostaganem
	Mourad **TERMOUL**	MCA	Université de Mostaganem
Directeur de thèse :	Abdelkader **CHOUAIH**	Pr	Université de Mostaganem
Co-directeur de thèse :	Nourdine **BOUKABCHA**	MCA	Université de Chlef
Invités :	Abdelouahab **ZANOUN**	Pr	ENP - Oran
	Youcef **MEGROUSS**	MCA	Université de Chlef

Année universitaire : **2023 - 2024**

Acknowledgments

I would like to express my deepest gratitude to my supervisor prof. Chouaih Abdelkader who during the five previous years guided me through the thesis preparation process with his valuable advice and enduring support, without which the successful completion of this work would not be imaginable.

In addition, I want to express my gratitude to all the members of the jury who agreed to evaluate the thesis and enhance its quality.

I would also like to thank Benhalima Nadia, Nourelhouda, Boukabcha Nouredine, and Megrouss Youcef for his help and encouragement during the first year of my PhD studies which set a strong foundation for my further achievements.

In addition, I acknowledge Atalay Yusuf and Necmi Dege who hosted my internship at Sakarya and Samsun University in Turkey and helped me gain valuable experience and knowledge in DFT calculation and X-Ray diffraction.

Similarly, I recognize the support of assoc. prof. Kaspars Traskovskis for accepting my internship at Riga Technical University in Latvia, during which I underwent training in molecular dynamic simulations.

Finally, I am eternally grateful to my mother who during the thesis preparation was always by my side with her unconditional support and encouragement, which allowed me to overcome all the hardships I encountered

Summary

Chapter I: Literature review on thiazolic compounds

Chapter II: Experimental methods for structure determination

References

Chapter III: Mathematical formalism of molecular modeling

References

Chapter 4: Structural analysis of EMTh ($C_{12}H_{14}N_2O_2S$), and TMTh ($C_{14}H_{18}N_2O_2S$) molecules

References

Chapter 5: Spectroscopic analysis of EMTh ($C_{12}H_{14}N_2O_2S$), and TMTh ($C_{14}H_{18}N_2O_2S$) molecules

References

Chapter 6: Molecular dynamics simulation and structure – activity relationship

Abstract:

This study focuses on synthesizing and thoroughly analyzing two different compounds. The first compound (Z)-3-N-(ethyl)-2-N'-((3-methoxyphenyl)imino)thiazolidine-4-one (EMTh) was characterized using FT-IR, ^{1}H and ^{13}C NMR spectroscopy, and single-crystal X-ray diffraction. The crystal structure analysis revealed a non-planar molecular configuration with a notable 86.0° dihedral angle between the benzene and thiazolidinone rings. The crystal's molecular arrangement was controlled by C-H•••O and C-H•••N hydrogen bonds, leading to a unique three-dimensional packing pattern. Quantum chemical simulations employing the B3LYP/6-311G(d,p) theory level revealed information about the molecule's electrostatic potential, HOMO-LUMO energy levels, and dipole moment orientations, validating the compound's stability and charge transfer capabilities. Subsequent analyses, such as reduced density gradient, natural bond orbital, and Hirshfeld surface analysis, identified intrinsic non-bonded interactions and interatomic linkages that impact the crystal structure. The ligand showed strong biological activity by establishing significant interactions with amino acids in the protein (PDB ID: 2AZ5), leading to a binding energy of -6.3 kcal/mol and effectively inhibiting necrosis tumour factor. The second compound (Z)-2N- (tert-butylimino)-3N'-(4-methoxyphenyl) thiazolidin-4-one (TMTh) was synthesized and examined by^{1}H and ^{13}C NMR, and FT-IR spectroscopy techniques. The monoclinic crystal structure containing eight molecules in the unit cell was determined using the single-crystal X-ray diffraction method. Density functional theory (DFT) calculations gave optimized molecular geometry in good agreement with experimental results. Weak interactions such as C-H···O and C-H···S hydrogen bonds and van der Waals interactions important for crystal packing were identified using Hirshfeld surface (HS) and RDG methods. PED analysis helped determine vibration frequencies, supported by experimental FT-IR data. Time-dependent density functional theory (TD-DFT) was used to study electronic transitions, charge transfer, and UV-vis spectra. Frontier molecular orbitals (FMOs), and Molecular Electrostatic Potential (MEP) distribution maps offered insights into charge transfer and reactivity. Significant nonlinear optical (NLO) activity was also predicted by computational simulations. Computational ADMET analysis, such as molecular docking, assessed physicochemical properties, pharmacokinetics, and biological impacts on certain receptors. This study provides a thorough examination of the structural, electronic, and biological properties of the synthesized molecule. Finally, by conducting extensive molecular dynamics (MD) simulations, we have uncovered the compound's ability to inhibit selected enzymes and its corresponding binding properties, providing crucial insights for its potential therapeutic use. The binding energies were calculated using MM-PBSA.

Keywords: EMTh, TMTh, FT-IR, NMR, NLO, ADMET analysis, MD simulations, and MM-PBSA

Résumé:

Cette étude se concentre sur la synthèse et l'analyse approfondie de deux composés différents. Le premier composé (Z)-3-N-(éthyl)-2-N'-((3-méthoxyphényl)imino)thiazolidine-4-one (EMTh) a été caractérisé par FT-IR, spectroscopie RMN 1H et 13C et diffraction des rayons X sur monocristal. L'analyse de la structure cristalline a révélé une configuration moléculaire non plane avec un angle dièdre notable de 86,0° entre les anneaux benzène et thiazolidinone. L'arrangement moléculaire du cristal était contrôlé par des liaisons hydrogène C-H---O et C-H---N, ce qui a donné lieu à un modèle d'emballage tridimensionnel unique. Des simulations de chimie quantique utilisant le niveau théorique B3LYP/6-311G(d,p) ont révélé des informations sur le potentiel électrostatique de la molécule, les niveaux d'énergie HOMO-LUMO et les orientations du moment dipolaire, validant ainsi la stabilité du composé et ses capacités de transfert de charge. Des analyses ultérieures, telles que le gradient de densité réduit, l'orbitale de liaison naturelle et l'analyse de la surface de Hirshfeld, ont permis d'identifier les interactions intrinsèques non liées et les liaisons interatomiques qui ont un impact sur la structure cristalline. Le ligand a montré une forte activité biologique en établissant des interactions significatives avec des acides aminés de la protéine (PDB ID : 2AZ5), conduisant à une énergie de liaison de -6,3 kcal/mol et inhibant efficacement le facteur de nécrose tumorale. Le deuxième composé (Z)-2N-(tert butylimino)-3N'-(4-méthoxyphényl) thiazolidin-4-one (TMTh) a été synthétisé et examiné par les techniques de spectroscopie RMN1H et 13C et FT-IR. La structure cristalline monoclinique contenant huit molécules dans la cellule unitaire a été déterminée par la méthode de diffraction des rayons X sur un seul cristal. Les calculs de la théorie de la fonctionnelle de la densité (DFT) ont donné une géométrie moléculaire optimisée en bon accord avec les résultats expérimentaux. Les interactions faibles telles que les liaisons hydrogène C-H···O et C-H···S et les interactions de van der Waals importantes pour la formation des cristaux ont été identifiées à l'aide de la surface de Hirshfeld (HS) et des méthodes RDG. L'analyse PED a permis de déterminer les fréquences de vibration, étayées par les données FT-IR expérimentales. La théorie de la fonctionnelle de la densité en fonction du temps (TD-DFT) a été utilisée pour étudier les transitions électroniques, le transfert de charge et les spectres UV-vis. Les orbitales moléculaires frontières (FMO) et les cartes de distribution du potentiel électrostatique moléculaire (MEP) ont permis de mieux comprendre le transfert de charge et la réactivité. L'analyse ADMET computationnelle, telle que l'amarrage moléculaire, a évalué les propriétés physicochimiques, la pharmacocinétique et les impacts biologiques sur certains récepteurs. Cette étude fournit un examen approfondi des propriétés structurelles, électroniques et biologiques de la molécule synthétisée. Enfin, en effectuant des simulations approfondies de dynamique moléculaire (DM), nous avons découvert la capacité du composé à inhiber des enzymes sélectionnées et ses propriétés de liaison correspondantes, fournissant ainsi des informations cruciales pour son utilisation thérapeutique potentielle. Les énergies de liaison ont été calculées en utilisant MM-PBSA.

Mots clés : EMTh, TMTh, FT-IR, NMR, NLO, L'analyse ADMET, simulation DM et MM-PBSA

المخلص:

تركز هذه الدراسة على التوليف والتحليل المتعمق لمركبين مختلفين. تم توصيف المركب الأول (Z)-3-N-(إيثيل)-2-N'-(ثنائي ميثوكسيفينيل) امينو) ثيازوليدين-4-واحد (EMTh) باستخدام تقنيات الأشعة تحت الحمراء بالتحويل الفوري وطيف الرنين النووي البروتوني والكربوني 13، وتحليل بنية البلورة بواسطة حيود الأشعة السينية للبلورة الفردية. أظهر تحليل بنية البلورة تكوين جزيئي غير مستوٍ مع زاوية تجاوبية بين حلقة البنزين وحلقات الثيازوليدينون بزاوية 86.0 درجة ملحوظة. تم التحكم في التركيب الجزيئي للبلورة بواسطة الروابط الهيدروجينية C-H•••O و C-H•••N، مما أدى إلى نمط تراص ثلاثي الأبعاد فريد. أظهرت المحاكاة الكيميائية الكمية باستخدام نظرية B3LYP/6-311G(d,p) معلومات حول الكثافة الكهروستاتيكية للجزيئ، ومستويات الطاقة HOMO-LUMO، واتجاهات عزم ثنائي القطب، مما يؤكد استقرار المركب وقدراته على نقل الشحنات. أظهرت التحاليل التالية، مثل التدرج الكثافي المخفض، والمدار الكيميائي الطبيعي للروابط، وتحليل سطح هيرشفيلد، التفاعلات غير المرتبطة الجوهرية والروابط بين الذرات التي تؤثر على بنية البلورة. أظهرت الليجند نشاطًا بيولوجيًا قويًا من خلال إنشاء تفاعلات مهمة مع الأحماض الأمينية في البروتين (PDB ID: 2AZ5)، مما أدى إلى طاقة ربط تبلغ 6.3- كيلوكالوري/مول وتثبيط فعال لعامل تكون الأورام النخري. تم تخليق المركب الثاني (Z)-2-N-(تيربيتيل امينو) N’-3 (4 - ميثوكسيفينيل) ثيازوليدين-4-واحد (EMTh)

وتم فحصه بواسطة تقنيات الرنين النووي المغناطيسي النووي للبروتونات والكربون 13، والتحليل الطيفي بالأشعة تحت الحمراء FT-IR. تم تحديد هيكل البلورة المونوكلينيكي الذي يحتوي على ثمانية جزيئات في الخلية الواحدة باستخدام طريقة حيود الأشعة السينية على بلورة واحدة. أظهرت حسابات نظرية الدوال الكثافية (DFT) عن هندسة الجزيء المُحسنة باتفاق جيد مع النتائج التجريبية. تم التعرف على التفاعلات الضعيفة مثل الروابط الهيدروجينية C-H···O و C-H···S والتفاعلات فان در فالز المهمة لترتيب البلورات باستخدام سطح هيرشفيلد (HS) وطرق RDG. ساعد تحليل PED في تحديد ترددات الاهتزاز، مع الدعم من البيانات التجريبية FT-IR. تم استخدام نظرية الدوال الكثافية الزمنية المعتمدة على الدوال (TD-DFT) لدراسة الانتقالات الإلكترونية، ونقل الشحنات، وطيف الأشعة فوق البنفسجية المرئية. عرضت مدارات الجزيئات الأمامية (FMOs)، وخرائط توزيع الإمكانات الكهروستاتيكية الجزيئية (MEP) رؤى حول نقل الشحنة والتفاعلية. كما تم التنبؤ بالنشاط البصري غير الخطي (NLO) ملحوظ أيضًا من خلال المحاكاة الحسابية. قام تحليل ADMET الحسابي، مثل التحامل الجزيئي، بتقييم الخصائص الفيزيوكيميائية، والصيدلانية، والتأثيرات البيولوجية على بعض المستقبلات. تقدم هذه الدراسة فحصًا شاملاً للخصائص الهيكلية والإلكترونية والبيولوجية للجزيء المركب.

أخيرًا، من خلال إجراء محاكاة حركة الجزيئات الديناميكية (MD) الشاملة، تمكنا من كشف قدرة المركب على تثبيط بعض الإنزيمات المحددة وخصائص الربط المقابلة له، مما يوفر رؤى حاسمة لاستخدامه العلاجي المحتمل. تم حساب طاقات الربط باستخدام MM-PBSA.

الكلمات المفتاحية: EMTh ، TMTh، FT-IR، NMR، NLO، تحليلADMET ، محاكاة MD ، وMM-PBSA

Figure list

Table list

List of abbreviations

ADMET	Absorption, distribution, metabolism, excretion, and toxicity
B3LYP	Becke 3-paramètres Lee-Yang-Parr
CCDC	Cambridge Crystallographic Data Centre
DFT	Density Functional Theory
XRD	X-Ray diffraction
ED	electron density, donors and acceptors
FMO	Frontier Molecular Orbital
GCRD	Global chemical reactivity descriptors
GGA	Generalized Gradient Approximation
GIAO	Gauge-independent atomic orbital
GTO	Gaussian Type Orbital
HF	Hartree-Fock
HOMO	Highest Occupied Molecular Orbital
ICT	Intramolecular Charge Transfer
IR	Infrared
IUPAC	International Union of Pure and Applied Chemistry
LCAO	Linear Combination of Atomic Orbitals
LDA	Local Density Approximation
LUMO	Lowest Unoccupied Molecular Orbital
L-RMSF	Ligand Root Mean Square Fluctuation
MEP	Molecular electrostatic potential
MM-PBSA	Poisson-Boltzmann equation and molecular mechanics
NLO	Nonlinear optical properties
Pa	Probable activity
PASS	Prediction of activity spectra for substances
PBE	Perdew-Burke-Ernzerhof exchange-correlation functional
PCM	Polarizable Continuum Model
PED	Potential Energy Distribution
Pi	Probable inactivity
RDG	Reduced density gradient
NMR	Nuclear Magnetic Resonance
RMSD	Root means square deviation

RMSF	Root Mean Square Fluctuation
RG	Radius of gyration
SASA	Solvent accessible surface area
SCF	Self Consistent Field (méthode du champ auto-cohérent)
HS	Hirshfeld Surface
STO	Slater Type Orbital
TD-DFT	Time-Dependent-Density Functional
TMS	Tetramethylsilane
UV	Ultraviolet
VDW	Van der Waals

General introduction

Thiazolic compounds are an intriguing family of chemicals that have attracted the curiosity of scientists from many fields. In the literature review, we delve into the historical relevance, synthetic processes, structural subtleties and recent breakthroughs concerning the class of thiazolic compounds. We also cover their numerous practical application directions. To gather useful knowledge that might lead to significant advancements in materials science or pharmacology, the literature research focuses on recently discovered thiazolic structures, particularly rhodanine, thiazoline, and iminothiazolidinone derivatives [1-6].In addition to their significant importance in medicinal chemistry, thiazole derivatives have also been studied due to their nonlinear optical properties [7,8]. The mentioned compounds were examined using the capacity of a multidisciplinary approach, which includes X-ray diffraction, spectroscopic techniques, and molecular modeling. This approach allows us to uncover the complicated association between molecular structure and compound characteristics, opening the path for the creation of new materials and medicinal substances. These findings have implications for many fields of research and improve our knowledge of organic chemistry.

The use of quantum mechanical approximations is essential for predicting the structural and reactive behaviours of organic materials. This approach serves as a valuable addition to experimental techniques such as X-ray diffraction and spectroscopic characterization, which is anessential part of scientific research in our team at the Laboratory of Technology and Solid Properties (LTPS), focusing on the physicochemical characterization of newly synthesized materials [9-13]. The structural interpretation of new materials by X-ray powder diffraction (DRXP) has made remarkable progress in recent years. This is mainly because of advances at the instrumental and methodological levels, as well as the evolution of crystallographic programs. While molecular spectroscopy methods provide information about an isolated structure, independent of the macroscopic organization, X-ray diffraction mainly looks at the extended regularly organized structures. To facilitate an all-encompassing examination of material properties, each method is linked to a specific energy band of the electromagnetic spectrum. Currently, it is impossible to determine a molecule's spatial arrangement, periodicity, or crystal packing pattern and molecular geometric properties without X-ray diffraction.

Computational science advancements facilitate the use of quantum mechanical approaches to model, calculate, and store molecule features. The processing of molecular species via digital methods relies on the fundamental principles of quantum physics, namely the solution of the Schrödinger equation. Density Functional Theory (DFT) and time-dependent density functional theory (TD-DFT) are used to examine molecular properties, advancing the theoretical understanding of complex chemical systems [14].

The primary objective of the present work is to examine the structure and properties of two novel thiazolic derivatives by using single-crystal X-ray diffraction and spectroscopic techniques, and molecular modeling. The second goal of this work is to establish the correlation between the molecular structure of these two novel organic materials and their physicochemical characteristics by providing the structure-property relationship.

This research consists of several chapters. Commencing with the first chapter, an extensive literature review explores thiazolic compounds, providing an in-depth understanding of their historical, synthetic, and applicative dimensions, as well as the fundamental domains of thiazolic molecular compounds used in electrooptics and biology.

The second chapter unfolds a description of the various experimental methods utilized for determining thiazolic compound structures. This chapter examines various techniques, including X-ray diffraction, unravelling the molecular architecture, and laying out several general concepts that need to be considered to determine the crystalline structures of new organic materials using X-ray diffraction data and elucidate their molecular structures through different spectroscopic analysis methods.

In Chapter 3, the focus shifts to molecular modeling, where theoretical approaches can be applied towards the exploration of the intricate nature of thiazolic compounds. Schrödinger's postulates, the Born-Oppenheimer approximation, and density functional theory (DFT) serve as the theoretical compass guiding our exploration of the molecular electronic landscape. Density Functional Theory (DFT) is a recognized approach in quantum mechanics that is employed to characterize stable molecular systems. The Time-Dependent Density Functional Theory (TD-DFT) is an extension of DFT that focuses on studying excited states of molecules. It allows researchers to explore and comprehend the dynamic behaviours of molecules as they undergo transitions between states or respond to external influences.

This combination facilitates a comprehensive characterization of molecular attributes and adds to the advancement in theoretical knowledge of complex chemical processes.

Moving beyond theory, Chapter 4 involves a focused experimental investigation of the specific thiazolic compounds, molecules EMTh ($C_{12}H_{14}N_2O_2S$) and TMTH ($C_{14}H_{18}N_2O_2S$), which were synthesized by our collaborators at the Applied Organic Synthesis Laboratory (AOSL) at the University of Oran and showed good crystallization tendency. Accordingly, we employed SC-X-ray diffraction to determine their three-dimensional geometries. Through organic synthesis, crystallization, and X-ray crystallography, this chapter unravels detailed molecular structures and sheds light on their theoretical underpinnings.

Chapter five of the study examines the structural properties of the compounds EMTh and TMTH using spectroscopic methods. The compound's fundamental vibrational frequencies are analyzed, focusing on carbon-hydrogen oscillations inside the aromatic ring. The experimental infrared spectra and theoretical predictions show a good agreement. To perform precise ^{1}H and ^{13}C nuclear magnetic resonance calculations isotropic shielding values and deuterated chloroform as solvent is used. The chapter also examines the stability of the molecules and their reactions with other chemicals. UV-visible spectroscopy is used to examine absorption phenomena. These investigations provide a comprehensive understanding of the compound's properties, potentially revealing its potential bioactivity and reactivity. This chapter aims to elucidate spectral fingerprints, chemical shifts, and electronic characteristics, providing acomprehensive understanding of the structural intricacies.

The research adopted in Chapter 6 is based on the study that employed Gaussian 09 software [15] to perform ground-state simulations of the title molecules (EMTh and TMTh), utilizing Density Functional Theory (DFT) and the B3LYP functional to optimize the molecular geometry. The investigation encompassed the examination of Molecular Electrostatic Surface (MEP) and Global Chemical Reactivity Descriptors (GCRD) traits, which comprised electronegativity, chemical potential, hardness, softness, electrophilicity, and nucleophilicity indices. The study further assessed the dipole moment, polarizability, and hyperpolarizabilities of the molecule to examine its non-linear optical characteristics. The PASS analysis was employed to predict the biological activity of the chemicals in question by identifying probable receptors and assessing both possible activity and inactivity.

The molecular docking software AutoDockVina was employed to predict the binding affinity and interaction energy between the ligand and receptor. The drug-likeness features were evaluated using Lipinski's rule of five, while the SwissADME server supplied data on pharmacokinetic and physicochemical properties. The Molecular Dynamics simulation in GROMACS 2021 was employed to calculate binding energies and assess biological activity using metrics such as RMSD, Rg, RMSF, SASA, and MM-PBSA. This comprehensive approach improves our comprehension of the chemical's structural, kinetic, and biological characteristics.

Collectively, these chapters form a cohesive narrative, unveiling layers of thiazolic compounds from historical roots through structural elucidation, theoretical modeling, and practical applications. The synthesis of knowledge across these chapters enriches our understanding, paving the way for future advancements and applications in the realm of chemistry and beyond.

At the end of this thesis, we will discuss the main results obtained and their significant contribution to this vast research theme.

References

[1] M. Krátký, S. Bősze , Z. Baranyai, J. Stolaříková, J. Vinšová, Synthesis and biological evolution of hydrazones derived from 4-(trifluoromethyl)benzohydrazide. Bioorg. Med. Chem. (2017). DOI: 10.1016/j.bmcl.2017.10.050

[2] T. Tomasic, L.P. Masic, Rhodanine as a privileged scaffold in drug discovery, Current Medicinal Chemistry, 16, 1596-1629. (2009). doi: 10.2174/092986709788186200

[3] Y. Momose, K. Meguro, H.Ikeda, C.Hatanaka, S.Oi, T. Sohda, Studies on antidiabetic agents. X. Synthesis and biological activities of pioglitazone and related compound. Chem. Pharm. Bull. (Tokyo), 39, 1440–1445. (1991)

[4] H. Jung, J. Lee, K. Chung, J. Hong, J. Choi, S. Kim, E. Roh, K. Shin, K. Lee, Novel Rhodanine Derivative, 5-[4-(4-Fluorophenoxy) phenyl]methylene-3-{4-[3-(4-methylpiperazin-1-yl) propoxy]phenyl}-2-thioxo-4-thiazolidinone dihydrochloride, Induces Apoptosis via Mitochondria Dysfunction and Endoplasmic Reticulum Stress in Human Colon Cancer Cells Molecules, 23, 2895. (2018). doi.org/10.3390/molecules23112895.

[5] C. Tintori, G. Iovenitti , E. R. Ceresola , R. Ferrarese, C. Zamperini, A. Brai, G. Poli, E. Dreassi, V. Cagno, D. Lembo, F. Canducci , M Botta, Rhodanine derivatives as potent antiHIV and anti-HSV microbicides. PLoS ONE 13(6): e0198478, (2018). doi.org/10.1371/journal.pone.0198478.

[6] T. Marinado, D. P. Hagberg, M. Hedlund, T. Edvinsson, E. M. J. Johansson, G. Boschloo,ya H. Rensmo, T. Brinck, L. Sun, A. Hagfeldty. Phys. Chem. Chem. Phys., 11. (2009). doi.org/10.1039/B812154

[7] V. Smokal, B. Derkowska, R. Czaplicki, O. Krupka, A. Kolendo, and B. Sahraoui, Opt. Mater., 31, 554 (2009).

[8] V. Smokal, A. Kolendo, B. Derkowska, R. Czaplicki, O. Krupka, and B. Sahraoui, Mol. Cryst. Liquid Cryst., 485, 1011 (2008).

[9]:N.E.L. Belkafouf, F. T. Baara, A. Altomare, R. Rizzi, A. Chouaih, A. Djafri, F. Hamzaoui, Synthesis, PXRD structural determination, Hirshfeld surface analysis and DFT/TD-DFT investigation of 3N-ethyl-2N'-(2-ethylphenylimino) thiazolidin-4-one, Journal of Molecular Structure. 1189 8-20. (2019)

[10]: Y. Megrouss, F. Triki Baara, N. Boukabcha, A. Chouaih, A. Hatzidimitriou, A. Djafri, F. Hamzaoui, Synthesis, X-Ray Structure Determination and Related Physical Properties of Thiazolidinone Derivative by DFT Quantum Chemical Method Acta Chim. Slov. 66. (2019).

[11] N. Boukabcha, A. Feddag, R. Rahmani, A. Chouaih, F. Hamzaoui, Molecular structure, multipolar charge density study and nonlinear optical properties of 4-methyl-N-[(5-nitrothiophen-2-ylmethylidene)] aniline, Journal of Optoelectronics and Advanced Materials Vol. 20, Iss. 3-4, pp. 140-148 (2018).

[12]: A Djafri, A Chouaih, J.C Daran, Ay. Djafri, F. Hamzaoui, Crystal and molecular structure of (2Z,5Z) -3-(2-methoxyphenyl) -2-[(2-methoxyphenyl)imino]-5-(4 nitrobenzylidene) thiazolidin-4-one. Acta crystallographica Section E: Crystallographic communications, , 73 (4), pp.511-514. (2017).

[13]: N. Khelloul, K. Toubal, N. Benhalima, R. Rahmani, A. Chouaih, Ayada Djafri and Fodil Hamzaoui. Crystal Structure, Hirshfeld Surface Analysis and Computational Studies of Thiazolidin-4-one derivative: (Z)-5-(4-Chlorobenzylidene) -3-(2-ethoxyphenyl)-2-thioxothiazolidin-4-one, Acta Chim. Slov. (2016).

[14] R.I. Bahoussi, Etude structurale, thermique et vibrationnelle d’un nouveau composé organique, le C18H20O3N4S, Thèse de doctorat, Université Abdelhamid Ibn Badis Mostaganem, (2017).

[15] M. J. Frisch, G. W. Trucks, H. B. Schlegel, G. E. Scuseria, M. A. Robb, J. R. Cheeseman, G. Scalmani, V. Barone, B. Mennucci, G. A. Petersson, H. Nakatsuji, M. Caricato, X. Li, H. P. Hratchian, A. F. Izmaylov, J. Bloino, G. Zheng, J. L. Sonnenberg, M. Hada, M. Ehara, K. Toyota, R. Fukuda, J. Hasegawa, M. Ishida, T. Nakajima, Y. Honda, O. Kitao, H. Nakai, T. Vreven, J. A. Montgomery, Jr., J. E. Peralta, F. Ogliaro, M. Bearpark, J. J. Heyd, E. Brothers, K. N. Kudin, V. N. Staroverov, R. Kobayashi, J. Normand, K. Raghavachari, A. Rendell, J. C. Burant, S. S. Iyengar, J. Tomasi, M. Cossi, N. Rega, J. M. Millam, M. Klene, J. E. Knox, J. B. Cross, V. Bakken, C. Adamo, J. Jaramillo, R. Gomperts, R. E. Stratmann, O. Yazyev, A. J. Austin, R. Cammi, C. Pomelli, J. W. Ochterski, R. L. Martin, K. Morokuma, V. G. Zakrzewski, G. A. Voth, P. Salvador, J. J. Dannenberg, S. Dapprich, A. D. Daniels, Ö. Farkas, J. B. Foresman, J. V. Ortiz, J. Cioslowski, D. J. Fox, Gaussian 09, Revision D.01(Computer Software), Gaussian, Inc.,Wallingford, CT, United States, 2013

Chapter I

Literature review on thiazolic compounds

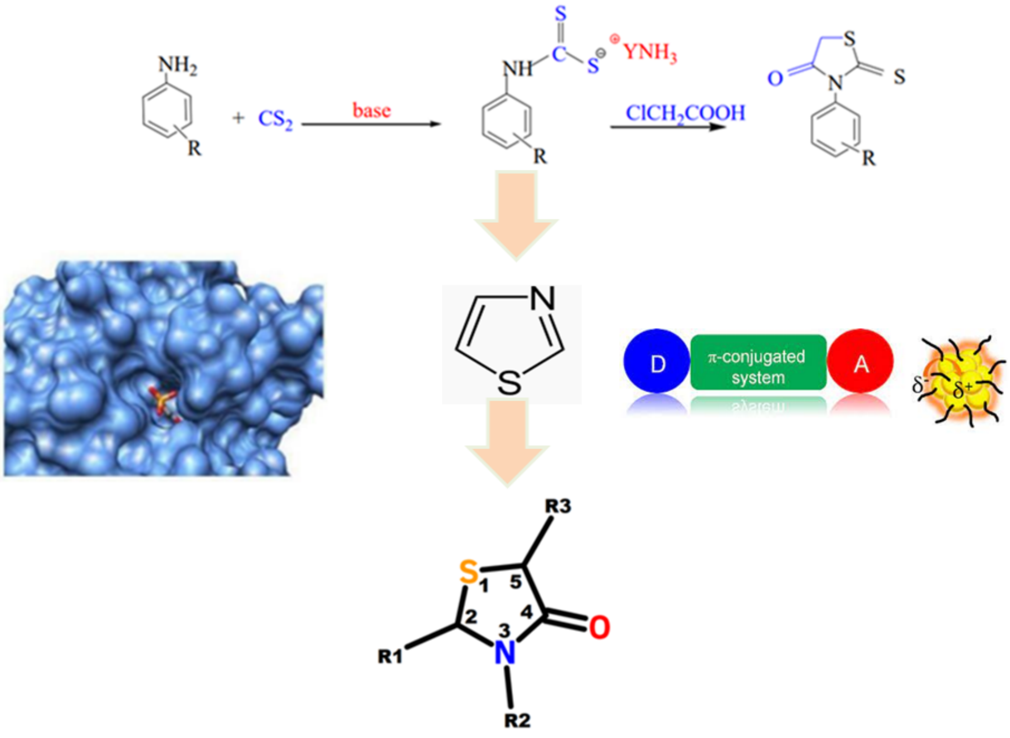

I.1. Introduction:

A flammable light yellow liquid with the chemical formula C3H3NS known as thiazole is made up of 5 atoms in the cycle, with nitrogen and sulphur serving as two of the ring's vertices and carbon serving as the other three. Thiazoles are the basic nucleus of many pharmaceuticals, including antibiotics, biocides, and fungicides, as well as colours and aromas. [1] Thiazole scaffolds have the potential to be used in the synthesis of derivatives with varied matrices due to the considerable flexibility of substituent introduction, namely at the C-2, C-4, and C-5 positions.

There are two types of thiazole subgroups:

- thiazoles, in which the sulphur and azote are separated by a carbon atome
- The isothiazoles, in which the sulphur and the azote are inextricably linked.

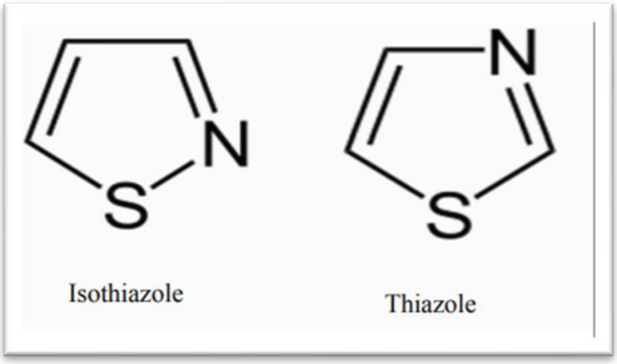

Figure I.1. Basic core structure of thiazole and isothiazole

Because of their planar structure and electrodonor effect, heterocycles such as thiazole play a key role in the structure of merocyanines. Since its discovery by Hantzsch, the thiazole has continued to pique the interest of scientists. Different synthetic methods are used in the laboratory.

Some of the most important naturally occurring physiologically active anticancer drugs, such as epothilone B [2], bleomycin [3], and dolastatin 10 [4] have thiazole in their structure. They are also commonly found in pharmaceutically powerful antibiotics such as Thiocillin I, Berninamycin, Thiostrepton methyl ester, Thiostrepton, and Siomycin A [5]. Some thiazole-containing polymers have been reported to be suitable sensors [6, 7], photocatalysts [8], and semiconductors [8] Thiazole-containing compounds are clearly among the most important organic molecules [9].

Thiazole scaffolds have long fascinated researchers because to their pharmacological and biological capabilities, which include anti-inflammatory [10,11], anticonvulsant [12], anticancer [13], anti-material [14], and antibacterial [15,16]. Thiazole Schiff base derivatives have received a lot of interest due to their unusual structure and antibacterial [17], antiviral [18], antiplasmodial [19], and anticancer [20] activities.

I.2. A Brief history of the thiazole ring's discovery

On November 18, 1887, Arthur Rudolf Hantzsch and his collaborator, J. H. Weber, signed the thiazole birth certificate. Under the title "Ueber Verbindungen des Thiazoles (F'yridins der Thiophenreihe)," Hantzsch and Weber (21) defined Thiazoles as "those Stickstoff und Schwefel in ringformiger Bindung enthaltenden Substanzen von Formel (CH),NS, die sich zum Pyridin verhalten, wie das Thiophen zum Benzol." They demonstrated the existence of thiazole (22) and isothiazole (23), despite the fact that neither was recognised in the free state at the time, likened them to glyoxaline and pyrazole, respectively, and proposed naming benzothiazole the "Methenylamidophenylmercaptan" recently found by A. W. Hofmann (24). Extending this definition, they proposed designating the three azole derivatives of thiophen, pyrrole, and furan, respectively, thiazole, imidazole, and oxazole, as well as their benzo-derivatives, benzothiazole, benzimidazole, and benzoxazole. They proposed the prefix meso for this location in the conventional azole series to account for the elevated reactivity of the groups linked to the carbon atom between sulphur and nitrogene. They observed that several thiazole derivatives might already be known without their proper constitution being described: they assigned all of the so-called a-thiocyano derivatives of ketones and aldehydes (26) ("Rhodanketone") to being thiazole derivatives, particularly meso-oxythiazoles (27).

I.2.1. A brief overview of the synthetic processes used to create the thiazole nucleus

The researchers used a variety of ways to create thiazole-containing scaffolds (Fig. 1). Hantzsch thiazole synthesis is the oldest and most widely used technique of thiazole synthesis, which involves the reaction of thioamides with -haloketones [21]. Another typical approach for thiazole synthesis is Robinson-Gabriel synthesis, which involves thialation of acylamino-ketone in the presence of phosphorus pentasulfide and heat to produce the appropriate 2,5-disubstituted thiazole [22]. Cook-Heilbron proposed a carbon disulphide-mediated synthesis of 5-amino-2-mercaptothiazole from comparable amino-nitriles [23]. Synthesis of N-substituted thiazoles by condensation of thiourea/thiamide with substituted acetophenones in the presence of bromine and ammonium hydroxide is an alternate technique [24,25]. A domino alkylation-cyclization reaction of propargyl bromide and thiourea in the presence of potassium carbonate and dimethylformamide was used to synthesis 2-aminothiazole derivatives (a green chemistry technique) [26]. -lactones create a large yield of corresponding thiazoles when reacting with Lawesson's reagent [27].

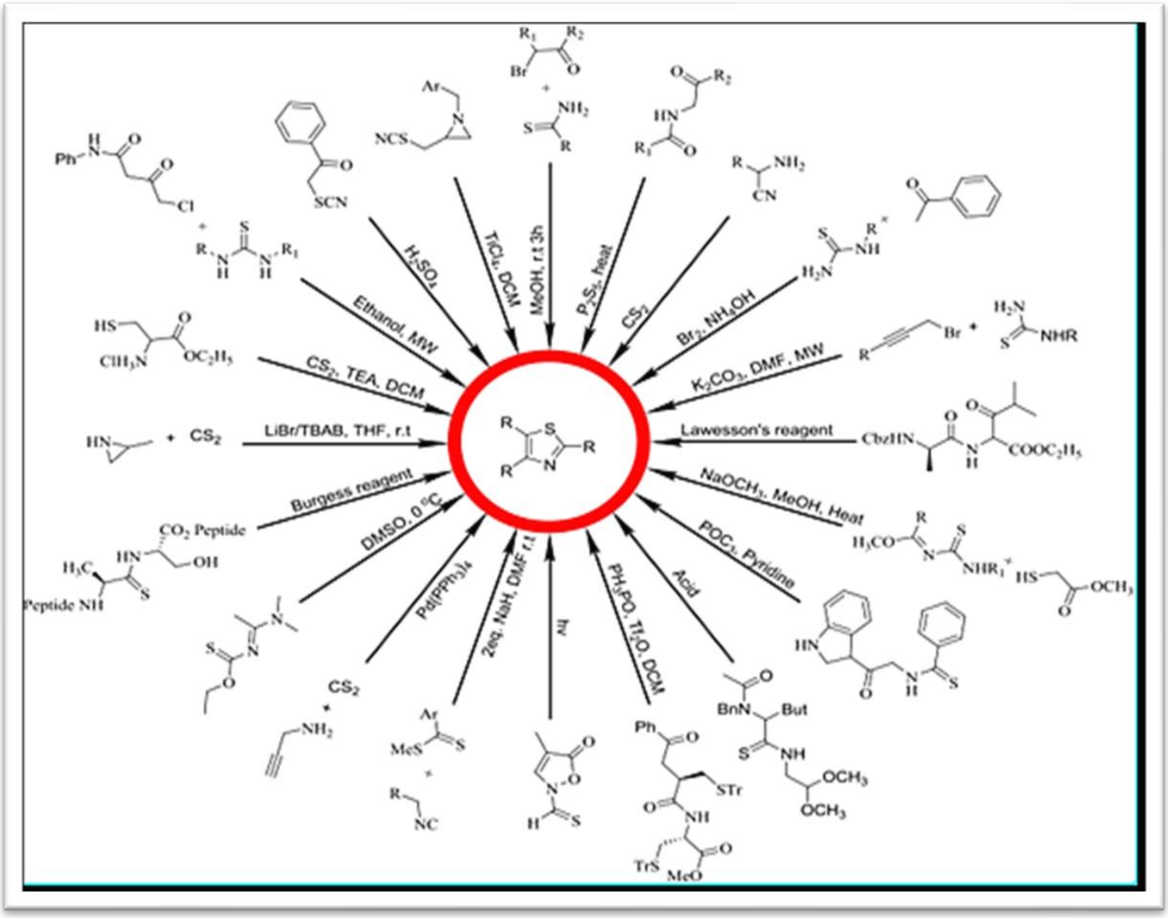

Figure I. 2. The synthetic processes ofthiazolic derivatives**.**

Another approach for producing substituted thiazoles is the reaction of thiocarbamoylimidate with methyl thioglycolate in the presence of methanol and sodium methoxide [28]. Thiazole scaffold was produced by reacting thiobenzamide with phosphorus oxychloride in the presence of pyridine [29].

Under acidic circumstances, endothiopeptide was transformed into a thiazole derivative [30]. Trifluoromethane sulfonic anhydride and triphenylphosphine oxide can also be treated with Cys-Cys-dipeptide in a solvent such as dichloromethane to produce substituted thiazole [31,32]. Under photochemical circumstances, intramolecular cyclization of iminocarbene in the presence of thiocyclisooxazol-5(2H)-ones yields substituted thiazoles [25,33]. 4,5-disubstituted thiazoles were synthesized by reacting methyl carbodithioates with active-methylene containing isocyanides in the presence of a base such as sodium hydride and dichloromethane as a solvent [22,25]. Proparglyamine is cyclized with carbon disulfide in the presence of a palladium catalyst to produce thiazole derivatives [25,34]. Trimethyl sulfonium was treated with Nthioacylamidone in the presence of dimethyl sulphoxide to produce thiazoline derivative [25]. Using the Burgess reagent, 2-thiazolines were synthesised from corresponding N-(hydroxyethyl)thiopeptides [35]. Using lithium bromide and TBAB as catalysts and tetrahydrofuran (THF) as the solvent, 1,3-thiazolidine-2-thione was synthesised by reacting 2-methylaziridine with carbon disulfide. In the presence of triethylamine, l-cysteine ethyl ester hydrochloride interacts with carbon disulfide to form thiazolidine ester. -Chloroketones were combined with asymmetrical thiourea under solvent-free circumstances and microwave irradiation reaction conditions to yield imino4-thiazolines [25,36]. Sulphuric acid treatment of -thiocyanatoacetophenones yields the equivalent 4-arylthiazol-2(3H)-ones [37]. Aziridines are catalysed by lewis acid titanium tetrachloride in dichloromethane to produce thiazolidine, which contains the basic core of thiazole [25,38].

I.3. Hantzsch procedure

Hantzsch's (1889) synthesis is a reaction between a halocetone and a thioamide. DiagramI-3 depicts the synthesis of 2,4-dimethylthiazole from acetamide and chloroacetone 2.

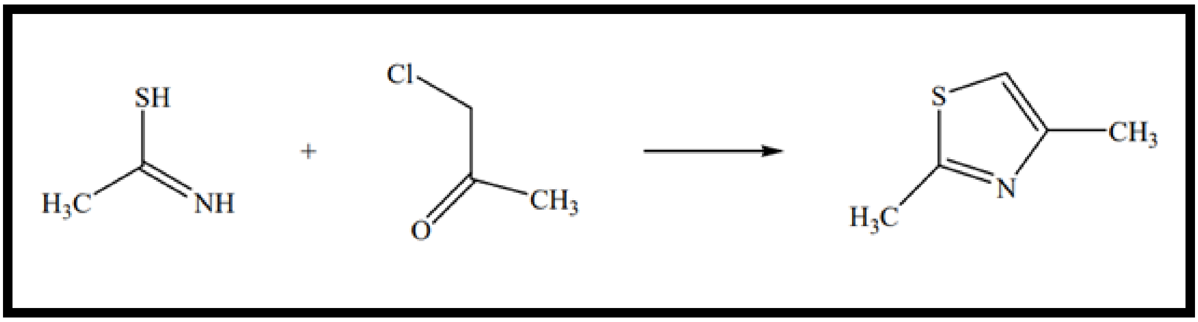

Figure I.3. Hantzsch synthesis

I.3.1. Thiazolidinones

The methods for synthesizing thiazolidinones and their derivatives are well discussed in the literature; we will provide an overview of some commonly used methods in the laboratory apply as a reagent for an acid α-halo or its derivatives.

Figure II-1 depicts the reactive approach for heterocyclization.

Yields range from 14 to 19%. 3

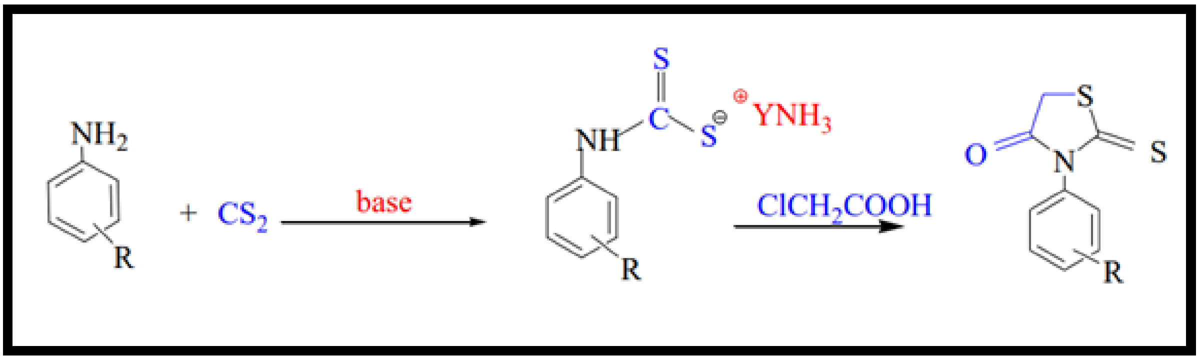

Figure I.4. Synthesis of thiazolidinones from α-halo acids or their derivatives

I.3.1.1. Thiazolidinone structure

According to IUPAC [39] thiazolidinones are five-membered cycles with two heteroatoms, a sulfur atom in position 1, an azote atom in position 3, a carbonyl grouping in position 4, and various chemical groups that can act as substituents in positions 2, 3, and 5, as shown in Figure I.5.

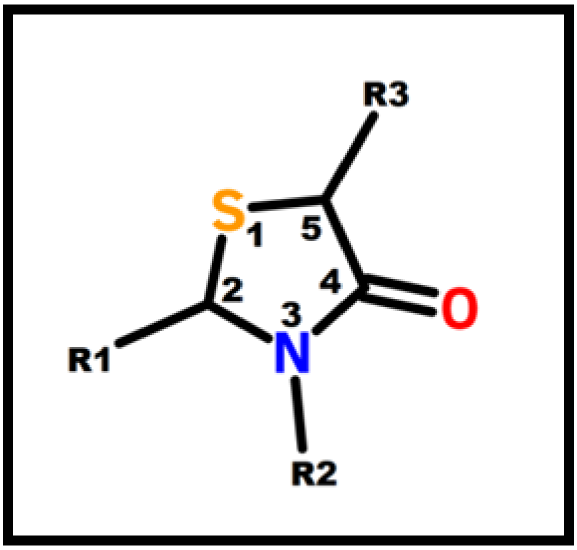

Figure I.5. Thiazolidinone nucleus

I.3.2. Thiazole ring numbering

Initially described by A. Hantzsch and J. Weber [40] as "the pyridine of the thiophene series," thiazole [40] received a nomenclature that corresponded to this definition [41]: the letters A and B were justified by the strong analogy of both positions with those of pyridine, while the meso position, to which P was assigned, had no equivalent in the pyridine ring. The sulfur atom was numbered 1, and the nitrogen atom was numbered 3 [42] in Richter's Lexikon and the second edition of Meyer-Jacobson's Lehrbuch der Organischen Chernie. T. B. Johnson [43] offered the number 3, although J. Metzger et al. [44-54] utilized a different system [45] than indicated by Grignard's “Traité de Chimie Organique”[56]. The Ring Index [57] and Chemical Abstracts provide the right numbering, which equates to 2.

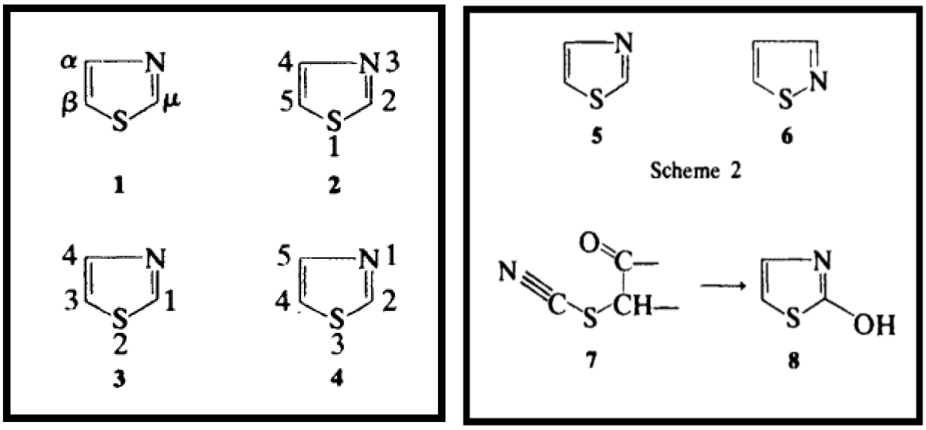

Figure I.6. Thiazole ring numbering.

I.3.2.1. Structure of thiazoles

The systematic names of chemical structures necessitate certain nomenclature systems, and each nomenclature system necessitates the use of specific nomenclature rules. There are other nomenclature systems1-8 accessible in the literature; however, the most significant systems approved by the IUP AC for identifying heterocycles are described.

I.3.2.2. System of nomenclature

The most systematic nomenclature of heterocycles is based on the names of carbocyclic analogues, and so the nomenclature systems are adaptations of those used for carbocycles. On the other hand, the nomenclature system, most widely used for heterocycles, combines trivial and systematic names.

I.4. Systematic nomenclature (Hantzsch-Widman system)

This is the most common systematic method for identifying three- to ten-membered monocyclic heterocycles with varying degrees of unsaturation and one or more heteroatoms. This method of naming describes the size of the ring the nature, type, and position(s) of the heteroatom(s).

The heteromonocycles are named according to the new regulation! No. 3 in the Hantzsch-Widman nomenclature scheme.

1) Prefix(es) combined with stem One or more 'a' prefixes for the heteroatom(s) are combined with a stem specifying the size of the ring to form the name of the heteromonocyclic system. The' a' prefix's terminal letter is dropped if the stem begins with a vowel. Prefixes: The prefixes represent the heteroatoms found in heterocyclic systems. Table 1 shows the preferred order of the prefixes for various heteroatoms.

Table I.1. Prefixes for heteroatoms (in decreasing order of priority, 'a' prefixes)

Heteroatom	Symbol (Valence)	Prefix
Oxygen	O(ll)	Oxa
Sulfur	S(ll)	Thia
Seleniwn	Se(ll)	Selena
Telluriwn	Te(ll)	Tellma
Nitrogen	N(Ill)	Aza
Phosphorus	P(Ill)	Phospha
Arsenic	As (ill)	Arsa
Antimony	Sb(lll)	Stiba
Bismuth	Bi(lII)	Bisma
Silicon	Si(IV)	Sila
Gennaniwn	Ge(IV)	Genna
Tin	Sn{lV)	Stanna
Lead	Pb(IV)	Plwnba
Boron	B(III)	Bora
Mercury	Hg(II)	Mercura

Stems: In heteromonocyclic systems, stems are employed to signify ring size and saturation or unsaturation, and are summarized in Table I.2.

Table .I.2. Employed stems In heteromonocyclic systems signifying the ring size and saturation or unsaturation,

Ring size	Unsaturation	Saturation
Three-membered	-irene i	-irane ii
Four-membered	-été	-etane ii
Five-membered	-ole	-olane ii
Six-membered	A* -ine	-ane
	B* -ine	-inane
	C* -inine	-inane
Seven-membered	-epine	-epane
Eight-membered	-ocine	-ocane
Nine-membered	-onine	-onane
Ten-membered	-ecine	-ecane

However, the following considerations should be made while naming heteromonocycles:

(i) For three-membered nitrogen-containing unsaturated heteromonocycles, the stem 'irine' is used.

(n) The nitrogen-containing saturated three-, four-, and five-membered heteromonocycles are denoted by the stems 'iridine,' 'etidine,' and 'olidine,' respectively.

(m) A numerical prefix's terminal vowel is not lost, even if the prefix begins with the same vowel, as in cyclotetraazoxane.

(iV) The Dame's ending is determined by the presence or absence of nitrogen.

(v) When the heteroatoms have the typical valences shown in Table I.1, unsaturated stems are employed to form rings with the greatest amount of noncumulative double bonds possible. (vi) For rings with no double bonds, saturated stems are employed.

(vii) If no stems are indicated for partially or completely saturated heteromonocycles, the prefixes 'dihydro-', 'tetrahydro-', and so on should be used.

(viii) the terminal 'e' used in all stems is optional (in CAS index nomenclature, stems without a terminal 'e' are used for unsaturated non-nitrogenous rings with six or more ring members, such as dioxin, dithiin, and oxathiin).

(Ix) The stems 'etine' and 'oline', which were previously used for nitrogen containing four- and five-membered rings with one double bond, respectively, are no longer suggested by IUP AC.

(x) For six-membered rings, the stems are determined by the least desired heteroatom in the ring, i.e. the heteroatom immediately before the stem.

The following set of least favored heteroatoms is chosen to establish the suitable stem for a six-membered ring: S, Se, Te, Bi, Hg, 6A * = 0 N, Si, Ge, Sn, Pb = 6B* The stems (syllables) signifying ring sizes (3, 4, 7, 8, 9, and 10) are thought to be derived from numerical prefixes (Table I.1.).

(xil) trivial names, such as pyrrole, pyrazole, imidiazole, pyridine, pyridazine, pyrimidine, and so on, should be preferred over systematic names for several heteromonocyclic systems approved by IUPAC.

(xiiI) The term oxine should not be used for pyran because it has been used as a synonym for quinolin-8-01.

Nomenclature of Heterocycles 7 (xiv) Because it is used as a class name for compounds having the =N - N = group, azine must not be used for pyridine.

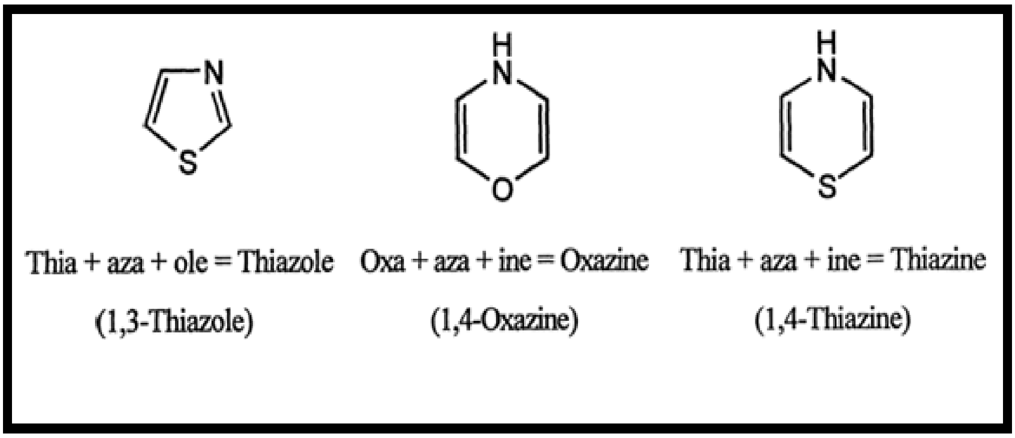

Figure I.7. Nomenclature examples

I.5. Electron densities at the frontier orbitals

The border electron densities are a feature of an isolated molecule, and their usage as reactivity indices assumes that the electron distribution in the transition state is similar to that in the beginning state. The distribution of frontier electron densities is substantially more irregular, and the relative order of the densities does not alter when approached by the reagent. The frontier electron densities are connected with electron exchange rather than electrostatic interaction, and if electron exchange (charge transfer) is important in stabilizing the transition state, the frontier electron densities influence the reactivity. The frontier electron density in electrophilic substitution is the density in the highest filled molecular orbital (HOMO), and these electrons are thought to be equivalent to the valence electrons. The frontier electron density in electrophilic substitution is the density in the highest filled molecular orbital (HOMO), and these electrons are thought to be equivalent to an atom's valence electrons. The interaction of the highest occupied molecular orbital (frontier orbital) of the heteroaromatic system with the lowest unoccupied molecular orbital of the electrophile results in the electrophilic substitution process. The activation energy is determined by the level of mixing, which is determined by the difference in energy between these two types of orbitals. The smaller the energy difference, the lower the activation energy and the faster the reaction with more efficient orbital mixing. The frontier molecular orbital in nucleophilic substitution is the lowest unoccupied molecular orbital (LUMO). The nucleophilic substitution process includes the mixing of the heteroaromatic system's lowest vacant molecular orbital with a nucleophile's filled molecular orbital. The electron pair in the transition state is accepted by the heteroaromatic molecule, and the frontier electron density at the carbon atom is then the electron density in this molecular orbital as if it were occupied by two electrons. The electrophilic and nucleophilic reactions occur when the relevant border electron density is greatest (Figure.I.8).

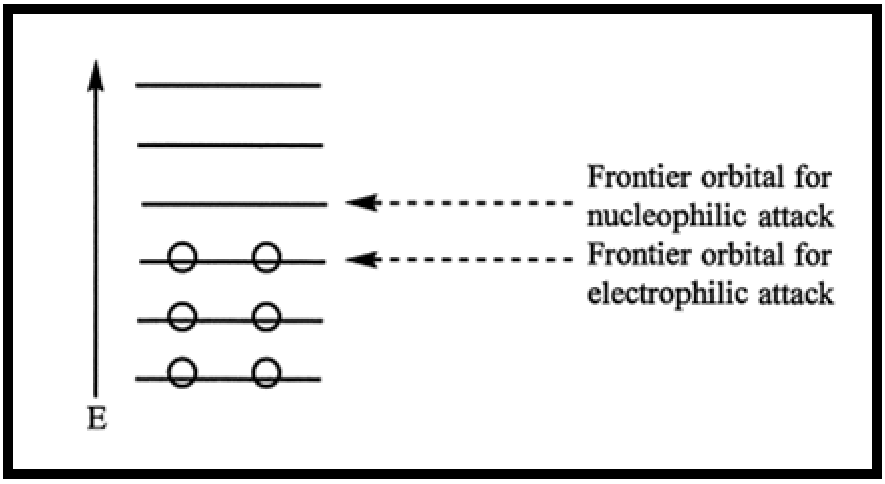

Figure I.8. Representation of frontier orbitals for electrophilic and nucleophilic attacks.

I.6. Thiazolidinones applications

4-Thiazolidinones andassociated heterocyclic-based compoundshave been widely investigated as sources of antiinflammatory, anticancer, antimicrobial, antidiabetic, and antibacterial agents. Since the 1960s[58-60], there has been a considerable increase in the number of scholarly papers [61], numerous reviews, and patents covering diverse 4-thiazolidinone compounds [62-67].

I.6.1. Non-linear optical activity

Non-linear optical (NLO) chemical compounds are employed in a variety of applications, including optical coupling between fibers and laser light generation, which is critical for photonic computation and logic operations[68]. Thiazolidinone derivatives have not been linked to any physiological or photochemical applications. [69]. Recently, the thiazolidinone moiety has been exploited to create polymeric models with improved NLO characteristics. The push-pull effect of rhodanine, also known as a 2-thioxo-4-thiazolidinone derivative, has been studied, and its favourable photochemical and photophysical properties have led to a wide range of NLO applications [70]. [71].In addition, Thiazolidinone compounds can have luminescence features [72,73] and are also known to have other attractive physicochemical features like optoelectronics and photovoltaics. [74,75].

I.6.2. Biological activity

Thiazolidinone derivatives represent a class of compounds of significant scientific interest owing to their chemical characteristics and diverse pharmacological effects, such as antimicrobials, [76,77] antioxidants, [78,79] antifungals, [80] antihyperglycemic, and [81] antibacterial. [82] They have been widely employed in synthesizing compounds with therapeutic applications since the discovery of MKT-077 [83,84], and they are thought to be powerful inhibitors of cancer cells. [85-87] Thiazolidinones pique the curiosity of researchers and open up new avenues in the fight against diseases such as allergies, cancer, and malaria. [88-90]

I.7. Conclusion

Researchers have found many interesting things about thiazolic cycles in organic compounds such as rhodanine, thiazoline, and iminothiazolidinone that have to do with how their molecules are structured. This relationship is crucial to understanding the behaviour and functionality of organic molecules. The research focuses on novel thiazolic structures, specifically rhodanine, thiazoline, and iminothiazolidinone, to gain valuable knowledge that could lead to significant breakthroughs in materials science and pharmacology. The research uses a multidisciplinary approach, including X-ray diffraction, spectroscopic approaches, and molecular modelling, to analyze these substances' molecular structures and functional capabilities. The aim is to unravel the complex correlation between molecular structure and properties, paving the way for the development of advanced materials and therapeutic compounds. This discovery not only enhances understanding of organic chemistry but also shows potential for various scientific disciplines.

[1] Easy access to the family of thiazole.Chemical Communications,(2006), 2262

[2] K.-H. Altmann, Epothilone B and its Analogs - A New Family of Anticancer Agents, Mini-Reviews Med. Chem. 3 (2) (2005) 149–158, https://doi.org/10.2174/1389557033405269.

[3] M. Linnert, J. Gehl, Bleomycin treatment of brain tumors: An evaluation, Anticancer. Drugs 20 (3) (Mar. 2009) 157–164, https://doi.org/10.1097/CAD.0b013e328325465e.

[4] S.B. Singh, Discovery and Development of Dolastatin 10-Derived Antibody Drug Conjugate Anticancer Drugs, J. Nat. Prod. 85 (3) (2022) 666–687, https://doi.org/10.1021/acs.jnatprod.1c01135.

[5] B. Pandit, U. Bhat, A.L. Gartel, Proteasome inhibitory activity of thiazole antibiotics, Cancer Biol. Ther. 11 (1) (Jan. 2011) 43–47, https://doi.org/10.4161/cbt.11.1.13854.

[6] F. Li, F. Meng, Y. Wang, C. Zhu, Y. Cheng, Polymer-based fluorescence sensor incorporating thiazole moiety for direct and visual detection of Hg2+ and Ag+, Tetrahedron 71 (11) (2015) 1700–1704, https://doi.org/10.1016/j.tet.2015.01.052.

[7] B.P. Biswal et al., Sustained Solar H2 Evolution from a Thiazolo[5,4-d]thiazoleBridged Covalent Organic Framework and Nickel-Thiolate Cluster in Water, J.Am. Chem. Soc. 141 (28) (2019) 11082–11092, https://doi.org/10.1021/jacs.9b03243.

[8] Y. Liu et al., High performance nanocrystals of a donor-acceptor conjugated polymer, Chem. Mater. 25 (13) (2013) 2649–2655, https://doi.org/10.1021/cm4011579.

[9] S. Pola, Significance of Thiazole-based Heterocycles for Bioactive Systems, in: Scope of Selective Heterocycles From Organic and Pharmaceutical Perspective, IntechOpen, Rijeka, 2016, p. p. Ch. 1., https://doi.org/10.5772/62077

[10] R.G. Kalkhambkar, G.M. Kulkarni, H. Shivkumar, R.N. Rao, Synthesis of novel triheterocyclic thiazoles as anti-inflammatory and analgesic agents, Eur. J. Med. Chem. 42 (2007) 1272–1276, https://doi.org/10.1016/j.ejmech.2007.01.023.

[11] R.N. Sharma, F.P. Xavier, K.K. Vasu, S.C. Chaturvedi, S.S. Pancholi, Synthesis of 4-benzyl-1,3-thiazole derivatives as potential anti-inflammatory agents: an analoguebased drug design approach, J. Enzyme Inhib. Med. Chem. 24 (2009) 890–897, https://doi.org/10.1080/14756360802519558.

[12] F. Azam, I.A. Alkskas, S.L. Khokra, O. Prakash, Synthesis of some novel N4-(naphtha[1,2-d]thiazol-2-yl)semicarbazides as potential anticonvulsants, Eur. J. Med. Chem. 44 (2009) 203–211, https://doi.org/10.1016/j.ejmech.2008.02.007.

[13] T.N. Minh An, M.A. Kumar, S.H. Chang, M.Y. Kim, J.A. Kim, K.D. Lee, Synthesis, anticancer and antioxidant activity of novel 2,4-disubstituted thiazoles, Bull. Korean Chem. Soc. 35 (2014) 1619–1624, https://doi.org/10.5012/ bkcs.2014.35.6.1619.

[14] H.N. Karade, B.N. Acharya, M. Sathe, M.P. Kaushik, Design, synthesis, and antimalarial evaluation of thiazole-derived amino acids, Med. Chem. Res. 17 (2008) 19–29, https://doi.org/10.1007/s00044-008-9089-0.

[15] S.K. Bharti, G. Nath, R. Tilak, S.K. Singh, Synthesis, anti-bacterial and anti-fungal activities of some novel Schiff bases containing 2,4-disubstituted thiazole ring, Eur. J. Med. Chem. 45 (2010) 651–660, https://doi.org/10.1016/j. ejmech.2009.11.008.

[16] S. Bondock, T. Naser, Y.A. Ammar, Synthesis of some new 2-(3-pyridyl)-4,5-disubstituted thiazoles as potent antimicrobial agents, Eur. J. Med. Chem. 62 (2013) 270–279, https://doi.org/10.1016/j.ejmech.2012.12.050.

[17] P. Karegoudar, M.S. Karthikeyan, D.J. Prasad, M. Mahalinga, B.S. Holla, N. S. Kumari, Synthesis of some novel 2,4-disubstituted thiazoles as possible antimicrobial agents, Eur. J. Med. Chem. 43 (2008) 261–267, https://doi.org/ 10.1016/j.ejmech.2007.03.014.

[18] S.S. Jadav, S. Kaptein, A. Timiri, T. De Burghgraeve, V.N. Badavath, R. Ganesan, B. N. Sinha, J. Neyts, P. Leyssen, V. Jayaprakash, Design, synthesis, optimization and antiviral activity of a class of hybrid dengue virus e protein inhibitors, Bioorg. Med. Chem. Lett. 25 (2015) 1747–1752, https://doi.org/10.1016/j.bmcl.2015.02.059.

[19] P. Makam, P.K. Thakur, T. Kannan, In vitro and in silico antimalarial activity of 2- (2-hydrazinyl)thiazole derivatives, Eur. J. Pharm. Sci. 52 (2014) 138–145, https:// doi.org/10.1016/j.ejps.2013.11.001.

[20] A. Ignat, T. Lovasz, M. Vasilescu, E. Fischer-Fodor, C.B. Tatomir, C. Cristea, L. Silaghi-Dumitrescu, V. Zaharia, Heterocycles 27. Microwave assisted synthesis and antitumour activity of novel phenothiazinyl-thiazolyl-hydrazine derivatives,

[21] A. Hantzsch, J. Weber, Ueber verbindungen des thiazols (pyridins der thiophenreihe), Ber. Dtsch. Chem. Ges. 20 (1887) 3118–3132.

[22] A. Ayati, S. Emami, A. Asadipour, A. Shafiee, A. Foroumadi, Recent applications of 1, 3-thiazole core structure in the identification of new lead compounds and drug discovery, Eur. J. Med. Chem. 97 (2015) 699–718.

[23] A.-.M. Borcea, I. Ionuț, O. Crișan, O. Oniga, An overview of the synthesis and antimicrobial, antiprotozoal, and antitumor activity of thiazole and bisthiazole derivatives, Molecules 26 (2021) 624.

[24] A. Prajapati, V.P. Modi, Synthesis and biological evaluation of some substituted amino thiazole derivatives, J. Chil. Chem. Soc. 55 (2010) 240–243.

[25] M.T. Chhabria, S. Patel, P. Modi, P.S. Brahmkshatriya, Thiazole: a review on chemistry, synthesis and therapeutic importance of its derivatives, Curr. Top. Med. Chem. 16 (2016) 2841–2862.

[26] D. Castagnolo, M. Pagano, M. Bernardini, M. Botta, Domino alkylation-cyclization reaction of propargyl bromides with thioureas/thiopyrimidinones: a new facile synthesis of 2-aminothiazoles and 5H-thiazolo [3, 2-a] pyrimidin-5-ones, Synlett (2009) 2093–2096 2009.

[27] T. Ozturk, E. Ertas, O. Mert, Use of Lawesson's reagent in organic syntheses, Chem. Rev. 107 (2007) 5210–5278.

[28] K. Dridi, M. El Efrit, B. Baccar, H. Zantour, Reaction of mercaptoacetate and halides containing activated methylenes with thiocarbamoylimidates: a novel approach to the synthesis of aminothiazole derivatives, Synth. Commun. 28 (1998) 167–174.

[29] A.A. Aly, A.B. Brown, A.A. Hassan, Heterocycles from the Reaction of Thione Groups With Acetylenic bonds, in: Advances in Heterocyclic Chemistry, Elsevier, 2014, pp. 245–304.

[30] U. Kazmaier, S. Ackermann, A straightforward approach towards thiazoles and endothiopeptides via Ugi reaction, Org. Biomol. Chem. 3 (2005) 3184–3187.

[31] S.L. You, H. Razavi, J.W. Kelly, A biomimetic synthesis of thiazolines using hexaphenyloxodiphosphonium trifluoromethanesulfonate, Angew. Chem. 115 (2003) 87–89.

[32] Q.-.Y. Chen, Y. Liu, W. Cai, H. Luesch, Improved total synthesis and biologicalevaluation of potent apratoxin S4 based anticancer agents with differential stability and further enhanced activity, J. Med. Chem. 57 (2014) 3011–3029.

[33] R. Prager, M. Taylor, C. Williams, The chemistry of 5-oxodihydroisoxazoles. Part 19. 1 The synthesis and photolysis of N-thioacylisoxazol-5 (2H)-ones, J. Chem. Soc., Perkin Trans. 1 (1997) 2673–2678.

[34] S. Arshadi, E. Vessally, L. Edjlali, R. Hosseinzadeh-Khanmiri, E. Ghorbani-Kalhor, N-Propargylamines: versatile building blocks in the construction of thiazole cores, Beilstein J. Org. Chem. 13 (2017) 625–638.

[35] P. Wipf, Synthesis and structure-activity studies of lissoclinum peptide alkaloids, Alkaloids 12 (1998) 187–228.

[36] S. Kasmi-Mir, A. Djafri, L. Paquin, J. Hamelin, M. Rahmouni, One-pot synthesis of 5-arylidene-2-imino-4-thiazolidinones under microwave irradiation, Molecules 11 (2006) 597–602.

[37] S. Pola, Significance of thiazole-based heterocycles for bioactive systems,Scope Select. Heterocycles Org. Pharm. Perspect. 1 (2016) 13–62.

[38] M. D’hooghe, A. Waterinckx, N. De Kimpe, A novel entry toward 2-imino-1, 3-thiazolidines and 2-imino-1, 3-thiazolines by ring transformation of 2-(thiocyanomethyl) aziridines, J. Org. Chem. 70 (2005) 227–232

[39] V. Smokal, A. Kolendo, O. Krupka, B. Derkowska, R. Czaplicki, B. Sahraoui, New methacrylic oxazolone and thiazolidinone containing polymers for nonlinear optical applications, Mol. Cryst. Liq. Cryst. 485, 1011–1018, (2008). doi: 10.1080/ 15421400801926172 .

[40] A. Hantzsch and H. J. Weber, Berichfe, 20,3118 (1887).

[41] A. Hantzsch, Justus Liebigs Ann. Chem., 249, l(1888).

[42] T. B. Johnson and E. Gatewood, J. Amer. Chem. Soc., 51,1815 (1929); Chem. Abstr.,

[43] J. Metzger, Thesis, University of Nancy, France, 1 (1948).

[44] A. Pullman and J. Metzger, Bull. Soc. Chim. France, 1021 (1948); Chem. Absrr., 43,

[46] J. Metzger and A. Pullman, Bull. Soc. Chim. France, 1166 (1948).

[47] J. Metzger and A. Pullman, Compt. Rend., 226, 1613 (1948); Chem. Abstr., 42,6657.

[48] B. Pullman and A. Pullman, “Les Theories Electroniques de la Chimie Organique.”

[49] J. Metzger and B. Koether, Ann. Uniu. Saraviensis, 1, 23 (1952); Chem. Absrr., 47,

[50] J. Metzger and B. Koether, Ann. Uniu. Sarauiensis, 1, 151 (1952); Chem. Abstr., 47,

[51] J. Metzger and B. Koether, Bull. Soc. Chim. France. 20,702 (1953); Chem. Ahstr., 48,

[52] J. Metzger and B. Koether, Bull. Soc. Chim. France, 20, 708 (1953); Chem. Absrr., 48,

[53] J. Metzger and J. Beraud. Compr. Rend., 242,2362 (1956); Chem. Abstr., 51,2741.

[54] J. Metzger and H. Kuhnen, Z. Naturforsch., 12B, 27 (1957); Chem. Abstr., 51, 14686.

[55] V. Grignard and R. Rambaud, “Traitc: de Chimie Organique,” Masson, Ed., Paris,

[56] A. M. Patterson, L. T. Capell, and D. F. Walker, “The Ring Index,“ American

[57] A. W. Hofmann, Berichre, 20, 2262 (1887).

[58] F.C. Brown, 4-Thiazolidinones, Chem. Rev. 61 (1961) 463e521.

[59]S. Singh, S.S. Parmar, K. Raman, V.I. Stenberg, Chemistry and biological activity of thiazolidinones, Chem. Rev. 81 (1981) 175e203.

[60] G.R. Newkome, N. Ashutosh, 4-Thiazolidinones, Adv. Heterocycl. Chem. 25 (1980) 83e112.

[61] T. Tomasic, L. Peterlin Masic, Rhodanine as a scaffold in drug discovery: a critical review of its biological activities and mechanisms of target modulation, Expert Opin. Drug Discov. 7 (2012) 549e560.

[62] A.C. Tripathi, S.J. Gupta, G.N. Fatima, K. Sonar, A. Verma, S.K. Saraf, 4-Thiazolidinones: the advances continue, Eur. J. Med. Chem. 72 (2014) 52e77.

[63] R.B. Lesyk, B.S. Zimenkovsky, 4-Thiazolidones: centenarian history, current status and perspectives for modern organic and medicinal chemistry, Curr. Org. Chem. 8 (2004) 1547e1577.

[64] T. Tomasic, L. Peterlin Masic, Rhodanine as a privileged scaffold in drug discovery, Curr. Med. Chem. 16 (2009) 1596e1629.

[65] R.B. Lesyk, B.S. Zimenkovsky, D.V. Kaminskyy, A.P. Kryshchyshyn, D.Ya Havrylyuk, D.V. Atamanyuk, I.Yu Subtel'na, D.V. Khyluk, Thiazolidinone motif in anticancer drug discovery. experience of DH LNMU medicinal chemistry scientific group, Biopolym. Cell. 27 (2011) 107e117.

[66] A. Verma, S.K. Saraf, 4-Thiazolidinone e a biologically active scaffold, Eur. J. Med. Chem. 43 (2008) 897e905.

[67] V.S. Jain, D.K. Vora, C.S. Ramaa, Thiazolidine-2,4-diones: progress towards multifarious applications, Bioorg. Med. Chem. 21 (2013) 1599e1620.

[68] A.A. Fedorchuk, Y. Slyvka, V. Kinzhybalo, I. Kityk, J. Jędryka, K. Ozga, M. Myskiv, Copper (I) π-coordination compounds with allyl derivatives of disubstituted pseudothiohydantoin: synthesis, structure investigation and nonlinear optical features, J. Coord. Chem. 72 (2019) 3222–3236.

[69] A. Fedorchuk, Y.I. Slyvka, E. Goreshnik, I. Kityk, P. Czaja, M. Mys'kiv, Crystal structure and NLO properties of the novel tetranuclear copper (I) chloride π-complex with 3-allyl-2-(allylimino)-1, 3-thiazolidin-4-one, J. Mol. Struct. 1171 (2018) 644–649.

[70] V. Smokal, B. Derkowska, R. Czaplicki, O. Krupka, A. Kolendo, B. Sahraoui, Nonlinear optical properties of thiazolidinone derivatives, Opt. Mater. 31 (2009) 554–557.

[71] B. Baroudi, K. Argoub, D. Hadji, A.M. Benkouider, K. Toubal, A. Yahiaoui, A. Djafri, Synthesis and DFT calculations of linear and nonlinear optical responses of novel 2- thioxo-3-N,(4-methylphenyl) thiazolidine-4 one, J. Sulfur Chem. 41 (2020) 310–325.

[72] D. Gautam, R. Chaudhary, X-ray Synthesis, DFT and photophysical properties of some new ferrocenyl hydrazono thiazolidin-4-ones and their derivatives, Spectrochimica Acta Part A Mol. Biomol. Spectr. 143 (2015) 256–264.

[73] A. Guerraoui, M. Goudjil, A. Direm, A. Guerraoui, ˙ I.Y. S¸ engün, C. Parlak, A. Djedouani, L. Chelazzi, F. Monti, E. Lunedei, A rhodanine derivative as a potential antibacterial and anticancer agent: Crystal structure, spectral characterization, DFT calculations, Hirshfeld surface analysis, in silico molecular docking and ADMET studies, J. Mol. Struct. 1280 (2023), 135025.

[74] A.L. Toumi, A. Khelil, K. Tobel, M. Makha, L. Hernandez, ´ Y. Mouchaal, L. Cattin, M. del Valle, F.R. Diaz, J.C. Bern`ede, On the exciton blocking layer at the interface organic/cathode in planar multiheterojunction organic solar cells, Solid State Electron 104 (2015) 1–5.

[75] N.E.H. Belkafouf, F.T. Baara, A. Altomare, R. Rizzi, A. Chouaih, A. Djafri, F. Hamzaoui, Synthesis, PXRD structural determination, Hirshfeld surface analysis and DFT/TD-DFT investigation of 3N-ethyl-2N'-(2-ethylphenylimino) thiazolidin-4-one, J. Mol. Struct. 1189 (2019) 8–20.

[76] A. Barakat, H. Najjar, A. Al Majid, S. Soliman,, Y. Mabkhot, , M. Al-agamy, H. Ghabbour, H.K. Fun, Synthesis, molecular structure investigations and antimicrobial activity of 2-thioxothiazolidin-4-one derivatives. J Mol Struct. 1081:519-529. (2015). doi:10.1016/j.molstruc.2014.10.038.

[77] T.J. Shah, V.A. Desai. Synthesis of some novel fluorinated 4-thiazolidinones containing amide linkages and their antimicrobial screening. Arkivoc. 2007:218-228. (2007).

[78] M. Cacić, M. Molnar, B. Sarkanj, E. Has-Schön, V. Rajković. Synthesis and antioxidant activity of some new coumarinyl-1,3-thiazolidine-4-ones. Molecules. 15(10):6795-6809. (2010). doi:10.3390/molecules15106795.

[79] M.H Shih, F.Y, Ke. Syntheses and evaluation of antioxidant activity of sydnonyl substituted thiazolidinone and thiazoline derivatives. Bioorganic Med Chem. 12(17):4633-4643. (2004). doi:10.1016/j.bmc.2004.06.033.

[80] A. Kunzler, P.D. Neuenfeldt, A.M. das Neves, C.M. Pereira, G.H. Marques, P.S. Nascente, M.H. Fernandes, S.O. Hübner, W. Cunico Synthesis, antifungal and cytotoxic activities of 2-aryl-3-((piperidin-1-yl)ethyl)thiazolidinones. Eur J Med Chem.; 64:74-80.(2013). doi:10.1016/j.ejmech.2013.03.030.

[81] M. R. Bhosle, J. R. Mali , S. Pal, A.K. Srivastava, R.A. Mane, Synthesis and antihyperglycemic evaluation of new 2- hydrazolyl-4-thiazolidinone-5- carboxylic acids having pyrazolyl pharmacophores. Bioorg. Med. Chem. Lett.;24:2651-2654. (2014). doi: 10.1016/j.bmcl.2014.04.064

[82] S. Jain, A. Kumar, M. Kumar, N. Jain. Synthesis and antibacterial studies of 2-aryl-3-alkanamido-4H-thiazolidin-4-one derivatives. Arab. J. Chem. 2016;9 :S290-S295. doi:10.1016/j.arabjc.2011.04.009.

[83] K. Koya, Y. Li, H. Wang, T. Ukai, N. Tatsuta, M. Kawakami, Shishido, L. B Chen. MKT077, a Novel Rhodacyanine Dye in Clinical Trials, Exhibits Anticarcinoma Activity in

Preclinical Studies Based on Selective Mitochondrial Accumulation. CANCER RESEARCH. ;56:538-543. 95, (1996). PMID: 8564968.

[84] J. Senkiv, N. Finiuk, D. Kaminskyy, D. Havrylyuk, M. Wojtyra, I. Kril, A. Gzella, R. Stoika, R. Lesyk. 5-Ene-4-thiazolidinones induce apoptosis in mammalian leukemia cells. Eur J Med Chem.;117:33-46. (2016). doi:10.1016/j.ejmech.2016.03.089.

[85] Z. Beharry, M. Zemskova, S. Mahajan, F. Zhang, J. Ma, Z. Xia, M. Lilly, C. D. Smith, A. S. Kraft. Novel benzylidene-thiazolidine-2,4-diones inhibit Pim protein kinase activity and induce cell cycle arrest in leukemia and prostate cancer cells. Mol Cancer Ther. 8(6):1473-1483. (2009). doi:1535-7163.MCT-08-1037

[86] R.K Rawal, R. Tripathi, S.B Katti, C. Pannecouque, E. De Clercq. Design, synthesis, and evaluation of 2-aryl-3-heteroaryl-1,13-thiazolidin-4-ones as anti-HIV agents. Bioorg Med Chem.;15(4):1725-1731. (2007). doi:10.1016/j.bmc.2006.12.003.

[87] K.D Hargrave, F.K Hess, J.T Oliver. N-(4-Substituted-thiazolyl) oxamic acid derivatives, new series of potent, orally active antiallergy agents. J. Med. Chem. 1983;26(8):1158-1163. doi: 10.1021/jm00362a014

[88] D. Havrylyuk, L. Mosula, B. Zimenkovsky, O. Vasylenko, A. Gzella, R. Lesyk. Synthesis and anticancer activity evaluation of 4-thiazolidinones containing benzothiazole moiety. Eur J Med Chem. 2010;45(11):5012-5021. doi:10.1016/j.ejmech.2010.08.008.

[89] D. Kaushik, D. Paliwal, A. Kumar. 2D QSAR and Molecular docking studies of chloroquinethiazolidinone derivatives as potential pfLDH inhibitors of Plasmodium falciparum. Int. J. Pharmacol. Pharm. Sci. 2015 ;2(5) :42-53. doi: 10.1.1.736.3692.

[90] L. Servant, G. Le Bourdon, T. Buffeteau, Comprendre la spectroscopie infrarouge : principes et mise en œuvre, Groupe de spectroscopie moléculaire, Institut des sciences moléculaires, Université Bordeaux 1, (2011).

Chapter II

Experimental methods for structure determination

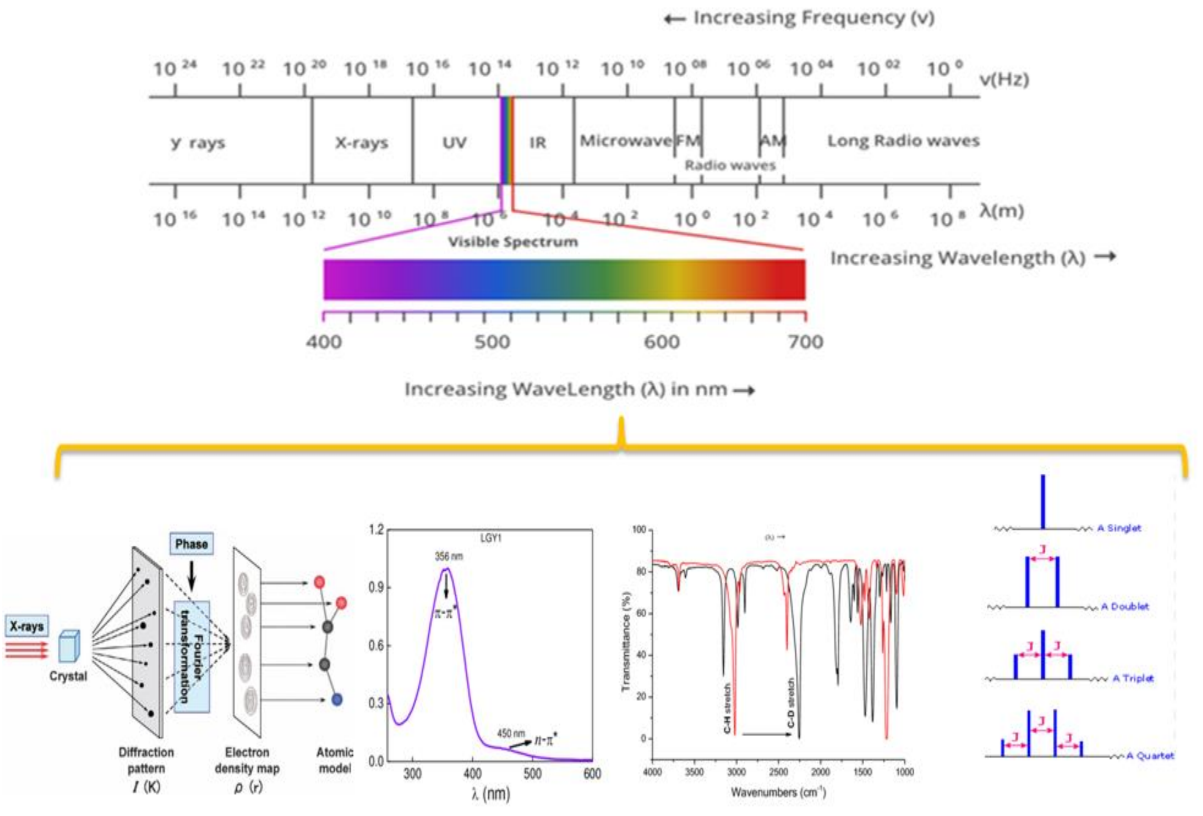

Single crystal X-ray diffraction **UV-Visible Spectroscopy** **IR spectroscopy** **Nuclear magnetic resonance**

II.1. Introduction to X-ray diffraction

In an X-ray diffraction experiment, a pattern is placed in the middle of a tool and X-ray illumination devices, and the X-ray tube and the detector move in a synchronized movement. The signal from the pattern is recorded and plotted. Peaks related to the shape of the atomic pattern are observed. Most substances are formed by many small crystals, like sand on a beach. Each of these crystals consists of a daily association of atoms, and each atom has a nucleus surrounded by a cloud of electrons. X-ray diffraction records begin at this scale. X-rays are an excessively soft force with a repetition time called a wavelength.

The wavelength of an x-ray is like the space between atoms in glass. Interference (diffraction) calls can be used to scale the space between atoms. Interference occurs when x-rays come into contact with each other. If the waves are aligned, the sign is amplified. This is called optimistic interference. If the waves are out of alignment, the sign is destroyed. This is called negative interference. When X-ray rays meets an atom. Its force absorbs that of the electron. Electrons occupy single force states around an atom, as it is not a sufficient force to launch the electron. The force must be reemitted as a new X-ray with the same intensity as the original. This method is known as ""elastic dispersion." In a crystal, the repetitive format of the atoms of the distinctive stage is separated by well described distances. When the atomic planes are discovered, X-rays are scattered by the often spaced atoms. The robust width of the emitted sign takes place in very precise corners in which the scattered waves interfere. This impact is the diffraction of the flames. The prospective between the twist and the scattered ray is known as Theta. In the case of interference, the scattered waves must be aligned, which means that the second wave must travel a whole number of wavelengths. So 1/2 of the wavelength is visited at the incident side and 1/2 at the scattered side, generating another wavelength.

A wavelength has been traveled inside the twist of fate and scattered appearance in the following X-ray case, generating an additional wavelength. This framework is produced alongside the glass. The true perspective in which the diffraction takes place can be determined by the purple triangle. The perspective above is theta, half of the perspective between the incident and scattered rays. The long aspect is the space between the atomic floor and the fast aspect, which we understand to be 1/2 a wavelength. The relationship between the diffraction perspective and the space between the atoms can be found using the sine function. Lambda/EEd = Sin Theta, Reorganization; therefore, the equation produces an equation normally called Bragg's law, which brings to mind Sir William Henry and William Lawrence Bragg, the father-and-son team that got the Nobel Prize in 1950 for its evaluation of jobs.

glass systems with X-ray diffraction.Thus, the ratio between the diffraction perspective and the perspective of the glass is theta, which is the ratio of the diffraction perspective to the perspective of the atomic floor. The relationship between the diffraction perspective and the space between the atoms can be found using the sine function. ${}^{\lambda}/_{2d} = \sin\theta$, Reorganization; therefore, the equation produces an equation normally called Bragg's law, which brings to mind Sir William Henry and William Lawrence Bragg, the father-and-son team that got the Nobel Prize in 1950 for its evaluation of jobs. Glass systems with X-ray diffraction. This approach to X-ray diffraction is now used for a wide range of substances, from thin glass epitaxial films to polycrystalline powder mixtures and even lightning diffraction from amorphous randomly oriented substances to help scientists develop new pharmaceuticals, classify rock formations based on their mineral additives, and understand how the association of atoms influences the conductivity of force accumulators. Scientists are pushing their ability to design atomic substances. X-ray diffraction is becoming an increasingly indispensable tool. Advances in team building have made X-ray diffraction easier and more efficient than ever.

II.1.2. The numerous techniques of X-ray diffraction:

According to the nature of the information sought and the nature of the material, many avenues of analysis are possible: The Bragg equation has three parameters, d(hkl)[1], and, the first of which is determined by the crystal structure. Only one of the remaining two parameters, et, can be freely specified to achieve the diffraction conditions on a family of (hkl) planes, the other one being variable. The variable parameters used will determine two sets of diffraction procedures.

- Fixed, λ variable: laüe method.[1]
- λ fixed, θ variable: powder method and rotating crystal method

II.1.2.1. The Laue method

It extends to solitary crystals (or large grains). The sample is fixed, and the crystal planes are fixed with respect to the incident X-ray field. As the surface is polychromatic, each crystal plane (hkl) known to cause diffraction results in a diffracted surface (figure II-1). This approach is mainly used for the crystallographic orientation of single crystals [2-3].

[1] ***MaxVonLaue***(1879-1960) He was a German physicist. He obtained the 1914 Nobel Prize «for his disjointed diffraction of the Middle Ages».

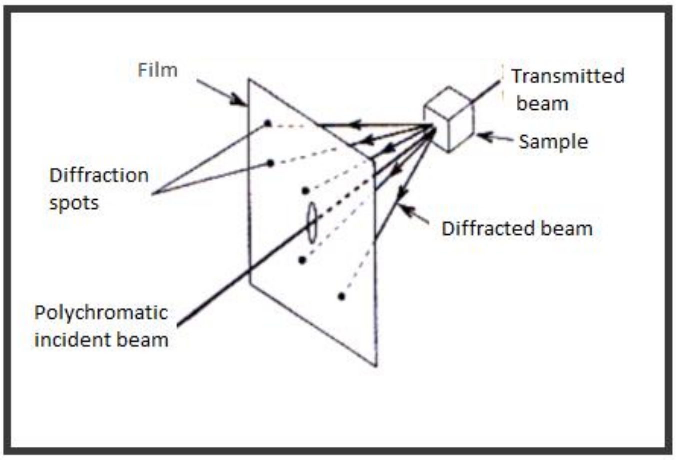

Figure II.1. Laue method

II.1.2.2. Powder method

The term derives from the fact that the sample studied is reduced to a fine powder composed of randomly aligned particles. The X-ray beam is monochromatic, and diffraction occurs only when it forms an angle (solution of the Bragg equation) with a group of crystal surfaces causing diffraction. Since the particles are randomly oriented, there will always be a family of hkl planes generating diffraction, so all the beams will be able to diffract at the same time, forming diffraction cones. These beams form half-angle cones at vertex 2 (Figure I-3). This method can also be used to evaluate a large polycrystalline sample composed of small grains the size of powder particles.

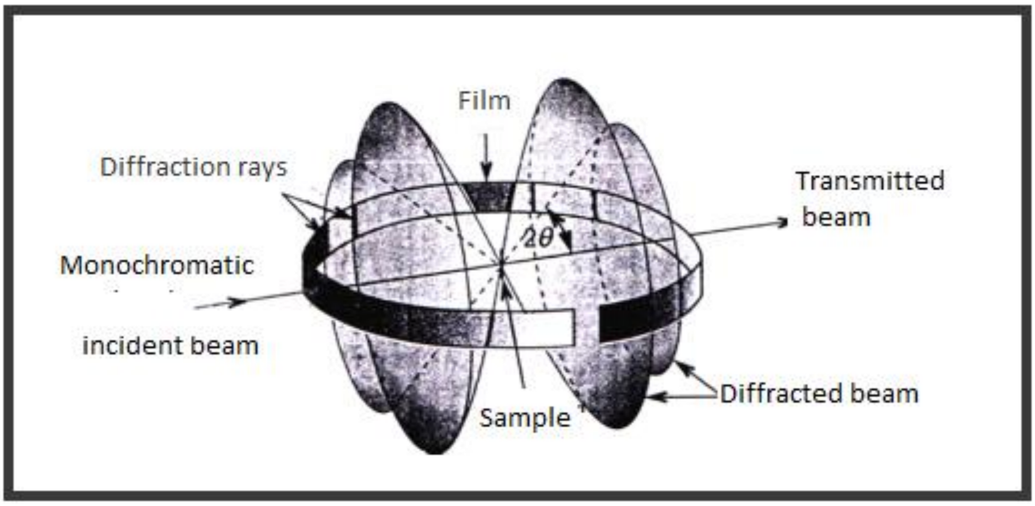

Figure II.2. Powder method

II.1.2.3. Single crystal X-ray diffraction:

A single crystal is a macroscopic object whose atoms are arranged in an orderly fashion in a three dimensional space. The use of crystals for X-ray diffraction [4, 5] is a useful way to determine the three-dimensional structure of molecules. Indeed, X-rays interact with the electron cloud of the atoms in the crystal. The scattered vibrations interact and cause diffraction since the crystal is a three-dimensional periodic medium. The measurement of the X-ray diffraction is a very important part of the analysis. Indeed, X-rays interact with the electron cloud of the atoms in the crystal. The scattered vibrations interact and cause diffraction since the crystal is a three-dimensional periodic medium. The measurement of these diffracted intensities gives access to the Fourier components of the electron density of the molecule.

After a number of computational steps, a structural determination consists in recognizing the electron density maxima that have been attributed to atomic positions. Compared to the performance of the automatic single-crystal diffractometer, the classical experimental methods of film recording of X-ray diffraction by a single crystal, such as the rotating crystal, Weissenberg, and precession for determining complex structures or refining already roughly established structures [1, 2, 6], may seem outdated (four-circle diffractometer).

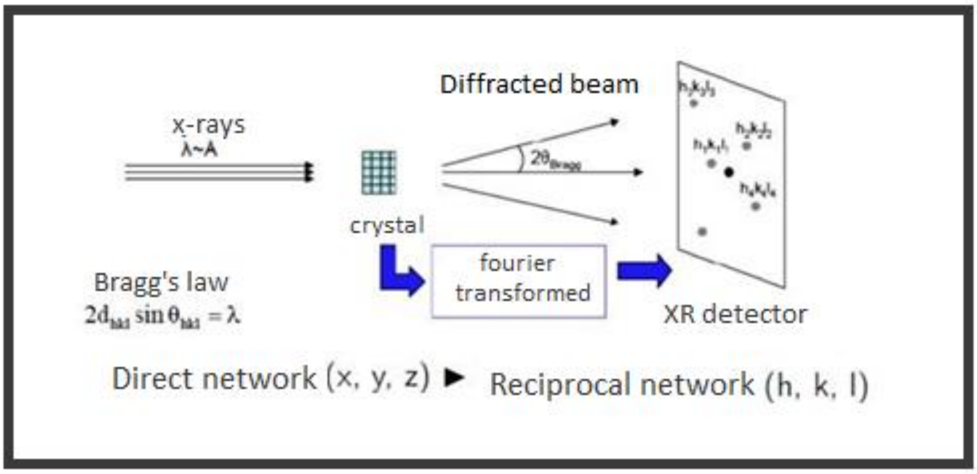

Figure II.3.X-ray diffraction on a single crystal

II.1.2.3.1. Single crystal choice

X-ray crystallography is a powerful technique for revealing the structure of materials at the molecular and atomic levels. It can only be performed in great detail on single crystal samples. The required single crystal must meet the following requirements:

- A sufficiently large diffracting volume.
- A tiny volume, so that absorption phenomena are minimized.
- Must be immersed in the homogeneous region of the beam.
- It must be as homogeneous and isotropic as possible.

To meet all these requirements, the average size of the crystal must be less than 0.5 mm.

II.1.3. Structure determination

The determination of the crystal structure by X-ray requires two main phases. The first phase consists of processing the crystallographic data, and the second phase consists of solving and improving the structure.

II.1.3.1. Integrated intensity

The experimental measurements determine the integrated intensity I as a function of the angle of Bragg. After subtracting the continuous background, the integrated intensityI_{hkl}, i.e. the area under the curve I_0can be measured for each diffraction peak. This integrated intensity can be used to calculate the square of the modulus of the structure factor, F_{hkl}, taking into account a number of proportionality factors.

The formula that relates the integrated intensity of a diffraction peak to the structure factor in an X-ray diffraction experiment is written

$$\frac{I_{hkl}}{I_0} = \lambda^3 r_o{}^2 \frac{V}{\mathrm{Vc}} \frac{1}{\varpi} [L] \times [P] \times [A] \times [T] \times [E] |F_{hkl}|^2 \qquad \text{(II.1)}$$

Where: I_0 is the intensity of the incident beam.

λWavelength.

r_0 the classical radius of the electron.

V_c the volume of the elementary mesh.

V the volume of the diffracting sample.

$\varpi$the angular scanning speed (rotation of the crystal around the axis ω).

[P] the polarization factor.

[A] is a factor that takes into account absorption effects.

[E] takes into account the effects of extinction.

[T]is the Debye-Waller factor, which comes from the fact that the atoms vibrate around their average position.

Considering that the vibrations of atoms are isotropic in the situation of a monoatomic solid:

$$T = e^{-\frac{B\sin^2\theta}{\lambda^2}} \qquad \text{(II.2)}$$

With B = $8\pi^2\langle U^2\rangle$,$\langle U^2\rangle$being the mean square displacement of the atoms at the considered temperature.

- [L]is a geometric factor, called the Lorentz factor, which depends on how the integrated intensity was measured.

The formula **(**I-5**)**, with the factor (A) and (E) taken equal to the unit, is valid for a crystal of small size or a mosaic crystal made of slightly disoriented crystallites.

II.1.3.2. Atomic scattering factor

In the study of X-ray diffraction, we can recognize, as a first estimate, that matter is composed of impartial atoms with the influence of chemical bonds in the electronic distribution neglected (rigid pseudo-atom approximation), which provides a great convenience of use when processing experimental results, especially when refining the structures by the method of least squares. The pseudo-atom is thus considered to have a nucleus and an electronic cloud.

The frequency scattered by an atom is the total of the amplitudes scattered by all its electrons. This is called the atomic scattering factor. The chemical composition of the atoms, the diffraction angle 2θ et and the X-ray wavelength all influence this quantity.

For each pseudo-atom, the associated electron distribution follows the motion of the nucleus without distortion and is given, at a point $\vec{r}$, for a given position of the nuclei in the scattering system by :

$$\rho(\vec{r},\vec{R}) = \sum\sum_{K,l}\left(\vec{r} - \overrightarrow{R_{K,l}}\right) \qquad \text{(II.3)}$$

Where R represents the set of instantaneous coordinates of the nuclei and $R_{K,l}$ is the position vector of the nucleus k in the mesh l. The diffusion factor relative to the pseudo-atom k is then defined as follows:

$$f_K(\vec{H}) = \int_K^{R_{K,l}} \rho_K(\vec{r}_K)e^{-2\pi i H r_K}dv \qquad \text{(II.4)}$$

II.1.3.3. Structure factor

The structure factor F_{hkl} is the sum of the waves scattered by all the atoms of the mesh in the direction of reflection hkl . It is determined by the location of each atom and its scattering factor. It represents the concept of X-ray diffraction.

$$\upsilon_j = 2\pi(\mathrm{h}.x_\mathrm{j} + \mathrm{k}.y_\mathrm{j} + \mathrm{l}.z_\mathrm{j}) \qquad \text{(II.5)}$$

It is defined as the sum of all atomic contributions each affected by its phase shift $\varphi_\mathrm{j}$depending directly on the position of atom j in the mesh:

$$\mathrm{F} = \sum_{j=1}^{N} \mathrm{f_j} \exp(\mathrm{i}\varphi_\mathrm{j}) \qquad \text{(II.6)}$$

where N is the number of atoms in the mesh, $\mathrm{f_j}$ is the scattering power of atom j, given by the International Crystallographic Tables as a function of $\frac{\sin\theta}{\lambda}$, where is the length $\lambda$of the X-radiation used, φ_j is the phase shift between individual atoms in the mesh, formulated by:

$$\varphi_\mathrm{j} = 2\pi(\mathrm{h}.x_\mathrm{j} + \mathrm{k}.y_\mathrm{j} + \mathrm{l}.z_\mathrm{j}) \qquad \text{(II.7)}$$

Where (x_j, y_j, z_j) are the coordinates of the atom j in the plane (hkl).

The structure factor is therefore written as:

$$F(\vec{H}) = \int_V \rho(\vec{r})\, e^{2\pi i H \vec{r}} \mathrm{dv} \qquad \text{(II.8)}$$

$$\mathrm{F(hkl)} = \sum_j f_j \exp\left(i2\pi\left(hx_j + ky_j + lz_j\right)\right) \qquad \text{(II.9)}$$

Or by separating the real part from the imaginary part:

$$F_{(hkl)} = A_{(hkl)} + iB_{(hkl)} = \left|F_{(hkl)} e^{i\varphi(hkl)}\right| \qquad \text{(II.10)}$$

With:

$$F(\vec{H}) = \sum_j f_j \left(\cos 2\pi\left(hx_j + ky_j + lz_j\right) + i \sin 2\pi\left(hx_j + ky_j + lz_j\right)\right) \qquad \text{(II.11)}$$

The structure factor involves:

- The atomic diffusion factors of the atoms in the pattern,

- The Debye factors which depend on the temperature and the nature of the atoms of the mesh,
- The relative positions of the atoms in the mesh.

II.1.3.4. Temperature factor

An atom in a crystal is held together by a multiplicity of factors. A disturbance results in an oscillation of the atom around its equilibrium position. Any crystal has a disorder at a temperature T due to the thermal agitation of the atoms in the crystal. The movement of these atoms around their equilibrium position within the mesh reduces the structure factor, which means that they have modified the diffracting power of the atom (temperature factor of the atoms). As a result, the amplitude of the atomic dispersion of a moving atom is reduced compared to that of a stationary atom [7]. The temperature factor is expressed in the harmonic hypothesis of the motion of the nuclei (small displacements) as follows

$$T_j =< e^{-\frac{1}{2}[2\pi]} \qquad \text{(II.12)}$$

Where Uj is the instantaneous displacement vector of atom j with respect to its equilibrium position.

Equilibrium position. Thus the structure factor is expressed as :

$$F(\vec{H}) = \sum_j f_j \, exp\left(i2\pi(hx_j + ky_j + lz_j)\right) \qquad \text{(II.13)}$$

In the direct reference frame,$\vec{U_j} = U_1\vec{a}_1 + U_2\vec{a}_2 + U_3\vec{a}_3$In the reciprocal normalized frame

Defined by: $\vec{\imath^*} = \frac{\overrightarrow{a_1^*}}{\left|\overrightarrow{a_1^*}\right|}; \; \vec{\jmath^*} = \frac{\overrightarrow{a_2^*}}{\left|\overrightarrow{a_2^*}\right|}; \overrightarrow{k^*} = \frac{\overrightarrow{a_3^*}}{\left|\overrightarrow{a_3^*}\right|} \qquad \text{(II.14)}$

The vector $\vec{H}$can be written in the form:

$$\vec{H} = \overrightarrow{H_1\overrightarrow{\imath^*}} + \overrightarrow{H_2\overrightarrow{\jmath^*}} + \overrightarrow{H_2\overrightarrow{k^*}} \quad \text{(II.15)}$$

After the calculations, we find that we can then calculate

$$\langle(\overrightarrow{\vec{H}.U_1})_2\rangle = (\langle hU_1 + kU_2 + lU_3\rangle)^2 \qquad \text{(II.16)}$$

$$= \sum_{i=1}^{3}\sum_{j=1}^{3} H_i U_{ij} H_j \qquad \text{(II.17)}$$

where

$$U_{ij} = \frac{\langle U_i U_j \rangle}{\vec{a_i^*}\vec{a_j^*}} \text{(II.18)}$$

The temperature factor is written as follows:

$$T_j = exp\left[-2\pi^2\left[h_1^2 a_1^{2*} u_{11} + h_2^2 a_2^{2*} u_{22} + h_3^2 a_3^{2*} u_{33} + 2h_1 h_2 a_1 a_2 u_{12} + 2h_2 h_3 a_2^* a_3^* u_{23} + 2h_1 h_3 a_1^* a_3^* u_{13}\right]\right] \quad \text{(II.19)}$$

Therefore, it becomes:

$$T_j = exp\left(-2\pi U_j \left(\frac{\sin\theta}{\lambda}\right)^2\right) \qquad \text{(II.20)}$$

Where, θ is the Bragg angle and λ is the wavelength of the radiation. If of $U_j$plus is the same for all atoms in the crystal mesh then (U_j =U), the thermal agitation is represented by an overall temperature factor B.

$$B = exp\left(-2\pi^2 U \left(\frac{\sin\theta}{\lambda}\right)^2\right) \qquad \text{(II.21)}$$

This has the effect of lowering the diffracted intensity. This phenomenon being all the more marked for large values of θ.

II.1.4. Crystallographic data processing

The diffracted intensities constitute the raw material from which the crystal structure is derived. Indeed, they are related to the structure factors observed by the relation:

$$I_{hkl} = |F_{obshkl}|^2 \quad \text{(II.22)}$$

II.1.4.1. Correction of intensities

Several errors impact the measurements of these intensities at the experimental level. Some are related to the diffraction angle; they lead to two types of corrections: the Lorentz correction and the polarization correction. The others are related to the physical characteristics and the nature of the crystal, which can be characterized as follows:

- The temperature correction.
- The absorption correction.
- The extinction correction.

It is essential to have high intensity values to determine the location of atoms in the crystal lattice. The primary material data for structure resolution is a series of intensities acquired by a diffractometer. Corrections to the observed intensities are made prior to structure determination.

II.1.4.1.1. Lorentz-Polarization correction

As this raw intensity of the diffracted beam is affected by the partial polarization of the input X-rays and as the speed of crossing of the Ewald sphere by the multiple nodes varies, a systematic correction is performed. This is done using the "XCAD4" application [8], which employs a combined Lorentz [6]-polarization correction [9] as described by the expression :

$$Lp = \frac{1}{2}\left[\frac{\cos^2 2\theta_m + \cos^2 26}{1+\cos^2 2\theta_m} + \frac{1+\cos 2\theta_m + \cos^2 2\theta_c}{1+\cos 2\theta_m}\right] \qquad \text{(II.23)}$$

while:

- θ_m:is the Bragg diffraction angle on the monochromator
- $2\theta_m$=12,2°for deletion $k_\alpha$of Mo.
- θ_c:is the Bragg angle of reflection considered.

The expression of this factor Lp depends on [10]:

1. The relative positions of the monochromator and the tube.
2. Of the degree of mosaicism of the graphite crystal.
3. The diffractometer used.

Once the Lorentz-Polarization correction is done, the diffracted intensities are transformed into structure factors by the relation:

with

$$F_{obs}^2 = \frac{I_{raw}}{Lp} \qquad \text{(II.24)}$$

while:

---

[6] ***Hendrik Antoon Lorentz***(1853 - 1928) is a Dutch physicist who has distinguished himself by his theoretical work on the nature of light and the constitution of matter. He is co-winner with Pieter Zeemandu the 1902 Nobelde Physical Prize.

$$I_{raw} = \frac{A.(C-R.B)}{Npi} \qquad \text{(II.25)}$$

A: Attenuation coefficient (ATN), ATN depends on the counter filter.

R: Ratio of task count time to continuous background count time (often taken as 2).

B: total count on continuous background.

Npi: scan speed.

II.1.4.1.2. Lorentz correction

By rotating the crystal at angular velocity ω, the reciprocal lattice rotates around its origin at the same angular velocity. Any node (h k l) in this plane acquires a linear velocity v equal in modulus to ω_{hkl}

The time it takes a node to traverse the Ewald sphere is inversely proportional to the normal component V_n along the direction of travel, which is that of vector s.[11]

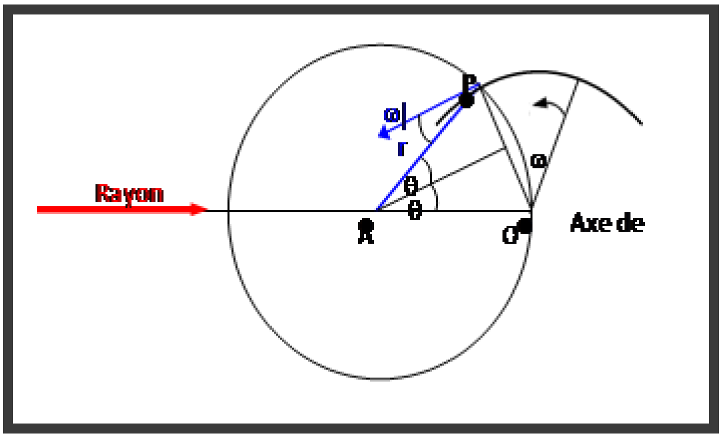

Figure II.4. Lorentz correction for a crystal rotating about an axis normal to the plane defined by the incident and scattered X-ray beams.

In a real crystal, the lattice is not infinite. For this reason, the nodes of the reciprocal lattice are no longer point-like, and are therefore represented by small spherical volumes (**Figure II.4)**

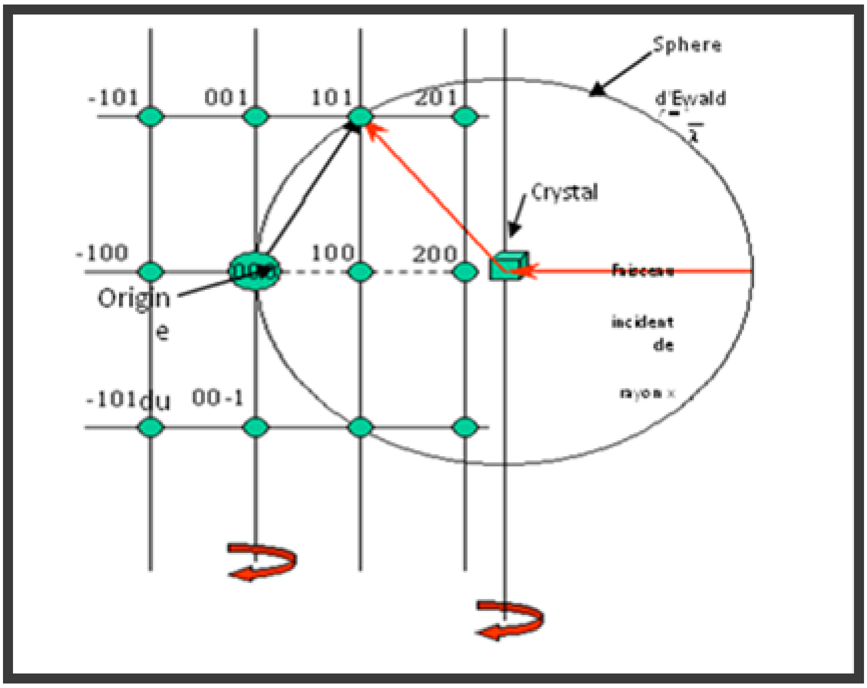

Figure II.5. Lorentz correction

The Lorentz factor is an angular correction given to any hkl reflection to account for the velocities V with which the hkl nodes pass through the Ewald sphere account for the velocities V with which the hkl nodes cross the Ewald sphere:

$$L = \frac{1}{\sin 2\theta} \quad \text{(II.26)}$$

The figure II.5 illustrates the fluctuation of this parameter with angle 2 θ. In reality, Lorentz correction is always associated with polarization correction. It is generally known as Lorentz-polarization correction, which is designated by the LP parameter.

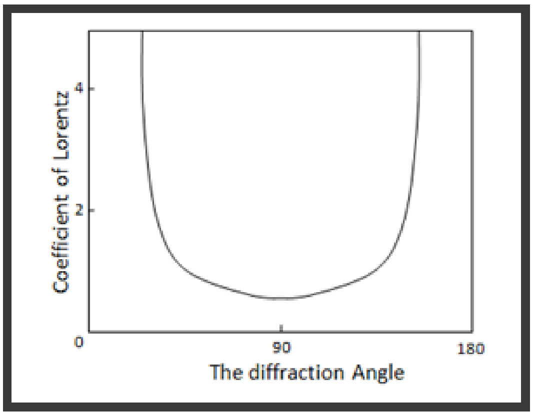

Figure.II.6. Lorentz factor

II.1.4.1.3. Polarization correction

X-rays undergo a partial polarization after diffraction. The scattered wave can be decomposed into a wave perpendicular and another parallel to the diffraction plane (figure I.6).

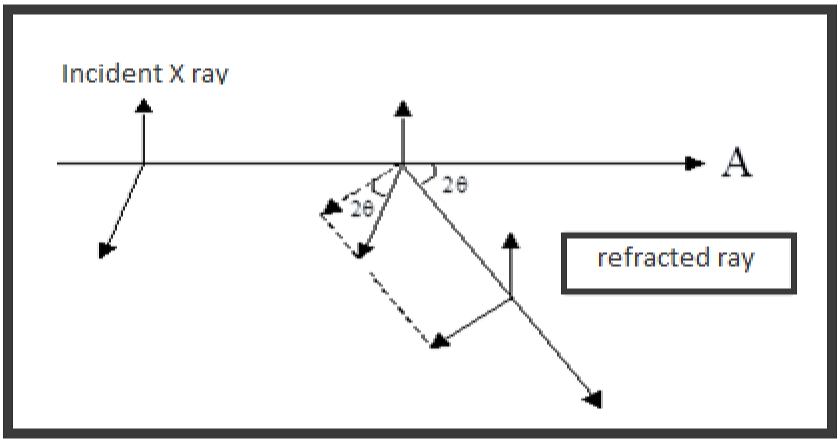

Figure.II.7. polarization of X-rays

Only the wave perpendicular to the plane of incidence is dispersed without change. The other is partially polarized in the direction 2θ (the dispersed wave is normal to the orientation of the diffraction). [12].

Therefore, the diffracted intensity decreases. The latter is multiplied by the polarization factor, as has been proven.

$$p = \frac{1}{2}(1 + \cos^2 2\theta) \qquad \text{(II.27)}$$

For a given reflection, the diffracted intensity is then, in the following form:

$$I = \frac{I_{mesured}}{P} \qquad \text{(II.28)}$$

Where ($I_{mesured}$ is the intensity measured by experiment)

$$I = \frac{I_0}{\frac{1+\cos^2 2\theta}{2}} \qquad \text{(II.29)}$$

The angle 2 θ varies between the extreme values 0 and , (figure I.8) and consequently the polarization factor P varies between 1/2 and 1. Thus for each reflection, the measured intensity is P times the real intensity.

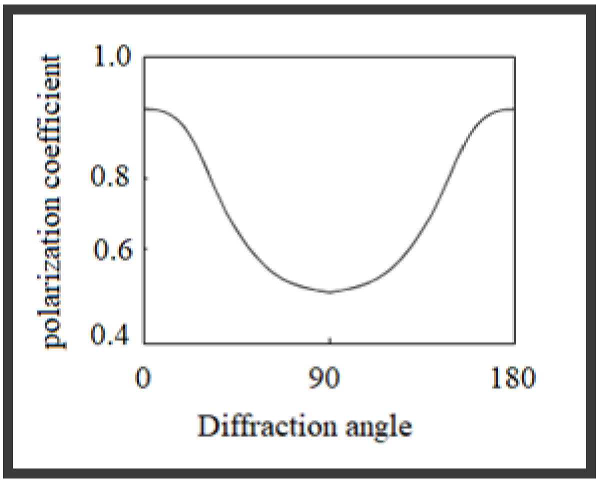

Figure II.8. Polarization factor

II.1.4.1.4. Temperature correction

The atoms of a crystal are not immobile, they are animated by vibrations around their equilibrium position, vibrations whose amplitude varies with the temperature according to the elements; this is the mechanism of thermal agitation. Because of their deformations, the electron density of each atom will be distributed in a volume greater than its volume of rest, resulting in a decrease in its atomic diffusion factor. Thermal agitation causes the atom to occupy a sphere, according to the Debye[7]-Waller [8] approximation [13], and the scattering factor of this atom is given by the relation [14].

$$\boldsymbol{f = f_0 e^{-\frac{B\sin^2\theta}{2}}} \qquad \text{(II.30)}$$

The associated temperature correction [12] is:

$$\boldsymbol{T = e^{-\frac{B\sin^2\theta}{2}}} \qquad \text{(II.31)}$$

.Where:

$f0$: The diffusion factor of the atom at rest; B: the isotropic temperature factor that can be expressed by the relation [15]:

$$B = 8\pi^2\langle U^2\rangle\text{(II.32)}$$

$\langle U^2\rangle$:is the root mean square amplitude of the vibration of the atom along the direction normal to the reflector plane.

---

[7] ***Peter Joseph Wilhelm Debye*** (1884 - 1966) is a Dutch physicist and chemist. He was awarded the Nobel Prize for Chemistry in 1936.

[8] ***IvarWaller***(1898-1991) is a Swedish professor of theoretical physics at Uppsala University

II.1.4.1.5. Absorption correction

When X-rays penetrate a crystal, part of the energy is absorbed, which lowers the intensity. The scattered intensity is given by the formula of Beer[9]-Lambert[10]

$$I = I_0 e^{-\mu L} \qquad \text{(II.33)}$$

while:

- I_0: Incident intensity.
- I : Transmitted intensity after passing through a thickness L.
- μ: Absorption coefficient.

The thickness L has two components (figureII.9) one L1 before diffraction by the volume element dV of the crystal and the other L2 after diffraction.[16]

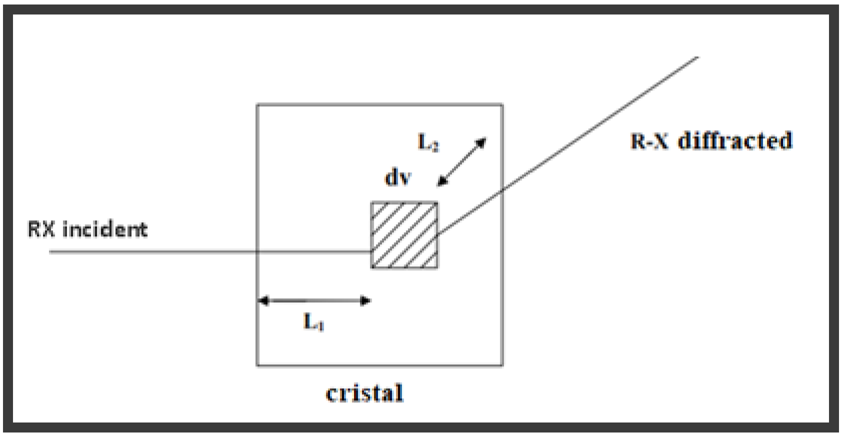

Figure II.9. X-ray path in the crystal

To evaluate the absorption of the whole crystal, we will calculate the transmission factor T Defined by :

$$T = \frac{1}{V}\int e^{-\mu(L_1+L_2)}\, dv \qquad \text{(II.34)}$$

[9] ***August Beer***(1825–1863) is a German mathematician, chemist and physicist.

[10] ***Jean-Henri Lambert***(1728-1777) is a mathematician and philosopher from the 18th century.

Which is generally very close to 1 and mainly affects structural factors with high modulus and low $\frac{\sin\theta}{\lambda}$

II.1.4.1.6. Extinction corrections

Extinction is a decrease in diffracted intensity caused by the volume of the crystal [17]. There are two categories of extinction: primary and secondary.

II.1.4.1.6.1. Primary extinction

The phenomenon of extinction is related to the calculation of the reflectivity of a perfect crystal, i.e. a crystal whose angular deviations of the reticular planes do not exceed a few seconds of arc. The kinematic theory is replaced by the dynamic concept for such a crystal [18-19].

Only the waves scattered by the different points of the crystal interfere in the kinematic theory, whereas in the dynamic theory, an interference state is established between the incident and scattered waves, forming a coupled system. The primary extinction coefficient is calculated as follows:

$$Y_p = \frac{I_c}{I_d} \qquad \text{(II.35)}$$

Where is the integrated intensity provided by the dynamic theory and I_c that provided by the kinematic theory; This coefficient is unknown which makes it difficult to solve it is the phase indeterminacy problem. The structure factorF_{hk}can be expressed as the vector sum of the atomic scattering factors fj associated with each atom in the crystal lattice [20] Figure II.10.

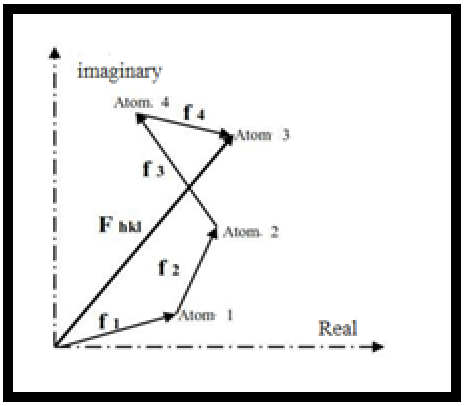

Figure II.10. A representation of the structure factor in the complex plane, sum of the contributions of each atom.

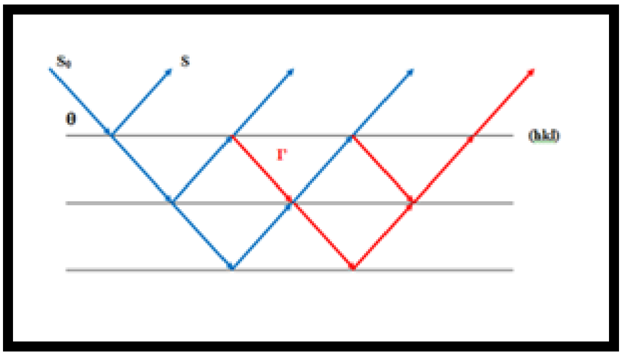

Figure II.11. Primary extinction

II.1.4.1.6.2. Secondary extinction

The impact of this extinction is particularly noticeable for low values of sin θ/λ where the intensities are high. Due to absorption and subsequent reflections by the contacted reticular planes, the intensity of the incident X-rays decreases as they enter the crystal volume (primary extinction). At the expense of the following planes, the first reticular planes refract more X-rays. Secondary extinction occurs when the intensity of the diffracted light decreases [21].

The secondary extinction can be corrected. The expression linking the calculated structure factor to the observed structure factor is written:

$$F_{cal} = F_{obs}(1 + g.I_{cal}) \qquad \text{(II.36)}$$

Where g: secondary extinction coefficient.

The value of g is 10^{-7} to 10^{-5} and can be refined by least square like any other parameter.

The secondary extinction can only be characterized by seeing the crystal as a mosaic, i.e. by creating perfect blocks of dimension t with minor disorientations from each other (less than 0.5 degree) (figure II.12).

In fact, we can confront two types of crystals: type I crystals, whose extinction is controlled by the width of the mosaic, and type II crystals, whose extinction is governed by the average dimension t, of the perfect domains.

The majority of crystals currently examined are type I [22]. Due to the complications of the extinction event, approximations have been used in the evaluation of secondary extinction. [23]. The distribution is assumed to be isotropic, which allows the formula for the secondary extinction factor to be derived easily.

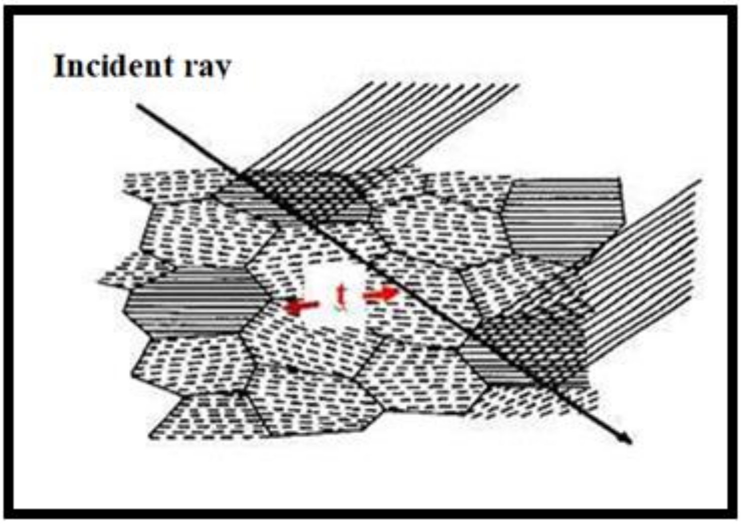

FigureII.12. mosaic crystal

II.1.5. Structure factor

The interatomic distances in a crystal are of the order of angstroms, which imply that the rays used in a diffraction experiment will have wavelengths ranging from 0.5 to 2 A°. The electrons of the atoms of the matter will interact with the X-rays, which are electromagnetic waves. Only the coordinated scattering of photons by the atoms without energy loss is important to us. The results of the diffraction experiments give us access to the electron density maps in the crystal lattice.

Indeed, each atom of atomic number Z contains Z electrons that are distributed around the nucleus.

Each electron j has its own electron density ρ(r)jet a form factor fe , fais the atomic form factor or atomic scattering factor which is the sum of the form factors of each electron in the atom :

$$f_a = \sum f_e(O) = \sum \rho(r) e^{iOr} dv(r) \quad \text{(II.37)}$$

Since the lattice often includes many atoms, the determination of the amplitude diffracted in a specific direction is acceptable, as is the combination of the complex amplitudes fa scattered by the atoms. This amplitude diffracted by all the atoms in the crystal is known as the structural factor, and it is recorded:

$$F_{hkl} = \sum N_j f_j exp\left(-B_j\left(\frac{\boldsymbol{sin\theta}}{\boldsymbol{\lambda}}\right)^{\mathbf{2}}\right)\left(exp\left(i2\left(hx_j + ky_j + lz_j\right)\right)\right) \qquad \text{(II.38)}$$

With:

Nj: number of atoms in the lattice.

fj: diffusion factor of atom j.

$exp\left(-B_j\left(\frac{\boldsymbol{sin\theta}}{\boldsymbol{\lambda}}\right)^{\mathbf{2}}\right)$: Fourier transform of the Gaussian probability cloud replacing the point position of the atom with Bj : isotropic atomic shift factor of atom j.
exp(i2(hx_j+ky_j+lz_j)) phase of the scattered waves with :
Xj, Yj, Zj : reduced coordinates of the atom and hkl Miller indices marking a family of lattice planes.
By definition, the diffracted intensity is none other than $I_{hkl}=|F_{hkl}|^2$, it is thus a matter of going from

- $Ihkl$ obtained by the experiment to the atomic coordinates Xj, Yj, j in the mesh. In reality only structure module is accessible to the experiment the phase of $Fhkl$ result V: the volume of the crystal (which must bathe entirely in X-rays).
- T: Transmission factor, it evaluates the fraction of intensity transmitted by the crystal. It is a number less than unity.

Multiply the measured intensity by T to obtain the absorption correction. As a result, the diffracted intensity is much greater than the recorded intensity. [24]
Many solutions have been devised to solve the problem of knowing T. In general, three absorption correction procedures are used. Namely:

1- The numerical corrections: analytical [25], Gaussian [26], spherical and cylindrical.
2- Semi-empirical corrections: Psi-Scans [27], CAMEL-JOCKEY [28] and Multi- scan [29].
3- Refined corrections: DIFABS [30], XABS2 [31] and SHELXA [32]

II.1.6. Scattering factor

The atomic scattering factor is the Fourier transform of the electron density of the atom. The atomic scattering factor is equal to the number of electrons Z for the zero value of 2θ. However, at the mesh, the electron cloud is not point-like, indicating that the atomic scattering factor decreases with the diffraction angle (destructive interference). As the atoms in the crystal fluctuate around their average atomic position (due to temperature), the X-rays do not perceive the atoms in the same position in the different crystal meshes.
In the case of an atom, the electron density has, to a first approximation, a spherical symmetry, and the intensity scattered by an atom is called the scattering factorand depends only $\frac{\boldsymbol{sin\theta}}{\boldsymbol{\lambda}}$. Figure II.13 gives some examples of atomic scattering factors.

Heavier atoms have a slower decay of the scattering factor, because of the greater (relative) electron density at the center of the atom.

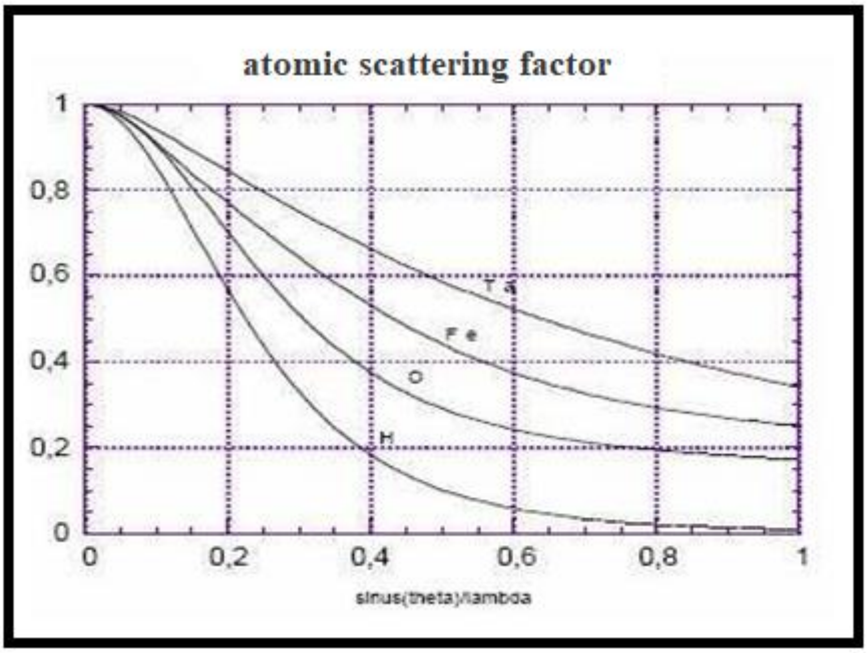

Figure II.13. Atomic scattering factors for some atoms (normalized to the total number of electrons).

II.1.7. Structural resolution

The search for the structural model using experimental data, including intensities from X-ray diffractometry, is called internal resolution. Exact determinations of the intensities of the allowed reflections, as well as the characteristics of the diffraction peak profile, are necessary for this method. In addition, the dimensions and multiplicity of the crystal lattice, the type and composition of the chemical species incorporated in the crystal lattice, and the appropriate space group must be specified. Once this data is accessible, the atomic positions within the crystal lattice can be recognized. Once this information is accessible, the atomic positions within the crystal lattice can be recognized. The structured decision must be made with the help of the program WINGX, which is currently under development. Realizes a Windows interface that gathers the majority of the software necessary for the treatment of most crystallographic problems, such as SHELX, which is a software for the resolution, analysis and refinement of structures.

It allows the use of X-ray or neutron diffraction data from single crystals, twinned crystals and crystalline powders. Of course, the algorithms and their improvements are formally valid and consistent with existing crystallographic practice. SHELX is widely used and can also be used to interact with other programs. Several strategies have been established in WINGX to solve structures from samples for example: Patterson's method [33], direct methods [34-35], direct space methods [36], maximum entropy method [37].

II.1.7.1. Patterson's method heavy atom method

It has been commonly used to determine crystal structures. It is simple to locate an atom that is much stronger than the rest. The interatomic paths of these atoms have a much higher weight than the rest. In this case, the Patterson function[11] is generally useful for locating the heavy atoms in the lattice and, consequently, for determining the approximate phase value of each structural component. As a result, the dreaded phase problem is often solved and the Fourier transform [12], which gives the electron density in the lattice [38], can be calculated. Then, using an incremental algorithm, more atoms are found and more atomic sites can be determined.

II.1.7.2. Direct methods

These direct techniques are frequently used to generate a reasonable approximation of the phases of structural factors. As phases are calculated using statistical and probability calculations, they are also called mathematical techniques. Phase recognition helps you calculate electronic density and determine atomic positions.[39]

[11] ***ArthurLindoPatterson***(1902–1966) He is a British crystallographic.

[12] ***JeanBaptisteJosephFourier***(1768-1830), is a French mathematician and physicist.

It is based on the following fundamental assumptions:

- Electronic density is positive throughout the space.
- Atoms are distinct entities. Electronic density is closely related to their position.
- The structural factor amplitudes carry phase information.

If the initial model is correct, there is convergence and the coordinates of the highlighted atoms are refined. In contrast to Patterson’s method, direct strategies [40, 41] attempt to determine a structural model without exploiting phase information. From the measured intensities, these methods attempt to predict the phase, or more precisely, the limits of conceivable phase values. These methods have been developed by two pioneers in the field, KARLE and HAUPTMAN [12], and are particularly well adapted to organic compounds. They are also considered mathematical methods since the phase is established via statistical and probability calculations. Phase recognition makes it possible to determine the electronic density and to deduce the atomic positions. The most commonly used numbers are U and E, which are closely linked to structural variables by direct processes.

$$(hkl)=\frac{F_{hkl}}{\sum_{l}^{n} f_j} \qquad \text{(II.39)}$$

$$|(hkl)|^2 = \frac{F_{hkl}}{\sum_{l}^{n} {f_j}^2} \quad \text{(II.40)}$$

U: called the unit structure factor; E: called the normalized structure factor.

n: number of atoms per cell; fj: diffusion factor of atom j.

Both resolution strategies (Patterson’s method and direct methods) find massive or moderately heavy atoms. Repeated Fourier difference synthesis uses the following relationship to predict the positions of the remaining atoms:

$$\rho_{obs} - \rho_{cal} = \frac{1}{v}\sum_h \sum_k \sum\left[|F_{obs}| - |F_{cal}|e^{-2\pi i(hx+ky+lz)}\right] \qquad \text{(II.41)}$$

cal: the estimated electronic density from the locations obtained during the resolution, i.e., from the calculated structural factors $F_{Cal;}$ $_{obs}$: the electronic density calculated from the observed structural factors F_{0bs} MULTAN and SHELX are two of the best known computational algorithms.

II.1.7.2.1. Standard structural factor

The Knowledge of the Standardized Structure Factor $|E_{hkl}|$ helps solve the phase problem. In addition, the study of the distribution of $|E_{hkl}$ $|$ allows us to clarify the possible existence of a centre of symmetry in the crystal and thus to lift the indeterminacy between the centered and the non-centric structures. The important role played by $|E_{hkl}$ $|$ values makes it essential to calculate their values with the greatest accuracy. Three methods are known and commonly used.

- **K curve method**

The module of the standard structure factor is defined by the:

$$\left|\vec{E}_H\right|^2 = \frac{|\vec{H}|}{\langle I \rangle} \qquad \text{(II.42)}$$

$$K(s) = \varepsilon\frac{I_{\vec{H}}}{\langle I \rangle} \ \text{(III.1)}_{\text{While}} S = \frac{\sin\theta}{\lambda} \qquad \text{(II.43)}$$

$\varepsilon$is a space group dependent parameter.

It is easy to plot this function, hence:

$$\left|\vec{E}_H\right|^2 = \frac{\left|F_{\vec{H}}\right|^2 K(s)}{\varepsilon \sum_j f_j^2} \quad \text{(II.43)}$$

Where the value of k(s) is read on the curve.

- **Wilson's method**

The previous technique has a critical defect in that it exploits the curve for significant values of sin; this problem can be solved by searching the value

$$\frac{log(\langle I \rangle)}{\varepsilon \sum_j f_j^2} \qquad \text{(II.45)}$$

depending on.

$$\frac{\sin\theta}{\lambda} \qquad \text{(II.46)}$$

The various points obtained are approximately on a straight line, so easy to exploit,

$$\langle I \rangle = A \sum_j f_j^2 exp\left(-B\left(\frac{\boldsymbol{sin\theta}}{\boldsymbol{\lambda}}\right)^{\mathbf{2}}\right) \qquad \text{(II.47)}$$

B is the temperature factor and A is the scale factor adjusting I to the experimental intensities. The value of A is the Y-axis and -2B is the slope of the line.

- **Debye method**

One of the limits of the Wilson curve is that the least squares line does not reach the bumps observed in the mean variations. I based on $\left(\frac{\boldsymbol{sin\theta}}{\boldsymbol{\lambda}}\right)^{\mathbf{2}}$ these bumps are generated by the molecular structure of the compound. This can be corrected by replacing $\sum_j f_j^2$

$$\text{By} \sum_n g_n^2 \qquad \text{(II.48)}$$

Where g is the diffusion factor calculated from the Debye formula:

$$g = \sum_i^m \sum_j^m f_i f_j \frac{\sin Kr_{ij}}{Kr_{ij}} \qquad \text{(II.49)}$$

Where $K = \frac{4\pi \sin\theta}{\lambda}$;$r_{ij}$the distance between atoms i and j; m being the number of atoms in the molecule.[42]

II.1.8. Structure refinement

The objective of structural refinement is to identify the best positions of atoms. At the same time, it makes it easier to spot hydrogen atoms. The latter, which are generally too light, do not appear before the refining process.

A quantity f is measured n times according to p parameters: x, y, z... Each evaluation i is liable to an error ei [12].

We have:

$$F_1 + e_1 = a_1x + b_1y + c_1z + \cdots \quad \text{(II.50)}$$

$$F_i + e_i = a_ix + b_iy + c_iz + \cdots \quad \text{(II.51)}$$

$$F_n + e_n = a_nx + b_ny + c_nz + \cdots \quad \text{(II.52)}$$

Based on the least squares principle, the best values of x, y, z, …are those that minimize the sum of error squares:

$$\sum_{i=1}^{N} {e^2}_i = \sum_{i=1}^{N}(a_ix + b_iy + c_iz \ldots - F_i)^2 \quad \text{(II.53)}$$

This sum must have a minimum value, which amounts to cancelling the derivative of this expression, namely , $\frac{\partial \sum_1^N {e^2}_i}{\partial x} = \frac{\partial \sum_1^N {e^2}_i}{\partial y} = \frac{\partial \sum_1^N {e^2}_i}{\partial z}$ (II.54)

The analysis of the results is particularly necessary to ensure that all the interatomic distances and angles between the bonds in addition Thermal agitation ellipsoids must have volumes compatible with adjacent atoms. Its development is controlled by relativity factors R1, R2, and GooF (Goodness of Fit) evaluation.

II.1.8.1. Least squares method

The refinement methods involve varying the parameters (atomic coordinates, thermal agitation factors) of each atom to minimize the reliability function:

$$R = \sum_s m_s(|F_s^{obs}| - K|F_s^{obs}|)^2 = \sum_s m_s\, \Delta F_s^2 \quad \text{(II.55)}$$

$\omega_s$isthe weight assigned to the reciprocal vector diffraction task S and k a scale factor between the calculated and observed factors.

$$R = R(X_1 \ldots\ldots\ldots\ldots\ldots\ldots, X_i, \ldots\ldots\ldots\ldots\ldots\ldots.. X_N) \quad \text{(II.56)}$$

When the minimum R is reached, all 6R/6xi derivatives are null and:

$$\sum_s m_s \Delta F_s \frac{6\Delta F_s}{6X_i} = 0 \Rightarrow \sum_s m_s \Delta F_s \frac{6|F_s^{cal}|}{6x_i} = 0 \qquad (II.57)$$

In the first order, we can write:

$$\Delta\left(\frac{6R}{6X_i}\right) = \sum_i \left|\frac{6}{6X_i}\sum_s - m_s \Delta F_s \frac{6|F_s^{cal}|}{6x_i}\right| .dX_i \qquad (II.58)$$

The best xi are the system solutions of N linear equation

$$\sum_s \Delta X_i \sum_s m_s \frac{6|KF_s^{cal}|}{6u_i} . \frac{6|KF_s^{cal}|}{6u_j} = \sum_s m_s \frac{6|F_s^{cal}|}{6u_j} \qquad (II.59)$$

By asking:

$$a_{ij} = \sum_s m_s \frac{6|KF_s^{cal}|}{6u_i} . \frac{6|KF_s^{cal}|}{6u_j} ; y_i = \sum_s m_s \frac{6|F_s^{cal}|}{6u_j} \qquad (II.60)$$

The system of normal equations is written:$\alpha_{ij}.\Delta x_i=y_i$The resolution of this system assumes a symmetrical matrix inversion:

$$\Delta X_i = \left(a_{ij}\right)^{-1} Y_i \qquad (II.61)$$

To simplify the problem, we can notice that each element of the matrix αij is a sum of a partial derivative product whose signs are random.

a. Reliability factors

We improve by using the least squares method, which improves the squares of the Fhkl components. We use relativity factors R (unweighted) and Rw (weighted), which are defined as follows:

$$R = \left\{\frac{\sum\left(|F_{obs}|^2 - |F_{cal}|^2\right)^2}{\sum |F_{obs}|^2}\right\}^{\frac{1}{2}} \qquad (II.62)$$

F_{0bs}:Observed structural factor;F_{Cal}:Calculated structural factor.

$$R_\omega = \left\{\frac{\sum\left(|F_{obs}|^2 - |F_{cal}|^2\right)^2}{\sum \omega |F_{obs}|^2}\right\}^{\frac{1}{2}} \qquad (II.63)$$

ωis the weighting factor attached to the F0bsmeasurement of the structure factor.

ω:is the weighting factor attached to the Fobsof the structure factor given by:

$$\omega = \frac{1}{[\sigma^2(F_{obs}^2) + (a\rho)^2 + b\rho]} \qquad (II.64)$$

(aAnd$b$are $constants$)

Where$\rho = \frac{2F_{cal}^2 + Max(F_{obs,a})}{3}$ (II.65)

The more the concordance between the Most the concordance between F_o , and F_{cal} is better the values of R_1 and ωR_2 tend towards zero.

$$R = \frac{\Sigma(||F_{obs}| - |F_{cal}||)}{\Sigma|F_{obs}|} \quad \text{(II.66)}$$

b. Goodness variance factor (GooF) estimation

The LSFM (least-Squares-Full-Matrix) program uses a mechanism similar to the R-factor to provide information on the divergence between the estimated model and the actual structure, namely the GooF (Goodness of fit) factor, which is described by:

$$GooF = S = \left\{\frac{\Sigma(|F_{obs}|^2 - |F_{cal}|^2)^2}{n-p}\right\}^{\frac{1}{2}} \quad \text{(II.67)}$$

n: number of reflections in the refinement; p: number of parameters in the refinement When S tends towards 1 we have a good refinement.

c. Fourier synthesis

These direct techniques often provide a rough approximation of the phases of structural factors. As phases are calculated using statistical and probability calculations, they are also called mathematical techniques. Knowledge of the phases makes it possible to calculate the electronic density and to establish the atomic positions. It is based on the following fundamental assumptions:

Fourier coefficients are defined as:

$$\Delta F = F_{obs} - F_{cal} \quad \text{(II.68)}$$

Where:

$F_{obs}$and$F_{Cal}$are the observed and calculated structural factors.

The difference synthesis calculation requires the use of the FCal phases obtained from the refinements and applied to both$F_{obs}$and F_{cal}, the Fourier coefficients are then defined as

$$\Delta F = (|F_{obs}| - |F_{cal}|)^{i\phi_{cal}} \quad \text{(II.69)}$$

$\O_{Cal}$:is the calculated structural factor phase.

$$\Delta\rho = \rho_{obs} - \rho_{cal} = \frac{1}{v}\Sigma_{hkl}\,\Delta F_{hkl} e^{-2i(hx+ky+lz)} \quad \text{(III.70)}$$

II.2. Spectroscopic analysis

II.2.1. Introduction

Spectroscopy depends entirely on a radiation interaction with matter (atom, molecule, ion, and so on); etymologically, spectroscopy reads the motion of an image by accurately identifying this item the structure identification. An orderly arrangement of electromagnetic radiation is categorized in ascending order based on the frequency, number of waves, or wavelength d of the known electromagnetic radiation (Figure I).

We differentiate between atomic and molecular spectroscopy, originating from a radiation-matter interaction. If the contact is with atoms, a spectrum of lines such as x-rays, atomic absorption, and so on will be produced.

If contact occurs with molecules, the spectra of bands under the envelope all cover lines of all the molecule atoms that are likely to suffer alterations due to the applied effect. These methods are often employed to obtain quantitative or qualitative data from small-scale chemical molecules. This may be done in scientific research (astronomy, atomic physics, chemistry, biology, and so on) and industrial sectors (chemical industries, medicines, food, and so on). Radiations are responsible for various spectroscopies that may be distinguished based on the excitation wavelength.

- UV-visible light has a wavelength range of 2000 to 800 nm.
- Infrared has a wave number range of 4000-200cm-1, which includes near-infrared, medium infrared, and far infrared.
- In the case of NMR, radio waves with a frequency of 800 to 10 MHZ are used.

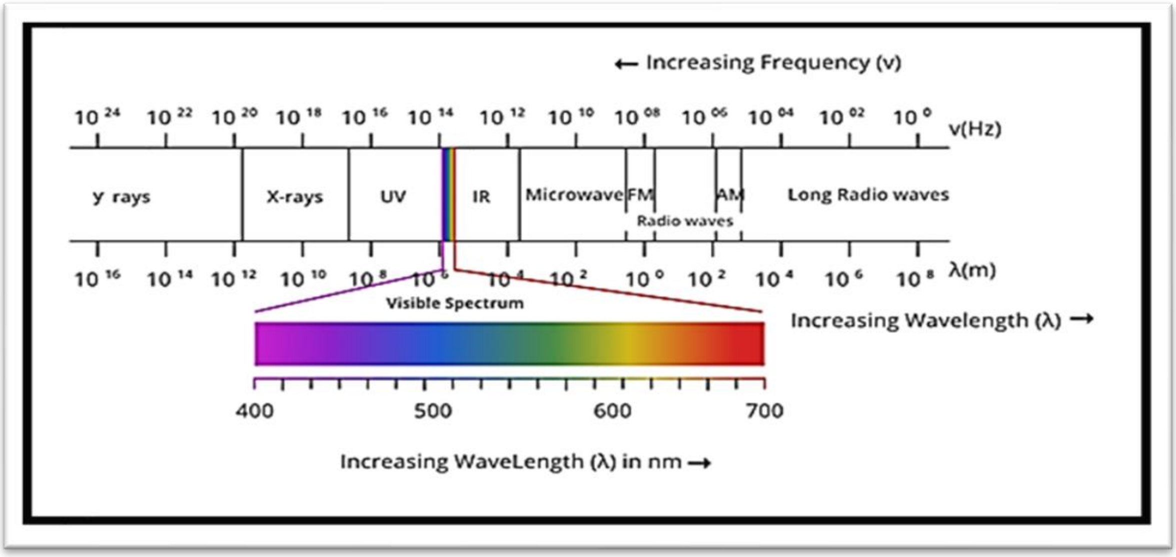

Figure II.14. Spectral domains of electromagnetic waves

II.2.2. IR spectroscopy

Spectroscopy being the study of the interaction between light and matter, there are many forms of spectroscopy that we can use to collect data on the structure of a molecule. The molecule irradiates a sample with infrared light, which can interact in some way with the compounds in the sample, and then ends up reaching a detector so that some of the light is absorbed by the sample, others not, still others pass and this is information that we can use to discover something about the structure of the reason why we use infrared light is that another molecule that we already know that molecules move has a translation movement.We know that thermal energy is converted into kinetic energy. It is converted into motion so that the molecule says that one gas or even one liquid moves relative to another, and thanks to conformation analysis, we also know that the bonds are in constant rotation. Time, so all sigma bonds have a rotation motion, but chemical bonds do other things too if they can do those other things that happen specifically when they are exposed to a very specific wavelength of infrared light. Something like a symmetrical or asymmetric stretch in which covalent bonds can contract and expand according to a certain oscillation, depending on whether they have absorbed this particular photon of ultraviolet light. One can also have an asymmetric stretch or an asymmetric stretch in the plane and a twist. [43, 44] These vibrations occur at a particular energy when the molecule absorbs a specific wavelength from the infrared and it will vary depending on the functional group, so the identity of the atoms in a molecule will affect the absorption photon, this information is used to generate an IR spectrum. The IR spectrum has two axes: At the bottom we have the wave number which indicates the particular energy of infrared light while the second axis propagates the transmittance or the percentage of the specific wavelength if we have 100% or nearly 100% information of transmittance. This means that the infrared light that corresponds to this number of waves passes through the sample. It is not absorbed by the sample. Then when we have peaks where we have information, it doesn’t get to the detector, they are therefore absorbed by the sample and there is a particular functional group in the molecule that is in the sample that absorbs the IR light from this wave number, which reveals the type of bonds in this compound.

Analytical infrared uses electromagnetic radiation between 1 and 50 m to detect or measure chemicals by methods based on the absorption or reflection of light by the sample. This localized radiation lies between the visible and microwave regions of the spectrum, beyond the wavelengths in the red. The infrared wavelength ranges from 0.8 m to 1000 m. It is arbitrarily classified into three wavelengths: near infrared (0.8-2.5 m or 12500-4000 cm-1), middle infrared (2.5-25 m or 4000-400 cm-1) and far infrared (25-1000 m or 400-10 cm-1).

The transition between these vibrational energy levels is analogous to the simultaneous occurrence of two processes:

- The interaction between the electric field of incoming radiation and the electrons within the material, resulting in changes in the electric dipole moment and, as a result, atomic vibrations.
- Planck's law governs the absorption of incoming light energy, which matches the energy gap between two vibrational levels.

$$\Delta E = h_{\nu} = (\nu_i) - E(\nu_j) \qquad \text{(II.71)}$$

With the Planck constant, the frequency of the incoming radiation, and$E(\nu_i)$,$E(\nu_j)$ are the energies of the molecule's vibrational states.

Infrared spectroscopy is the process of exposing a sample to infrared radiation, then detecting and analyzing the radiation after it interacts with the substance. This high selectivity analytical approach is mostly used for chemical identification. It does, however, give useful information on intermolecular and intramolecular interactions, molecule shape, and the structural arrangement of substances [45].

Harmonic oscillators are used to show the composition of a material in the field of infrared spectroscopy. Chemical bonds serve as spring-like forces, connecting atoms together. In this case, Hooke's law governs the vibration frequency, which is determined by the spring stiffness constant (k) and the decreased mass (μ),

$$\nu_{vib} = \frac{1}{2\pi}\sqrt{\frac{k}{\mu}} \qquad \text{(II.72)}$$

Referring back to the preceding link, the strength of chemical connections and the particular atomic group involved influence vibrational frequencies. In layman's words, each vibrational frequency correlates to a unique chemical connection. As a result, when incoming radiation is absorbed at a certain frequency, it resonates with the vibration of a specific chemical bond, resulting in a unique infrared absorption spectrum typical of the sample being analysed [46].

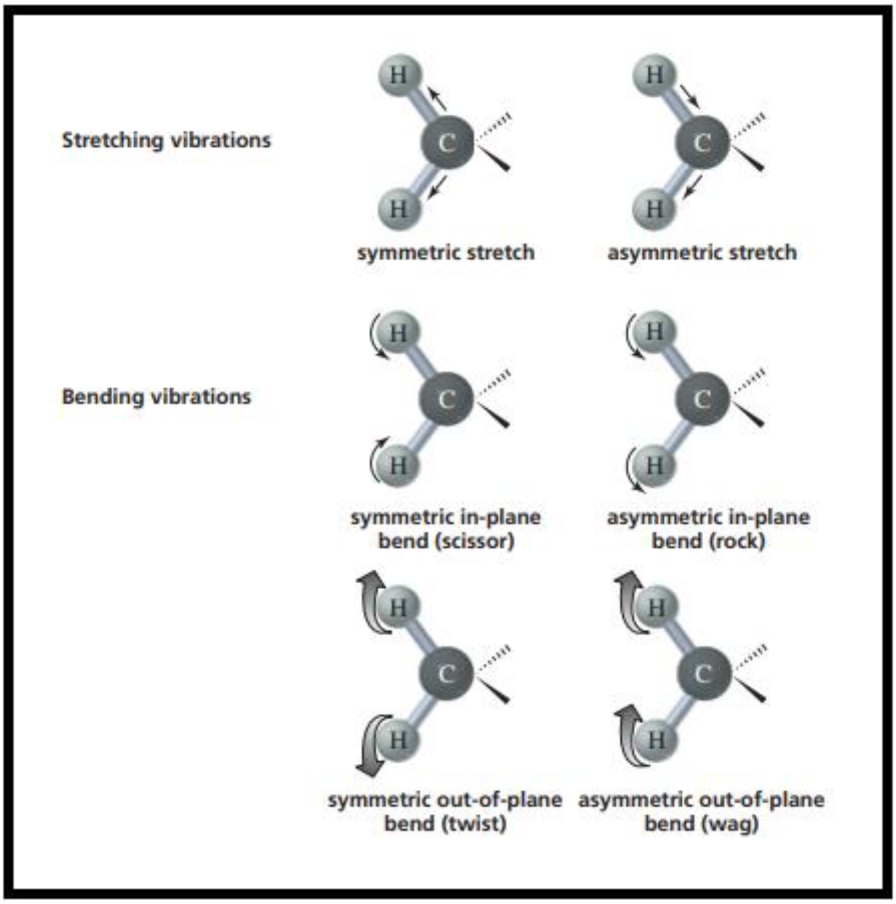

Figure II.15. Types of vibrations.

In addition to the figure described stretching and bending vibrations, there are four forms of bending vibrations: wagging, scissoring, rocking, and twisting. Each vibration would absorb a particular frequency of IR. Shown in the following chemical vibrations:[44]

1. **Rocking:** A rocking vibration occurs when the atoms of a molecule move back and forth, changing the angle between them. This may cause a change in the molecule's dipole moment.
2. **Scissoring:** A scissoring vibration occurs when the atoms of a molecule move in opposing directions, changing the angle between them. This may also cause a change in the molecule's dipole moment.
3. **Twisting vibrations** occur when atoms in a molecule spin around a bond axis, causing the molecule to alter form. This may cause a change in the molecule's dipole moment.
4. **Wagging:** A wagging vibration occurs when the atoms of a molecule travel back and forth, changing the angle between them, similar to a rocking vibration. This may also cause a change in the molecule's dipole moment.

Each of these kinds of vibrations may be seen in a molecule's infrared spectrum, and they can provide important information about the molecule's structure and capabilities.

If the bonds between atoms in the target material enable these atoms to vibrate at this frequency, a photon of light with an infrared frequency will be absorbed [47].

II.2.3. Nuclear magnetic resonance (NMR)

Nuclear magnetic resonance is a method that uses magnetic discipline and electromagnetic frequencies to examine molecular systems. To obtain excessive magnetic fields, superconducting magnets are used; decreasing fields can be generated by permanent magnets or electromagnets. The model is thus positioned at the level of the most powerful discipline and the maximum homogeneity of the magnet.

The NMR probe includes coils that can be used to excite the model and document signal responses to the radio frequency. The foundation of NMR is that nuclei behave like microscopic magnets in a magnetic discipline, they revolve around the primary magnetic discipline like a rotating pinnacle; this movement is called possession; the frequency of precessions is proportional to the energy of the magnetic field; additional variations of the discipline nearby are brought through the conversion of electronic densities in a molecule.

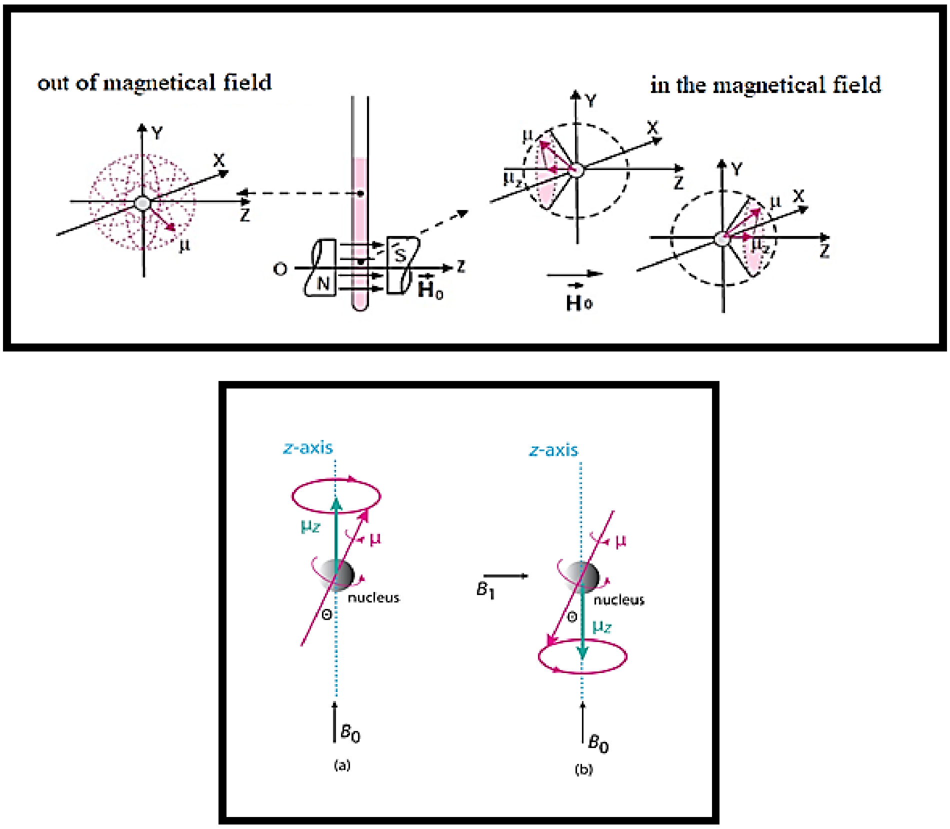

Figure II.16: Effect of a magnetic field on a 1/2 spin number nucleus present in a solution compound.

Alternatively, the quantum number of nuclear spin I can take the values: 0, ½, 1, 3/2 … in the case each atomic nucleus possesses a rotating charge known as nuclear spin, similar to tiny magnets, resulting in a nuclear magnetic moment. When subjected to a uniform external magnetic field, the atomic nucleus (its nuclear magnetic moment) can adopt various orientations. These orientations correspond to distinct energy levels: a lower-energy state when the magnetic moment aligns parallel to the external field's direction and a higher-energy state when the alignment is opposite. [48]The energy difference ΔE between these two states is directly proportional to the strength of the external magnetic field. The transition from the lower energy state to the higher energy state can occur by absorbing radiation at a specific frequency denoted by υ, where $\Delta E = h\upsilon$.

NMR spectroscopy, as the name implies, is a type of spectroscopy - an analytical technique that looks into the energy levels of a chemical species; in the case of NMR (Nuclear Magnetic Resonance that is), one particular atom at a time is looked at by interacting it with electromagnetic radiation.

The fundamental components of organic and biological molecules primarily consist of hydrogen and carbon atoms. As previously explained, NMR spectroscopy is applicable exclusively to nuclei that exhibit NMR activity, which includes nuclei with non-zero spin ($I \neq 0$). Hydrogen, being the most prevalent isotope, demonstrates NMR activity (1H, 99.98%, I = ½). Conversely, carbon's most abundant isotope does not exhibit NMR activity (12C, 98.89%, I = 0). NMR spectrometers can solely detect the 13C isotope, which constitutes only 1.11% of carbon atoms. Furthermore, the gyromagnetic ratio of 13C is also four times lower than that of 1H. These two factors combine to result in 13C NMR being considerably less sensitive compared to 1H NMR, as shown in Table 1. This variance in sensitivity necessitates longer experimental durations for 13C NMR (hours) as opposed to 1H NMR (seconds or minutes) [49].

Atomic nuclei possessing an odd mass number exhibit a unique property known as nuclear spin, enabling them to engage with radio waves in the presence of an external magnetic field. This external magnetic field is what these nuclear spins interact with. Each element whose nuclei possess this property is characterized by specific resonance frequencies[50-51]. For instance, among the most common elements, hydrogen and carbon have isotopes with nuclear spins that resonate at 200 MHz and 50 MHz, respectively (these isotopes being ^{1}H and ^{13}C).

When the nuclear spins of these atoms are aligned with the external magnetic field, they can absorb energy, and this absorption is influenced by the local atomic surroundings. It's important to note that ^{1}H and ^{13}C are not the sole isotopes capable of interacting with an external magnetic field; numerous others can do so and can thus be detected through NMR spectroscopy due to their distinct resonance frequencies, including isotopes like ^{19}F, ^{31}P, and more. In NMR spectroscopy, the signals arising from the interaction of these nuclei with electromagnetic radiation are compared against a reference compound. In the case of ^{1}H NMR, this reference compound is $Si(CH_3)_4$, commonly referred to as tetramethylsilane [52].

NMR is a powerful tool to retrieve info about the local environment of such nuclei (one at a time, that is) and this is the reason why chemists use it on a daily routine for many purposes:

- identification of compounds;
- structure;
- progress of reactions;
- local environments;
- Identification of same atoms on different regions of a compound.

II.2.3.1 Relaxation phenomenon

Better electron density leads to greater protection and, consequently, a decrease in proximity discipline and protection frequency. In NMR, the frequency of the pins of the excited nuclei can be measured from the electrical day they trigger inside the coil. Fourier's transformation of the time zone alerts the consequences of the frequency spectrum with a sign for each type of nucleus. Single frequencies are called chemical shifts because they depend on the chemical form of the nuclei. In the exercise, spectra are measured for all hydrogen nuclei without delay, resulting in the ethanol spectrum with 3 unique peaks at unique chemical shifts. As nuclear spins behave like magnets, they also have an impact on their associates, notably through electrons shared in chemical bonds within the molecule, what we call a coupling j. Each spin can have states along the magnetic discipline or against the magnetic discipline. As an example, we look at the 2 spins of methyl hydrogen that could be chemically equal; they could give 4 mixtures: one spin down, one spin up, each spin down, one up, one down, spins up Each mixture has a unique strength stage and has an impact on neighboring spins; in addition, mixtures up and down and up have equal strength stage and impact on, they have an impact on is seen as a division of the methyl institution sign into 3, this is called a multiplet. Similarly, the 3 spins of methyl hydrogen break down the reaction of methylene into 4 alerts. In the end, NMR makes it possible to discover molecular systems from chemical displacements and multiplets.

In NMR, certain nuclei have the ability to assume two distinct orientations when aligned with an external magnetic field (B_0). One orientation corresponds to the nucleus's lowest energy state (aligned parallel to the external magnetic field), while the other corresponds to its highest energy state (aligned antiparallel to the external magnetic field) (Figure II.4). The difference in energy levels (ΔE) depends on both the strength of the magnetic field and the gyromagnetic ratio γ.

$$\Delta E = \frac{\gamma h B_0}{2\pi} \qquad \text{(II.73)}$$

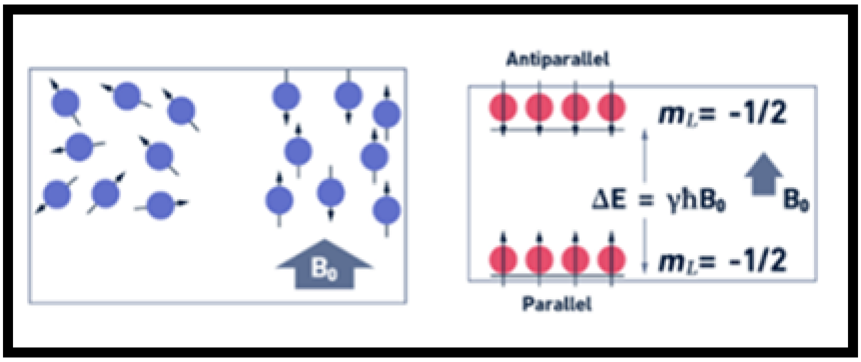

Figure II.17. .Nuclear spin orientations of an aligned sample (parallel and antiparallel) with the direction of an external magnetic fieldB_0.

II.2.4. UV-Visible Spectroscopy

II.2.4.1. Definition

UV-Visible spectrophotometry is a standard qualitative method used daily in many laboratories, it owes its popularity to its simplicity, in fact it has a wide field of application and does not require complex sample preparation; Easy to perform and producing results in seconds, a standard measurement requires only a small amount of samples and since it is a non-destructive method, the samples can be reused for further analysis.

II.2.4.2. Principle

The principle of visible UV spectrophotometry is based on the absorption of radiation by a molecule in the range of 200 to 800 nm; from 200 to 400 nm it is close UV, glass absorbs in UV but it protects against ultraviolet radiation so cannot be used in UV spectrophotometry, it is replaced by quartz tanks, from 4000 to 800 nm it is the regions of the electromagnetic spectrum detected by the eye unlike the UV one can use glass tanks, [53-54] the color it is the manifestation of the absorption of the visible light, when the wavelength is less than 200nm it is the far UV or all the absorbed substances it is a method based on the modification of the electronic structure of the molecules, in visible UV the electronic energy of transition masks the other secondary energies vibrational and rotational because it is much more important, for a diatomic molecule that it was in the ground state after the absorption of a radiation it passes to an excited state that it has for energy.

$$E_1=E_0+h\,\nu \qquad (II.74)$$

$$Et\ \Delta E=h\,\nu=hc/\lambda \qquad (II.75)$$

From or:

E_1: energy after excitation

E_0: energy in a ground state

h: is the board constant

ν: is the frequency in hertz Hz

C: is the speed of light in the medium where the wave propagates and λ: is the wavelength

The increase of the energy of an electron or a valence light when an isolated molecule absorbs a photon in the field, UV-visible, the electron passes from a binding orbital to an anti binding orbital, the return to the ground state is done by a relaxation, the non-radiation is accompanied by a restitution of excitation energy in the form of heat ,the electronic transition from a fundamental level to an excited level is accompanied by numerous vibrational and rotational transitions that condition the pace of the spectrum, the UV spectrum will therefore be a succession of very little distant rais, each other resulting in a spectrum of bands when the transition takes place that does not mean that the electron changes its orbital except that the energy that changes the electrons concerned are the furthest from the nucleus (valences electrons those of the outer layer), there are 5 energy levels: sigma, n, n* so sigma* and the two excited levels are sigma* and pi* the electrons n are the non binding electrons, sigma electrons are those which are simple monovalent of saturated hydrocarbons pi electrons involved in unsaturated multiple bonds are formed by binding by sigma electrons and one or more binding by pi electrons, The different types of effects on a spectrum, bathochrome effect λ +, hypochrome effect λ -, hyper chrome effect ε + and hypsochrome effect ε -.

Thus, hundreds of functions will induce absorption; these are chromophores.

- Sigma transition - sigma* in the far UV this transition has no analytical interest, it is the least studied, it results in an absorption located in the lowest wavelength and requires a high energy, molecules that exhibit this transition like alkanes can be used as solvents in UV-vis spectroscopy

- The n- sigma* transition: the absorption wavelength is around 180 to 190nm with an average intensity.
- The pi - pi* transition: it is when there are several double bonds that the wavelength can be between 200 and 800 nm otherwise for the isolated chromophore has only one double bond it has no interest in the UV, these pi - pi* transitions are average over energy level and wavelength.
- The n-pi* transition: it is found for molecules with a heteroatom carrying a double free electronics and belonging to an unsaturated system it is the least energetic transition with a high wavelength.

In the case of the sigma-sigma* and pi-pi* transition the energy levels of the ground state and the excited state are on the same axis and are considered possible transitions and absorption and intense, in the case of the n-pipi* and n-sigma*, ground state and excited state energy levels are not on the same axis and it is the least energetic transition with a high wavelength. In the case of the sigma-sigma* and pi- pi* transition, the energy levels of the ground state and the excited state are on the same axis and we consider that these are possible transitions and absorption and intense, in the case of the n-pipi* and n-sigma*, ground state and excited state energy levels are not on the same axis and this type of transition is normally impossible but probable, we consider:

- If ε is greater than 10^4 the transition is allowed
- If ε is less than 10^4 the transition is not allowed

The parameters which characterize the absorption bands are: The maximum absorption wavelength or the frequency and intensity expressed as ε_{max}, we find:

- R (radical) bands: those of the n-pi* transition found in the chromophore with heteroatoms carrying free electrons.
- K-bands (conjugate): follows the conjugate double-bond system respond.
- B-bands (benzoids): in the aromatic and heteroaromatic molecule.
- E (ethylene) bands: in aromatic molecules substituted by oxo-chromatic groups.

This strategy is widely applicable in a variety of sectors. For example, it may be used to ensure the safety of electrical energy supply by monitoring the color index of transformer oil as a preventative precaution.

It is essential in the medical field, for example, in determining hemoglobin concentrations by evaluating hemoglobin absorbance. This use is very useful in cancer research [55].

UV-Vis spectroscopy is a useful technique in kinetic investigations of water treatment and control. It aids in the verification of the successful removal of certain dyes or dye by-products by tracking changes in their spectra over time [56]. It is also commonly used in the investigation of food authenticity and the assessment of air quality.

UV-Vis spectroscopy is also useful in more specialized study fields. Monitoring wavelength changes associated with absorbance peaks is useful for analyzing exact structural variations in proteins [57] and determining the composition of batteries [58]. Such wavelength changes are also useful in modern applications, such as identifying very minuscule nanoparticles [59]. This technique's potential uses are vast and almost unlimited.

II.3. Conclusion

X-ray powder diffraction and molecular spectroscopy approaches have distinct functions in structural investigation, offering distinct perspectives on the atomic and molecular structure of materials. X-ray diffraction primarily examines the extended regularity of atomic organization, whereas molecular spectroscopy techniques offer insights into the immediate structure, irrespective of the long-range atomic organization. Every approach is associated with a distinct energy range within the electromagnetic spectrum, enabling a comprehensive analysis of material characteristics. X-ray diffraction is essential for identifying the spatial configuration of molecules, their periodicities, and crystallographic and molecular geometric characteristics. Infrared spectroscopy (IR) is employed to identify distinctive molecular geometry groups, UV-visible spectroscopy is utilized to assess electronic structure, and Nuclear Magnetic Resonance (NMR) spectroscopy is valuable for ascertaining the hydrogen-carbon skeleton of molecular structures. The density functional theory approach may theoretically validate the outcomes derived from various methodologies, so augmenting the reliability and precision of experimental data.

References

[1]. Jeffry, J. W. (1971). Method in X-Rays Crystallography. Academic Press, London. Buėrger, M. J. (1958). X-Ray Crystallography. J. Wilen and Sons, INC, New York. Guinier, A. (1964). Théorie et techniques de la radiocristallographie. Dunod, Paris.

[2]. Wilson, A.J.C. (1962). X-rays Optics. Methuen & Co LTD, London.

[3]. Rietveld, H.M. (1967). ActaCryst. 6, 266.

[4]. Jeffry, J. W. (1971). Method in X-Rays Crystallography. AcademicPress, London.

[5]. Buėrger, M. J. (1958). X-Ray Crystallography. J. Wilen and Sons, INC, New York

[6]. Guinier, A. (1964). Théorie et techniques de la radiocristallographie. Dunod, Paris.

[7]. Williams, L., Press, W., &Zachariasen, W. H. (2000). Dover Publication, New-York.

[8]. Harms, K., &Wocadlo, S. (1995). XCAD4, Program for Computing Data Reduction of CAD4-Diffractometer data. University of Marburg, Germany

[9]. Vand, V., Eiland, P. F., &Pepinsky, R. (1957). ActaCryst., A10, 303.

[10]. Molen. (1990). An Interactive Solution Structure Procedure. ENRAF NONIUS. Deflt, Netherlands

[11]. Darwin, C. G. (1922). Phil. Mag, N°43, p.800.

[12]. Ouahes, R. (1995). Eléments de Radiocristallographie. Office des Publications Universitaires.

[13]. Kittel, C. (1983). Physique de l'état solide (5ème édition). Dunod, Paris.

[14]. Van Meersseneef, M., &Dupont, J.F. (1973). Introduction à la cristallographie et à la chimie structurale. Vander-édition.

[15]. Arndt, U.W., & Willis, B.T.M. (1966). Single crystal diffractometry. Cambridge University Press.

[16]. Giacovazzo, C., Monaco, H. L., Viterbo, D., Scordari, F., Gilli, G., Zanotti, G., &Catti, M. (1998). Fundamentals of Crystallography. IUCR, Oxford Science Publications.

[17]. Stout, G.H., &Jenson, L.H. (1968). X-ray Structure Determination: A Practical Guide. Macmillan Publishing Co, Inc, New York, Collier Macmillan Publishers London.

[18]. Darwin, C.G. (1922). Phil. Mag, N°43, p. 800.

[19]. Ewald, P.P. (1971). Ann. Phys, N°54.

[20]. Giacovazzo, C. (2002). The Diffraction of X-rays by Crystals. In: Fundamentals of Crystallography, 2nd edition (Ed. C. Giacovazzo), Oxford University Press, pp. 157-158.

[21]. Kato, N. (1976). ActaCryst, A32, 458.

[22]. Dunsteller, F. (1981). Thèse de doctorat, Université Pierre et Marie Curie, Paris-VI.

[23]. Zachariasen, W. H. (1967). Acta Cryst, 23, 558.

[24]. Giacovazzo, C. (2002). The Diffraction of X-Rays by Crystals. In: Fundamentals of Crystallography, 2nd edition (Ed. C. Giacovazzo), Oxford University Press, Oxford, pp. 157-158.

[25]. de Meulenaar, J., &Tompa, H. (1965). ActaCryst, A19, 1014-1018.

[26]. Flack, H.D. (1974). ActaCryst, A30, 569.

[27]. North, A.C.T., Phillips, D.C., & Mathews, F.S. (1968). ActaCryst, A24, 351-359.

[28]. Flack, H.D. (1975). J. Appl. Cryst, 8, 520-521.

[29]. Blessing, R.H. (1995). ActaCryst, A51, 33-38.

[30]. Walker, N., & Stuart, D. (1983). ActaCryst, A39, 158-166.

[31]. Parkin, S., Moezzi, B., & Hope, H. (1995). J. Appl. Cryst, 28, 53-56.

[32]. Sheldrick, G.M. (1997). SHELX: A Suite of Programs for Crystal Structure Analysis. University of Göttingen, Germany.

[33]. Patterson, A.L. (1934). A Fourier Series Method for the Determination of the Components of Interatomic Distances in Crystals. Physical Review, 46, 372-376.

[34]. Hauptman, H.A., &Karle, J. (1953). Solution of the Phase Problem. I: The Centrosymmetric Crystal. American Crystallographic Association Monograph. Polycrystal Book Service, Dayton, Ohio, 3.

[35]. Hauptman, H.A., &Karle, J. (1956). Structure Invariants and Seminvariants for Noncentrosymmetric Space Groups. ActaCrystallographica, 9, 45-55.

[36]. Deem, M.W., &Newsam, J.M. (1992). Framework Crystal Structure Solution by Simulated Annealing: Test Application to Known Zeolite Structures. Journal of the American Chemical Society, 114, 7189-7198.

[37]. Gilmore, C.J. (1996). Maximum Entropy and Bayesian Statistics in Crystallography: A Review of Practical Applications. Acta Crystallographica, A. 525, 561-589.

[38]. Teobald, F. (1991). Cours de Cristallographie pour la Chimie et les Matériaux. Paris Onze Edition.

[39]. Rawiya, Bahoussi (2017). Étude Structurale, Vibrationnelle et Thermique d'un Nouveau Composé Organique, le C18H20O3N4S. Thèse de Doctorat, MOSTAGABEM.

[40]. Sheldrick, G.M. (1990). Acta, A46, 467-473.

[41]. Karle, J., &Hauptman, H. (1950). Acta Cryst. A9, 181.

[42]. BoukabchaN.(2017). Étude des Propriétés Structurales des Composés Organiques Poly-Substitués. DoctorateThesis.

[43]. Marshan, H., Usha, D., Amalanathan, M., Geetha, R. R. J., & Mary, M. S. M. (2021). Vibrational spectral, density functional theory and molecular docking analysis on 4-nitrobenzohydrazide. Journal of Molecular Structure, 1223, 128948. https://doi.org/10.1016/j.molstruc.2020.128948.

[44]. McQuarrie, D. A., & Simon, J. D. (1997). Physical chemistry: A molecular approach. University Science Books.

[45]. Stuart, B. H. (2004). Infrared spectroscopy: Fundamentals and applications. John Wiley and Sons.

[46]. Jamroz, M. H. (2004). VibrationalEnergy Distribution Analysis, VEDA 4 Computer Program. Poland.

[47]. Djafri, A. (2017). Synthèse, étude structurale et propriétés physico-chimiques associées de quelques composés hétérocycliques [Doctoral dissertation, Université Abdelhamid Ibn Badis de Mostaganem].

[48]. Wong, K. C. (2014). Review of NMR Spectroscopy: Basic Principles, Concepts and Applications in Chemistry. Journal of Chemical Education, 91(8), 1103–1104. https://doi.org/10.1021/ed500324w.

[49]. Silverstein, R. M. (1991). Spectrometric identification of organic compounds. Wiley.

[50]. Anderson, R. J., Bendell, D. J., & Groundwater, P. W. (2004). Organic Spectroscopic Analysis. Royal Society of Chemistry.

[51]. Silverstein, R. M., Webster, F. X., &Kiemle, D. J. (2014). Spectrometric identification of organic compounds. John Wiley & Sons.

[52]. Hollas, J. M. (2004). Modern spectroscopy. John Wiley & Sons.

[53]. Rao, C. N. R. (1967). Ultra-Violet and Visible Spectroscopy. Butterworths.

[54]. Silverstein, R. M. (1968). Identification spectrométrique de composés organiques.

[55]. Brown, J. Q., Vishwanath, K., Palmer, G. M., &Ramanujam, N. (2009). Advances in quantitative UV–visible spectroscopy for clinical and pre-clinical application in cancer. Current Opinion in Biotechnology, 20(1), 119.

[56]. Pinheiro, H. M., Touraud, E., & Thomas, O. (2004). Aromatic amines from azo dye reduction: status review with emphasis on direct UV spectrophotometric detection in textile industry wastewaters. Dyes and Pigments, 61(1), 121.

[57]. Kristo, E., Hazizaj, A., &Corredig, M. (2012). Structural Changes Imposed on Whey Proteins by UV Irradiation in a Continuous UV Light Reactor. Journal of Agricultural and Food Chemistry, 60(25), 6204.

[58]. Patel, M. U. M., Demir-Cakan, R., Morcrette, M., Tarascon, J.-M., Gaberscek, M., &Dominko, R. (2013). Li-S Battery Analyzed by UV/Vis in Operando Mode. ChemSusChem, 6(6), 1177.

[59]. Begum, R., Farooqi, Z. H., Naseem, K., Ali, F., Batool, M., Xiao, J., &Irfan, A. (2018). Applications of UV/Vis Spectroscopy in Characterization and Catalytic Activity of Noble Metal Nanoparticles Fabricated in Responsive Polymer Microgels: A Review. Critical Reviews in Analytical Chemistry, 48(6), 503.

Chapter III

Mathematical formalism of molecular modeling

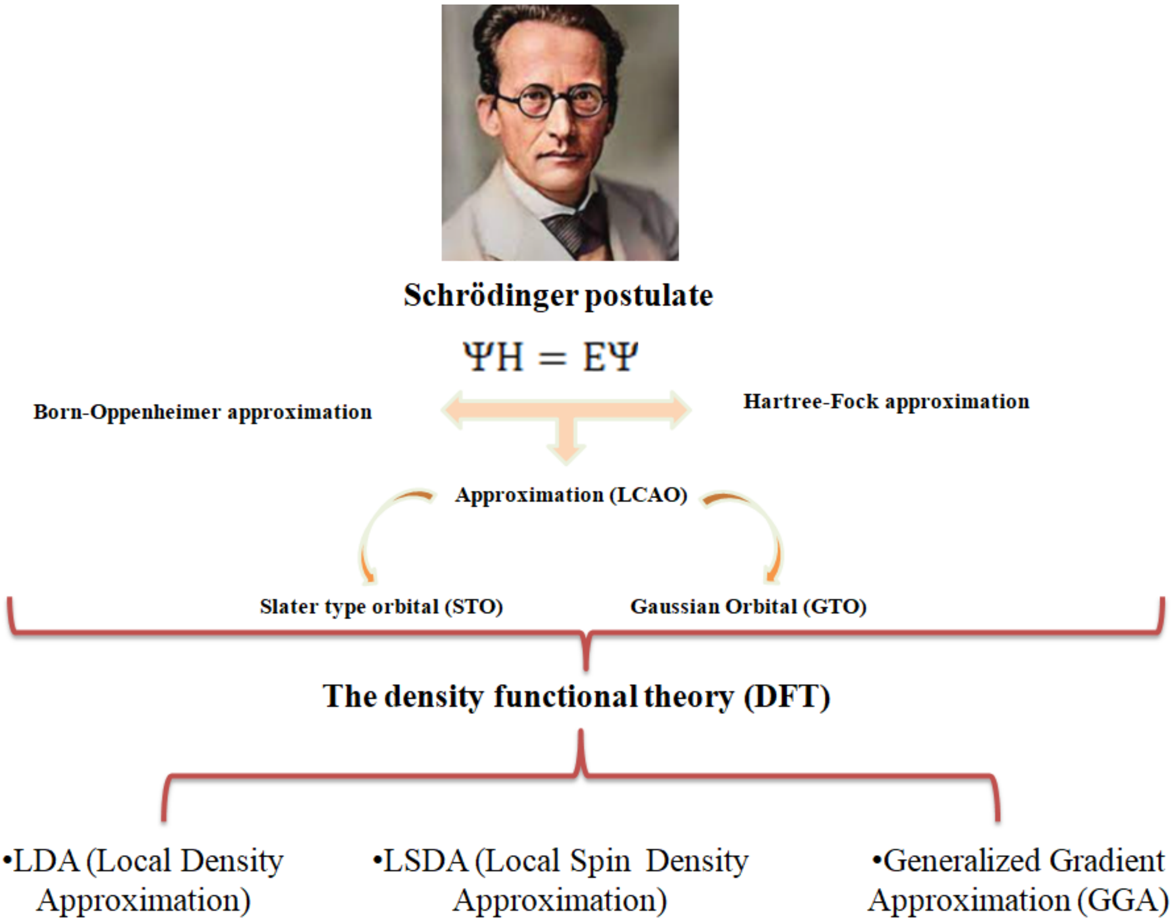

III.1. Introduction

The modeling of organic structures using molecular graphics and quantum mechanical approximations is crucial for predicting structural and reactive behaviors in systems. This method is recognized as a theoretical approach that complements experimental methods like X-ray diffraction and spectroscopy analyses. Advancements in computational science have made this possible, enabling the modeling, calculation, and storage of molecular characteristics analyzed using quantum mechanical methods. These methods are implemented as computer algorithms to theoretically determine the physicochemical properties of molecular species. The digital processing of molecular species is based on the fundamental postulates of quantum physics, with a particular emphasis on solving the Schrödinger equation. Density Functional Theory (DFT) is a prominent approach to quantum mechanics, widely used for describing the properties of a molecular system in a steady state. Time-dependent density functional theory (TD-DFT) is an extension of DFT designed to handle excited molecular states, enabling the exploration and comprehension of the dynamic behaviors of molecules during transitions between states or external stimuli. Combining DFT and TD-DFT provides a powerful approach to investigating molecular properties, advancing theoretical understanding of complex chemical systems.

III.2. The postulate of Schrödinger

Introduced in 1926, Schrödinger's postulate constituted the central equation of quantum physics whose main role was to give the laws that govern the behaviour of objects in the microscopic state and their evolution over time in the same way as Newton's equations in classical mechanics [1].

It is a linear equation to the partial derivatives of the first order in time that allows determining with precision the instantaneous modification of the wave and therefore to define completely the function of wave $\Psi(r, t)$ of a particle at any time if we know it-here at an initial moment. The Schrödinger equation for a system consisting of several electrons placed in a potential or force field cannot be rigorously solved. Approximate or approximate methods of calculation can only be used for the determination of the different permissible energy values and the corresponding atomic wave or orbital functions.

$$\Psi H = E\Psi \qquad \text{(III.1)}$$

Schrödinger equation for a stationary state while the understanding of the time-evolution problems of particle motion consists in solving the Schrödinger equation by imposing certain conditions on the limits to the wave function. At first, and with the help of mathematician Herman Weyl, Schrödinger was able to calculate all the solutions of his equation for a steady state that is-when the forces acting on the system are independent of time and the total energy E of the system is constant[2]. He then finds all the empirical formulas of the spectroscopic phenomena established by Balmer and Rydberg. The solution of the equation consists in seeking the part of space corresponding to the wave function describing the studied system starting from the equation of propagation of a wave according to the law of De Broglie which is written in the general case:

$$\upsilon^2 \Delta\Psi(\mathrm{r},\mathrm{t}) = \frac{\partial^2\Psi(\mathrm{r},\mathrm{t})}{\partial \mathrm{t}^2} \qquad \text{(III.2)}$$

$$\upsilon^2 \Delta\Psi(\mathrm{x},\mathrm{y},\mathrm{z},\mathrm{t}) = \frac{\partial^2\Psi(\mathrm{x},\mathrm{y},\mathrm{z},\mathrm{t})}{\partial \mathrm{t}^2} \qquad \text{(III.3)}$$

$$\Delta = \frac{\partial^2}{\partial \mathrm{x}^2} + \frac{\partial^2}{\partial \mathrm{y}^2} + \frac{\partial^2}{\partial \mathrm{z}^2} \qquad \text{(III.4)}$$

$$\Delta\Psi(\mathrm{x},\mathrm{y},\mathrm{z}) + \frac{4\pi^2}{\lambda^2}\Psi(\mathrm{x},\mathrm{y},\mathrm{z}) = 0 \qquad \text{(III.5)}$$

Generalization of the Schrödinger equation The Schrödinger equation can only be rigorously solved for single-electronic systems. The description of more complex systems requires a number of approximations. [51] The exact Hamiltonian operator of a system comprising N nuclei and ne electrons, where the nuclei are designated by A and B and the electrons by k and l. This operator takes into account the different interactions, it is written as follows according to several operators, namely: the electron kinetic operator, the electron attraction operator by nuclei, the electron repulsion operator, the nucleus kinetic operator, and the nucleus repulsion operator. Hence the expression:

$$\hat{\mathrm{H}} = -\frac{1}{2}\sum_{\mathrm{k}=1}^{\mathrm{n_e}} \frac{\hbar^2}{\mathrm{m_e}} . \nabla_{\mathrm{k}}^2 - \sum_{\mathrm{k}=1}^{\mathrm{n_e}} \sum_{\mathrm{A}=1}^{\mathrm{N}} \frac{\mathrm{e}^2}{4\pi\varepsilon_0} . \frac{\mathrm{Z_A}}{\mathrm{r_{kA}}} + \sum_{\mathrm{k}=1}^{\mathrm{n_e}} \sum_{\mathrm{I}>k}^{\mathrm{n_e}} \frac{\mathrm{e}^2}{4\pi\varepsilon_0 . \mathrm{r_{kI}}} - \frac{1}{2}\sum_{\mathrm{A}=1}^{\mathrm{N}} \frac{\hbar^2}{\mathrm{M_A}} \nabla_{\mathrm{RA}}^2 + \sum_{\mathrm{A}=1}^{\mathrm{N}} \sum_{\mathrm{B}>A}^{\mathrm{N}} \frac{\mathrm{e}^2}{4\pi\varepsilon_0} \frac{\mathrm{Z_A} . \mathrm{Z_B}}{\mathrm{R_{AB}}} \qquad \text{(III.6)}$$

$$\hat{\mathrm{H}} = \hat{T}_{\mathrm{e}} + \hat{V}_{ne} + \hat{V}_{\mathrm{ee}} + \hat{T}_{n} + \hat{V}_{nn} \qquad \text{(III.7)}$$

The first two terms refer respectively to the kinetic energy of electrons T e and nuclei(T n). The following three terms constitute the potential energy part of hamiltonian and represent successively the attractive electrostatic interaction between nuclei and electrons(V ne), the repulsive potentials due to electron- electron(V ee) and nucleus-nucleus (V nn)[4].

The molecular properties that can be calculated by solving the Schrödinger equation are multiple. These include:

- Molecular structures and energies
- Energies and structures of transition states
- Vibration frequencies
- IR and Raman Spectra
- Thermochemical properties
- Binding energies
- Reactive paths
- Molecular orbitals
- Atomic charges
- Multipolar moments
- NMR chemical displacements and magnetic susceptibilities
- Electronic affinities and ionization potentials
- Polarities and Hyperpolarities
- Electrostatic potentials and electronic densities
- etc.

III.2.1. Born-Oppenheimer approximation

The approximation of Born-Oppenheimer (1927) [3] (adiabatic approximation) is to simplify the resolution of the Schrödinger equation by separating the electronic part from the nuclear part in the wave function. This approximation is based on the fact that electrons are lighter than nuclei (the mass of a proton is 1836 times that of the electron) [4], they move faster and therefore react instantly to any change in the position of the nuclei. The Schrödinger equation can thus be separated into a nuclear part and an electronic part. The approaching wave function of the system, the solution to this equation, is then written as a product of two functions:

$$\Psi(\bar{r},\bar{R}) = \Psi_{n}(\bar{R})\Psi_{\acute{e}le}(\bar{r},\bar{R}) \qquad \text{(III.8)}$$

$$\hat{H} = \hat{H}_{e}(\bar{r},\bar{R}) + \hat{H}_{n} \qquad \text{(III.9)}$$

: and $\hat{H}_n$ The nuclear operator , $\hat{H}_e$: is the electronic operator.

Subsequently, the electronic Schrödinger equation is written:

$$\hat{H}_e(\bar{r},\bar{R})\Psi_{\acute{e}le}(\bar{r},\bar{R}) = \varepsilon(R)\Psi_{\acute{e}le}(\bar{r},\bar{R}) \qquad \text{(III.10)}$$

The Born-Oppenheimer energy, for a set of positions R of the fixed nuclei is :

$$E(R) = \varepsilon(R) + \sum_{A=1}^{N}\sum_{B>A}^{N}\frac{e^2}{4\pi\varepsilon_0}\frac{Z_A.Z_B}{R_{AB}} \qquad \text{(III.11)}$$

This energy allows, for the totality of the positions of the nuclei, to define the Born-Oppenheimer potential energy surface whose lowest energy minimum corresponds to the equilibrium geometry of the system. Knowing this energy, one can solve the following nuclear equation and thus have access to the force constants of the system and its vibration frequencies.

$$\left[-\frac{1}{2}\sum_{A=1}^{N}\frac{\hbar^2}{M_A}\nabla_{RA}^2 + E(R)\right].\Psi_n(\bar{R}) = E_n\,\Psi_n(\bar{R}) \quad \text{(III.12)}$$

However, the equation thus formulated can only be solved exactly for hydrogen systems. For a poly-electronic system, it is necessary to introduce new approximations to define the interacting electrons. Two approaches are known and will be briefly introduced in this part of the course and more fully detailed in the second part. The first approximation uses the wave function and the second one uses the electron density.

III.2.2. Hartree-Fock approximation

The orbital approximation, introduced by Hartree in 1928, consists in writing the wave function for a polyelectronic system as a product of single-electron spin-orbitals assumed to be normalized

$$\Psi_e(1,2,3,\dots,n_e) = \varphi_1(1).\varphi_2(2).\varphi_3(3)\dots\dots\varphi_{n_e}(n_e) \qquad \text{(III.13)}$$

Knowing that each spin-orbital is the product of an electron position function $\phi_i(r_i)$ and a spin function$\eta(s_i)$

$$\varphi_{i(n_i)} = \phi_i(r_i).\eta(s_i) \qquad \text{(III.14)}$$

The function $\eta(s_i)$ is associated with two forms: α for the spin $\left(\frac{1}{2}\right)$ et β for the spin $\left(-\frac{1}{2}\right)$

This notion was then generalized by Hartree and Fock by writing the wave function in the form of a Slater determinant [4] constructed on the basis of the wave functions of each electron to satisfy the Pauli principle [5]. It allows, in this case, to evaluate the best wave function for such a system by minimizing the energy using the variational principle.

$$\Psi_e(1,2,3,\ldots,n_e) = \frac{1}{\sqrt{n_e!}}\begin{vmatrix} \varphi_{1(1)} & \varphi_{2(1)} & \varphi_{3(1)} & \cdots & \varphi_{n_e(1)} \\ \varphi_{1(2)} & \varphi_{2(2)} & \varphi_{3(2)} & \cdots & \varphi_{n_e(2)} \\ \cdots & \cdots & \cdots & \cdots & \cdots \\ \varphi_{1(n_e)} & \varphi_{2(n_e)} & \varphi_{3(n_e)} & \cdots & \varphi_{n_e(n_e)} \end{vmatrix} \text{(III.15)}$$

$\frac{1}{\sqrt{n_e!}}$ is the normalization factor

Despite the very satisfactory results obtained, this approach neglecting the correlation term, has a major limitation: it overestimates the average distance between electrons since it is assumed that each electron is in an average field created by all the others without taking into account the inter-electronic interactions and it overestimates the electronic repulsion energy. To describe the system correctly, Löwdin defined the correlation energy Ecorr as the difference between the energy defined by the Hartree-Fock method (EHF) and the exact non-relativistic energy of the system

$$E_{corr} = E_{exacte} - E_{HF} \qquad \text{(III.16)}$$

These electronic interactions, which are not negligible, have been taken into account to improve the results and have given rise to new methods called post-Hartree-Fock including the configuration interaction method (CI), the multiconfiguration method SCF (MC-SCF), the Moller-Plesset perturbation (MP) and the Coupled-Cluster method (CC) . Note that in this case, the wave function is expressed as a linear combination of several Slater determinants. Although they give good results, these methods are very expensive in terms of time and computational power and are, therefore, only applicable for small systems.

III.2.3. Approximation (LCAO)

C.C.J.Roothaan [7] and G.G.Hall [8] proposed in 1951 a method of solving the Hartree-Fock equations based on the theory of molecular orbitals. This theory is now widely used because it makes it possible to obtain the Hartree-Fock equations in matrix form which will facilitate their resolution. It is based on the approximation LCAO [8] (Linear Combination of Atomic Orbital), which consists in expressing each orbital Ψi as a linear combination of atomic orbital m:

$$T_a(r_i) = \sum_{\mu=1}^{L} C_{\mu a}\phi_\mu(r_i) \qquad \text{(III.17)}$$

where $C_{\mu a}$ are the coefficients of molecular orbitals and ϕ_μ is the set of atomic orbitals serving as the basis for the development of molecular orbital $\Psi(r)$. In a more pictorial way, within the framework of the theory of molecular orbitals the atoms partially retain their identity.

Each function ϕ_μ corresponds to an atomic orbital, solution of the Schrödinger equation for a given atom, and centered on that atom. It should be remembered, however, that this is an approximation of the fact that the base of function $\phi_\mu(r_i)$ is finite, while an exact expression of orbitals $\Psi_a(r_i)$would require $m \rightarrow \infty$ The equation (I.15) becomes:

$$f_a(r_i) \sum_{\mu=1}^{L} C_{\mu a} \phi_\mu(r_i) = S_i \sum_{\mu=1}^{L} C_{\mu a} \phi_\mu(r_i) \qquad \text{(III.18)}$$

We will now multiply by $\phi(r_i)$ and integrate in relation to $d\vec{r}$. The different elements the following matrices can then be introduced:

- the overlay matrix S_μ representing the overlay between each orbital:

$$S_{\mu v} = \int_v \phi_\mu^*(r) \phi_1(r)\, dr \text{ avec } \mu et v = 1 \ldots \ldots K \qquad \text{(III.19)}$$

- The Fock matrix $F_\mu$representing the average effect of the field created by all electrons on each orbital:

$$F_{\mu v} = \int \phi_\mu^*(r) \phi_v(r) dr \text{ avec } \mu et v = 1 \ldots \ldots K \qquad \text{(III.20)}$$

We finally get the Roothaan-Hall equations:

$$\sum_\mu F_{\mu v}\, C_{vi} = s_i \sum_\mu S_{\mu v}\, C_{vi} \qquad \text{(III.21)}$$

Or more simply in matrix form:

$$FC = SC_s \qquad \text{(III.22)}$$

being the matrix of coefficients C_μ.

This equation is resolved iteratively from a set of test coefficients. Equations with eigen values, then iteratively resolved, give both the energy and a new and improved set of molecular orbitals. A new iteration can then begin. The process ends when the convergence criterion (variation of the energies of the different iterations below a certain limit) is reached. This iterative procedure is called the SCF procedure for Self Consistent Field.

III.2.3.1. Atomic bases

HF equations are not always easy to solve. Therefore, the molecular orbitals OM are expressed as linear combinations of predefined sets of mono-electronic functions (3μ), hence the qualifier of this approximation: LCAO. Thus, the molecular orbital equation will write:

$$T_i = \sum_{\mu=1}^{K} C_{\mu i} 3_{\mu} \, aveci = 1,2,3 \ldots, K \qquad \text{(III.23)}$$

There are four types of basic functions (also called atomic orbitals) commonly used for the calculation of electronic structure:

- The Slater or STO orbitals of the English Slater Type Orbitals
- Gaussian or GTO orbitals of the English Gaussian Type Orbitals
- The basic digital functions
- The flat waves

Among the atomic orbitals commonly used for the calculation of electronic structures, also called basic functions, only two will be developed.

III.2.3.1.1. Slater type orbitals (STO)

The general expression of a Slater function [10,11] is given by the following relation:

$$3_{c\ldots m}(r,\theta,\varphi) = NY_{l,m}(\theta,\varphi) r^{n-1} e^{c_r} \qquad \text{(III.24)}$$

Where N is a normalizing factor, Çis the orbital exponential (exponent of Slater, determining the size of the orbital), (n, l, m) are quantum numbers and $Y_{l,}$,m is a usual spherical harmonic function.

III.2.3.1.2. Gaussian Orbitals (GTO)

Gaussian orbitals [12] can be formulated as follows:

$$3(r - R_A) = (r - R_A) \sum_P d_{P\mu} g_P \left(\alpha_{P\mu} | r - R_A |\right) \qquad \text{(III.25)}$$

Where and (r)are defined as follow:

$$\begin{cases} g_P(a,r) = e^{-ar^2} \\ P(r) = Cx^n x^n y^m xz^l \end{cases} \qquad \text{(III.26)}$$

α being a positive number that represent the exponent of the Gaussian. The sum (n+ l+ m) defines the type of atomic orbital. This type of function has an essential property: the product of two Gaussian $g_{Æ}(\alpha_{Æ})$ and $g_B(\alpha_B)$centered on two different atoms A and B is also a Gaussian

$g_c(\alpha_c)$,located between centers A and B.

III.2.3.1.3. Contracted bases

Let us consider a carbon atom (1s22s12p3). Either for this atom a base composed of several functions describing the orbitals and p . In a Hartree-Fock computation, molecular. As the electrons located on the 1s orbital are the ones that contribute the most to the total energy because of their proximity to the nucleus, the function base will be, during a Hartree-Fock calculation, optimized mainly for the core electrons, not for the valence electrons. However, during the formation of a molecule with the participation of this carbon atom, orbital 1s (very low in energy) will contribute little to the formation of the chemical bond. It is the electrons located on orbitals 2s and 2p of valence that will be pooled with those of another atom in order to create the chemical bond . Thus, the most internal functions (with the largest exponents) will serve to describe the orbital 1s then the remaining functions will allow the description of the valence orbitals. The majority of the functions will therefore be responsible for describing orbital 1s, whose coefficients will be only slightly modified by the response of another atom.

The internal function coefficients can therefore be considered as constant for a molecular calculation. Thus, orbital 1s will be described by a linear combination of a number of functions. This reduces the number of coefficients to be processed by the Hartree-Fock method. This reduction procedure is called base contraction:

$$3(CGTO) = \sum_{i}^{K} a_i 3_i\,(PGTO) \qquad \text{(III.27)}$$

In this equation (I.24), the Primitive Gaussian Type Orbitals (PGTO) is contracted into a contracted orbital (Contracted Gaussian Type Orbital: CGTO).

In the case of valence orbitals, we can keep more flexibility by leaving some basic functions relaxed. The influence of the contraction is not negligible, because the fixing of the heart orbital coefficients will increase the energy during a variational calculation (because of the addition of a constraint to the lagrangian), but the calculation time will be greatly reduced. The segmented method is to use only once a certain number of primitives to create a contract. For example, a base containing ten GTOs can be contacted in three GTOs by taking the first six GTOs to form the first GTCO, the next three to form the second GTCO, and the last GTCO to form the third GTCO. For this method, each OTMP is used only once. The general method involves all primitive orbitals for the formation of all contracted. Thus, we will use a linear combination of ten primitives to form the 1s, another linear combination of the same ten primitives to form the

2s, etc.

The rating for contracted bases is:

$$\frac{(10s3p)}{[2s1p]} \qquad \text{(III.28)}$$

With parenthesis the primitive orbitals and between brackets the contracted orbitals. Here, ten Gaussian functions and three p are contracted into two and one function respectively.

III.3. The density functional theory (DFT)

III.3.1. Historical overview

The target of density functional theory is to represent a system using the basis variable density ρ(r). Thus, instead of the 3n dimensional space of the wave function Ψ, the n-electron issue is analyzed in the space of ρ(r). In another way, it is to identify a functional that allows us to relate density and energy. As it provides a viable alternative to post-Hartree-Fock

In 1927, L. H. Thomas [13] and E. Fermi [14] were the first persons who express energy as a function of density. In their model, the electronic interactions are handled classically and the kinetic energy is calculated by assuming the homogeneous electron density while P. A. Dirac [15] improved this model with an exchange term in 1930.

A little later, in 1951 A model based on the study of a uniform gas improved with a local potential was proposed by J. C. Slater [16]. In the 1970s, this method, known as Hartree-Fock-Slater or Xα, was primarily used in solid state physics.

Hohenberg and Kohn [16] created the basic foundations of DFT in 1964, demonstrating the feasibility of computing the characteristics of a system using electron density then followed Kohn and Sham [17], who enabled the use of DFT in quantum chemistry.

This theory has many advantages that make it worthwhile in many fields, particularly chemistry and material science.

For starters, it includes a large part of electronic correlation in its formalism and can be applied to systems as diverse as covalent ionic materials.

The mono-electronic aspect allows for a chemical explanation of the wave function.

In the case of the Hartree Fock techniques, it was about representing the system's energy as a function of the wave function, but in the case of the DFT, the energy will be a function of the system's electronic density. Before we proceed to the DFT's foundations, we must first define what the electronic density is.

III.3.2. Electronic density

The electron is defined as an indissociable particle, or as an isolated particle; The electron cannot be localized; rather, we speak of its probability of presence in a given volume element, defining the Electronic density; in fact, electrons are considered in their entirety (Electronic cloud), and the density will localize the regions of space where electrons are most likely. Electronic density is defined as the integral multiple of the square of the wave function of the spin coordinates of all electrons and all space variables. It is a positive function which only relies on three spatial coordinates (x,y,z). This quantity is limitless; when it is integrated across all of space; it corresponds to the total number of electrons N.

$$\rho(r \to \infty) = 0 \qquad \text{(III.29)}$$

$$\int \rho\,(r)dr = N \qquad \text{(III.30)}$$

III.3.3.Theorem of Hohenberg and Kohn

Even if cores and electrons can be separated, the Schrödinger equation, which applies to hundreds or even thousands of atoms, should be solved. The first move toward this resolution was achieved in 1920, when Thomas and Fermi established that the energy of an electron-rich gas depends on its electronic density [19-20]. Hohenberg and Kohn's idea in 1964 was to generalize this approach to any electronic system [21].

The density (r) function is the only one required to capture all of a system's electronic properties in its fundamental state. The intention of Hohenberg and Kohn's formulation is to simplify energy expression and to make DFT a precise theory for aging multiple bodies.

The electronic density also determines the number of electrons in the system via the condition:

$$n = \int (r)dr \quad \text{(III.31)}$$

Where (r) is the electronic density and r the coordinates are the electron coordinates. It is specifically defined:

$$(r) = \int |\Psi(r)|^2 dr \quad \text{(III.32)}$$

While the solution of the electronic Schrödinger equation with the wave function Ψ:

$$H\Psi = [\mathrm{T} + \mathrm{V_{Ne}} + \mathrm{V_{ee}}]\Psi = \mathrm{E}\Psi \qquad \text{(III.33)}$$

In practice, the term electron-nuclei attraction $\mathrm{V_{Ne}}$ is often replaced by an external potential $\mathrm{V_{ext}}$, which includes, in addition to$\mathrm{V_{Ne}}$, different environmental disturbances (such as voltage drops).

The overall electronic density may be calculated using the spin densities. ρ_α and ρ_β:

$$(r) = \rho_\alpha(r) + \rho_\beta(r) \qquad \text{(III.34)}$$

So the electronic energy is a functional of density that can be noted as $E[\rho]$or $\rho = (\rho_\alpha, \rho_\beta)$ and expressed by three parts in the following equation:

$$E[\rho] = T[\rho] + E_{Ne}[\rho] + E_{ee}[\rho] \qquad \text{(III.35)}$$

Where :

$[\rho]$is the kinetic energy ;

$E_{Ne}[\rho]$is the energy resulting of the core electron interaction ;

$E_{ee}[\rho]$ is the result of electron-electron interaction. She can also be broken down into two terms: a Coulomb term $J[\rho]$J[] and an exchange term $K[\rho]$

The following formulas represent the electron-noyau interaction $E_{Ne}[\rho]$ and the Coulomb interaction term $J[\rho]$

$$E_{Ne}[\rho] = \sum_\alpha \int \frac{Z_\alpha(r)}{|R_\alpha - r|} d^3r \qquad \text{(III.36)}$$

And

$$J[\rho] = \frac{1}{2} \iint \frac{\rho(r)\rho(r')}{|r-r'|} d^3r d^3r' \qquad \text{(III.37)}$$

The energy $E_{Ne}[\rho]$is obtained by the potential $V_{Ne}(r)$:

$$E_{Ne}[\rho] = \int \rho(r) V_{Ne}(r) d^3r \qquad \text{(III.38)}$$

Another term of expression was established by Kohn and Sham for $E[\rho]$.

III.3.4. Kohn and Sham's approach

The Khon and Sham strategy incorporates a novel notion not only in DFT, but also within relation to all quantum theory simplifications: the concept of an effective system. [22] Particularly. The idea was to construct a gas of n atoms with no interaction, described by their orbitals $\boldsymbol{\phi_i(r)}$,The electronic density is given by the relationship

$$(\boldsymbol{r}) = \sum_i^N |\boldsymbol{\phi_i(r)}| \qquad \text{(III.39)}$$

The kinetic energy of Kohn and Sham Ts$[\rho]$ seems to have the following equation in an electron-free system:

$$T[\rho] = \sum_{i}^{N} \langle |\boldsymbol{\phi_i \rho^2}| \rangle \tag{III.40}$$

This provides us the Schrödinger equations system for interacting electrons, which has the form:

$$\left[\frac{\rho^2}{2} + V_{eff}(r)\right] \boldsymbol{\phi_i} = \boldsymbol{s_i \phi_i} \tag{III.41}$$

Where $V_{eff}(r)$ is the average field created by an electron gas and subtracted by any electron. The total energy of this system is thus:

$$E_s[\rho] = T_s[\rho] + E_{SNe}[\rho] \tag{III.42}$$

In fact, electrons will interact with one another, and $E_s[\rho]$ is not the complete amount of energy. This energy corresponds to 99% of the energy of an independent gas of electrons, but it must include a term for electron interaction (just as the Hartree-Fock method does not include electronic correlation). To include electron interaction in the energy equation, recast in terms of $T_s[\rho]$ and $J[\rho]$.

$$E[\rho] = ([\rho] - T_S[\rho]) + T_S[\rho] + E_{Ne}[\rho] + (E_{ee}[\rho] - J[\rho]) + J[\rho] \tag{III.43}$$

That mean :

$$E[\rho] = T_S[\rho] + E_{Ne}[\rho] + J[\rho] + E_{xc}[\rho] \tag{III.44}$$

Where $E_{xc}[\rho]$ is the energy containing all of the interacting electrons' correlation

$$E_{xc}[\rho] = (T[\rho] - T_S[\rho]) + (E_{ee}[\rho] - J[\rho]) \tag{III.45}$$

with:

$T[\rho] - T_S[\rho]$: The kinetic correlation is represented by (the difference between the exact kinetic energy of the correlated electrons and the exact kinetic energy of a non-interacting electron system);

$E_{ee}[\rho] - J[\rho]$:is the energy containing all of the interacting electrons' correlation:

With:

$$V_{xc}(r) = \frac{dE_{xc}[\rho]}{d\rho(r)} - J[\rho] \tag{III.46}$$

the exchange-correlation potential.

Then the system of equations to solve can be written as:

$$\left[\frac{\rho^2}{2} + V_{Ne}(r) + \int \frac{\rho(r')d^3r'}{|r-r'|} + V_{xc}(r)\right]\boldsymbol{\phi_i}(r) = \boldsymbol{s_i}\boldsymbol{\phi_i}(r) \qquad \text{(III.47)}$$

Finally, we can define the Kohn-Sham Hamiltonian, h_{HS} :

$$h_{HS}\boldsymbol{\phi_i} = \boldsymbol{s_i}\boldsymbol{\phi_i} \qquad \text{(III.48)}$$

Because of the difficulties in assessing its integrals, the Kohn-Sham approach can be evaluated analytically. The Vxc term, which should allow the DFT to have the appropriate energy and hence all the correlation, is the difference between these two techniques. This is not the case with the HF technique, as configuration interaction is not explained.

III.3.5. The correlation exchange hole

The spin density $\rho_2(r_1, r_2)$ denotes the likelihood of discovering two electrons with any spin in two elements of volumed_{r1} andd_{r2}.

$$\rho_2(r_1, r_2) = N(N-1)\int \dots \int |\Psi(r_1, r_2 \dots r_N)|^2 d_{r1} d_{r2} \dots . d_{rN} \qquad \text{(III.49)}$$

For charged fermions such as electrons, the probability of finding 1 in $r_1$is largely dependent on the position of the electron2: we will say that their movements are correlated. However, the nature of fermions causes electrons to reject each other due to coulombic repulsion. Through the exchange-correlation hole XC, the prince of pauli and the inter-electronic correlation prevent the presence of spin electrons$\sigma = \pm\frac{1}{2}$ in the same region of space. The term (hole) denotes a decrease in electron density inr_2 caused by non-classical electron-electron interactions. The likelihood of spatial occupancy is therefore stated as follows:

$$\rho_2({r_1}^{\sigma_2}, {r_2}^{\sigma_2}) = \rho_2(r_{1/2}) \qquad \text{(III.50)}$$

$$\rho_2(r_{1/2}) = \rho(r_1)[\rho(r_2) + \rho_{XC}^{trou}] = \rho(r_1)\rho(r_2) + \rho(r_1)\rho_{XC}^{trou} \qquad \text{(III.51)}$$

The first term reflects the coulombic interaction, whereas the second term indicates an electron density's interaction with an exchange-correlation hole.

The density matrix is therefore created and normalized for the spin electron pairs r1 and r2.

$$\sum_{\sigma_1\sigma_2} \iint d^3r_1 d^3r_2\, \rho(r^{\sigma_1}, r^{\sigma_2}) = N(N-1) \qquad \text{(III.52)}$$

As a result, the exchange-correlation density may be written as

$$V_{ee} = \frac{1}{2}\iint d^3r_1 d^3r_2 \frac{\rho(r_1,r_2)}{|r_1-r_2|} = \frac{1}{2}\iint d^3r_1 d^3r_2 \frac{\rho(r_1)\rho(r_2)}{|r_1-r_2|} + \frac{1}{2}\iint d^3r_1 d^3r_2 \frac{\rho(r_1)\rho_{XC}^{trou}(r_1,r_2)}{|r_1-r_2|} \quad \text{(III.53)}$$

$$V_{ee} = U + E_{XC} \quad \text{(III.54)}$$

E_{XC} is defined as the interaction of an electron density with the probabilistic one of an exchange-correlation hole. U is the electrostatic energy term. Another parameter can be supplied to specify the correlation's amplitude: $\lambda\lambda = 0$,[23]. the correlation is zero and there is no interaction on the system, whereas for $\lambda = 1$, the system will be fully correlated.

The probability density will then write

$$\rho_\lambda(r_1\sigma_1, r_2\sigma_2) = \rho_\sigma(r_1) n_\lambda(r_1\sigma_1, r_2\sigma_2) \quad \text{(III.55)}$$

$n_\lambda(r_1\sigma_1, r_2\sigma_2)$: is the probability of finding a spin$\sigma_2$electron in basic volume d^3r_2 in r_2 provided that a spin electron σ_1 is in volume d^3r_1inr_1

DFT's fundamental functionals are based on the following approximations:

- LDA (Local Density Approximation)
- LSDA (Local Spin Density Approximation).
- Generalized Gradient Approximation (GGA)

III.3.5.1. Local Density Approximation (LDA)

In this approach, the density is addressed locally from a homogeneous electron plasma. Density is therefore a spatially variable function [24]. The electronic density and wave function are assumed to be constant locally and the function of exchange-correlation is written as follow:

$$E_{XC}^{LDA}[\rho(R)] = \int \rho(r)\, \varepsilon_{XC}(r) d^3r \quad \text{(III.56)}$$

The term $\rho(r)\varepsilon_{XC}$ denotes the particle-based exchange-correlation energy of the uniform electron gas of density$\rho(r)$. Furthermore, $\rho(r)\varepsilon_{XC}$ may be seen as the total of an exchange and a correlation contribution:

$$\varepsilon_{xc}(\rho(r)) = \varepsilon_x(\rho(r)) + \varepsilon_c(\rho(r)) \quad \text{(III.57)}$$

This distribution allows the use of Dirac's exchange energy for the homogeneous electron gas.

$$\varepsilon_{xc}(\rho(r)) = -\frac{3}{4\pi}\left(\frac{3}{\pi}\right)^{\frac{1}{3}} \rho^{\frac{4}{3}} \quad \text{(III.58)}$$

Using the results of a homogeneous gas of electrons of equal density to the local density of an inhomogeneous system, the LDA concept could indeed estimate the exchange-correlation energy of an inhomogeneous system. A uniform electron gas's correlation is not accurately determined. However, several approximation expressions permitted for the description of low or high electrical densities. This local consensus approximation allows us to correctly describe systems with low spatial density. The LDA, on the other hand, has some disadvantages: Certain quantities, such as cohesion factors, are overestimated, while others, such as link lengths, are underestimated. The LDA, on the other hand, has drawbacks: certain variables are overstated, such as cohesion factors, while others are underestimated, such as link lengths 25. The LDA technique treats the change locally, but the HF method treats it throughout the system, making it more suited to this type of problem.

III.3.5.2. Introduction of the spin term (LSDA)

The LSDA (Local Spin Density Approximation) introduces the concept of spin into the LDA's approximation. Electronic density is splitting into two populations. $\rho(\uparrow)$ spin high and $\rho(\downarrow)$ spin low, and the energy will be released.

$$E_{XC}^{LSDA}[\rho_\uparrow,\rho_\downarrow] = \int \varepsilon_{XC}^{hom}\big(\rho_\uparrow(r),\rho_\downarrow(r)\big)\rho(r)d^3r \qquad \text{(III.59)}$$

$$\varepsilon_{xc}^{lsda}(\rho_\uparrow,\rho_\downarrow) = \varepsilon_x(\rho_\uparrow,\rho_\downarrow) + \varepsilon_c(\rho_\uparrow,\rho_\downarrow) \qquad \text{(III.60)}$$

$\varepsilon_{xc}^{lsda}(\rho_\uparrow,\rho_\downarrow)$ is the exchange correlation energy

The estimation of exchange energy represents the most common source of error in LSDA. Correlation energy is overstated, but because it contributes so little to overall energy, the inaccuracy is minimal. Because electrical density is assumed to be spatially constant, systems with radically varying densities cannot be properly characterized. But the LSDA is as suitable to systems with slow electronic density variation as it is to systems with fast density variation, making it a more popular choice than the LDA. However, she also exaggerates the energy of interface and provides insufficient gaps for semiconductors and isolant compounds [26].

III.3.5.3. Generalized Gradient Approximation (GGA)

Using a non-uniform electron gaz increases the precision of the LDA approach. In this scenario, the function characterizing the exchange-correlation is no longer exclusively dependent on the electronic density, but also on its derivatives. The first density derivative is added as a variable in the functional characterizing the exchange-correlation in GGA approaches. The GGA techniques are then extended to allow this term to be dependent on derivatives of the higher order electronic density. So the function is affected by both density and gradient [27].

We usually write E_{XC}^{GGA}in the form:

$$E_{XC}^{GGA}[\rho,\nabla\rho] = E_{X}^{GGA}(\rho,\nabla\rho)+E_{C}^{GGA}(\rho,\nabla\rho) \quad \text{(III.61)}$$

As noted previously, the difficulty of LDA was the exchange; special attention will be paid to the development of this component.

$$E_{X}^{GGA}[\rho,\nabla\rho] = E_{X}^{GGA} - \int F\big(S(r)\big)\,\rho^{\frac{4}{3}}(r)dr \qquad \text{(III.62)}$$

F: is the function of the reduced gradient

$$S(r) = \frac{|\vec{\nabla}\rho(r)|}{\rho^{\frac{4}{3}}(r)} \qquad \text{(III.63)}$$

Becke's functional for the exchange is the most well-known: Be88 [28]., The functional LYP [29] of Lee, Yang, and Parr and the functional PW86 and PW91 [30] of Perdew and Wang are two extensively used functionals for correlation. These functions improve structural and energy results in a variety of situations.

- **B88**: the exchange functional B88: is based on a two-dimensional study of the exchange density

  $$F^{88}(s) = \frac{\beta_S^2}{1+6\sin^{-1}h(s)} \qquad \text{(III.64)}$$

  β, which is an empirical parameter determined by the least squares analysis of the exchange energies of the six rare gas atoms (He a Rn): the beta value that minimizes error equals 0.0042 u.a.
- **PW91:** perdew and wang [31]: this is due to a modification of this functional F in order to satisfy other conditions.
- **PW86:** this function is based on an expansion of the exchange hole gradient correlation around its LSDA shape.

$$F^{PW88}(s) = \left[1 + 1{,}296\left(\frac{s}{p}\right)^2 + 14\left(\frac{s}{p}\right)^4 + 0{,}2\left(\frac{s}{p}\right)^6\right]^{\frac{1}{15}} \text{ Avec } (24\pi^2)^{\frac{1}{3}} \text{(III.65)}$$

It should be noted that correlation functionalities have much more complicated analytical forms that cannot be understood by simple current physical reasoning.

III.3.6. Hybrid functional

Kohn and Sham were the first to formalise a formal expression for the energy of exchange-correlation, based on the approximation of Hartree-Fock, while the term of correlation remained unchanged compared to that of the LDA. The use of this functional allowed the effective potential to have a correct asymptotic 83ehaviour.

Although it works properly on atoms, the results for molecules are disappointing. GGA delivers better results. This is due to the artificial nature of the separation of the exchange and correlation terms: by combining the nonlocal exchange term from the HF equation with a local correlation hole (LDA), the autocoherence of the description of the local hole has been lost. Becke's solution was to use the exact exchange in a different way, by incorporating a portion of it into the expression of the energy of exchange-correlation. The resulting expression, which has three parameters, is referred to as B3[13]:

$$E_{XC} = E_X^{LDA} + a_0(E_{\mathrm{K}}^{\mathrm{exact}} - E_{\mathrm{K}}^{LDA}) + a_{\mathrm{K}}\Delta E_{\mathrm{K}}^{\mathrm{B88}} + a_{\mathrm{C}}\Delta E_{\mathrm{C}}^{\mathrm{pw91}} \qquad \text{(III.67)}$$

The semi-empirical coefficientsa_0, a_{K}, and $a_{\mathrm{C}}$are found by fitting to the experimental data. Eexact denotes the exact exchange energy received from an HF calculation. a_0 is related to the system's "independent particle" nature. a_{K} and a_{C} aid in the optimization of gradient corrections for exchange and correlation. Thus, the goal of the above equation is to account for the exact exchange in the simplest way possible while also recovering the limit of the uniform electron gas. An intriguing result of this approximation is improved energy accuracy, which is superior to that obtained by using the GGA approximation.

The requirement to consider accurate exchange in instances where substantially inhomogeneous (Hartree-Fock) E_X^{HF} is the concept of hybrid functional, and it is produced by combining GGA exchange and correlation functions with a specific proportion of exchange given by the HF theory. B3LYP [32], the most prevalent hybrid functional and was proposed by Stephens[33]in 1994, uses Becke's E_x^{B88} exchange feature from 1988 and Lee's E_c^{LYP} correlation feature, which Yang and Parr both employed as LDA exchange and correlation functional gradient corrections.:

$$E_{XC}^{B3LYP} = (1-a)E_X^{LSDA} + aE_{XC} + bE_x^{B88} + cE_c^{LYP} + (1-a)E_c^{LSDA} \qquad \text{(III.68)}$$

With a=0.20, b=0.72, and c=0.81. The parameter λ represents the "strength of the coupling" between the electrons: λ=0 for a system without interaction and λ =1 for the real system. The three parameters a, b and c were optimized based on experimental data from the G2 database.

The hybrid B3LYP functional is one of the most widely used in recent years because it gives good results on ionization and binding energies as well as electronic affinities [34, 42, 43].

III.4. Energetic forms functions in a force field in molecular modeling

Interactions between bonded atoms correspond to bond deformation energies, valence angles, and sharp angles that are clean and improper (out of plane). Interactions between unbound atoms are represented by the Van der Waals energy, electrostatic interactions, and hydrogen bonds. Figure III.2 illustrates the geometric parameters utilized to describe the energy functions' shape [34].

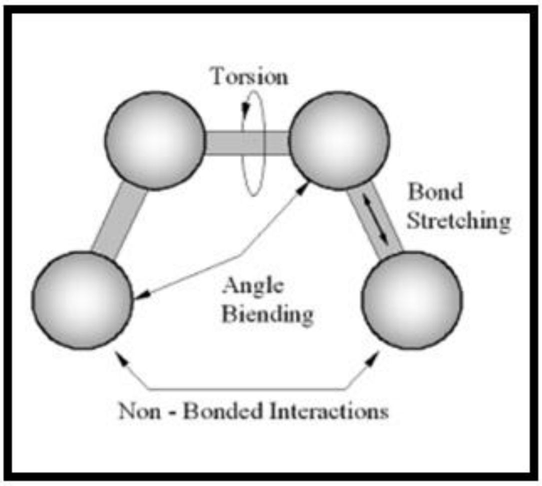

Figure III.1. Intramolecular interactions between bound and unbound atoms

Molecular mechanics treats molecules as spheres connected by bonds, using classical physics equations. These equations allow for the calculation of atomic interactions and the effects of energy (force fields)[8]. Empirical force field approach is founded on classical mechanics and the fundamental idea that the entire "steric" energy of a structure can be described as a sum of contributions from various forms of interactions. [35]

$$E_{Steric} = E_{BoundedAtom} + E_{Non-boundedAtom} \qquad \text{(III.69)}$$

III.4.1. The interaction energy of atoms that are bonded together

The energy involved in fluctuations in the length r of links following extension and compression from their equilibrium values is defined as elongation energy.

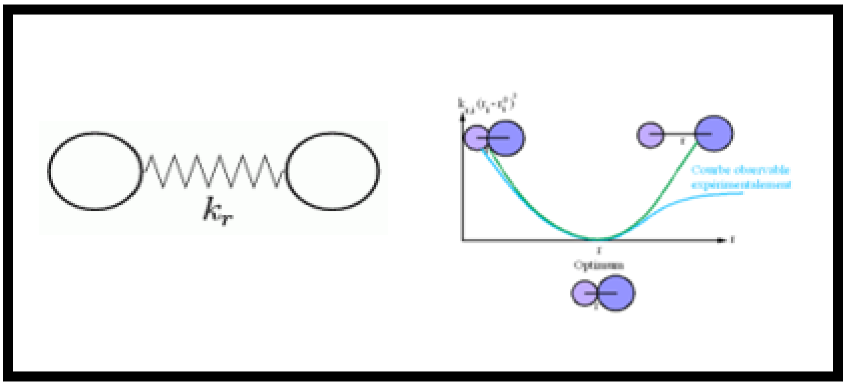

Figure III.2. Elongation between two atoms

$$E(r) = {}^{1}\!/_{2}\,[K_r(r-r_0)^2] \qquad \text{(III.70)}$$

r0: the length of the link to the equilibrium

kr, the force constant

III.4.1.1. Angles of valence deformation energy

Define the energy included in the fluctuations in the angle θ between two contiguous connections centred on an equilibrium value of θ_0.

$$E\theta = {}^{1}\!/_{2}\,[K_\theta(\theta-\theta_0)^2] \qquad \text{(III.71)}$$

θ0: angle at equilibrium

kθ: force constant

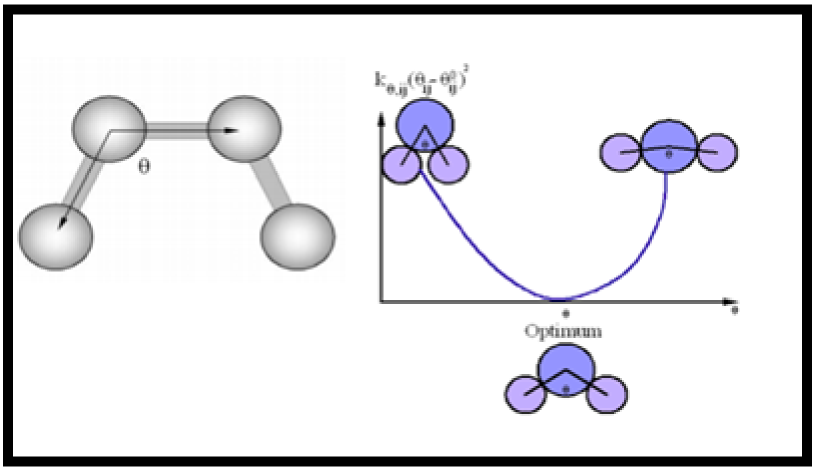

Figure III.3. Angles of valence

III.4.1.2. Torsion energy

The energy required to rotate a molecule's portion around a bond.

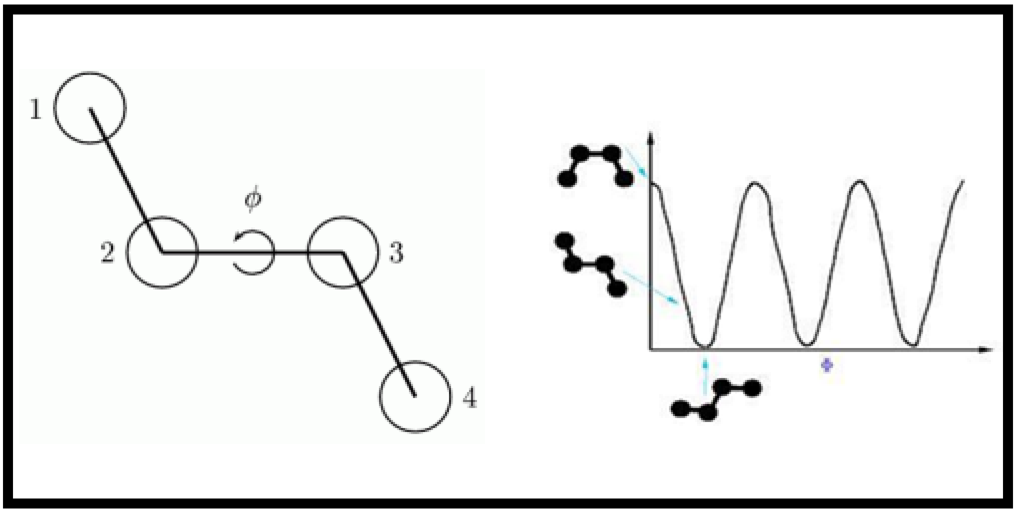

Figure III.4. dihedral angle formed by the atomes 1-2-3-4

$$E\varphi = K_{\varphi}(1 + \cos n\varphi) \tag{III.72}$$

K_{φ}: Force constant

n: periodicity (n = 1, 2, 3, 4, 6) [35]

III.4.2. Interaction energy of non-listed atoms

The interactions between unbound atoms cause steric congestion, which is significant in the shape of a molecule. Aside from interactions 1-3, vibrational spectroscopy does not consider interactions between unbound atoms. For a field force to be transferable from one molecule to another, the MM considers interactions between more distant atoms, those separated by more than two links [36].

This term is expressed in the form

$$E_{Non-boundedatom} = E_{Van-der-waals} + E_{Electrostatic} + E_{hydrogenebond} \tag{III.73}$$

The general expression of these terms is: [35]

III.4.2.1. Van der Waals energy

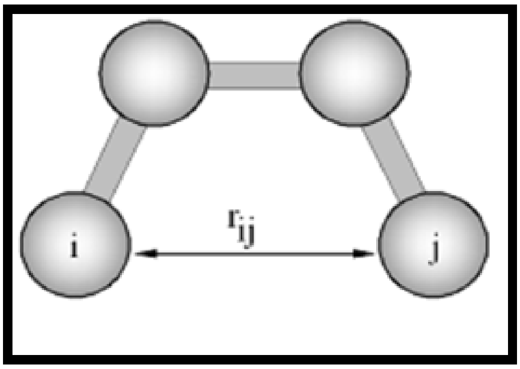

Figure III.5. Van der Waals Energy

The van der Waals energy function, $E_{van\_der\_Waals}$, represents the attraction and repulsion between two atoms that form a dipole. She takes the form of a Lennard-Jones potential, comprised of an attracting energy term in $\frac{1}{r_{ij}^{6}}$ and a repulsive energy term in$\frac{1}{r_{ij}^{12}}$. Thus, Van der Waals interactions occur between atoms that are close together. When the distance between the two atoms is less than the sum of the van der Waals radiations, the term repulsion predominates; when the distance is greater, the term attractive predominates:

$$E_{Van-der-waals} = \sum_{i,j}\left[\frac{A_{ij}}{r_{ij}^{12}} - \frac{B_{ij}}{r_{ij}^{6}}\right] \qquad \text{(III.73)}$$

A_{ij}, B_{ij}: parameters based on the nature of the atoms i and j distant fromr_{ij}.

Electrostatic interactions energy

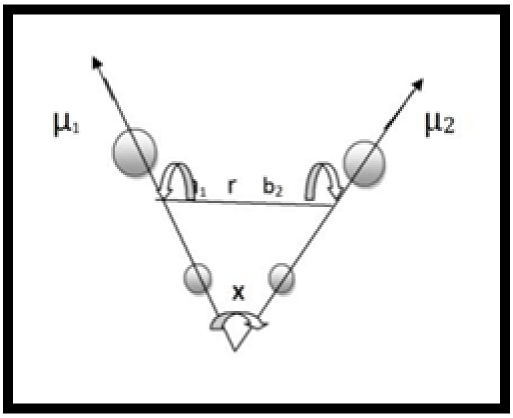

Figure III.6. Electrostatic contact between two atoms

The energy of electrostatic interactions is written as a coulombian potential between atoms considered carriers of a net charge.

$$E_{electrostatic} = \sum_{ij}\frac{q_i q_j}{\varepsilon_{ij} r_{ij}} \qquad \text{(III.74)}$$

qi, qj: partial charges of the atoms i and j, separated by rij.
ij: constant dielectric constant accounting for the attenuation of electrostatic interaction by the environment (solvent or molecule itself).

III.4.2.2. Hydrogen connection energy

The hydrogen bond is a low-energy interaction (8 to 20 KJ/mol) between electron-deficient hydrogen and an electron-dense atom with a doublet of free electrons. When the distance A-B is great, the electrostatic model cannot adequately represent these interactions. The processes of repulsion and electronic relocation occur at a shorter distance. Several forms of potential energy functions have been devised to account for the directivity of the hydrogen bond. Currently, the most often used functions for expressing these interactions in major chemical systems are frequently obfuscated [36].

La fonction 10-12

$$E_H = \frac{A_{ij}}{r_{ij}^{12}} - \frac{B_{ij}}{r_{ij}^{6}} \qquad \text{(III.75)}$$

La fonction 6-12

$$E_H = \frac{A'_{ij}}{r_{ij}^{12}} - \frac{B'_{ij}}{r_{ij}^{6}} \qquad \text{(III.76)}$$

A, B, A', and B' are the specific coefficients of hydrogen bonds.
rij: the distance between two atoms i and j.

III.5. Molecular docking and dynamic studies

III.5.1. Molecular docking study

III.5.1.1. Introduction

Molecular modeling is a crucial tool in chemistry that compares the physicochemical properties of molecules to study supramolecular interactions responsible for biological phenotypes. Various mathematical models, including quantum mechanics and molecular mechanics, are used to determine conformations associated with each structure [37]1. One of the most essential molecular modeling methods is molecular docking, which merges two or more molecules simultaneously. This computational procedure involves the in silico interaction of a ligand and a proteine, focusing on the energetic and geometrical adaptation of the ligand to the protein's connection site. This method has been extensively researched to understand the development of intermolecular complexes, with the ligand's molécular connection to the receptor's pocket being responsible for a specific medicinal activity and forecasts potential interactions between ligands and amino acids in the receptor structure (protein). The molecular docking technique has proven to be an effective tool for discovering new drugs targeting proteins. The proteine-ligand docking type is particularly relevant in the medical industry, as it helps determine the precise conformations of the ligand within a specific protéine when the structure of the proteines is known. Molecular docking is divided into two stages: placing the ligand in the appropriate protein location and evaluating potential energy interactions between the ligand and the protein. The development of this technology has led to the creation of numerous methodologies and algorithms.[38]

III.5.1.2. Docking approach

The standard concept of docking approaches was founded on the lock-and-key theory proposed by Fischer [39], where both the ligand and the receptor can be considered rigid systems to discover the correct orientation for the “key” to open up the “lock” (Figure I.6). Subsequently, Koshland presented the "induced-fit" theory, which accounted for the flexibility of both ligand and receptor during the docking process. This change sought to boost prediction accuracy [40]. Understanding the complicated interactions between target and ligand at the molecular level holds tremendous importance for numerous diseases. This insight aids in the design of ligands capable of either restricting or activating target proteins, thereby substantially altering critical biochemical processes like signal transmission, gene transcription, and enzyme catalysis. Molecular docking technologies present an appealing and cheap option for experimental procedures like high-throughput screening (HTS). These experimental methodologies demand large investments in the field of drug development [41].

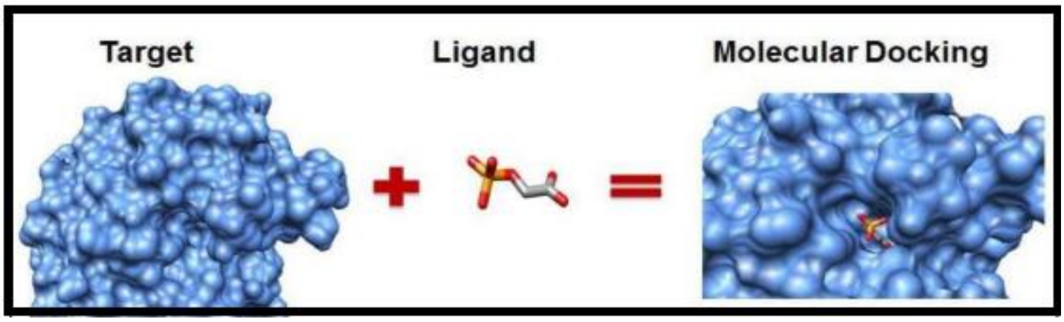

Figure III.7. Molecular Docking process

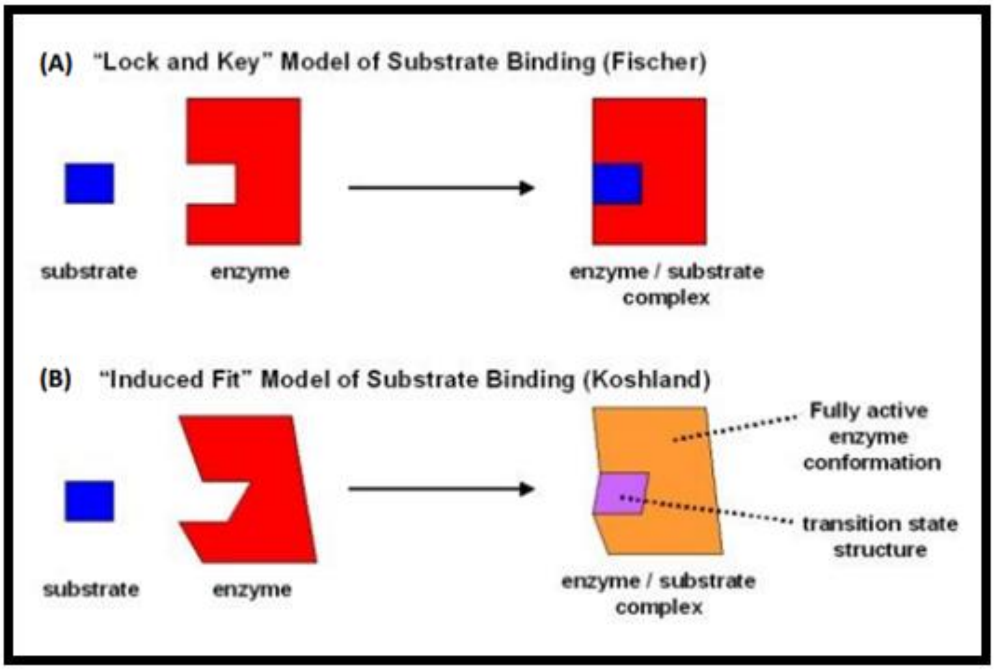

Figure III.8. Schematic diagram of two binding models for enzyme-substrate. interaction. (A) The lock-and-key model, (B) induced-fit model describing the conformational changes in the active site, adapted from [42]

III.5.1.3.Typical molecular docking steps

In molecular docking, a ligand interacts with a receptor (often a protein in nature). The docking procedure consists of four basic steps

III.5.1.3.1. Structure determination

The initial step in molecular docking involves determining the receptor and ligand structures using three analytical procedures: NMR, microscope electronic, and X-ray crystallography. These experimental approaches are currently used to determine protein structure. The Protein Data Bank is a vast collection of protein structures, enabling the collection of important data. When experimental methods are not feasible or not yet realized, a comparison modelling approach should be examined first.

III.5.1.3.2. Structure preparation

The receiver for docking processing must be prepared by addressing issues of steric clashes and protonation states. The process involves removing any water molecule found on the protein's surface, verifying missing sections in the polypeptide chain near the known active site, confirming the existence of side chains, checking for steric clashes after adding missing hydrogen atoms, and verifying histidine protonation in contact with the ligand. If errors occur, it is crucial to manually repair them. If direct contact between the ligand's hydroxyl or amide grouping and the amide function of histidine's imidazole group indicates correct positioning, the H of histidine should be removed and repositioned on the nitrogen atom in sp2 on the other side of the imidazole grouping. Once these procedures are validated, lacking residues like glutamine or asparagine can be completed by the amide groups. This ensures accurate docking and improved ligand-protein interactions.

III.5.1.3.3. Docking of molecules

Docking is a method in molecular modelling that calculates the preferred orientation of a molecule to a second when bound to form a stable8 complex. When you do not have any true understanding of the active site, the employment of the «docking» technique looks to be a very interesting alternative. The most significant issue for the docking step is to cover the conformational space as well as possible Sampling of the space of the ligand-receptor complex configurations.

III.5.1.3.3.1. Types of molecular docking

Docking simulations are classified into three types based on the degrees of freedom they consider:

III.5.1.3.3.1.1. Rigid docking (in which both the target and the ligand are viewed as wooden structures): This technique employs the most straightforward docking algorithm, which ignores molecular flexibility and assumes that the receptor and ligand are rigid entities with constant bond angles, bond lengths, and torsion angles at all stages of complex formation. It reduces the number of degrees of freedom from several thousand to six (three translational and three rotational), limiting the ligand's search space to fit in the binding site [43]. Rigid docking is frequently employed to investigate complex systems, such as protein-protein interactions. DOCK is a well-known program that uses this approach to locate molecules that are similar in shape [44–45].

III.5.1.3.3.1.2. Semi-flexible docking (with a flexible ligand and a rigid target): This technique is the most commonly used in docking software because it allows ligands to be flexible while maintaining proteins challenging throughout docking. This allows for the investigation of probable torsion angles and bond rotations. It may dock small ligand molecules and more giant molecules, such as proteins or nucleic acids [45]. Semi-flexible docking involves sampling six degrees of translational and rotational freedom in addition to the ligand's conformational space, though this takes more computing effort. MOE [46], FlexX [47], Glide [48], and AutoDock [49] are the industry leaders in semi-flexible docking.

III.5.1.3.3.1.3. Flexible docking (containing a partially flexible target and a flexible ligand): It has recently become clear that the flexibility of side chains is critical to how protein-ligand complexes are recognized at the molecular level. This is because target molecules can take on different forms when unbound than when attached to a ligand. Notably, when unattached, the protein's central chain torsion angles might change from their initial conformations, something earlier approaches have struggled to capture. Modern docking technologies have arisen to solve these issues, allowing both the target and the ligand to undergo dynamic conformational changes. This method more accurately depicts the interactions that occur during binding because it better emulates the behaviour of biological molecules.However, because of the significantly increased degrees of freedom, fully flexible docking takes longer than rigid-body docking. As a result, to adequately investigate the many binding configurations of protein-ligand complexes, a broader search space is necessary [50]. MOE [51], GOLD [52], ICM [53], Surflex [54], and AutoDock Vina [55] are some of the most well-known docking applications in this area.In this instance, both molecules are viewed as flexible. The emphasis switches to identifying the various conformations that the receptor and ligand molecules can assume during complex formation, as shown in Figure I.7.

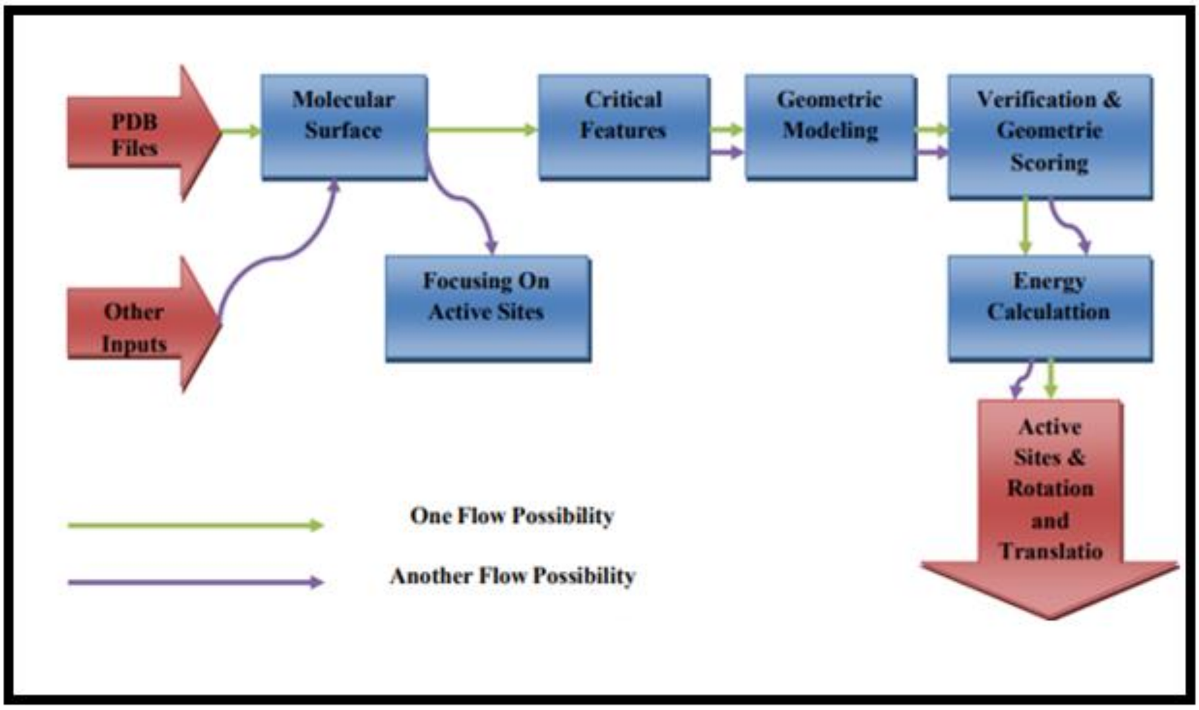

Figure III.9. Rigid and Flexible Docking

III.5.1.3.4. Prediction and Evaluation

After establishing the molecular docking parameters, the program proceeds to the step prediction and evaluation. This enables the evolution of interaction modes.

This phase is completed as follows:

III.5.1.3.4.1. Evaluating docking results

The precision of predicting protein-ligand interactions through docking simulations can be gauged by determining the Root Mean Square Deviation (RMSD) between the resulting structure (the top-scored pose) and the co-crystallized ligand (the experimental conformation) within the protein. This measure of similarity is characterized by the Euclidean distance between the atom coordinates of the two aligned structures, formulated as:

$$RMSD = \sqrt{\frac{1}{N}\sum_{i=1}^{N} di^2} \qquad \text{(III.77)}$$

Where N signifies the overall count of atoms in the molecule, and di represents the separation between the coordinates of atom i in the two structures [56]. RMSD remains consistently positive, with a value of 0 (rarely realized in practical situations) signifying a flawless alignment of data. Typically, a satisfactory outcome is often indicated when the RMSD is below 2Å.

- **SFs (scoring functions):**

The addition of scoring functions, which make use of various assumptions and simplifications, improves sampling algorithms. These functions prioritize the generated conformations based on their predicted binding affinity, allowing the search algorithm to discover the most relevant posture from the many others created. As a result, a diverse set of scoring functions has been developed to appropriately define interactions within protein-ligand complexes [57–58]. These functions are divided into four categories: force-field, empirical, knowledge-based, and consensus scoring.

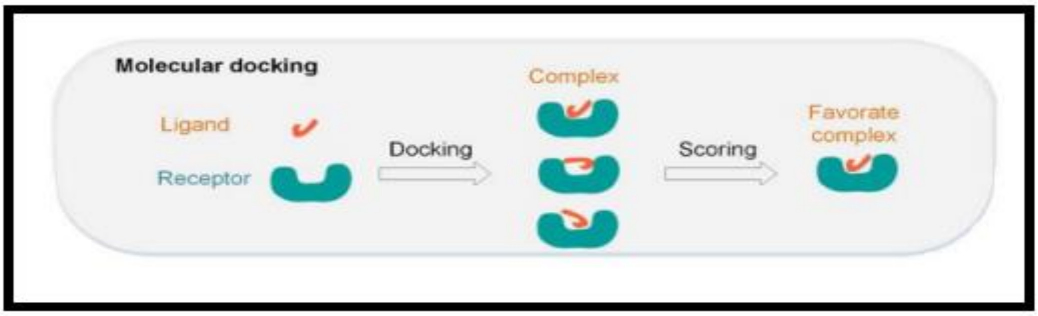

Figure III.10. The SF role as pose selector.

A calculating energy incorporating a number of approximations is typically used to estimate affinity. There are various score functions for this. There have been various publications [59-61] on the latter changes in docking programs. These scoring functions are broadly categorized into four families:

- force field-based scoring functions
- empirical score functions
- consensus score functions
- knowledge-based scoring functions

❖ Force-field based scoring functions

Scoring functions based on force fields characterize the binding free energy of a complex by summing up various uncorrelated molecular mechanics terms, including van der Waals interactions and electrostatic interactions within and between the docked molecules. Typically, these functions do not account for a majority of solvent effects and solute entropies. A common example of this type of scoring function employed in molecular docking, particularly with DOCK, involves two energy components derived from the Amber force fields: Lennard-Jones van der Waals interactions and an electrostatic term. This is expressed through equation (I.3):

$$E = \sum_{i} * \sum_{j} * \left(\frac{Aij}{r_{ij}^{12}} - \frac{Bij}{r_{ij}^{6}} + \frac{qiqj}{\varepsilon(rij)rij}\right) \tag{III.78}$$

Where r_{ij} represents the distance between a protein atom i and a ligand atom j, and A_{ij} and B_{ij}stand for the van der Waals parameters, while q_i and q_j denote the atomic charges. The term (r_{ij}) within the Coulombic component refers to the distance-dependent dielectric constant, often set as $4r_{ij}$. This value accounts for the implicit solvent effect [62].

❖ Empirical scoring functions

Empirical scoring functions gauge the binding affinity of a complex by summing individual energy components, which include factors like hydrogen bonding, ionic interactions, hydrophobic effects, binding entropy, and the number of rotatable bonds within the ligand. The coefficients linked to these functional elements are determined through regression analysis involving experimentally derived binding energies and x-ray structures. The computation of binding scores using empirical scoring functions is notably swifter compared to force field scoring functions, largely due to the straightforward nature of their energy terms. The initial empirical scoring system designed for forecasting binding free energies was established using data from 45 complexes, incorporating experimental binding free energies and crystal structures of protein-ligand interactions. This system was integrated into LUDI as follow: shown in equation (eq I.4):

$$\Delta G_{binding} = \Delta G_0 + \Delta G_{hb}\sum_{h-bonds} f(\Delta R, \Delta\alpha) + \Delta G_{ionic}\sum_{ionicint.} f(\Delta R, \Delta\alpha) + \Delta G_{lipo}|A_{lipo}| + \Delta G_{rot}N_{RO} \qquad \text{(III.79)}$$

Where ΔG_0 stands for an energy contribution to binding that doesn't rely on any proteininteractions, ΔG_{hb} represents the contribution from an optimal hydrogen bond, ΔG_{ionic} signifies the effect of undisturbed ionic interactions, ΔG_{lipo} depicts the influence of hydrophobic interactions, with $Alipo$ representing the contact area for such interactions between the protein and the ligand. Moreover, ΔG_{rot} reflects the decrease in binding energy caused by the restriction of internal ligand motion, and $NROT$ denotes the count of rotatable bonds in the ligand. The function $(\Delta R, \Delta\alpha)$ serves as a penalty function, penalizing significant deviations from the ideal geometry of hydrogen bonds [63].

❖ Knowledge-based scoring functions

Within knowledge-based functions, the occurrences of interactions between pairs of atoms in protein-ligand complexes are analyzed. This information is then translated into atomic potentials on a pairwise basis, illustrating the favored arrangements of atoms within protein-ligand pairs. Well-known examples of these functions include the Potential of Mean Force (PMF) and the DrugScore component of the FLEX program. Utilizing these functions offers a balanced solution between precision and speed when compared to force field and empirical scoring functions. The complete score is computed using the equation (I.5):

$$(r) = -k_B T \ln[g(r)],\ g(r) = \rho(r)\ \rho* / (r) \qquad \text{(III.80)}$$

Where k_B represents the Boltzmann constant, T stands for the absolute temperature of the system, $\rho(r)$ signifies the number density of the atom pair from the protein and ligand located at a distance r, $\rho*(r)$ denotes the reference state pair density where interatomic interactions are absent, and $g(r)$ represents the pair distribution function [64].

❖ Consensus scoring functions

Consensus scoring is a contemporary approach in scoring that assesses docked configurations by amalgamating multiple scoring functions. This technique substantially diminishes the occurrence of erroneous positive identifications observed when using individual scoring functions alone. Consequently, this approach strengthens the capacity to differentiate between enzyme inhibitors that are active and inactive, resulting in a considerable enhancement of the precision of docking [65-66].

III.5.1.4. Interaction of proteins and ligands

The operation of biological systems relies on low-energy non-covalent molecular interactions between proteins and ligands. This information is expressed through specialized relationships with other partners. The prediction of the ligand's conformation and orientation relative to the protein's active site is challenging during docking. Docking is crucial for the generation of novel medications at each target protein of known structure [67-69]. Protein-ligand complexes contain various types of non-covalent interactions, including polar and hydrophobic interactions between the ligand and protein.

A. Van der Waals interactions: J.D. van der Waals, a Dutch scientist and Nobel Prize laureate, studied dipole interactions based on the interactions of dipoles generated by molecules. These interactions are classified into three types: permanent dipole interactions, also known as the Keesom orientation effect, which occurs between two polar molecules, permanent dipole interactions; or immediate dipole interactions, also known as the Debye induction effect, which occurs between a polar molecule and any polar or apolar molecule, and the London scatter. These are transitory changes in electron distribution that result in non-permanent dipoles. These encounters take place over a relatively short distance. They are plentiful, and their primary function is to achieve a favourable spatial match between the ligand and the receptor protein via steric alignment.[70]

B. Electrostatic interactions: A Coulomb potential calculates the energy associated with electrostatic interactions between atoms that are not covalently linked.

C. Hydrogen bond energy: Hydrogen bonds form as a result of a combination of electrostatic interactions (70%) and van der Waals interactions (30%) between an electronegative atom, typically oxygen or nitrogen, with an available electron pair and a hydrogen atom linked to another electronegative atom. The hydrogen bond is a non-covalent chemical bond formed by the partial transfer of a single electron to the H group between two molecules or groups of molecules. It can be intramolecular or intermolecular, and examples can be provided. It is made up of an electron-donor atom interacting with an electron acceptor atom. [71]

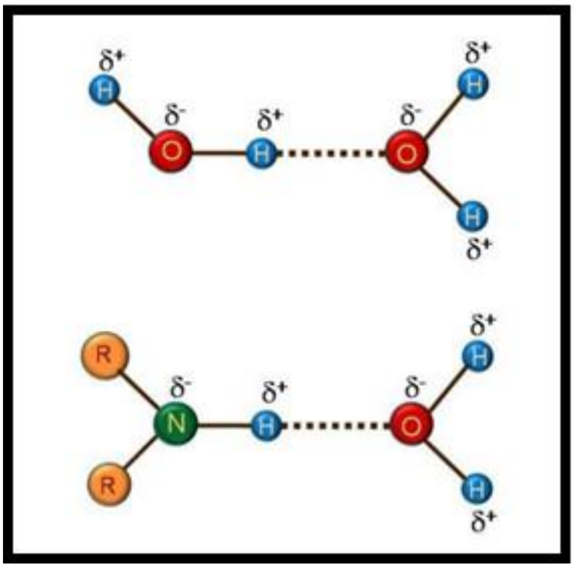

Figure III.11. Hydrogen bond

D. Interaction of ions

The Coulomb law governs interactions between electric charges in molecules. The potential interaction energy of two distinct charges separated by a distance d is calculated by calculating the work required to separate them.

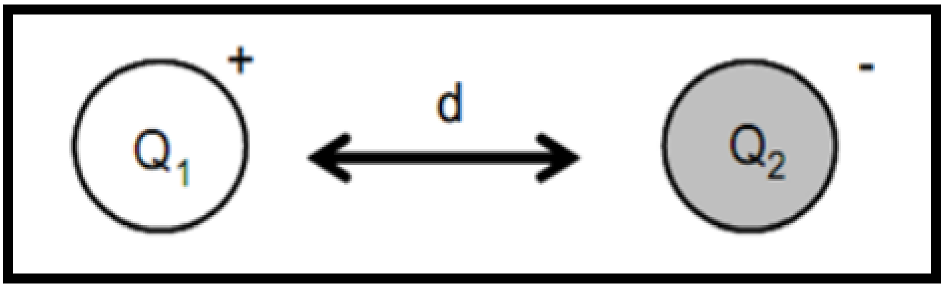

Figure III.12. Interaction of ions

E. Hydrophobic interactions

Non-polar and low polarizable molecules often cluster and form hydrophobic bonds due to their low affinity for the solvent they dissolve in, water. These interactions are drawn together by dispersion forces and are facilitated by complementarity, where several hydrophobic amino acids come into contact at the interface. This results in a stabilizing interaction, and non-polar amino acids tend to interact with one another, creating a hydrophobic "patch."

[72]

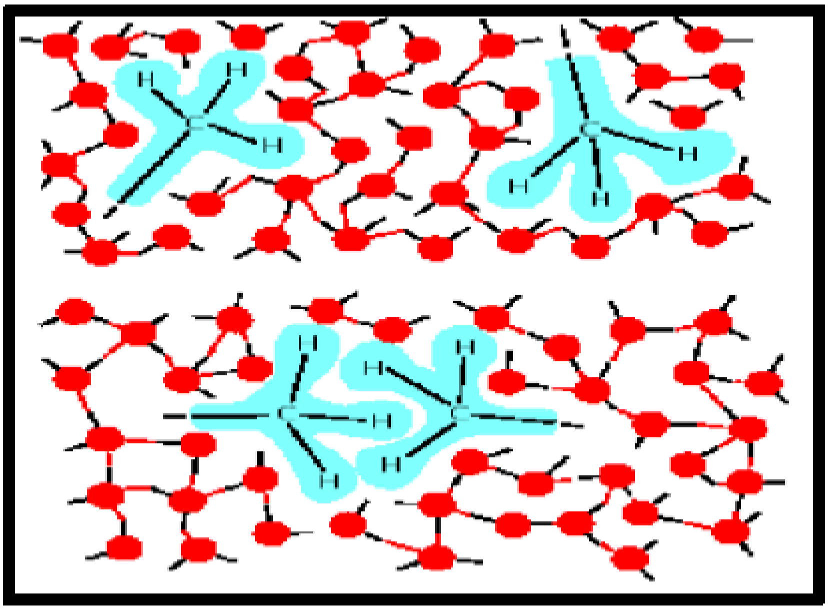

Figure III.13. hydrophobic patch

III.5.1.5. Softwares used in the molecular docking

a) AutoDock

This free docking program was created at the Scripps Research Institute by the team of Arthur J. It is based on a genetic algorithm, such as " GOLD " [73]. AutoDock and GOLD are based on an objective function based on a force field combined with an AE, which allows for the easy implementation of heuristic sampling on one side and objective function on the other. As a result, the combination of these elements appears to be a sure bet for success.4 AutoDock allows you to use three different search methods 3:

1. a research method based on a traditional genetic algorithm in which chromosomes are actually character chains. These chromosomes are made up of three cartographic coordinates that represent the ligand's translation, followed by four variables that define a quaternion. This latter is a mathematical ensemble that defines the rotation of the ligand in space, yielding a real value at the end for each angle of torsion representing each ligand connection.
2. (III) To save energy, a second local search method based on a Monte Carlo simulation circuit can be added.
3. (IIIi) a hybrid method of global and local research based on the genetic principles established by Jean Baptiste Lamarck at the turn of the century. According to Larmarck, an individual's acquired characteristics (phenotype) can be passed on to his descendants

(genotype), implying that an individual's phenotype might influence his genotype. This Larmarck theory can be applied in the context of molecular docking.

b) AutoDock Vina

AutoDock Vina is a docking program derived from AutoDock, as the name implies, which was also developed by the Arthur J. Olson group at the "Scripps Research Institute" (http://autodock.scripps.edu/).[74] .

In its local optimization procedure, AutoDock Vina employs a sophisticated gradient optimization method. The gradient provides an optimization algorithm for a "sense of orientation" based on a single evaluation and a simulation program for flexible ligand docking on a rigid receptor.

Vina's AutoDock ligand positioning technique is a global application of a local iterative search ("Iterated Local Search global optimizer") [75,77]. This type of technique is used to remove local minima that no longer allow for better conformation. To do this, the algorithm is relaunched from a slightly different geometric form. These various starting positions are saved in memory in order to avoid repeating the same route and so save time. Vina employs the Broyden-Fletcher-Goldfarb-Shanno (BFGS) local optimisation technique.[77]

c) Discovery Studio

Discovery Studio is a comprehensive software suite that allows researchers in the life sciences to examine and model molecular structures, sequences, and other data. The product includes data visualization and editing features and tools for performing database analysis. Discovery Studio Visualize is a free visualization tool that may be used to view data generated by other Discovery Studio software. It is intended to provide an interactive environment for visualizing and modifying molecular structures, sequences, X-ray reflection data, scripts, and other data. It also includes a comprehensive set of visualizes for displaying data diagrams and other graphic representations. The application runs on Windows and Linux and provides a fully integrated office environment that allows access to basic operating system functions such as the file system, printing services, and printing services.

Molecular docking is used to determine a bond's affinity and predict the intermolecular interactions of molecules in active sites (proteins or enzymes). We performed docking on an essential enzyme involved in the homeostasis control of the Escherichia coli ADN gyrase, which targets antibacterial compounds. This structure was discovered using data from a protein data bank (RCSB Protein Data Bank (PDB)).[78] Our research is based on the crystal structures of the enzyme under investigation, which lacks a ligand for this test with our ligands (composed of synthesized 1-3), and they can be regarded as reference ligands. The docking study was carried out using the program Autodocktools 1.5.6. In summary, the steps of our calculation are as follows:

- Selection and preparation of the receptor
- Selection and preparation of the ligand
- Molecular docking and post-docking analysis

III.5.2. Molecular Dynamics simulation

III.5.2.1. Introduction

Molecular Dynamics is a widely used method for studying molecular systems with high atom counts. It allows for the observation of a system's behavior over time, as total system energy decomposes into potential energy and kinetic energy linked to temperature. The addition of kinetic energy, in the form of temperature, stimulates the system, causing it to deviate from the local minimization path. This energy can then be used to perform conformation transformations via energy barriers, thereby enabling the creation of stable structures with low energies. [79]

III.5.2.2. Principle of the molecular dynamics

It is a method for predicting the trajectories of atoms under certain settings based on the forces (of potential origin) that they are subjected to. The configurations (the system's x, y, and z coordinates) are generated by numerically incorporating Newton's laws of motion. The result is presented in the form of a trajectory that specifies how the locations $\vec{r_i}(t)$and $\vec{v_i}(t)$ change over time.

The fundamental dynamic equation (second law of Newton) may be used to describe the motion of atoms:

$$\sum_j F_{ij} = m_i \alpha_i \qquad \text{(III.81)}$$

Where $F_{ij}$the forces are exerted by the atoms j on the atom i of mass m and acceleration an at time t. F_{ij}et a can be easily calculated using atomic coordinates:

$$\alpha_i(t) = \frac{d^2 r_i}{dt^2} \qquad \text{(III.82)}$$

$$F_{ij}(t) = -\nabla_r U_p(r_i, t) \qquad \text{(III.83)}$$

With $r_i$the atomic's instantaneous location i. knowing the acceleration, one may determine an atom's speed at the following step: time$(\mathrm{t} + \nabla)$the new locations, atomic speeds, and accelerations of the following stage are calculated from positions, atomic speeds, and accelerations at any point in time. Integration by the phases infinitesimal results in determining of the system's trajectory, followed by a change in its potential energy.

III.5.2.3. The Verlet-leapfrog integration method

The Verlet-leapfrog integration technique is used in molecular dynamics simulations based on finite difference methods with variable time.[80, 81] The algorithm remains unchanged due to a time inversion, and the values calculated and stored in memory for all system attributes are locations, instantaneous accelerations, and half-time speeds. The initial distribution of speeds is not balanced, and a period of system equilibration is required to stabilize the simulation. The periodic limits conditions (IIII-5-4) are crucial in calculating interactions proportional to the number of particles in the square. To solve this problem, the authors use a simulation box with a few molecules repeated indefinitely in all directions, giving the impression of a dense system. The minimal image convention approximation, which involves each time interacting with the closest picture to all other atoms, is an alternative approach that can minimize errors in non-linear interactions.

III.5.2.4. Simulations in various thermodynamic settings

The dynamic molecular simulation begins when interaction potentials, boundary conditions, and beginning circumstances are determined. As a result, the system changes over time, with the magnitudes of the number of atoms N, temperature T, pressure P, volume V, and energy E being affected. There are many thermodynamic systems, each defined by three independent variables that define a representative ensemble (NPT, NVT, NVE, etc.). To produce more accurate simulations, the T and P parameters are adjusted. The two ensembles used in this study are NVT and NPT. The canonical ensemble is the NVT system, which preserves the number of atoms N, pressure P, and temperature T. The system is in thermodynamic equilibrium and exchanging energy with a thermostat or external reservoir. The thermostat provides thermal comfort by maintaining the system's average internal temperature around the required temperature. The amount saved over time is the Helmholtz free energy, which is the sum of the system's internal microcanonical energy (NVE) and the energy supplied by the thermostat. The NPT isobare-isotherme ensemble represents the laboratory's actual experimental circumstances.

The canonical system is connected to a barostat to maintain external pressure, and its volume varies isotropically in response to applied pressure. The system's temperature and pressure regulation are crucial aspects of molecular dynamics. [82]. Digital isothermal simulations can be executed using methods like the Andersen method [83], which links the modeled system to a thermostat, saving energy and allowing for realistic trajectory generation[84]. However, stochastic collisions do not allow for realistic trajectory generation, and time-dependent properties cannot be determined from a trajectory whose temperature was calculated using this method. To maintain constant pressure in an NPT thermodynamic ensemble, readjusting the total volume at each dynamic step is necessary. [85]. The Berendsen barostat allows for connection between the system and a barostat, with volume and positional correction factors[86].However, molecular dynamics has significant limits, including simplified potential energy functions, stability time for integration, and traditional interaction processing.

III.5.2.4.1. Modeling solvation approaches

The human body, composed of 80% water, has an aqueous phase, making a precise representation of the solvent crucial for accurately describing bimolecular. There are various methods for representing the solvent, from simple to complex. The most detailed depiction involves each water molecule, while more approximate descriptions reproduce the solvent's global properties. Molecular mechanics calculations can be performed in a vacuum, but dipoles and charge-containing molecules require solvent effects. Force fields optimize interactions, resulting in a low energy conformation that is stable yet unstable. The dielectric constant, dependent on distance, can deceive and avoid interactions with distant atoms, allowing simulation of the interaction target. When the ligand approaches the interaction target, solvent molecules move.

Energy calculations are performed on the molecules of the centre box. The non-related interactions of solvent molecules on the edges of the core box are calculated using virtual solvent molecules from neighbouring boxes.

There are two main approaches to modeling solvation, which differ depending on whether the solvent’s impact is treated implicitly or explicitly. In the first case, the goal is to recreate the aqueous solvent's screen effect by focusing on the non-linear interactions of the potential energy function, specifically the 46 value of the dielectric constant (E). Adjust all of these parameters to account for the architecture that may be used to solve the problem in an aqueous environment [87]. In the second case, the solvent molecules are explicitly treated together with the solution. This implies that they have energy, which is described by an appropriate potential energy function. Several water force fields have been developed. Among the most well-known are the TIP3P [88], TIP4P [88], SPC [89], and SPC/E [89] models. Because the dielectric effects of the aqueous system are included into these models, the dielectric constant (>) is assigned a relatively low value (on the order of 1 to 3). The explicit methods are obviously more expensive in terms of computation time than the implicit methods, but they have the undeniable advantage of allowing for a detailed analysis of the structure and dynamics of the solvent near the solution. The free energy of solvation, denoted by ΔGsol, is the energy difference observed during the transfer of a molecule of water to the solvent.

$\Delta Gsol = \Delta Gelec + \Delta Gnonelec$

Gelec is an electrostatic component.

Gnonelec is the non-electrostatic component that exists between the solution and the solvent.

Models such as "Generalized Born" and "Poisson-Boltzmann" estimate average free electrostatic energy but do not account for entropies caused by constraints imposed by the solution on water molecules or, more broadly, on solvants. Implicit solvatation models may be improved by include terms that account for hydrophobic effects.

III.5.2.4.2. The CHARMm force field

The Force Fields of CHARMM The CHARMM programme (Chemistry at HARvard Using Molecular Mechanics) [90] was created in the early 1980s, similar to Amber, and initially employed an extended atom force field with no specified hydrogens. By 1985, this had been superseded by the CHARMM19 parameters, which clearly depict hydrogen atoms bound to nitrogen and oxygen, whereas hydrogens bonded to carbon or sulphur are considered as extended atoms [91,92]. Fits to quantum simulations at the HF/6-31G level of hydrogen bonded complexes between water and the Hbond donors or acceptors of the amino acids or fragments were critical in parameterizing this model. At each of numerous contact sites, a sequence of supermolecular computations of the model chemical, such as formamide or N-methylacetamide, and a single water molecule is performed. Before fitting, the interaction energies are scaled by a factor of 1.16, which is the ratio of the TIP3P model's anticipated water dimerization energy to that predicted at the HF/6-31G level. The objective here, as with the Amber parameterizations discussed above, was to achieve a balanced interaction between solute-water and water-water energies when the latter were represented by TIP3P. Fitting the peptide-water interactions in this manner resulted in peptidepeptide hydrogen bonds that were also larger than HF/6-31G values by a factor close to 1.16 for peptides; in other cases, explicit fitting to solute-solute hydrogen bonded dimers may be required for parameter generation [93].

III.5.2.5. Simulation protocols

GROMACS 2021 [94] was used to conduct a molecular dynamic simulation. The CHARMM force field [90] was used to reduce structural conflict in the protein structure. The protein was solved cubically by water using a basic point charge model. The solvated system was neutralised by substituting Na and Cl ions for water. Furthermore, the whole system was minimised to release the stearic conflict contacts using the steepest decent technique for 50000 steps. The system's isothermal-isochoric (canonical) equilibration was also accomplished using a leap-frog integrator, with the cut-off scheme set to verlet. The system was equilibrated under periodic boundary conditions for 100 ps, and the temperature was adjusted to 300 K. The system's pressure was adjusted to 1 bar, the Parrinello-Rahman coupling was used for pressure, and the system was equilibrated in the periodic boundary condition for 100 ps. Finally, the Molecular Dynamics was run for 30 ns using a leap-frog integrator, and the system coordinates were collected every 10 ps for subsequent study.

The typical molecular dynamics simulation protocol includes the following steps:

- creating the starting molecular structure
- minimizing energy • heating the system
- adjusting the system to the study temperature
- producing the trajectory
- analysing the trajectory

These steps are summarized in the figure1

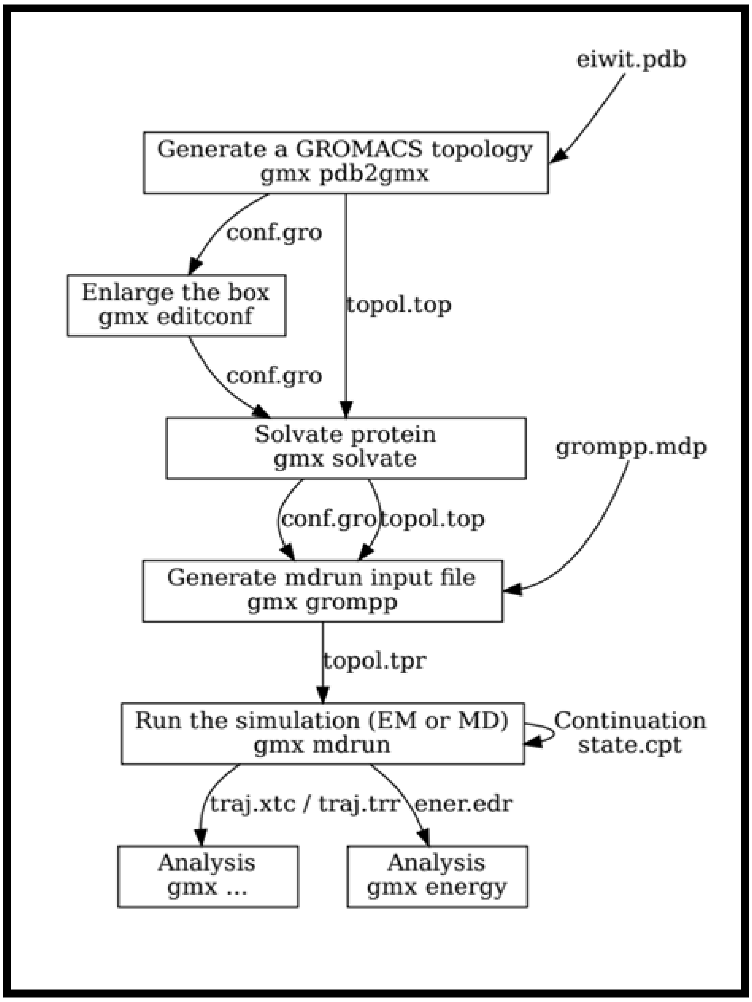

Figure III.14. The typical molecular dynamics simulation protocol

III.5.2.6. MM-PBSA evaluation

The MM-PBSA analysis is a post-processing analysis that is done on the final trajectories generated from the protein-ligand complex MD simulation. The g_mmpbsa tool was used to perform the MM-PBSA analysis of the protein-ligand complex [95-96, 94]. Because it employs the poison-boltzmann equation, it is the most efficient and precise approach for analysing protein-ligand interactions. For the protein-ligand complex, the binding free energy change, molecular mechanics potential energy change, solvation free energy change in terms of polar and non-polar, solvent accessible surface area (SASA), solvent accessible volume (SAV), and Weeks-Chandler-Andersen (WCA) energies were calculated using Eqs. (1), (2), (3), (4), (5), (6), and (7) respectively.[95,97-100]

$$\Delta G_{binding} = G_{complex} - \left(G_{protein} + G_{ligand}\right) \qquad \text{(III.84)}$$

$$EMM = E_{bonded} + E_{nonbonbed} = E_{bonded} + (E_{vdw} + E_{elec}) \qquad \text{(III.85)}$$

$$G_{solvation} = G_{polar} + G_{nonpolar} \tag{III.86}$$

$$\nabla[\varepsilon(r)\nabla\varphi(r)] - \varepsilon(r)k(r)^2 \sin h[\varphi(r)] + 4\pi\rho f(r)/kT \tag{III.87}$$

$$G_{nonpolar} = G_{cavity} + G_{vdw} \tag{III.88}$$

$$G_{nonpolar} = \gamma A + b \tag{III.89}$$

$$G_{nonpolar} = pV + b \tag{III.90}$$

$$G_{nonpolar} = \gamma A + pV + G_{vdw} \tag{III.91}$$

Where EMM is vacuum potential energy, Eelec is electrostatic, EvdW is van der Waals, (r) is electrostatic potential, (r) is the dielectric constant, f (r) is the fixed charge density, k is Boltzmann constant, is a coefficient related to the solvent's surface tension, A is SASA, b is a fitting parameter, p is a coefficient related to the solvent's pressure, and V is SAV.

III.6. Conclusion

The combination of molecular graphics and quantum mechanical approximations is a crucial method for predicting the structural and reactive behaviors of various systems, enabling the modeling of organic structures. This method, along with practical techniques like X-ray diffraction and spectroscopic examinations, has been significantly simplified by advancements in computer science. These quantum mechanical techniques, implemented as advanced computer algorithms, are essential in theoretically establishing the physicochemical features of molecule species. The computational manipulation of molecular entities is based on fundamental principles of quantum physics, with a focus on solving the Schrödinger equation. Density Functional Theory (DFT) is a famous methodology in quantum mechanics used to describe stable molecular systems. The Time-Dependent Density Functional Theory (TD-DFT) is an important expansion of DFT, designed to address excited molecule states, enabling researchers to investigate and understand the dynamic behaviors of molecules as they transition between states or respond to external stimuli. This combination provides in-depth understanding of molecular characteristics and contributes to the progress in theoretical understanding of intricate chemical systems.

References

[1]. Schrödinger, E. (1926). Annalen der Physik, 84, 361. DOI: 10.1002/andp.19263810404.

[2]. Atkins, P. W. (1990). Physical Chemistry (4ème édition). Oxford University Press.

[3]. Levy, M. (1979). Proceedings of the National Academy of Sciences, 76, 6062. DOI : 10.1073/pnas.76.12.6062.

[4]. Born, M., & Oppenheimer, J. R. (1927). Annalen der Physik, 84. DOI: 10.1002/andp.19273892002.

[5]. Slater, J. C. (1929). Physical Review, 34, 1293. DOI : 10.1103/PhysRev.34.1293.

[6]. Pauli, W. (1925). Zeitschrift für Physik, 31, 765.

[7]. Roothaan, C. C. J. (1918). (informations manquantes sur la publication de C.J. Roothaan).

[8]. Hall, G. G. (1925). (informations manquantes sur la publication de George Garfield Hall).

[9]. Mulliken, R. S. (1955). Journal of Chemical Physics, 23, 1833-1840. DOI : 10.1063/1.1740589.

[10]. Slater, J. C. (1930). Physical Review, 57, 57. DOI : 10.1103/PhysRev.57.57.

[11]. Clementi, E. (1965). IBM Journal of Research and Development, 9(2).

[12]. Boys, S. F. (1950). Proceedings of the Royal Society of London. Series A, Mathematical and Physical Sciences, 200, 542.

[13]. Thomas, Llewellyn Hilleth (1903-1992).

[14]. Fermi, E. (1927). Rendiconti dell'Accademia Nazionale dei Lincei, Classe di Scienze Fisiche, Matematiche e Naturali, 6, 602-607.

[15]. Dirac, P. A. M. (informations manquantes sur la publication de Paul Adrien Maurice Dirac).

[16]. Corminboeuf, C., Tran, F., & Weber, J. (2006). Journal of Molecular Structure: THEOCHEM, 762.

[17]. Hohenberg, P., & Kohn, W. (1964). Physical Review, 136, B864-B871. DOI : 10.1103/PhysRev.136.B864.

[18]. Kohn, W., & Sham, L. J. (1965). Physical Review, 140, A1133-A1138. DOI : 10.1103/PhysRev.140.A1133.

[19]. Fermi, E. (1927). Rendiconti dell'Accademia Nazionale dei Lincei, 6, 602-607.

[20]. Thomas, L. H. (1927). Proceedings of the Cambridge Philosophical Society, 23, 542.

[21]. Hohenberg, P., & Kohn, W. (1964). Physical Review, 136, B864-B871. DOI : 10.1103/PhysRev.136.B864.

[22]. Kohn, W., & Sham, L. J. (1965). Physical Review, A140, 1133. DOI : 10.1103/PhysRev.140.A1133.

[23]. Zupan, A. (1996). Thèse de doctorat, Université de Ljubljana.

[24]. Dirac, P. A. M. (1930). Proceedings of the Cambridge Philosophical Society, 26, 376.

[25]. Cazade, P.-A. (2008). Thèse de doctorat, Université de Pau et des Pays de l'Adour.

[26]. Berbouche, D. (2014). Étude théorique et modélisation de quelques molécules biologiques actives. Thèse de doctorat, Université Mohamed Khider, Biskra.

[27]. Perdew, J. P., Chevary, J. A., Vosko, S. H., Jackson, K. A., Perderson, M. A., Singh, D. J., & Fiolhais, C. (1992). Physical Review, B46, 6671.

[28]. Becke, A. D. (1988). Physical Review A, 38, 3098-3100.

[29]. Lee, C., Yang, W., & Parr, R. G. (1988). Physical Review B, 37, 785-789. DOI : 10.1103/PhysRevB.37.785.

[30]. Perdew, J. P. (1986). Physical Review B, 33, 8822-8824.

[31]. Perdew, J. P., & Wang, Y. (1992). Physical Review B, 45, 244.

[32]. Jensen, F. (2007). Introduction to Computational Chemistry. John Wiley & Sons, Ltd.

[33]. Stephens, P. J., Devlin, F. J., Chabalowski, C. F., & Frish, M. J. (1994). The Journal of Physical Chemistry, 98, 11623.

[34]. Bo-tao, F., & Rui-sheng, Z. (1999). Introduction to Computer Chemistry. Lanzhou University Press.

[35]. Leach, A. (1996). Quantum Mechanical Models. In Molecular Modelling: Principles and Applications (pp. 25-130). Addison Wesley Longman Ltd.

[36]. Marle, C. (2003). De la mécanique classique à la mécanique quantique. Université Pierre et Marie Curie, Paris, France.

[37]. https://www.techniques-ingenieur.fr/base-documentaire/mesures-analyses-th1/etudes-destructure-et-caracterisation-42386210/modelisation-moleculaire-et-conception-de-nouveauxligands-d-interets-biologiques-pha1015/

[38]. https://bioinfo-fr.net/la-modelisation-moleculaire

[39]. Reedijk, J. (2014). Reference Module in Chemistry, Molecular Sciences, and Chemical Engineering. Elsevier, Oxford.

[40]. Jiang, W., Li, W., Hong, Y., et al (2016). Cloning, Expression, Mutagenesis Library Construction of Glycerol Dehydratase, and Binding Mode Simulation of Its Reactivase

61 with Ligands. Applied Biochemistry and Biotechnology, 178, 739-752. DOI : 10.1007/s12010-015-1906-6.

[41]. Molecular Operating Environment (MOE) (2014). Chemical Computing Group Inc, 1010 Sherbrooke St. West, Suite # 910, Montreal QC, Canada H3A 2R7.

[42]. Rarey, M., Kramer, B., Lengauer, T., & Klebe, G. (1996). A Fast Flexible Docking Method using an Incremental Construction Algorithm. Journal of Molecular Biology, 261, 470-489. DOI : 10.1006/jmbi.1996.0477.

[43]. Friesner, R. A., Banks, J. L., Murphy, R. B., et al (2004). Glide: A New Approach for Rapid, Accurate Docking and Scoring. 1. Method and Assessment of Docking Accuracy. Journal of Medicinal Chemistry, 47, 1739-1749. DOI : 10.1021/jm0306430.

[44]. Morris, G. M., Goodsell, D. S., Halliday, R. S., et al (1998). Automated Docking Using a Lamarckian Genetic Algorithm and an Empirical Binding Free Energy Function. Journal of Computational Chemistry, 19, 1639-1662. DOI : 10.1002/(SICI)1096-987X(19981115)19:14<1639::AID-JCC10>3.0.CO;2-B.

[45]. Jones, G., Willett, P., Glen, R. C., et al (1997). Development and Validation of a Genetic Algorithm for Flexible Docking. Journal of Molecular Biology, 267, 727-748. DOI : 10.1006/jmbi.1996.0897.

[46]. Schapira, M., Abagyan, R., & Totrov, M. (2003). Nuclear Hormone Receptor Targeted Virtual Screening. Journal of Medicinal Chemistry, 46, 3045-3059. DOI : 10.1021/jm0300173.

[47]. Jain, A. N. (2003). Surflex: Fully Automatic Flexible Molecular Docking Using a Molecular Similarity-Based Search Engine. Journal of Medicinal Chemistry, 46, 499-511. DOI : 10.1021/jm020406h.

[48]. Eberhardt, J., Santos-Martins, D., Tillack, A. F., & Forli, S. (2021). AutoDock Vina 1.2.0: New Docking Methods, Expanded Force Field, and Python Bindings. Journal of Chemical Information and Modeling, 61, 3891-3898. DOI : 10.1021/acs.jcim.1c00203.

[49]. Dar, A. M., & Mir, S. (2017). Molecular Docking: Approaches, Types, Applications, and Basic Challenges. Journal of Analytical & Bioanalytical Techniques, 8, 356. DOI : 10.4172/2155-9872.1000356.

[50]. Pagadala, N. S., Syed, K., & Tuszynski, J. (2017). Software for molecular docking: a review. Biophysics Reviews, 9, 91-102. DOI : 10.1007/s12551-016-0247-1.

[51]. Irwin, J. J., Sterling, T., Mysinger, M. M., et al (2012). ZINC: A Free Tool to Discover Chemistry for Biology. Journal of Chemical Information and Modeling, 52, 1757-1768. DOI : 10.1021/ci3001277.

[52]. Gaulton, A., Bellis, L. J., Bento, A. P., et al (2012). ChEMBL: a large-scale bioactivity database for drug discovery. Nucleic Acids Research, 40, D1100-D1107. DOI : 10.1093/nar/gkr777.

[53]. Armstrong, J. F., Faccenda, E., Harding, S. D., et al (2019). The IUPHAR/BPS Guide to PHARMACOLOGY in 2020: extending immunopharmacology content and introducing the IUPHAR/MMV Guide to MALARIA PHARMACOLOGY. Nucleic Acids Research gkz951. DOI : 10.1093/nar/gkz951.

[54]. Dunkel, M. (2006). SuperNatural: a searchable database of available natural compounds. Nucleic Acids Research, 34, D678-D683. DOI : 10.1093/nar/gkj132.

[55]. Bolton, E. E., Wang, Y., Thiessen, P. A., & Bryant, S. H. (2008). PubChem: Integrated Platform of Small Molecules and Biological Activities. In: Annual Reports in Computational Chemistry. Elsevier, pp 217-241.

[56]. Tai, H. K., Jusoh, S. A., & Siu, S. W. I. (2018). Chaos-embedded particle swarm optimization approach for protein-ligand docking and virtual screening. Journal of Cheminformatics, 10, 62. DOI : 10.1186/s13321-018-0320-9.

[57]. Betzi, S., Suhre, K., Chétrit, B., et al (2006). GFscore: A General Nonlinear Consensus Scoring Function for High-Throughput Docking. Journal of Chemical Information and Modeling, 46, 1704-1712. DOI : 10.1021/ci0600758.

[58]. Wang, R., Lai, L., & Wang, S. (2002). Further development and validation of empirical scoring functions for structure-based binding affinity prediction. Journal of Computer-Aided Molecular Design, 16, 11-26. DOI : 10.1023/A:1016357811882.

[59]. Gohlke, H., & Klebe, G. (2002). Approaches to the description and prediction of the binding affinity of small-molecule ligands to macromolecular receptors. Angewandte Chemie International Edition, 41(15), 2644-2676.

[60]. Ferrara, P., Gohlke, H., Price, D. J., & Klebe, G. (2004). Assessing scoring functions for protein-ligand interactions. Journal of Medicinal Chemistry, 47, 3032-3047.

[61]. Wang, R., Lu, Y., Fang, X., & Wang, S. (2004). An extensive test of 14 scoring functions using the PDB bind refined set of 800 protein-ligand complexes. Journal of Chemical Information and Computer Sciences, 44(6), 2114-2125.

[62]. Böhm, H-J. (1994). The development of a simple empirical scoring function to estimate the binding constant for a protein-ligand complex of known three-dimensional structure. Journal of Computer-Aided Molecular Design, 8, 243-256. DOI : 10.1007/BF00126743.

[63]. Bar-Haim, S., Aharon, A., Ben-Moshe, T., et al (2009). SeleX-CS: A New Consensus Scoring Algorithm for Hit Discovery and Lead Optimization. Journal of Chemical Information and Modeling, 49, 623-633. DOI : 10.1021/ci800335j.

[64]. Teramoto, R., & Fukunishi, H. (2008). Structure-Based Virtual Screening with Supervised Consensus Scoring: Evaluation of Pose Prediction and Enrichment Factors. Journal of Chemical Information and Modeling, 48, 747-754. DOI : 10.1021/ci700464x.

[65]. Khireddine, A. (2022). Étude théorique des propriétés structurales et optiques des composés organométalliques, thèse de doctorat, Université Ferhat Abbes de Sétif.

[66]. Chouaih, A. (2006). Etude par diffraction des rayons X des propriétés structurales de molécules d'intérêt industriel, thèse de doctorat, Université Abdelhamid Ibn Badis, Mostaganem.

[67]. Leach, A. R., & Kuntz, I. D. (1992). Conformational analysis of flexible ligands in macromolecular receptor sites. Journal of Computational Chemistry, 13, 730-748.

[68]. Böhm, H-J. (1992). LUDI: rule-based automatic design of new substituents for enzyme inhibitor leads. Journal of Computer-Aided Molecular Design, 6(6), 593-606.

[69]. Böhm, H-J. (1994). The development of a simple empirical scoring function to estimate the binding constant for a protein-ligand complex of known three-dimensional structure. Journal of Computer-Aided Molecular Design, 8(3), 243-256.

[70]. Gerschel, A. (2012). Liaisons intermoléculaires : Les forces en jeu dans la matière condensée. Paris, EDP Sciences, 2e édition, 288p.

[71]. Atkins, P. W. (1997). Chimie Physique, 6ème édition.

[72]. Israelachvili, J. N. (1997). Intermolecular and surface forces (2e édition). Academic Press, Londres.

[73]. Morris, G. M., Goodsell, D. S., Halliday, R. S., Huey, R., Hart, W. E., Belew, R. K., & Olson, A. J. (1998). Automated docking using a Lamarckian genetic algorithm and an empirical binding free energy function. Journal of Computational Chemistry, 19(14), 1639-1662.

[74]. Trott, O., & Olson, A. J. (2010). AutoDock Vina: improving the speed and accuracy of docking with a new scoring function, efficient optimization, and multithreading. Journal of Computational Chemistry, 31(2), 455-461.

[75]. Baxter, J. (1981). Local optima avoidance in depot location. Journal of the Operational Research Society, 815-819.

[76]. Lourenço, H. R., Martin, O. C., & Stützle, T. (2010). Iterated local search: Framework and applications. In Handbook of Metaheuristics (pp. 363-397). Springer.

[77]. Wright, S., & Nocedal, J. (1999). Numerical optimization. Springer New York.

[78]. Protein Data bank PDB. http://www.rcsb.org

[79]. Soury-Lavergne Navizet, I. (2004). Modélisation et analyse des propriétés mécaniques des protéines, thèse de doctorat, Université Paris 6 Pierre & Marie Curie.

[80]. Verlet, L. (1967). Phys. Rev. 159, 98.

[81]. Hockney, R. W., Goel, S. P., & Eastwood, J. W. (1974). J. Comput. Phys., 14(2).

[82]. Anoukou, K. (2012). Modélisation muliti-échelle du comportement mécanique de nanocomposites polymères à renforts d'argile de type montmorillonite-approche micromécanique et simulation de dynamique moléculaire, thèse de doctorat, Université de Lille 1.

[83]. Andersen, H. C. (1980). J. Chem. Phys. 72.

[84]. Solar, M. (2010). Simulations numériques de dynamique moléculaire du contact normal et tangentiel sur surfaces de polymères amorphes linéaires : vers une meilleure compréhension de la physique locale du contact, Thèse de doctorat, Université de Strasbourg.

[85]. Haile, J. M. (1997). Molecular Dynamics Simulation. Wiley Interscience.

[86]. Berendsen, H. J. C., Postma, J. P. M., Van Gunsteren, W. F., Dinola, A., & Haak, J. R. (1984). J. Chem. Phys. 81.

[87]. McCammon, J. A., & Harvey, S. C. (1987). Dynamics of proteins and nucleic acids. Cambridge University Press, Cambridge.

[88]. Jorgensen, W. L., Chandrasekhar, J., Madura, J. D., Impey, R. W., & Klein, M. L. (1983). Comparison of simple potential functions for simulating liquid water. J. Chem. Phys. 79, 926-935.

[89]. Berendsen, H. J. C., Grigera, J. R., & Straatsma, T. P. (1987). The missing term in effective pair potentials. J. Phys. Chem. 91, 6269-6271.

[90]. Brooks, B. R., Bruccoleri, R. E., Olafson, B. D., States, D. J., Swaminathan, S., & Karplus, M. (1983). J. Comput. Chem, 4, 187–217.

[91]. Reiher, W. E., IIII. (1985). Theoretical Studies of Hydrogen Bonding. Ph.D. thesis, Harvard University.

[92]. Neria, E., Fischer, S., & Karplus, M. (1996). J. Chem. Phys, 105, 1902–1921.

[93]. MacKerell, A. D., Jr. (2001). In Computational Biochemistry and Biophysics (pp. 7–38). Marcel Dekker, New York.

[94]. Bekker, H., Berendsen, H. J. C., Dijkstra, E. J., Achterop, S., van Drunen, R., van der Spoel, D., ... & Renardus, M. K. R. (1993). Gromacs: A parallel computer for molecular

dynamics simulations. In Physics Computing 92, Proceedings of the 4th International Conference, Prague, Czech Republic, 24–28 August 1992 (pp. 252–256). World Scientific.

[95]. Kumari, R., Kumar, R., Open Source Drug Discovery Consortium, & Lynn, A. (2014). g_mmpbsa - a GROMACS tool for high-throughput MM-PBSA calculations. Journal of Chemical Information and Modeling, 54(10), 1951–1962. https://doi.org/10.1021/ci500020m

[96]. Baker, N. A., Sept, D., Joseph, S., Holst, M. J., & Andrew Mc Cammon, J. (2001). Electrostatics of nanosystems: application to microtubules and the ribosome. Proceedings of the National Academy of Sciences of the United States of America, 98(18), 10037–10041. https://doi.org/10.1073/pnas.181342398

[97]. Wagoner, J. A., & Baker, N. A. (2006). Assessing implicit models for nonpolar mean solvation forces: the importance of dispersion and volume terms. Proceedings of the National Academy of Sciences of the United States of America, 103(22), 8331–8336. https://doi.org/10.1073/pnas.0506715103

[98]. Vishvakarma, V. K., Singh, P., Kumari, K., & Chandra, R. (2017). Rational design of threo as well erythro noscapines, an anticancer drug: a molecular docking and molecular dynamic approach. Biochemical Pharmacology, 6(3), 1–7. Hospital, A., Goni, J. R., Orozco, M., & Gelpí, J. L. (2015). Molecular dynamics simulations: advances and applications. Advances in Applied Bioinformatics and Chemistry, 8, 37–47. https://doi.org/10.2147/AABC.S70333

[99]. Salsbury Jr., F. R. (2010). Molecular dynamics simulations of protein dynamics and their relevance to drug discovery. Current Opinion in Pharmacology, 10(6), 738–744. https://doi.org/10.1016/j.coph.2010.08.011

[100]. Kufareva, I., & Abagyan, R. (2012). Methods of protein structure comparison. Methods in Molecular Biology, 857, 231–257.

Chapter IV

Structural analysis

of EMTh($C_{12}H_{14}N_2O_2S$), and TMTh ($C_{14}H_{18}N_2O_2S$) molecules

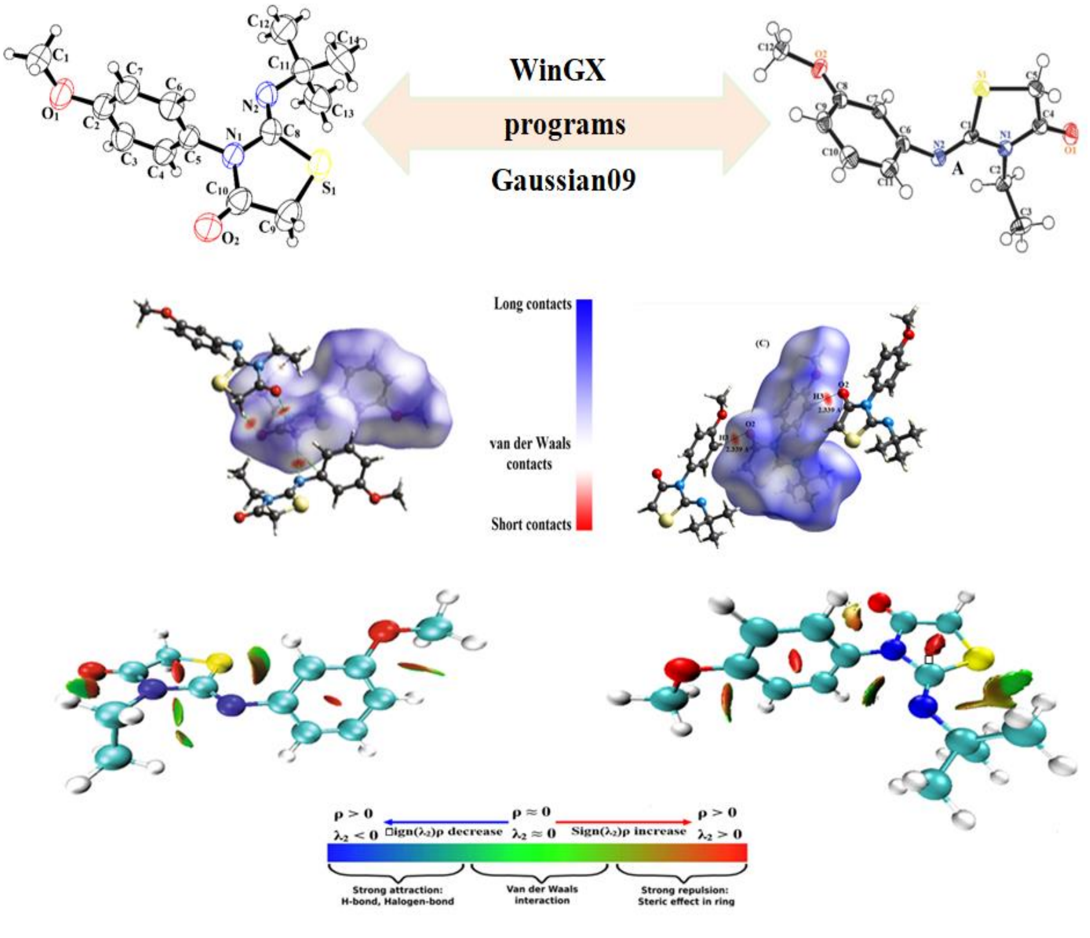

IV.1. Introduction

X-ray diffraction on single crystals (SC-XRD) serves as crucial technique for Understanding the crystalline and molecular structures by collecting excellent single crystals for structural analysis of an organic compound. This diffraction method is the simplest for figuring out the three-dimensional molecular arrangement of a crystal structure. The new organic compounds under study EMTH($C_{12}H_{14}N_2O_2S$), and TMTH ($C_{14}H_{18}N_2O_2S$) molecules, which were synthesized by our collaborators at the Applied Organic Synthesis Laboratory (AOSL) at the University of Oran through chemical mechanism, showed a good recrystallization, so we used SC-X-ray diffraction to determine their three-dimensional geometries.

To conduct an X-ray diffraction investigation for the compounds EMTHand TMTH (figure IV.1), ABruker Kappa Apex2, and STOE IPDS 2 diffractometer and a two-dimensional detector (CCD) on a single crystal with dimensions of (0.31 × 0.28 × 0.19) and (0.220 × 0.203 × 0.190)mm; respectively, were employed while the Graphite is utilised as the monochromator with the molybdenum wavelength (MoK = 0.71073). The diffracted intensities were obtained at a low and the room temperature 130 and 296 K, respectively.

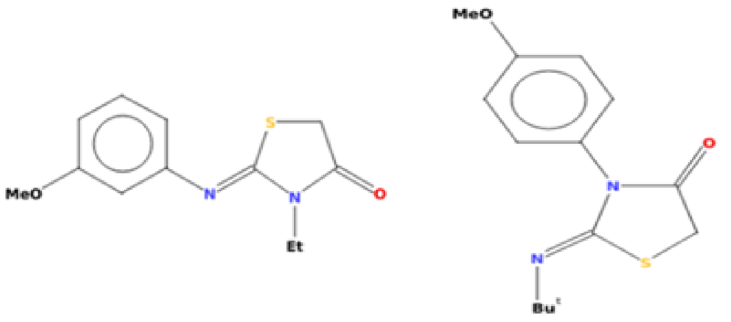

(Z)-3-N-(ethyl)-2-N'-((3- methoxyphenyl) imino) thiazolidine-4-one
(Z-Emit)
$C_{12}H_{14}N_2O_2S$

(Z)-2N-(tert-butylimino)-3N'-(4-methoxyphenyl) thiazolidin-4-one
(TMTh)
$C_{14}H_{18}N_2O_2S$

Figure IV.1. Identification of the two new synthetic organic compounds

IV.2. Organic synthesis of the EMTh and the TMth

- *Synthesis and Crystallization*

An equimolar solution of N-ethyl-3-N'-(3-methoxyphenyl)thiourea and ethyl bromoacetate in absolute ethanol, in the presence of sodium acetate, underwent reflux for 6 hours. Following vacuum distillation to remove the solvent, the resulting residue was isolated, cold-water washed, filtered, dried, and subjected to crystallization from ethanol, resulting in the formation of (Z)-3-N-(ethyl)-2- N'-((3-methoxyphenyl)imino)thiazolidin-4-one, as outlined in the scheme. Similarly, for the synthesis of (Z)-2N-(tert-butylimino)-3N'-(4-methoxyphenyl) thiazolidin-4-one, a solution of 1-tert-butyl-3-(4-methoxyphenyl) thiourea and ethyl bromoacetate in ethanol with acetic acid was stirred at room temperature for 6 hours. Recrystallization of (Z)-2N-(tert-butylimino)-3N'-(4-methoxyphenyl) thiazolidin-4-one (TMTh) from ethanol was achieved through slow evaporation, followed by solvent removal using vacuum distillation. The resulting solid was filtered, water-washed, and dried to obtain the final product.

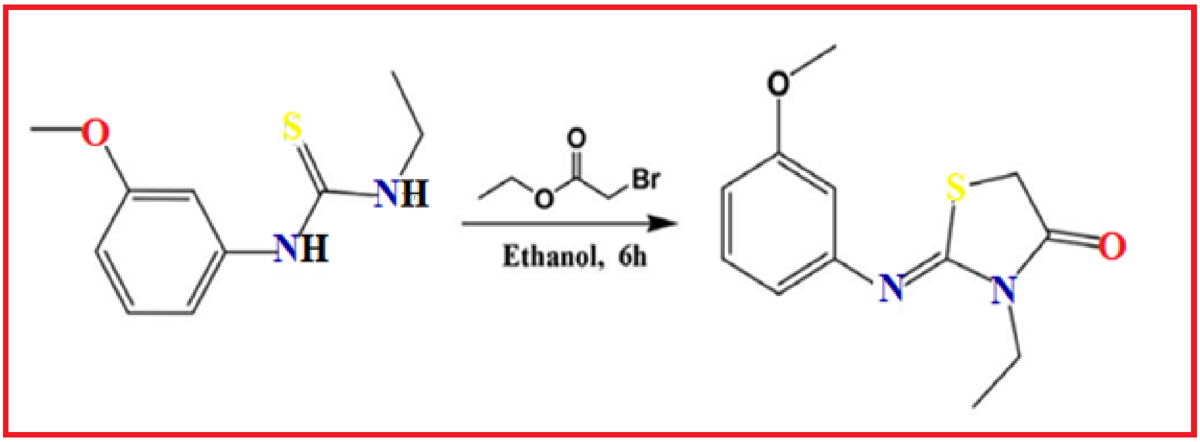

Figure IV.2. Reaction sequence for the title compound synthesis

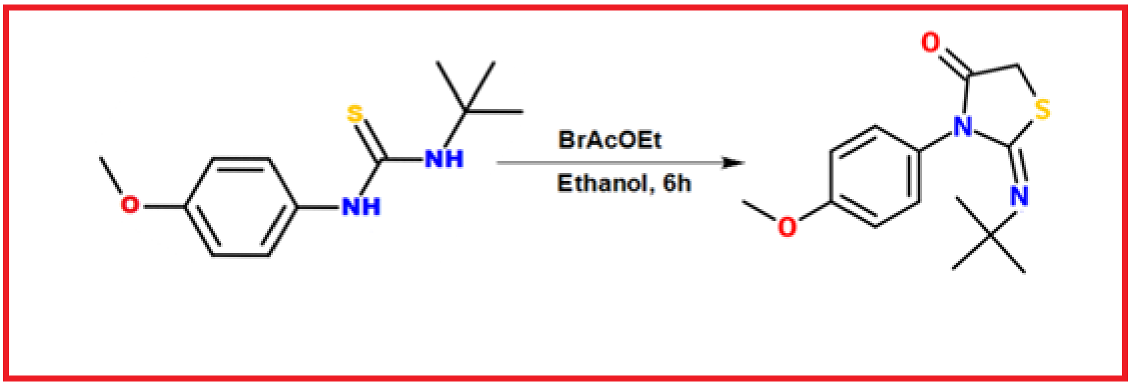

Figure IV.3. Synthesis of chemical pathway for TMTh

- *Characterization of (Z)-2N-(tert-butylimino)-3N'-(4-methoxyphenyl) thiazolidin-4-one*

Experimental techniques (including FT-IR, NMR, and UV-Vis) were used to characterize TMTh. On a Perkin-Elmer FT-IR spectrometer, the IR spectrum of a KBr pellet was recorded in the range 400–4000 cm^{-1}. The measured wavenumbers are reported in cm^{-1}. In DMSO-

d$_6$solvent at 25 °C, the ^{1}H and ^{13}C NMR spectra were measured using a Bruker AC-500 MHz spectrometer relative to TMS which serves as an internal standard, chemical shifts are reported as δ (ppm). Electronic UV–Visspectrum was recorded using a Shimadzu UV-2900 Pc-spectrophotometer in the range from 200 to 700 nm in chloroform solution.

IV.3. Collecting information and X-ray crystallography

Transparent yellowish parallelepiped crystals of C12H14N2O2S were selected, and the mother liquid was removed before rapid chilling to 130 K. The crystal was then mounted on a Bruker Kappa APEX 2 diffractometer equipped with a Triumph monochromator and MoKa radiation. No signs of deterioration were observed during data collection. Employing a narrow-frame method, frames obtained from running ϕ and ω scans were merged using the Bruker SAINT Software package [1], and the SADABS program[2] was utilized for data rectification. The structure was solved using the SUPERFLIP package[3], with subsequent refinement and computations performed using full-matrix least-squares on F2 in the Crystals software package version 14.40 [4]. Anisotropic refinement was applied to all non-hydrogen atoms, while hydrogen atoms were positioned and refined by riding limitations to the pivot atoms. For the C14H18N2O2S molecule, brown-colored crystals were chosen for an X-ray diffraction experiment conducted on a STOE IPDS II single crystal diffractometer at room temperature, using monochromated MoK radiation (λ = 0.71073). The structure was solved and improved using the Shelxs-97 [5] and Shelxl-97 [6] programs implemented in the WinGX programs. All non-hydrogen atoms were refined anisotropically using reflections with I > 2 (I). Mercury and ORTEP software programs[7-8] were employed for geometric analysis and crystal structure visualization. The table presents an overview of the crystallographic and experimental data for both C14H17N2O2S and C14H18N2O2S molecules.

Table IV.1. crystallographic data of the EMTh and TMth compounds

crystallographic properties	EMTh	TMth
Crystal data		
Chemical formula	$C_{12}H_{14}$ N_2O_2S	$C_{14}H_{18}N_2O_2S$
M_r (g/mol)	250.32	277.35
Crystal system. space group	Monoclinic. C2/c	Monoclinic, I2/a
130	130	296
a. b. c (Å)	23.7067 (19), 6.8884 (6) , 15.7244 (12)	13.6185 (6), 5.7532 (2), 37.1790 (17)
β(°)	111.6504 (17)	91.349 (4)
V (Å ^{3})	2386.66 (18)	2912.2 (2)
Z	8	8
Radiation type	Mo Kα, 0.71073	Mo Kα
μ(mm^{-1})	0.26	0.222
Crystal size (mm)	0.31 × 0.28 × 0.19	0.220 × 0.203 × 0.190
Data collection		
Diffractometer	Bruker Kappa Apex2	STOE IPDS 2
Absorption correction	(De Meulenaer & Tompa, 1965)	X-RED32; Stoe & Cie. 2002
T_{min}. T_{max}	0.93, 0.95	0.900. 0.990
No. of measured. independent and observed [I > 2σ(I)] reflections	17268, 3006, 2843	19866, 3225, 2169
h.k.l	−17→17.−7→7.−47→47	−17→17, −7→7, −47→47
R_{int}	0.015	0.015
(sin θ/λ) $_{max}$ (Å^{-1})	1.	1.
Refinement		
R[F^2> 2(F^2)]. wR(F2). S	0.029, 0.066, 1.00	0.046, 0.134, 1.032
No. of parameters	154	172
No. of restraints	0	0
H-atom treatment	H-atom parameters constrained	H-atom parameters constrained
$\Delta\rho_{max}$. $\Delta\rho_{min}$ (e Å^{-3})	0.33, 0.21	0.38, −0.29

IV.4. Structure solution and refinement results

The resolution and refinement of the crystal structures were carried out using the WinGX program, employing SHELXS for structure resolution and SHELXL for subsequent refinement. The refinement process involved several steps, including refining non-hydrogen atoms, locating hydrogen atoms, refining the entire structure, and determining the molecular geometry. The refinement aimed to optimize the positions and displacement parameters, along with thermal agitation parameters, for non-hydrogenic atoms in the molecule. The least squares method was utilized to refine structural parameters such as atomic positions (x, y, z), isotropic displacement parameters (Uiso), or anisotropic ones (Uaniso), and the static occupation of crystallographic sites. The reliability factor was minimized during the refining steps to enhance the accuracy of the generated model.

The SHELXS program facilitated the resolution process by applying direct and Patterson methods to solve both simple and macromolecule structures. It assisted in specifying atomic positions on a Fourier map card, locating "heavy" atoms, and calculating electronic density, binding lengths, and valence angles. Similarly, SHELXL, through its Nom.INS file, provided instructions for various refining aspects, such as

L.S.: To specify the number of cycles for refining.

BOND: For calculating bond angles and interatomic lengths.

FMAP 2: For computing the electrical density difference.

PLAN n: To highlight the difference in furrier synthesis's n first, highly intense peaks.

OMIT: Removes dimly-lit reflections.

ACTA: To produce Nom. fcf and Nom. Cif files.

The refinement process involved anisotropic refinement for non-hydrogen atoms, while hydrogen atoms were placed in ideal positions based on isotropic thermal agitation. The conclusion of this phase yielded known positions for each atom in the molecule within the primary cell. The structural description included fractional coordinates, interatomic distances, valence angles, and torsion angles, providing optimal placements for the atoms. The resulting atomic positions for the two compounds under study are summarized in the tables below, reflecting the successful resolution and refinement of their crystal structures.

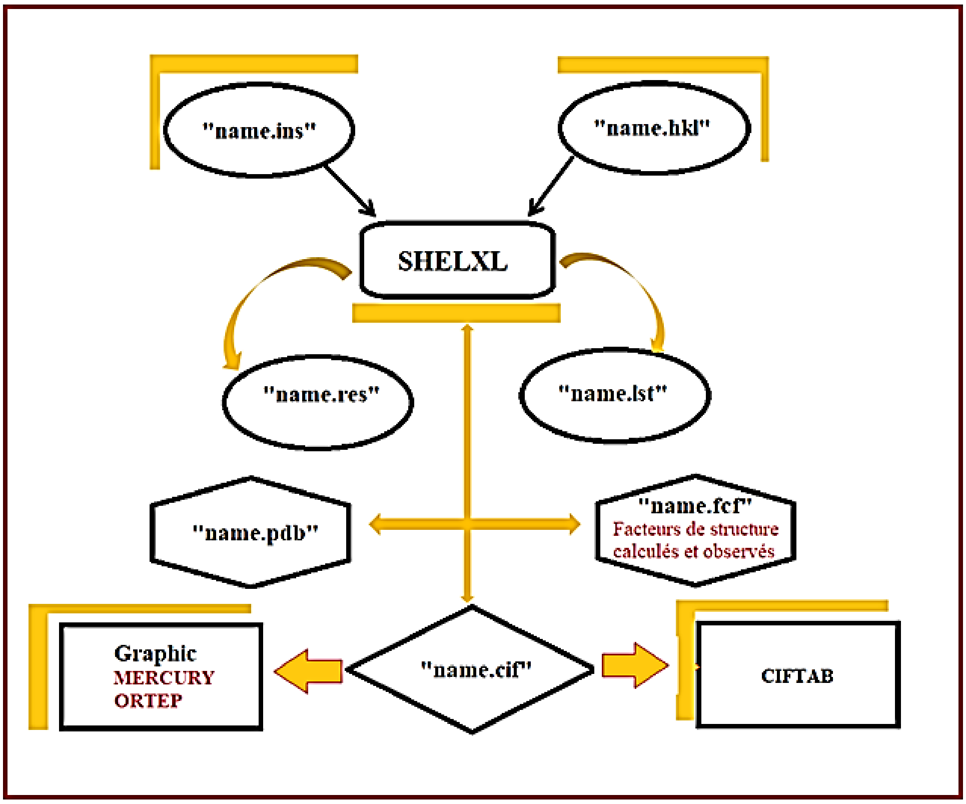

Figure IV.4. SHELXL program execution diagram.

TableIV.2. Fractional coordinates and isotropic displacement parameters of $C_{12}H_{14}N_2O_2S$ atoms

Atoms	X	Y	z	U
S(1)	0.10788	0.50228	0.15994	0.01797
O(2)	-0.05914	0.62932	0.11818	0.02501
N(2)	-0.00321	0.36893	0.10548	0.01554
N(1)	0.06829	0.13208	0.11211	0.01769
O(1)	0.22667	0.03724	-0.00145	0.02168
C(6)	0.12946	0.07703	0.12928	0.01646
C(7)	0.15233	0.09485	0.06005	0.01662
H(7)	0.12957	0.15665	0.00559	0.02142
C(9)	0.04899	0.66706	0.16222	0.02010
H(9A)	0.05728	0.71133	0.22423	0.03191
H(9B)	0.04725	0.77935	0.12411	0.02880
C(11)	-0.05546	0.23707	0.07029	0.01727
H(11A)	-0.04474	0.12768	0.04043	0.02542
H(11B)	-0.08897	0.30482	0.02483	0.02153
C(8)	0.05618	0.30706	0.12250	0.01410
C(10)	-0.01043	0.55817	0.12652	0.01743
C(4)	0.22114	-0.08311	0.22376	0.02178
H(4)	0.24443	-0.14126	0.27896	0.02877
C(2)	0.20958	0.01981	0.07231	0.01666
C(12)	-0.07573	0.16244	0.14530	0.02474
H(12A)	-0.10997	0.07782	0.11917	0.04456
H(12B)	-0.08697	0.27006	0.17449	0.04327
H(12C)	-0.04306	0.09225	0.18966	0.04017
C(3)	0.24437	-0.06958	0.15451	0.02005
H(3)	0.28252	-0.11944	0.16298	0.02573
C(5)	0.16413	-0.01190	0.21228	0.02004
H(5)	0.14910	-0.02298	0.25898	0.03092
C(1)	0.28818	-0.01044	0.01246	0.02591
H(1A)	0.29480	0.00731	-0.04370	0.03966
H(1B)	0.29594	-0.14330	0.03167	0.02645
H(1C)	0.31507	0.07267	0.05875	0.02885

Table IV.3. Anisotropic (Å) thermal agitation parameters of the different atoms of the $C_{12}H_{14}$ N_2O_2S molecule

Atoms	U11	U22	U33	U12	U13	U23
S(1)	0.0130	0.0159	0.0237	-.0026	0.0052	-.0005
O(2)	0.0186	0.0241	0.0318	0.0068	0.0087	0.0020
N(2)	0.0108	0.0172	0.0181	-.0007	0.0047	0.0000
N(1)	0.0127	0.0172	0.0237	-.0017	0.0074	-.0018
O(1)	0.0158	0.0259	0.0254	0.0025	0.0101	0.0015
C(6)	0.0127	0.0127	0.0233	-.0016	0.0058	-.0034
C(7)	0.0132	0.0143	0.0204	-.0001	0.0039	0.0004
H(7)	0.014(	0.025(	0.040(	-0.010(	0.028(	-0.011(
C(9)	0.0192	0.0143	0.0271	-.0004	0.0089	-.0005
H(9A)	0.016(	0.029(	0.048(	0.011(	0.008(	-0.001(
H(9B)	0.021(	0.022(	0.043(	-0.005(	0.011(	-0.005(
C(11)	0.0118	0.0227	0.0165	-.0034	0.0042	-.0024
H(11A)	0.012(	0.032(	0.025(	-0.016(	-0.002(	-0.004(
H(11B)	0.017(	0.030(	0.016(	-0.004(	0.005(	0.000(
C(8)	0.0110	0.0172	0.0140	-.0018	0.0044	0.0009
C(10)	0.0171	0.0179	0.0173	0.0015	0.0063	0.0027
C(4)	0.0196	0.0214	0.0198	0.0018	0.0019	0.0004
H(4)	0.024(	0.035(	0.039(	0.002(	0.025(	-0.002(
C(2)	0.0139	0.0143	0.0213	-.0015	0.0058	-.0030
C(12)	0.0220	0.0326	0.0195	-.0100	0.0075	-.0007
H(12A)	0.06(1	0.05(1	0.02(1	-0.04(1	0.02(1	-0.01(1
H(12B)	0.06(1	0.05(1	0.04(1	-0.01(1	0.03(1	0.00(1
H(12C)	0.023(	0.061(	0.035(	-0.009(	0.008(	0.017(
C(3)	0.0134	0.0189	0.0248	0.0027	0.0034	-.0018
H(3)	0.04(1	0.03(1	0.00(1	0.00(1	0.00(1	0.01(1
C(5)	0.0200	0.0204	0.0194	-.0020	0.0069	-.0022
H(5)	0.016(	0.035(	0.030(	0.003(	-0.005(	-0.004(
C(1)	0.0174	0.0252	0.0394	0.0019	0.0156	0.0009
H(1A)	0.02(1	0.07(1	0.04(1	0.00(1	0.02(1	0.01(1
H(1B)	0.012(	0.032(	0.044(	0.005(	0.021(	0.003(
H(1C)	0.026(	0.026(	0.042(	-0.002(	0.020(	-0.004(

TableIV.4. Fractional coordinates and isotropic displacement parameters of $C_{14}H_{18}N_2O_2S$ atoms

Atoms	X	Y	z	U
S1	0.18790(4)	0.46223(13)	0.41195(2)	0.0716(2)
O1	0.63822(11)	0.6489(3)	0.27673(4)	0.0746(5)
O2	0.22953(11)	0.8264(4)	0.32727(4)	0.0806(5)
N1	0.31399(11)	0.5718(3)	0.36341(4)	0.0532(4)
N2	0.38378(12)	0.3379(3)	0.40787(4)	0.0561(4)
C5	0.40007(13)	0.5823(4)	0.34186(5)	0.0485(4)
C8	0.30955(14)	0.4415(4)	0.39548(5)	0.0527(5)
C2	0.55849(14)	0.6147(4)	0.29753(5)	0.0551(5)
C6	0.41680(15)	0.4111(4)	0.31732(6)	0.0587(5)
H6	0.374701	0.284085	0.315621	0.070
C7	0.49695(16)	0.4266(4)	0.29481(6)	0.0607(5)
H7	0.508598	0.310239	0.278083	0.073
C10	0.23261(14)	0.7004(4)	0.35315(6)	0.0603(5)
C4	0.46149(15)	0.7712(4)	0.34455(5)	0.0584(5)
H4	0.449306	0.888084	0.361144	0.070
C3	0.54146(16)	0.7867(4)	0.32249(6)	0.0639(6)
H3	0.583819	0.913065	0.324453	0.077
C11	0.38603(16)	0.2114(4)	0.44261(5)	0.0597(5)
C9	0.14982(15)	0.6706(5)	0.37869(6)	0.0719(7)
H9	0.089583	0.746718	0.377464	0.086
C13	0.3778(2)	0.3855(5)	0.47328(6)	0.0810(7)
H13A	0.379222	0.304262	0.495843	0.122
H13B	0.431834	0.492474	0.472664	0.122
H13C	0.317131	0.469513	0.470669	0.122
C1	0.6627(2)	0.4735(5)	0.25181(7)	0.0816(8)
H1A	0.719991	0.519675	0.239033	0.122
H1B	0.675973	0.330911	0.264439	0.122
H1C	0.608889	0.450819	0.235047	0.122
C14	0.3074(2)	0.0255(5)	0.44472(8)	0.0908(8)
H14A	0.312243	-0.050530	0.467681	0.136
H14B	0.243777	0.095776	0.441857	0.136
H14C	0.316453	-0.086589	0.425951	0.136
C12	0.4861(2)	0.0950(6)	0.44542(7)	0.0935(9)
H12A	0.491491	0.010099	0.467603	0.140
H12B	0.493434	-0.009814	0.425573	0.140
H12C	0.536621	0.211281	0.444848	0.140

Table IV.5. Anisotropic (Å) thermal agitation parameters of the different atoms of the $C_{14}H_{18}N_2O_2S$ molecule

Atom	U11	U22	U33	U23	U13	U12
S1	0.0510(3)	0.0987(5)	0.0655(4)	0.0101(3)	0.0120(2)	-0.0035(3)
O1	0.0658(9)	0.0827(11)	0.0765(10)	-0.0045(9)	0.0274(8)	-0.0030(8)
O2	0.0672(9)	0.1067(14)	0.0682(10)	0.0258(10)	0.0050(8)	0.0262(9)
N1	0.0438(8)	0.0704(11)	0.0457(8)	0.0046(8)	0.0041(6)	0.0053(8)
N2	0.0545(9)	0.0668(11)	0.0471(9)	0.0066(8)	0.0023(7)	0.0016(8)
C5	0.0427(8)	0.0589(12)	0.0438(9)	0.0034(9)	0.0025(7)	0.0038(9)
C8	0.0508(10)	0.0617(12)	0.0456(10)	-0.0014(9)	0.0035(8)	-0.0044(9)
C2	0.0491(10)	0.0661(13)	0.0504(10)	0.0019(9)	0.0072(8)	0.0032(9)
C6	0.0573(11)	0.0606(13)	0.0585(12)	-0.0048(10)	0.0066(9)	-0.0069(10)
C7	0.0637(12)	0.0597(13)	0.0593(12)	-0.0109(10)	0.0119(9)	0.0012(10)
C10	0.0485(10)	0.0804(15)	0.0519(11)	-0.0011(11)	-0.0018(8)	0.0073(10)
C4	0.0597(11)	0.0611(13)	0.0548(11)	-0.0090(10)	0.0085(9)	-0.0007(10)
C3	0.0621(12)	0.0645(14)	0.0655(13)	-0.0058(11)	0.0099(10)	-0.0111(11)
C11	0.0684(12)	0.0638(13)	0.0471(10)	0.0082(10)	0.0076(9)	0.0025(10)
C9	0.0432(10)	0.111(2)	0.0614(12)	0.0051(13)	0.0033(9)	0.0083(11)
C13	0.1065(19)	0.0829(18)	0.0534(13)	0.0040(12)	-0.0054(12)	0.0006(15)
C1	0.0818(16)	0.0894(19)	0.0750(15)	0.0043(14)	0.0315(13)	0.0207(14)
C14	0.112(2)	0.0680(17)	0.0927(18)	0.0186(15)	0.0024(16)	-0.0150(15)
C12	0.0934(18)	0.119(2)	0.0683(15)	0.0322(15)	0.0097(13)	0.0358(17)

The obtained structure has been legally deposited at the Cambridge Crystallographic Data Centre (CCDC) under the reference number CCDC 1871013, and CCDC 1547696 for $C_{12}H_{14}N_2O_2S$, and $C_{14}H_{18}N_2O_2S$ molecules, respectively.

IV.5. Theoretical calculation methodology

The Gaussian 09 [9] molecular modeling software, installed at the Laboratory of Solid Properties and Technology (LTPS) at the University of Mostaganem, was used to theoretically analyze the examined organic compounds'. Our compounds' molecular geometries have been improved for this purpose. This was accomplished by applying quantum theory to optimize the molecular geometries of our molecules.

Using the appropriate calculating approach is crucial to obtain findings that are close to the experimental. We selected the density functional theory (DFT) with the functional B3LYP and the basis 6-311G (d, p), was chosen for our investigation.This basis set uses three Gaussian functions for the description of valence electrons, three Gaussian processes for the definition of core electrons, and a final Gaussian function to describe the outer (or valence) electrons that are the furthest out from the nucleus to describe an atomic orbital. D and P stand for the utilization of polarization orbitals. These mathematical techniques can produce exact predictions for optimizing geometric angles and lengths of the connections and are often well-suited for organic molecules. The GAUSSIAN09 computer program [9] and its GAUSS VIEW graphical user interface version 5.0.8 [10] were used for all calculations.

IV.5.1. Structure description

The molecular geometry of the EMTh compound is characterized by the interaction of two structural components, namely the methoxyphenyl and thiazolidine rings, resulting in a dihedral angle of 86°. Detailed information on atomic positions and thermal parameters is available in the CIF file, and Tables IV. 7, and 8 present selected bond lengths, bond angles, and torsion angles obtained through both X-ray diffraction and theoretical calculations. An ORTEPIII diagram in Figure 1 illustrates the X-ray structure with thermal ellipsoids alongside the theoretical structure. The study employed full geometry optimization without symmetry constraints, revealing distinctive characteristics of single and double bonds in specific S1–C5, S1–C1, C1–N1, N1–C2, N1–C4, C6–N2, and O2–C8 bonds. while C4–O2 (1.23 Å) and N2–C1 (1.26 Å) bonds show typical double bond characteristics [11]. The amine N2 atom exhibits an sp2 geometry, and the thiazole ring bonds show minimal discrepancies between theoretical and experimental values. Bond angles, such as C6–N2–C1, C2–N1–C4, and C1–N1–C4, approximate 120° (119.56°, 121.08° and 116.72°, respectively) [12]. The C1 atom is of sp2 hybridization type because the total adds up to 360° at B3LYP/6-311G (d, p) level. The corresponding theoretical value of this angle is 64° (C7–C6–N2– C1). The C8–O2–C12 angle is 116.98°, and the C2–N1–C4–O1 fragment is approximately planar (Table 4). Generally, the observed difference between experimental and calculated geometrical parameters does not seem very large. The X-ray crystallographic structure in Figure 1, along with optimized molecular geometry, is presented, and Table 2 details the experimental and computed bond lengths, angles, and dihedral angles. While the optimized geometrical parameters of TMTh at the same basis set reveal that the title compound crystallizes in the I2/a space group of the monoclinic system and it has a typical double bond nature for the C10–O2 bond. Despite slight variations in C–S bond lengths at 1.81 Å, the study demonstrates consistent results [13, 14], with most C–N bonds exhibiting single bond characteristics. d [15,16]. The molecular structure comprises two planar moieties, one with the methoxyphenyl group and the other with the tert-butylimino-thiazolidin-4-one group, forming a dihedral angle of approximately 68°. Overall, the DFT-derived optimized bond lengths and angles align well with X-ray structural geometry and previous research on related compounds, providing a comprehensive understanding of the molecular structure **[17-18].**

Table IV.7. Selected bond lengths (Å) and angles (◦) by X-ray diffraction and theoretical calculations for EMTH.

Bond lengths	X-ray	DFT	C9–C10–C11	121.52	120.98
S1–C5	1.811(1)	1.887	O2–C8–C7	115.23	115.22
S1–C1	1.767(1)	1.893	O2–C8–C9	124.48	124.87
O1–C4	1.216(1)	1.233	C7–C8–C9	120.27	119.91
N1–C2	1.469(1)	1.485	C10–C9–C8	119.01	119.34
N1–C1	1.399(1)	1.392	C6–C11–C10	118.98	119.96
N1–C4	1.371(1)	1.388	Torsion angles	X-ray	DFT
N2–C6	1.425(1)	1.407	C1–S1–C5–C4	3.6	2.4
N2–C1	1.263(1)	1.264	C5–S1–C1–N1	–4.7	–2.4
O2–C8	1.367(1)	1.386	C5–S1–C1–N2	174.5	176.7
O2–C12	1.431(1)	1.459	C1–N1–C2–C3	–99.6	–86.2
C6–C7	1.389(1)	1.398	C4–N1–C2–C3	77.9	92.2
C6–C11	1.402(1)	1.408	C2–N1–C1–S1	–177.7	–179.7
C7–C8	1.398(1)	1.401	C2–N1–C1–N2	3.1	1.1
C5–C4	1.509(1)	1.527	C4–N1–C1–S1	4.7	1.8
C2–C3	1.518(1)	1.537	C4–N1–C1–N2	–174.6	–177.3
C10–C9	1.393(1)	1.399	C2–N1–C4–O1	–0.2	1.7
C10–C11	1.386(1)	1.387	C2–N1–C4–C5	–179.5	–178.4
C8–C9	1.395(1)	1.397	C1–N1–C4–O1	177.4	–179.9
Bond angles	X-ray	DFT	C1–N1–C4–C5	–1.9	0.1
C5–S1–C1	92.24	90.13	C1–N2–C6–C7	86.0	64.5
C2–N1–C1	122.15	120.13	C1–N2–C6–C11	–100.2	–119.3
C2–N1–C4	121.08	119.58	C6–N2–C1–S1	1.6	4.4
C1–N1–C4	116.72	29.83	C6–N2–C1–N1	–179.2	–176.7
C6–N2–C1	119.56	129.18	C12–O2–C8–C7	–170.8	179.8
C8–O2–C12	116.98	117.97	C12–O2–C8–C9	10.9	–0.1
N2–C6–C7	119.43	124.07	N2–C6–C7–C8	172.3	178.5
N2–C6–C11	119.94	116.82	C11–C6–C7–C8	–1.5	0.6
C7–C6–C11	120.34	119.08	N2–C6–C11–C10	–173.1	–179.4
C6–C7–C8	119.87	120.72	C7–C6–C11–C10	0.6	–1.3
S1–C5–C4	107.51	108.27	C6–C7–C8–O2	–177.2	–179.5
N1–C2–C3	112.36	111.42	C6–C7–C8–C9	1.3	0.4
S1–C1–N1	110.92	109.07	S1–C5–C4–O1	178.9	178.06
S1–C1–N2	127.32	129.12	S1–C5–C4–N1	–1.8	–1.9
N1–C1–N2	121.76	121.81	C11–C10–C9–C8	–0.8	–0.1
O1–C4–N1	123.71	123.73	C9–C10–C11–C6	0.5	1.1
O1–C4–C5	123.91	124.08	O2–C8–C9–C10	178.2	179.2
N1–C4–C5	112.37	112.18	C7–C8–C9–C10	–0.1	–0.7

Table IV.8. Selected bond lengths (Å) and angles (◦) by X-ray diffraction and theoretical calculations for TMTh.

Bond lengths	X-ray	DFT	Bond angles	X-ray	DFT
S1−C8	1.784(2)	1.823	N2−C11−C14	113.02(19)	111.27
S1−C9	1.790(3)	1.827	N2−C11−C12	106.03(17)	105.48
O1−C2	1.362(2)	1.368	C14−C11−C12	108.6(2)	109.02
O1−C1	1.415(3)	1.429	N2−C11−C13	109.22(19)	110.70
O2−C10	1.205(3)	1.218	C14−C11−C13	111.1(2)	111.09
N1−C5	1.437(2)	1.439	C12−C11−C13	108.7(2)	109.06
N1−C8	1.411(3)	1.422	C10−C9−S1	107.68(15)	108.34
N1−C10	1.379(3)	1.396	Dihedral angles	X-ray	DFT
N2−C8	1.252(3)	1.265	C10−N1−C5−C6	-98.2(2)	118.33
N2−C11	1.482(3)	1.477	C8−N1−C5−C6	84.0(2)	-62.78
C5−C6	1.365(3)	1.396	C10−N1−C5−C4	77.8(2)	-60.39
C5−C4	1.374(3)	1.402	C8−N1−C5−C4	-100.0(2)	118.48
C2−C7	1.371(3)	1.406	C11−N2−C8−N1	175.71(19)	-178.94
C2−C3	1.380(3)	1.407	C11−N2−C8−S1	-3.5(3)	1.15
C6−C7	1.394(3)	1.399	C10−N1−C8−N2	-173.6(2)	178.64
C4−C3	1.382(3)	1.391	C5−N1−C8−N2	4.2(3)	-0.25
C10−C9	1.501(3)	1.524	C10−N1−C8−S1	5.7(2)	-1.43
C11−C13	1.524(3)	1.544	C5−N1−C8−S1	-176.43(15)	179.66
C11−C14	1.517(4)	1.544	C9−S1−C8−N2	173.0(2)	-178.83
C11−C12	1.520(3)	1.542	C9−S1−C8−N1	-6.28(16)	1.25
Bond angles	X-ray	DFT	C1−O1−C2−C7	-3.4(3)	-0.40
C8−S1−C9	93.68(9)	92.67	C1−O1−C2−C3	176.9(2)	179.60
C2−O1−C1	118.17(19)	117.65	C4−C5−C6−C7	0.2(3)	-0.38
C10−N1−C8	117.96(16)	111.64	N1−C5−C6−C7	176.23(18)	-179.11
C10−N1−C5	118.97(16)	120.42	O1−C2−C7−C6	-179.32(19)	179.93
C8−N1−C5	123.04(15)	121.13	C3−C2−C7−C6	0.3(3)	-0.06
C8−N2−C11	123.67(17)	126.64	C5−C6−C7−C2	-0.1(3)	0.41
C6−C5−C4	120.57(18)	119.88	C8−N1−C10−O2	176.5(2)	-179.03
C6−C5−N1	119.58(18)	119.77	C5−N1−C10−O2	-1.5(3)	-0.12
C4−C5−N1	119.73(18)	120.32	C8−N1−C10−C9	-1.7(3)	0.803
N2−C8−N1	120.92(17)	121.17	C5−N1−C10−C9	-179.63(19)	179.71
N2−C8−S1	130.84(16)	129.93	C6−C5−C4−C3	-0.7(3)	0.006
N1−C8−S1	108.24(13)	108.88	N1−C5−C4−C3	-176.68(18)	178.74
O1−C2−C7	124.51(19)	124.68	O1−C2−C3−C4	178.9(2)	179.68
O1−C2−C3	115.27(19)	115.67	C7−C2−C3−C4	-0.8(3)	-0.30
C7−C2−C3	120.22(19)	119.64	C5−C4−C3−C2	1.0(3)	0.34
C5−C6−C7	120.0(2)	120.41	C8−N2−C11−C14	56.1(3)	62.80
C2−C7−C6	119.5(2)	119.73	C8−N2−C11−C12	175.0(2)	-179.40
O2−C10−N1	123.81(19)	125.25	C8−N2−C11−C13	-68.1(3)	-61.25
O2−C10−C9	124.17(19)	123.09	O2−C10−C9−S1	178.7(2)	-179.93
N1−C10−C9	111.99(19)	111.64	N1−C10−C9−S1	-3.2(2)	0.22
C5−C4−C3	119.6(2)	120.07	C8−S1−C9−C10	5.38(18)	-0.84
C2−C3−C4	120.0(2)	120.24			

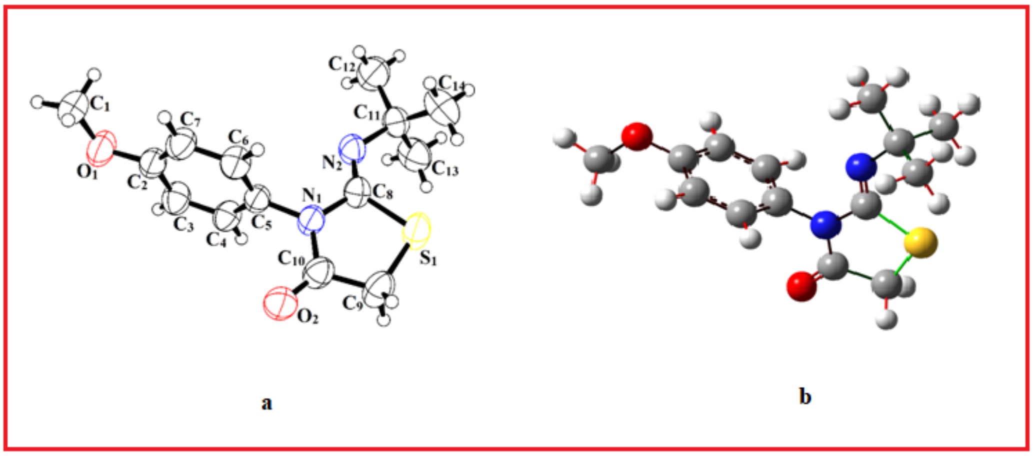

Figure IV.5. Molecular structure of TMTh (left) X-ray structure, (right) optimized structure using B3LYP/6-311G(d,p)

IV.5.2. Crystal packing, HS and RDG analyses

IV.5.2.1. Hydrogen Bonding

Hydrogen bonding plays a pivotal role in the stabilization of the crystal structure of the title compound, orchestrating the linkage of molecular chains along the b-axis in the unit cell. The crystal lattice is fortified by almost linear hydrogen bonding interactions, notably C–H•••O and C–H•••N intra- and intermolecular connections. The molecular conformation is intricately influenced by two weak intramolecular hydrogen bonds (C2–H22•••O1 and C2–H21•••N1), forming S(5) rings, as depicted in Figure 2 and Table 5. These interactions, where carbon atoms such as C2, C3, C5, C12, and C7 act as donors and oxygen and nitrogen atoms serve as acceptors, contribute significantly to the stability of the molecular packing. The hydrogen bond interactions are comprehensively presented in Table 5, and Figure 2 illustrates the diverse interaction types within the crystal structure. Figure 3 further reveals the molecular stacking facilitated by these hydrogen bonds, displaying the presence of eight molecules in the unit cell, consistent with the space group C2/c multiplicity. Examining the crystal packing, additional intermolecular interactions are identified, with a focus on C–H•••O and C–H•••S hydrogen bonds (Table 3) creating a three-dimensional framework in the crystal structure. Electronegative atoms S1, O1, and O2 engage in primary interactions, forming hydrogen bonds with H13B, H14A, H1A, H1B, H3, and H7 atoms. The carbon atoms (C13, C14, C1, C3, and C7) connected to this hydrogen atoms act as donors, while O1, O2, and S1 function as acceptors. The crystal packing also features π–π stacking interactions, [19,20] as evidenced by a centroid-to-centroid distance of 3.39 Å between thiazole rings of neighboring molecules, further contributing to the intricate and stabilized architecture of the title compound's crystal lattice.

Table IV.9. The possible hydrogen bonds within the EMTh molecule

D-H...A	D-H(Å)	D-A(Å)	H…A(Å)	D-H…A(Å)	Equivalent positions
C2-H21…N2	0.981	2.852	2.453	121.09	*x, y, z*
C2-H22…O1	0.962	3.817	2.582	126.23	*x, y, z*
C5-H51…O1	0.987	3.380	2.489	163.98	*(-x, y, -z+1/2*
C7-H7…O1	0.947	3.432	2.508	121.87	*(-x, -y, -z*
C5-H52…N2	0.955	3.370	2.514	119.7	*x, -y, z+1/2*

Table IV.10. The possible hydrogen bonds for TMTh molecule

D−H•••A	D−H(Å)	D−A(Å)	H•••A (Å)	D−H•••A(Å)	Equivalent positions
C13–H13B•••S1	1.08	3.437	2.752	121.09	*x,y,z*
C14–H14A•••S1	1.08	3.221	2.462	126.23	*x,y,z*
C3–H3•••O2	1.08	3.396	2.345	163.98	*x, –1/2,–y–1,+z*
C7–H7•••O1	1.08	3.57	2.88	121.87	*–x, +y+1/2,-z+1/2*
C1–H1A•••O2	1.08	3.425	2.75	119.7	*–x, +y+1/2,-z+1/2*
C1–H1A•••O1	1.08	3.655	2.695	147.83	*–x–1/2, –y–1/2, –z+1/2*
C1–H1B•••O2	1.08	3.399	2.517	138.23	*x–1/2,–y,+z*

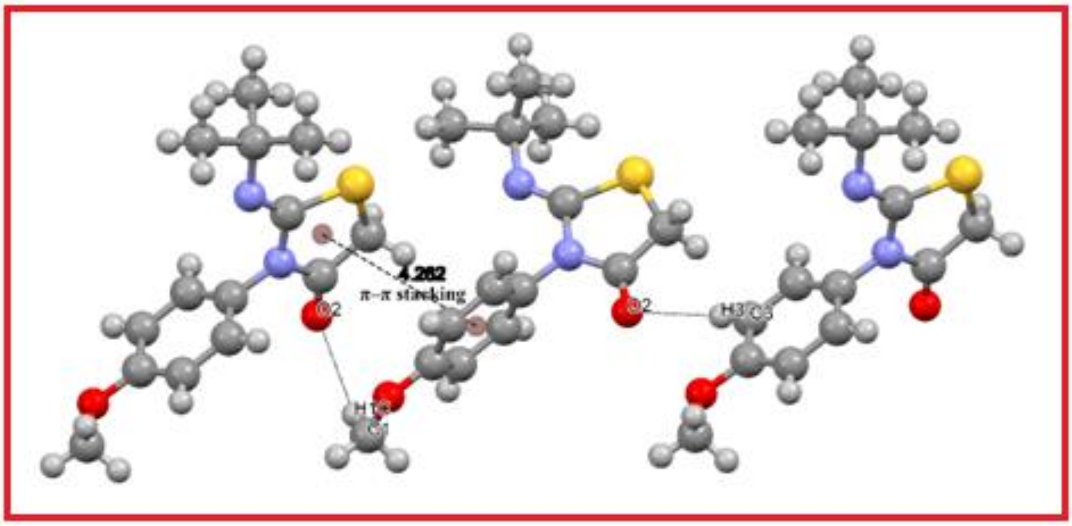

Figure IV.6. Crystal packing diagram viewed along the c axis with hydrogen bonds and π–π stacking interaction shown as dashed lines

IV.5.2.2. Hirshfeld Surface (HS) analysis

Hirshfeld Surface (HS) analysis serves as a powerful method for investigating intermolecular interactions, providing valuable insights into the crystalline environment of the title compound. [21]. This analysis, crucial for understanding crystal engineering, aims to assess the strength and significance of intermolecular contacts, thereby gauging their impact on crystal lattice stability based on the HS analysis equation, elucidating the d_{norm} (normalized connection distance), which is calculated from the atoms' *de*, *di*, and van der Waals radii ($r_i^{vdw}$and r_e^{vdw}):

$$d_{norm} = \frac{(d_i - r_i^{vdw})}{r_i^{vdw}} + \frac{(d_e - r_e^{vdw})}{r_e^{vdw}}$$

where d_e and d_i stand for, respectively, the internal and external distances from the site to the closest nucleus. The 3D-HS map and their related 2D fingerprint plots were obtained using the Crystal Explorer software [22] accepts a structure input file in the CIF format. The red regions represent shorter contacts with negative d_{norm} value and the blue regions represent longer contacts with positive d_{norm} value. The white regions represent van der Waals contacts with zero d_{norm} value (dnorm ≈ 0)[23, 21, 24]. Figure 9 presents the HS drawn for the EMTh crystal, emphasizing hydrogen bonding close contacts highlighted by dark green broken lines. Surfaces mapped over normalized contact distance (dnorm), curvedness, shape index, and de (distance from a point on the surface to the nearest nucleus outside the surface) offer comprehensive insights into the nature of interactions. The dnorm mapping discerned through a red–blue–white color scheme, reveals prominent hydrogen bonding interactions, particularly C–H···O and C–H···N, with the strongest interaction being the hydrogen bonding vdW between the methoxy group's oxygen and hydrogen atoms in thiazolidinone rings. This is evident as a bright red zone in the Hirshfeld surfaces (Fig. 10a). The qualitative and quantitative study of intermolecular close contacts is facilitated by the size and shape of the Hirshfeld surface, employing shape index and curvature to identify planar stacking arrangements. [25] The full fingerprint plot (Fig. 11) unveils the contribution of each interaction type, with H···H interactions dominating (49.1%), followed by O···H/H···O (16.8%), H···C/C···H (15.8%), S···H (9.5%), and N···H (4.7%). The percentage contributions, along with the comprehensive fingerprint plot, provide a detailed understanding of the intermolecular interactions shaping the crystal structure. The 3D-HS map for the TBMT, color-coded from -0.150 to 1.849 Å, reveals C–H···O and C–H···S hydrogen bonds, while the shape index surface depicts π–π stacking interactions. The 2D-fingerprint plots highlight the significant contributions of H···H (56.3%), H···O/O···H (16.9%), C–H/H–C (12.7%), C•••H/H•••C (12.7%), S···H/H···S (6.6%), and N···H/H···N (3.2%) to the HS. Overall, the Hirshfeld Surface and Fingerprint Analysis provide a comprehensive understanding of the intermolecular interactions governing the crystal structure of the title compound, offering valuable insights into its stability and packing arrangement.

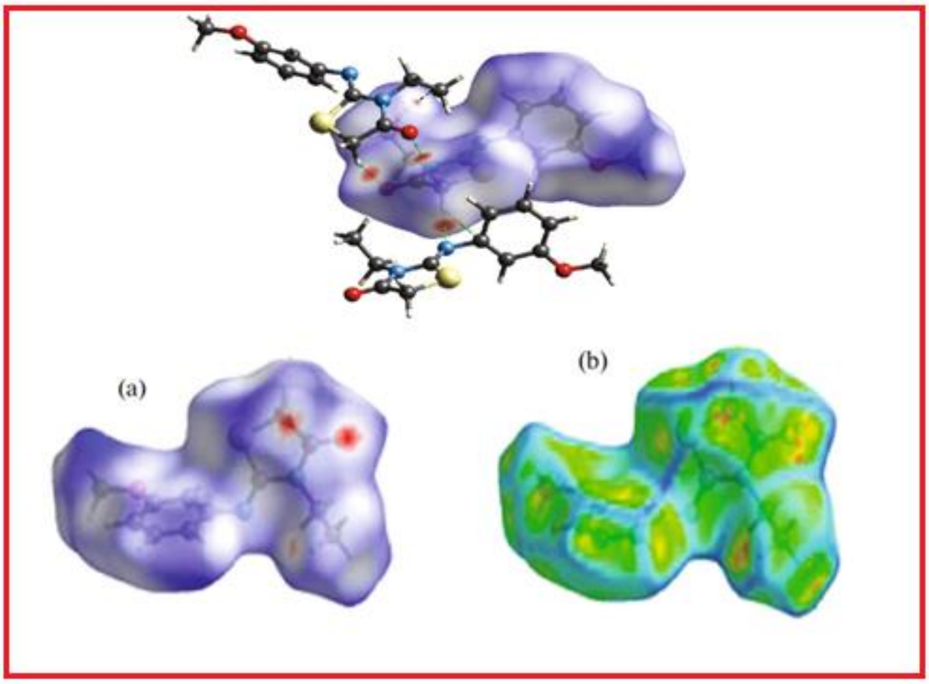

Figure IV.7. Hirshfeld surfaces for visualizing the intermolecular contacts of the EMTh compound: (a) d_{norm} Hirshfeld surface, (b) shape index and (c) d_{norm} selected intermolecular contacts.

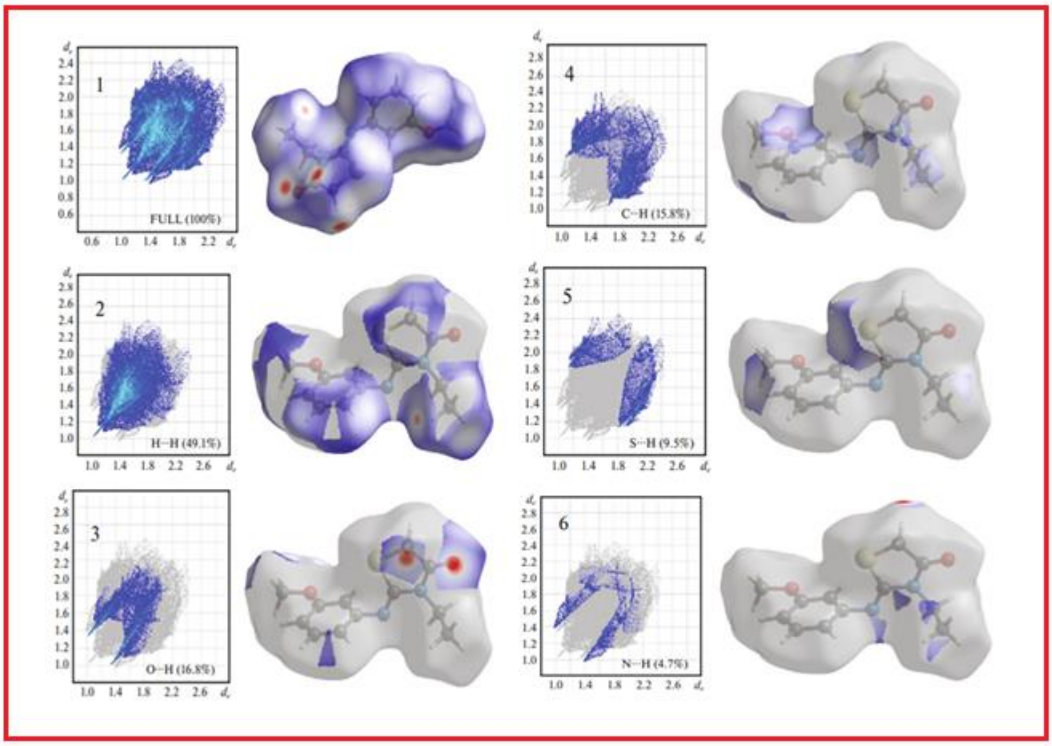

Figure IV.8. Fingerprint plots of the EMTh compound showing the most important interactions with their contributions

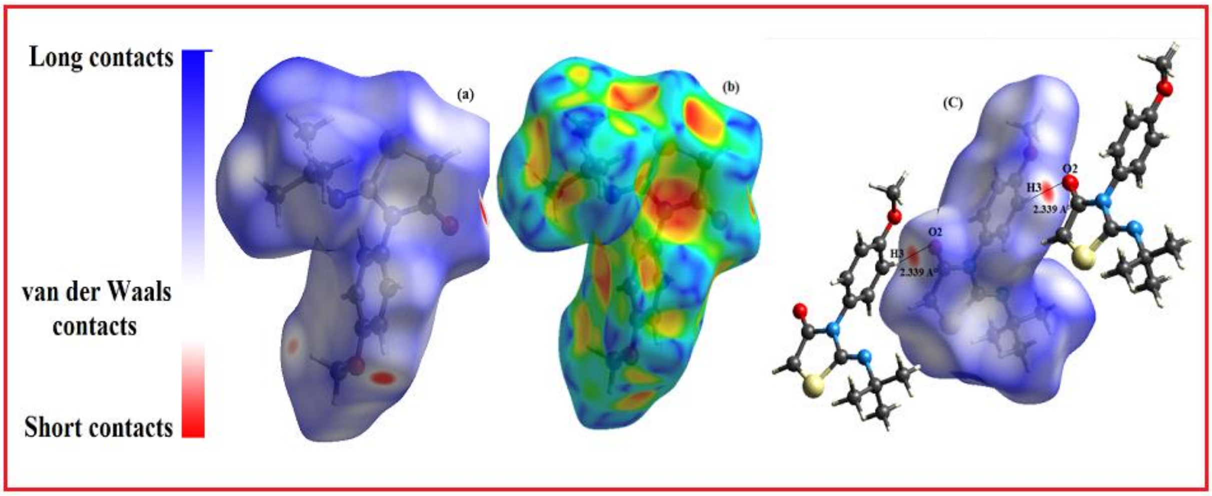

Figure IV.9. Hirshfeld surfaces for visualizing the intermolecular contacts of the TMTh compound: (a) d_{norm} Hirshfeld surface, (b) shape index and (c) d_{norm} selected intermolecular contacts

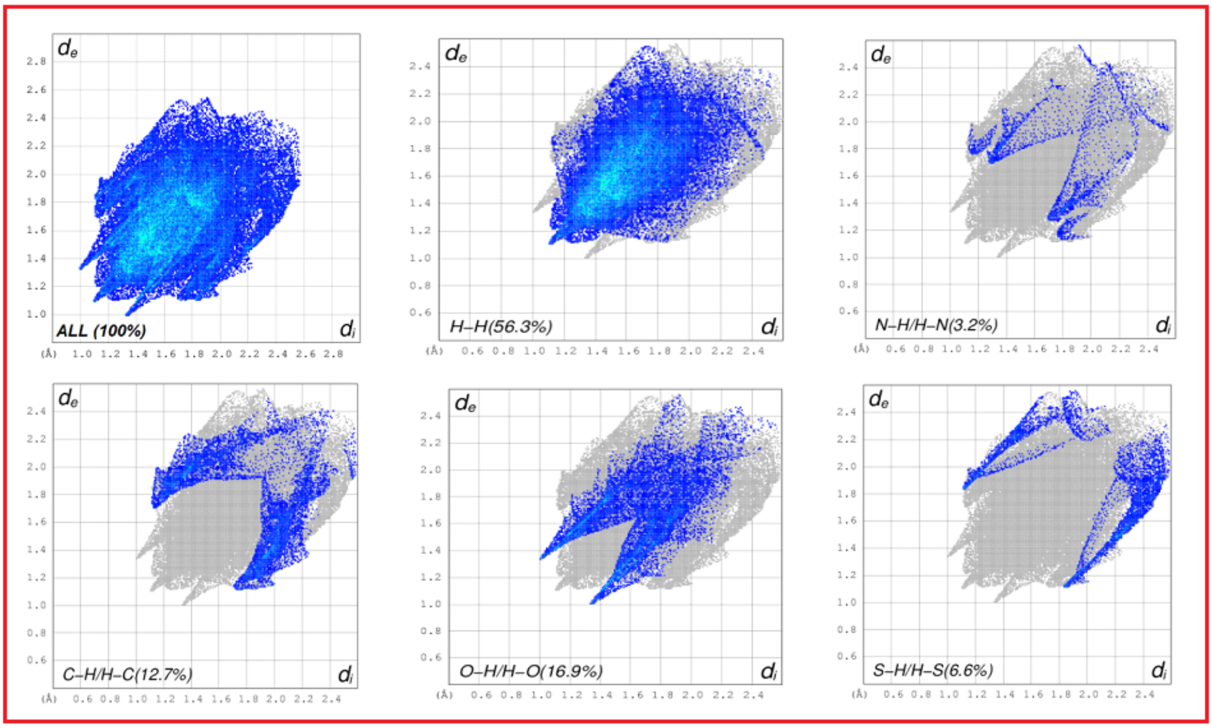

Figure IV.10. Fingerprint plots of the TMTh compound showing the most important interactions with their contributions

IV.5.2.3. Reduced density gradient analysis.

In our exploration of intra non-bonded interactions within the studied chemical system, we employed the Reduced Density Gradient (RDG) analysis, a valuable tool based on the electron density and its derivatives. The RDG equation, represented as

$$RDG(r) = \frac{1}{2(3\pi r^2)^{1/3}} \frac{|\nabla\rho(r)|}{\rho(r)^{4/3}}$$

, where ρ(r) is the electron density, and ∇ρ(r) is the gradient of ρ(r) at the point r, serves as a quantitative measure of the strength of noncovalent interactions, encompassing hydrogen bonding, steric effects, and van der Waals interactions [26]. The RDG assessment involves the use of software programs like Multiwfn and VMD to generate 2D scatter plots and 3D isosurface densities,[27, 28] offering visual representations of noncovalent interaction areas. Figure 7 depicts RDG functions against the product sgn(λ2) and ρ, where positive values of λ2 signify repulsive nonbonded interactions, negative values indicate attractive interactions, and the intermediate region corresponds to weak Van der Waals interactions. The color scale bar below Figure 7 represents the product sgn(λ2)ρ. The 3D isosurface in Figure 8 further visualizes the molecular interactions, with red regions indicating strong steric repulsion in centers of aromatic and thiazole rings, according to the color scale bar, green to light brown elliptical slabs between S1–C7 and N2–C3, denoting van der Waals interaction regions, and mixed red and green areas illustrating weak repulsive zones between O1–C2 and C2–N2 as well around C8–O2–C12 and C9. Notably, the absence of RDG surface blue indicates the lack of hydrogen bonds in the studied molecule.

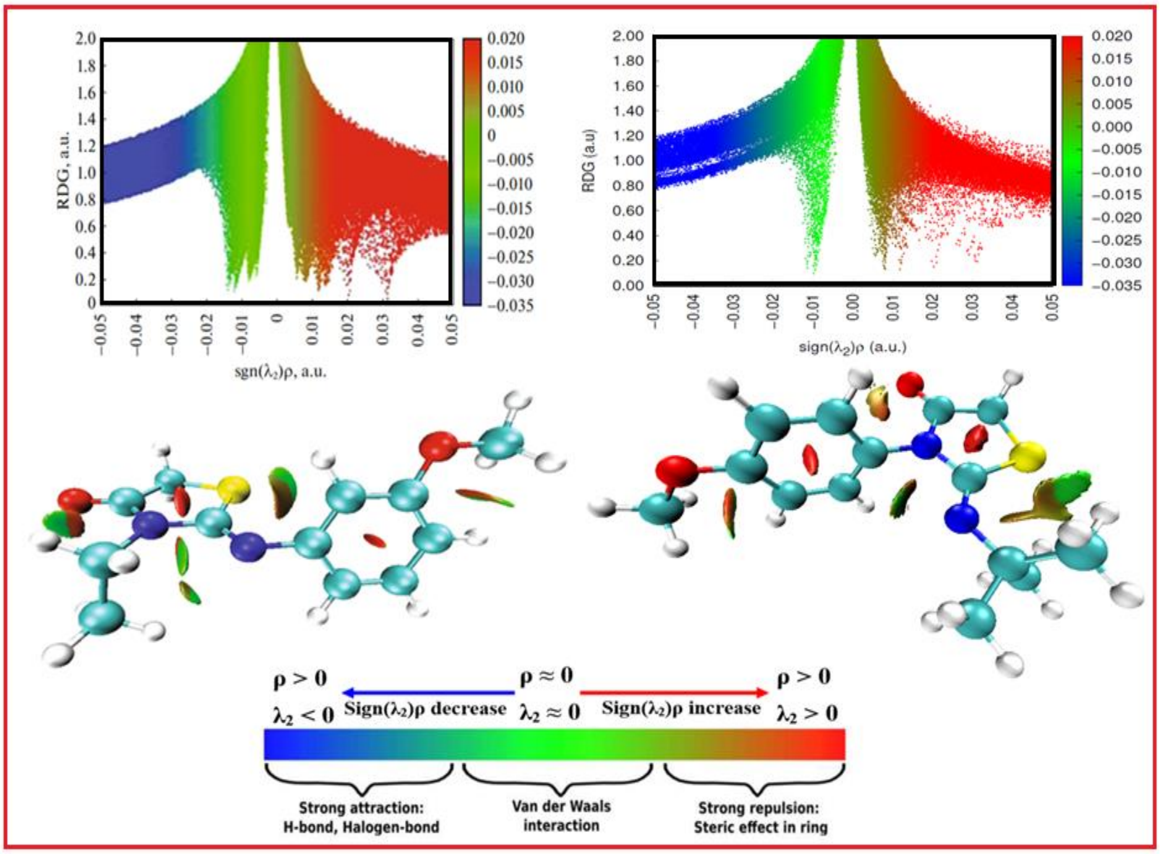

Figure IV.11. RDG graph and scatter map of EMTh and TMTh compounds

IV.5.2.4. Fukui functions:

The functions of Fukui may be accessed from the electronic densities of the N, N +1, and N 1 electron systems. From there, one can access the limps local, local electrophilic authorities, and canonical and large dual descriptors canonical depending on the type of population used (Mulliken, Hirschfeld, natural, or other) different values are obtained for the Fukui condensed indices. From the condensed Fukui indices, it is possible to construct the indices condensed corresponding to other local reactivity descriptors (local softness, authorities local electrophiles, dual descriptors)

The local reactivity descriptors, specifically Fukui functions, offer valuable insights into the reactivity patterns of molecules in terms of electron transfer [29]. The Fukui function, a key local reactive parameter, aids in assessing the reactivity and selectivity of organic molecules[30]. In this study, the Fukui function, employed through density functional theory (DFT), allows for the identification of electrophilic and nucleophilic sites within the molecule. [31]. Table 3 displays the Fukui function and local electrophilicity descriptor values for various atomic sites existing the EMTh compound, revealing that the S atom exhibits relatively high local reactivity descriptors, making it the most electrophilic center. Similarly, C4 and C8 display elevated values, indicating their susceptibility to electrophilic attacks. The Dual descriptors (Δf(k)) and local electrophilicity for each atomic site of the title chemical [32] (Morell et al., 2005) and it condensed form (Δ**ω**) are defined as follows:

$$\mathbf{\Delta f == f_k^+ - f_k^- \quad ; \quad \Delta\omega \ = \omega(f_k^+ - f_k^-) = \omega\Delta f}$$

If **Δf / Δω**> 0, the site is favored for a nucleophilic assault or the atom acts as an electrophile, whereas **Δf / Δω** < 0, the site is unlikely to be sensitive to a nucleophilic attack but may be favorable for an electrophilic attack. According to table 1.The signal +, − and 0, referring to nucleophilic, electrophilic, and radical reactions, respectively. During an electrophile–nucleophile interaction, the electrophile preferably interacts through its most electrophilic sites (those with high $\boldsymbol{\omega^-_k}$ values), and the nucleophile preferably interacts through its most nucleophilic sites [33]. The nucleophilic and electrophilic character of various atomic sites is detailed in Table 1 as follows: **C6 > H4 > C2 > O2 >H9B> C7> H9A> C12> C1 3B >C9 >C13> H13C > H14C.** The atomic sites which expose the electrophilic behavior are in the following order: **H14B > H8 > H5 > H14B > C14 > H2A > H13A > C5 > H4 > H3A H12C > C10 > S1 > C11 > H7 > H12B > H12A > N1 > C3 > N2 > O1,** with hydrogen atoms being electron-deficient and prone to nucleophilic attacks due to the higher electronegativity of surrounding carbon, oxygen, and nitrogen atoms. This study provides a comprehensive exploration of local reactivity, shedding light on potential reaction sites and contributing to a deeper understanding of the molecular behavior.

Table IV.11. Atomic charges, Fukui functions, local softness and local electrophilicity indices for atomic sites of (Z)-3-N- (ethyl)-2-N'-((3-methoxyphenyl) imino) thiazolidine-4-one using B3LYP/6-311G(d,p) level

Atom	**f^+_k**	**f^-_k**	**S^+_k**	**S^-_k**	**ω^+_k**	**ω^-_k**	**Δf**	**$\Delta\omega$**	**ΔS**
1C	-0,0938	-0,269	-0,0178	-0,051	-0,2214	-0,634	0,1752	0,4136472	0,0331128
2C	-0,0266	-0,062	-0,005	-0,012	-0,062	-0,141	0,0354	0,0835794	0,0066906
3C	-0,14	-0,271	-0,0266	-0,051	-0,331	-0,63	0,131	0,309291	0,024759
4C	0,1365	0,422	0,0269	0,08	0,32	0,995	-0,2855	-0,6740655	-0,0539595
5C	-0,301	-0,276	-0,057	-0,052	-0,72	-0,651	-0,025	-0,059025	-0,004725
6C	-0,137	0,281	-0,0259	0,053	-0,291	0,663	-0,418	-0,986898	-0,079002
7C	0,1285	0,1985	0,0242	0,037	-0,292	0,468	-0,07	-0,16527	-0,01323
8C	-0,12	0,4126	0,0779	0,078	0,269	0,972	-0,5326	-1,2574686	-0,1006614
9C	0,114	-0,1924	0,02	-0,036	0,188	-0,448	0,3064	0,7234104	0,0579096
10C	0,0805	0,0572	0,015	-0,01	0,195	-0,118	0,0233	0,0550113	0,0044037
11C	0,083	-0,1286	0,0157	-0,02	0,188	-0,302	0,2116	0,4995876	0,0399924
12C	-0,102	-0,0971	-0,0193	-0,018	-0,24	-0,229	-0,0049	-0,0115689	-0,0009261
13N	-0,361	-0,16	-0,068	-0,03	-0,85	-0,377	-0,201	-0,474561	-0,037989
14N	0,079	-0,4515	-0,015	-0,085	-0,18	-1,078	0,5305	1,2525105	0,1002645
15O	0,033	-0,383	0,0057	-0,07	0,077	-0,91	0,416	0,982176	0,078624
16O	-0,165	-0,363	-0,0312	-0,0686	-0,387	-0,858	0,198	0,467478	0,037422
17S	0,524	-0,415	0,099	-0,078	1,2371	-0,979	0,939	2,216979	0,177471

Table IV.12. Atomic charges, Fukui functions, local softness and local electrophilicity indices for atomic sites of TMTH compound using B3LYP/6-311G(d,p) level

Atom	f^0_k	f^+_k	f^-_k	**Δf**	ω^+_k	ω^-_k	**Δω**
S1	-0,1038	-0,1071	-0,1004	-0,0066	-1,3712	-1,2854	-0,0845
O1	-0,0609	-0,1044	-0,0173	-0,0871	-1,3366	-0,2215	-1,1151
O2	-0,0700	-0,0502	-0,0898	0,0396	-0,6427	-1,1497	0,5070
N1	-0,0045	-0,0197	0,0106	-0,0302	-0,2522	0,1353	-0,3866
N2	-0,0900	-0,1094	-0,0706	-0,0389	-1,4006	-0,9039	-0,4980
C1	-0,0488	-0,1105	0,0129	-0,1234	-1,4147	0,1653	-1,5799
C2	-0,0164	0,0137	-0,0465	0,0602	0,1754	-0,5953	0,7710
C3	-0,0478	-0,0646	-0,0311	-0,0335	-0,8271	-0,3982	-0,4289
C4	-0,0665	-0,0242	-0,1087	0,0845	-0,3098	-1,3917	1,0820
H4	-0,0229	-0,0255	-0,0202	-0,0053	-0,3265	-0,2586	-0,0679
C5	-0,0382	-0,0408	-0,0356	-0,0052	-0,5224	-0,4558	-0,0666
H5	-0,0261	-0,0267	-0,0256	-0,0011	-0,3419	-0,3278	-0,0141
C6	-0,0577	-0,0006	-0,1148	0,1143	-0,0077	-1,4699	1,4630
C7	-0,0071	0,0025	-0,0168	0,0193	0,0323	-0,2151	0,2474
H7	-0,0229	-0,0276	-0,0183	-0,0092	-0,3534	-0,2343	-0,1178
C8	-0,0904	-0,0798	-0,1010	0,0213	-1,0218	-1,2932	0,2723
H8	-0,0282	-0,0286	-0,0279	-0,0007	-0,3662	-0,3572	-0,0090
C9	0,0091	0,0114	0,0067	0,0047	0,1458	0,0863	0,0595
C10	0,0084	0,0052	0,0116	-0,0064	0,0666	0,1489	-0,0819
H9A	-0,0340	-0,0244	-0,0436	0,0192	-0,3124	-0,5583	0,2458
H9B	-0,0346	-0,0242	-0,0451	0,0210	-0,3099	-0,5775	0,2685
C11	-0,0069	-0,0105	-0,0032	-0,0072	-0,1344	-0,0410	-0,0922
H1A	-0,0068	-0,0073	-0,0062	-0,0011	-0,0935	-0,0794	-0,0141
H2A	-0,0242	-0,0255	-0,0229	-0,0026	-0,3265	-0,2932	-0,0333
H3A	-0,0013	-0,0042	0,0017	-0,0059	-0,0538	0,0216	-0,0755
C12	0,0117	0,0165	0,0069	0,0096	0,2114	0,0885	0,1229
H12A	-0,0190	-0,0263	-0,0116	-0,0147	-0,3368	-0,1485	-0,1882
H12B	-0,0186	-0,0253	-0,0120	-0,0133	-0,3240	-0,1537	-0,1703
H12C	-0,0254	-0,0285	-0,0222	-0,0062	-0,3650	-0,2843	-0,0794
C13	-0,0004	0,0018	-0,0027	0,0045	0,0230	-0,0346	0,0575
H13A	-0,0011	-0,0025	0,0003	-0,0028	-0,0320	0,0038	-0,0359
H13B	-0,0238	-0,0206	-0,0269	0,0063	-0,2638	-0,3445	0,0803
H13C	-0,0056	-0,0054	-0,0058	0,0004	-0,0692	-0,0743	0,0055
C14	0,0014	0,0004	0,0023	-0,0019	0,0056	0,0300	-0,0243
H14A	-0,0026	-0,0029	-0,0023	-0,0006	-0,0371	-0,0295	-0,0077
H14B	-0,0207	-0,0213	-0,0201	-0,0012	-0,2728	-0,2574	-0,0154
H14C	-0,0033	-0,0032	-0,0035	0,0003	-0,0410	-0,0448	0,0042

References

[1]. Bruker Analytical X-ray Systems, Inc. (2006). Apex2, Version 2 User Manual (M86–E01078). Madison, WI.

[2]. Siemens Industrial Automation, Inc. (1996). SADABS: Area-Detector Absorption Correction. Madison, WI.

[3]. Betteridge, P. W., Carruthers, J. R., Cooper, R. I., Prout, K., & Watkin, D. J. (2003). J. Appl. Crystallogr., 36, 1487. DOI: 10.1107/S0021889803021800

[4]. Palatinus, L., & Chapuis, G. (2007). J. Appl. Crystallogr., 40, 782–785. DOI: 10.1107/S0021889807029238

[5]. Sheldrick, G. M. (2008). A short history of SHELX. Acta Cryst A, 64, 112–122.

[6]. Sheldrick, G. M. (2015). Crystal structure refinement with SHELXL. Acta Cryst A, 71, 3–8.

[7]. Macrae, C. F., Edgington, P. R., McCabe, P., Pidcock, E., Shields, G. P., Taylor, R., Towler, M. (2006). Mercury: visualisation and analysis of crystal structures. J. Appl. Cryst., 39, 453–457.

[8]. Farrugia, L. J. (1997). ORTEP-3 for windows - a version of ORTEP-III with a graphical user interface (GUI). J. Appl. Crystallogr., 30, 565. DOI: 10.1107/S0021889897003117

[9]. Frisch, M. J., Trucks, G. W., Schlegel, H. B., Scuseria, G. E., Robb, M. A., Cheeseman, J. R., ... & Wallingford, CT. (2009). Gaussian 09, Revision A.02. Gaussian Inc.

[10]. Dennington, R. D., Keith, T. A., & Millam, J. M. (2008). GaussView 5.0.8. Gaussian Inc.

[11]. Yahiaoui, S., Moliterni, A., Corriero, N., Cuocci, C., Toubal, K., Chouaih, A., ... & Hamzaoui, F. (2019). J. Mol. Struct., 1177, 186–192. DOI: 10.1016/j.molstruc.2018.09.052

[12]. Khelloul, N., Toubal, K., Benhalima, N., Rahmani, R., Chouaih, A., Djafri, A., & Hamzaoui, F. (2016). Acta Chim. Slov., 63, 619–626. DOI: 10.17344/acsi.2016.2362

[13]. Wilson, A. J. C. (1995). International Tables for Crystallography. Kluwer, Dordrecht, vol C.

[14]. Gupta, R., & Chaudhary, R. P. (2013). J. Mol. Struct., 1049, 189–197.

[15]. Toubal, K., Boukabcha, N., Tamer, O., Benhalima, N., Altürk, S., Avcı, D., ... & Hamzaoui, F. (2017). J. Mol. Struct., 1147, 569–581. DOI: 10.1016/j.molstruc.2017.06.102

[16]. Boulakoud, M., Toubal, K., Yahiaoui, S., Chita, G., Chouaih, A., Djafri, A., & Hamzaoui, F. (2015). J. Struct. Chem., 56(7), 1373–1378. DOI: 10.1134/S0022476615070197

[17]. Nekrouf, A., Toubal, K., Megrouss, Y., Belkafouf, N. E. H., Djafri, A., Khelloul, N., ... & Djafri, A. (2022). J. Mol. Struct., 1262. DOI: 10.1016/j.molstruc.2022.133002

[18]. Belkafouf, N. E. H., Baara, F. T., Altomare, A., Rizzi, R., Chouaih, A., Djafri, A., & Hamzaoui, F. (2019). J. Mol. Struct. DOI: 10.1016/j.molstruc.2019.04.028

[19]. Djafri, A., Chouaih, A., Daran, J. C., Djafri, A., & Hamzaoui, F. (2017). Acta Cryst. E, 73, 511–514. DOI: 10.1107/S2056989017003218

[20]. Megrouss, Y., Triki-Baara, F., Boukabcha, N., Chouaih, A., Hatzidimitriou, A., Djafri, A., & Hamzaoui, F. (2019). Acta Chim. Slov., 66, 490–500. DOI: 10.17344/acsi.2019.5066

[21]. Khelloul, N., Toubal, K., Benhalima, N., Rahmani, R., Chouaih, A., Djafri, A., & Hamzaoui, F. (2016). Acta Chim. Slov., 63, 619. DOI: 10.17344/acsi.2016.2362

[22]. Wolff, S. K., Grimwood, D. J., McKinnon, J. J., Jayatilaka, D., & Spackman, M. A. (2012). Crystal Explorer 3.1. Univ. Western Austral., Perth, Australia.

[23]. Ayers, P. W., Yang, W., & Bartolotti, L. J. (2010). In P. K. Chattaraj (Ed.), Chemical Reactivity Theory: A Density Functional View. CRC, Taylor and Francis Group, Boca Raton.

[24]. Vafazadeh, R., Kazemi-nasab, A., & Willis, A. C. (2019). Acta Chim. Slov., 66, 1010. DOI: 10.17344/acsi.2019.5333

[25]. Bejaoui, L., Rohlíček, J., Eigner, V., Ismail, A., El Bour, M., & Ben Hassen, R. (2019). Acta Chim. Slov., 66, 603. DOI: 10.17344/acsi.2019.5002

[26]. Johnson, E. R., Keinan, S., Mori-Sanchez, P., Contreras-Garcia, J., Cohen, A. J., & Yang, W. (2010). J. Am. Chem. Soc., 132, 6498–6506.

[27]. Lu, T., & Chen, F. (2012). J. Comput. Chem., 33, 580. DOI: 10.1002/jcc.22885

[28]. Humphrey, W., Dalke, A., & Schulten, K. (1996). J. Mol. Graph., 14, 33.

[29]. Cerón, M., Gomez, T., Calatayud, M., & Cárdenas, C. (2020). J. Phys. Chem. A, 124, 2826. DOI: 10.1021/acs.jpca.0c00950

[30]. Yang, W., & Parr, R. G. (1985). Proc. Natl. Acad. Sci. USA, 82, 6723–6726. DOI: 10.1073/pnas.82.20.6723

[31]. Ayers, P. W., Yang, W., & Bartolotti, L. J. (2010). In P. K. Chattaraj (Ed.), Chemical Reactivity Theory: A Density Functional View. CRC, Taylor and Francis Group, Boca Raton.

[32]. Chattaraj, P. K., Giri, S., & Duley, S. (2011). Chem. Rev., 111, PR43–PR75.

[33]. Domingo, L., Aurell, M., Pérez, P., & Contreras, R. (2002). J. Phys. Chem. A, 106, 6871–6875. DOI: 10.1021/jp020715j.

Chapter V:

Spectroscopic analysis
of EMTh ($C_{12}H_{14}N_2O_2S$),
and TMTh ($C_{14}H_{18}N_2O_2S$) molecules

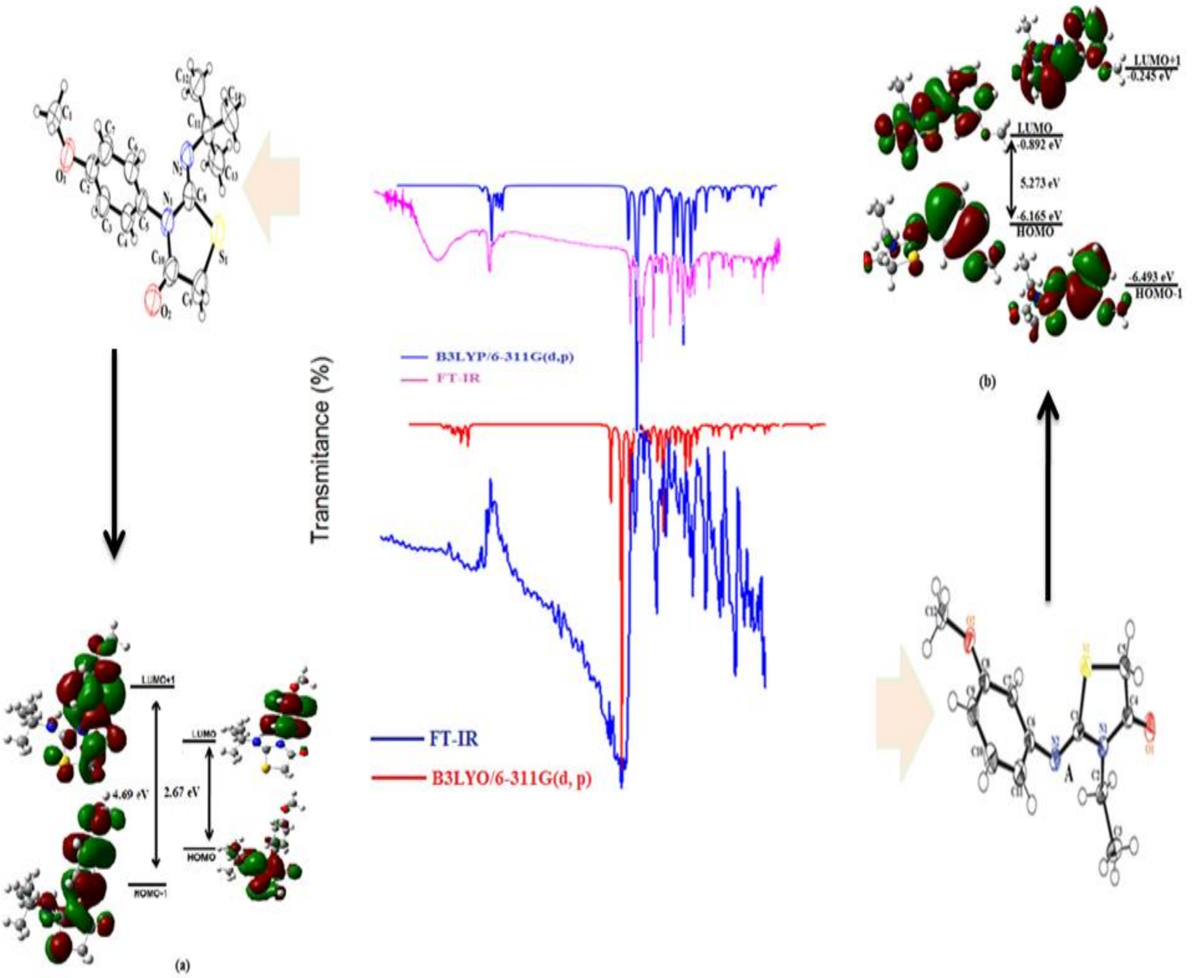

V.1. Introduction

Spectroscopic analysis methods assist in elucidating atom configurations in molecular structures, which can be the essential subject of a novel organic molecular crystal. These spectroscopic examinations are non-destructive physicochemical processes that are simple to perform experimentally. The EMTh and TMTh molecules were characterized experimentally by infrared, UV-Visible, and NMR. Molecular infrared (IR) spectrum (z)-3-n-(ethyl)-2-n'-(3-methoxyphenyl imino) thiazolidine-4-one was measured in the (500-4000cm-1) range on a Nicolet FT-IR 6700 spectrometer using KBr pellets. The molecule's spectra were captured using 1H NMR (500 MHz) and 13C NMR (125 MHz) in CDCl 3 solvent.On a Perkin-Elmer FT-IR spectrometer, the TMTh IR spectrum of a KBr pellet was recorded in the range 400–4000 cm^{-1}. The measured wavenumbers are reported in cm^{-1}. In DMSO-*d*$_6$ solvent at 25 °C, the ^{1}H and ^{13}C NMR spectra were measured using a Bruker AC-500 MHz spectrometer relative to TMS, which serves as internal standard, chemical shifts are reported as δ (ppm). Electronic UV–Visspectrum was recorded using a Shimadzu UV-2900 Pc-spectrophotometer in the range from 200 to 700 nm in chloroform solution. The theoretical Vibrational frequencies were calculated by the functional B3LYP accompanied by the potential energy distribution (PED) that was investigated by the VEDA 4 software for the assignments of the vibrational modes **[1]**. There was no negative frequency identified, confirming that the molecule's ideal geometry is located in a local minimum on the potential energy surface. Because the vibration frequencies computed by functional are greater than those measured experimentally for the majority of normal modes of vibration, the scaling factors **0.9679[2]**is employed for the hybrid functional B3LYP/6-311G (d,p) for the EMTh and TMTh molecules, respectively.. Additionally, ^{1}H and ^{13}C - NMR chemical shifts were calculated using the same level of theoryusing the method of invariant atomic Gauge orbitals (GIAO). [3] The resonance signals of the TMS's molecular structure were determined using the same type of calculation. The electronic spectrum, absorption wavelengths and oscillator strengths of the title compound were calculated using the TD-DFT method based on the previously optimized structure **[4]**.

V.2. Structural characterization by electron spectroscopy

V.2.1. Structural characterization for the (Z)-3-n-(ethyl)-2-n'-(3-methoxyphenyl-imino) thiazolidine-4-one

V.2.1.1. Vibrational frequencies assignments of (Z)-3-n-(ethyl)-2-n'-(3-methoxyphenyl-imino) thiazolidine-4-one

Using analytic second derivatives to validate the convergence to minima on the potential energy surface the fundamental frequencies of the studied molecule have been calculated. To understand the nature of these modes of vibration IR absorption spectroscopy based on DFT calculation. A theoretical analysis has been realized using B3LYP/6-311G(d,p) level of theory in gas phase. The probable assignments were performed by means of VEDA 4 program [1]. The vibrational frequencies obtained from B3LYP functional calculations have been scaled by a factor of 0.967 [5]. Table 2 shows the calculated (unscaled and scaled) and experimental frequencies of the title compound. Simulated and experimental IR spectra of (Z)-3-N-(ethyl)-2-N'-(3 methoxyphenylimino) thiazolidin-4-one are shown in Figure V. 1.The experimental fundamentals are in better agreement with the scaled fundamentals**.**

V.2.1.1.1. Carbon–hydrogen vibrations

In the aromatic compounds, multiple weak bands are exhibited in the region of 3100–3000 cm^{-1}[6]. They appear in this range of like multiple weak bands due to the stretching vibrations of C – H [7]. In the present work, the carbon-hydrogen of aromatic ring (C – H) stretching (νCH modes) was found in a range of 3000 and 3100 cm^{-1} using the B3LYP/6–311G(d,p) calculations. These modes involve exact contribution of >91% suggesting that they are pure stretching modes. The C - H stretching of aromatic ring showed symmetric modes at 3001, 3070 and 3080 cm^{-1} while asymmetric stretching mode is observed at 2989 cm^{-1}.

V.2.1.1.2. C=O and C=N Vibrations

Usually, the C=O stretching vibration mode can be easily observed as strong band in the region 1850-1550 cm^{-1} [8]. The π-π bonding between carbon and oxygen is responsible for forming a double bond between the carbon and oxygen atoms. The electronic distribution in this link is not equally because these atoms have different electronegativities. The lone pair of electrons on oxygen is responsible for the polar nature of carbonyl group. In the present study, the single C = O stretching vibration mode observed as a high intense peak in FT-IR at 1716 cm $^{-1}$whil calculated value shows at 1726 cm-^{1} with a PED 79%. The stretching frequency of the double bond C= N is perfectly observed at the high absorption 1640 cm $^{-1}$. DFT/B3LYP functional with 6-311G(d,p) basis set gives exactly the same value of 1640 cm^{-1} for the C=N vibration.

V.2.1.1.3. Thiazolidine ring vibrations

The C-S stretching vibration presents average bands in the region 1020 –1010 cm^{-1} [9]. In this paper C-S vibrations are observed in 704, 647 and 526 cm^{-1}. The examination of the theoretical results gives us the following values with their PED contribution, 720 (21%), 642 (10%), 522 (12%) and 482 (23%) respectively, which shows a good agreement between theoretical and experimental ones as shown in the Table 2. C-N vibration is a difficult task to identify since the appearance of several bands is possible in the region, Gunasekaran et al [10]. C-N stretching band have observed at 1312 cm^{-1}[11] and C-N assigned stretching vibration in the region 1350–1000 cm^{-1} for amines. In thiazolidine, C-N stretching band is found to be present at 1382 and 1307 cm $^{-1}$. The C-N stretching vibrations are expected to occur in the region 1200–1130 cm $^{-1}$ [12]. In our present work of title molecule FTIR bands are observed at 896 cm^{-1} and 1234 cm^{-1}, the theoreticallycalculated band at 940,1405, 1357, 1301, 1257, 1131are shifted down by scaling the previous values to 902 (10%), 1348 (13%), 1302 (46%), 1248 (12%), 1206 (16%), 1085 (15%), respectively with the percentage of the PED contribution indicated between brackets.

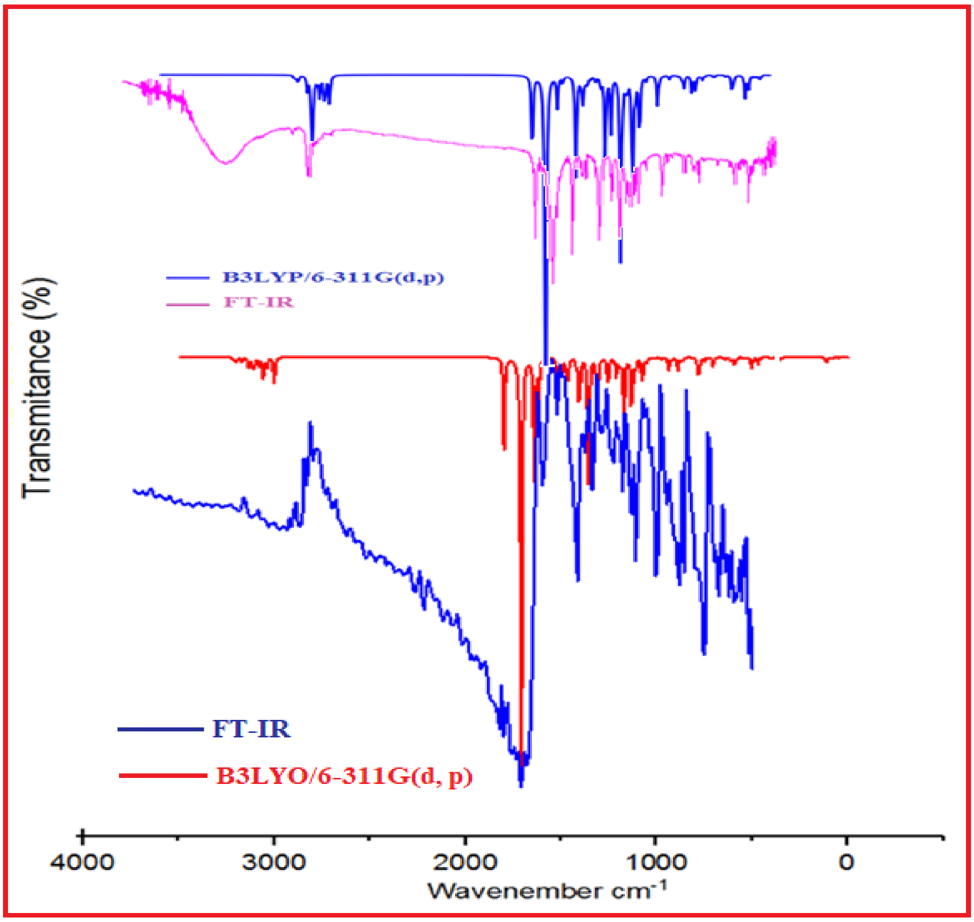

Figure V. 1. **C**omparison of FT-IR and calculated IR Spectra for EMTh and TMTh compounds

Table V. 1 Comparison of the calculated harmonic frequencies using B3LYP method 6-311G(d,p) basis set and experimental (FT-IR) wavenumbers (cm^{-1}) for (z)-3-n-(ethyl)-2-n’-(3-methoxyphenyl imino) thiazolidine-4-one

No.	Experimental	Unscaled	Scaled	IIR	Assignments with PED>10%
62		3209	3080.64	8.75	ν CH (91%) ar ring
61		3198	3070.08	0.77	ν CH (92%) ar ring
60		3127	3001.92	9.61	ν CH (100%) ar ring
59		3139	3013.44	9.25	ν CH (79%) + νas CH (11%)
58		3127	3001.92	0.33	ν CH (100%)
57	2971	3114	2989.44	13.61	νas CH (92%)
56		3001	2880.96	61.94	ν CH (92%)
55	1716	1798	1726.08	182.70	ν C=O (79%)
54	1640	1709	1640.64	943.72	ν N=C (73%)
53		1640	1574.4	329.64	ν CCasy (63%)ar rıng +δ HCC (14%) ar rıng
52		1617	1552.32	93.33	ν CC (51%)asyar rıng+δ HCC (11%) ar rıng+δ CCC (12%)ar rıng
51	1482	1518	1457.28	72.82	δ HCC asy (44%)ar rıng+δ CCC (19%) ar rıng
50		1508	1447.68	33.99	δ HCH (67%)+
49		1506	1445.76	3.59	δ HCH(71%)+ τHCCNasy (22%)th ring
48		1498	1438.08	8.56	δ HCH(71%)+ τHCCNasy (24%) th ring
47		1492	1432.32	7.71	δ HCHasy(69%)+ τHCOCasy(24%) ar rıng
46		1482	1422.72	0.82	δ HCH(48%)
45		1465	1406.4	40.95	ν CCasy (31%)ar rıng+ δ HCC (31%) ar rıng+ δ HCCasy(16%)
44		1462	1403.52	8.14	δ HCH (88%)
43	1391	1420	1363.2	18.06	δ HCC (13%)+ δ HCH (15%)+ τHCNC (46%)th ring
42		1405	1348.8	110.90	ν NC(13%)th ring+ δ HCC (10%)+ δ HCH (39%)+ τHCNCasy (10%) th ring
41		1401	1344.96	12.94	δ HCC (56%)+ δ HCH (14%)
40		1357	1302.72	247.21	ν NC(46%)th ring
39	1284	1350	1296	24.41	ν CCasy (59%)ar rıng+ δ HCC (23%)
38		1312	1259.52	111.70	ν COasy(79%) ar rıng+ δ HCC (37%) ar rıng
37	1234	1301	1248.96	13.79	ν CC (10%) ar rıng+ ν NCth(12%) ar rıng+ δ HCC (11%) ar rıng+ δ HCHasy(14%)
36		1257	1206.72	43.11	ν NCasy (16%)+ th ring +ν CO(13%) ar rıng+ τHCCN (12%)th ringasy

35		1253	1202.88	25.58	τHCSC asy(84%)th ring
34		1212	1163.52	40.44	δ HCHasy(15%)+ τHCOC(44%) ar ring
33	1148	1194	1146.24	22.35	ν CC (10%)ar ring+ δ HCC (38%) ar ring+ τHCOCasy(14%) ar ring
32		1172	1125.12	45.03	δ HCH(21%)+ τHCOC(35%) ar ring
31		1171	1124.16	101.55	δ HCCasy(13%) ar ring+ τHCOCasy(17%) ar ring
30		1148	1102.08	3.08	δ HCSasy(52%) th ring+ τHCSC(28%) th ring
29		1131	1085.76	146.72	ν NCasy (15%) th ring+ ν CC(11%) th ring
28		1111	1066.56	17.22	δ HCHasy(12%)+ δ CCNasy(13%) th ring+ τHCCN (36%)th ringasy
27		1109	1064.64	12.00	ν CC(14%) ar ring+ δ HCC(33%)ar ring+
26	1046	1075	1032	63.45	ν OC(55%) ar ring+ δ HCC(17%)ar ring
25		1007	966.72	0.82	ν CCasy (52%) ar ring+ δ CCCasy(39%)ar ring
24		973	934.08	4.63	ν CCasy (33%) th ring
23	927	968	929.28	0.03	τHCCC (77%) ar ring
22	896	940	902.4	27.82	ν NC(10%) ar ring+ ν OCasy(10%) ar ring+ ν CCasy (27%) th ring
21		922	885.12	7.21	δ HCS(45%) th ring+ τHCSC (21%) th ring+ τCCNCasy(19%) th ring+ γ OCNCasy(15%)
20		891	855.36	29.40	ν CCasy (12%) th ring+ δ NCNasy (10%)+ τHCCC (12%) ar ring
19		872	837.12	7.58	τHCCC (68%) ar ring
18		863	828.48	5.52	τHCCC (68%) ar ring
17	775	791	759.36	5.21	δ NCNasy (32%) th ring+τHCNC (33%) th ring
16		782	750.72	30.71	τHCCC (17%) ar ring+ τHCCCasy (17%) ar ring+τCCCCasy(29%) ar ring
15	740	779	747.84	20.41	δ CNC (27%) th ring
14	704	751	720.96	8.75	ν CCasy (10%) ar ring+ ν CC(10%) th ring+ ν SC(21%) th ring
13		705	676.8	22.45	τHCCCasy (56%) ar ring+ τCCCCasy(10%) ar ring
12	647	669	642.24	0.28	ν SC(10%) th ring+ τHCCCasy (12%) ar ring+ τCCCC(43%) ar ring
11	609	643	617.28	4.95	ν CC(28%) th ring+ δ CCCasy(11%)ar ring
10		617	592.32	4.44	γSNNC asy(54%)ar ring
9	584	610	585.6	5.88	δ CNCasy (11%) th ring
8		593	569.28	17.41	δ CCCasy (14%) ar ring+ γOCNC(19%) th ring
7		581	557.76	1.53	τHCSCasy (16%) th ring+ γOCNCasy (30%) th ring
6	526	544	522.24	3.20	ν SC(12%) th ring+ δ CCC (25%) ar ring+ τCCCC (12%) ar ring
5		503	482.88	23.21	ν SCasy (23%) th ring+ δ CCNasy(14%)ar ring

4	484	464.64	0.63	δ CNCasy(10%)ar rıng+ δ CCOasy(32%)ar rıng
3	471	452.16	16.37	δ CNCasy(19%) th ring+ δ CCNasy(16%) th ring+ δ CCOasy(12%) th ring
2	454	435.84	1.08	δ CCOasy(11%) ar rıng+ τCCCCasy (36%) ar rıng
1	403	386.88	2.62	δ CCC(12%) ar rıng+ δ COCasy (21%) ar rıng

ν : stretching(elongation); sy : symmetric; asy : asymmetric; β : in plane bending; γ : out–of plane bending, ω : wagging; τ : twisting; δ: bending; ρ: rocking; vibrational modes are based on potential energy distribution (PED) and only contributions over 10% are given; scaled frequencies are in unit of cm^{-1}; I_{IR} infrared intensities are in unit of km.mol^{-1}.

V.2.1.2. ^{1}H and ^{13}C NMR calculations

To calculate isotropic chemical shifts δ with respect to tetramethylsilane (TMS) $\delta^{x}_{iso}= \sigma^{TMS}_{iso} -\sigma^{x}_{iso}$ [13], isotropic shielding values 184.2796 and 32.2899 ppm of σ^{TMS}_{iso} are used for C and H NMR spectra, respectively. It is known that the range of ^{13}C-NMR chemical shifts for analogous organic molecules usually are >100 ppm [14, 15]. Methanol solvent has been used for chemical shift measurements. The atom labels were numbered according to Figure V. 2. Calculated and experimental values for ^{1}H and ^{13}C NMR have been collected in Table V. 2. In this research, aromatic carbons give signals in overlapped areas of the spectrum with chemical shift values from 106 to 170 ppm while experimental chemical shift values of aromatic carbon atoms are in the range107 to 160 ppm as they would be expected (Table V. 2).Carbon atoms (C1, C4 and C6) attached to the N atom have a larger chemical shifts through more electronegative property of the N atom which polarizes the electron distribution in its binding to the atomadjacent carbon and reduces the value of the chemical shifts.Usually, the chemical shifts obtained and calculated for the ^{1}H atoms of the methyl groups are quite weak. The maximum chemical shift value for all the hydrogen atoms is 7.24 ppm.

V.2.1.3. Frontier molecular orbitals (FMOs)

The highest occupied molecular orbitals (HOMOs) and the lowest unoccupied molecular orbitals (LUMOs) are named as frontier molecular orbitals (FMOs). The HOMO represents the ability to donate an electron, and LUMO as an electron acceptor represents the ability to obtain an electron [16]. The calculation of these parameters is very important because it allowed us to verify a lot of properties such as the kinetic stability and chemical reactivity. Figure V. 3 shows the atomic orbital HOMO–LUMO plot of the frontier molecular orbitals computed at B3LYP/6-311G (d, p) level for the title compound. As shown in Figure V. 3, in HOMO density, electrons are mainly located on the methoxyphenyl group. However, when an electron transmission occurs, the electron enters into the LUMO, and then the electron will mainly be localized on thiazole ring and carboxylic group. The positive phase is red and the negative one is green colour. The HOMO–LUMO energy gap of our molecule was calculated at the B3LYP/6-311G (d,p) level with HOMO energy = –6.165 eV, LUMO energy = –0.892 eV and HOMO–LUMO energy gap = 5.273 eV. The second highest occupied MO’s (HOMO−1) and the second lowest unoccupied MO’s (LUMO +1) were calculated using the same level of theory. 3D plots of the HOMO–1, HOMO, LUMO and LUMO+1 orbitals of the studied molecule are drawn in Figure V.3.

Table V. 2. Experimental and calculated ^{1}H and ^{13}C NMR data for (Z)-3-N-(ethyl)-2-N'-(3-methoxyphenyl imino) thiazolidine-4-one.

Chemical shifts		
^{1}H	Experimental	B3LYP/6–311G(d)
H_{51}	3.78	4.03
H_{52}	3.78	3.94
H_{21}	3.90	4.49
H_{22}	3.90	4.25
H_{31}	1.29	1.02
H_{32}	1.29	1.92
H_{33}	1.29	1.19
H_{9}	6.52	6.26
H_{7}	6.67	6.71
H_{11}	6.56	6.64
H_{10}	7.24	7.42
H_{121}	3.79	4.32
H_{122}	3.79	3.74
H_{123}	3.79	3.73
^{13}C		
C1	154.23	158.27
C2	32.76	37. 78
C3	12.52	15.06
C4	171.55	176.61
C5	38.26	37.57
C6	149.32	158.15
C7	110.39	113.89
C8	160.37	170.89
C9	107.22	106.29
C10	129.99	136.22
C11	113.20	120.10
C12	55.25	58.70

V.2.2. Structural characterization for (Z)-2N-(tert-butylimino)-3N'-(4-methoxyphenyl) thiazolidin-4-one

V.2.2.1 Vibrational frequencies assignments of (Z)-2N-(tert-butylimino)-3N'-(4-methoxyphenyl) thiazolidin-4-one

It is well known that infrared spectroscopy is a very powerful tool for identifying functional groups in a molecular system. To achieve this identification, the VEDA program **[1]** was used giving the total PED assignments based on the findings obtained by the theoretical calculation. The PED analysis indicates that the title molecule contains 36 atoms with 105 vibrational modes and the results are gathered in Table S1 along with the experimental frequencies. A comparison of the theoretical and experimental FT-IR spectra for TMTh is shown in Figure V.3. To minimize frequency discrepancies between experimental and theoretical vibration levels, a scaling factor of 0.96 was applied **[2]**. Usually, the C–H stretching vibrations in aromatic compounds are responsible for a number of weak bands that could be observed in the range 3100–3000 cm^{-1}**[6]**. The C–H stretching vibrations of the aromatic ring for TMTh were investigated to be located in the range of 3087 – 3064 cm^{-1} comparable with the experimental values between 3081 and 3054 cm^{-1}. In a molecular system, CH_3 and CH_2 functional groups are characterized by nine and six vibration modes, respectively. These modes are observed in the range 3000-2865 cm^{-1} and can be easily identified using the PED assignments [**17**]. As shown in Table S1, the calculated stretching vibrations in our current work are expected to be in the range 3013–2886 cm^{-1}. The bands between 1503 and 1488 cm^{-1} were assigned to the deformation modes for the CH_3 group. According to the literature findings, the C–C stretching vibrations can be appeared between 1300-800 cm^{-1}, and the C=C stretching vibrations occur in the region 1700-1500 cm^{-1}**[18]**. The stretching vibration of the aromatic C–C in TMTh appeared at 1591 cm^{-1} with a PED contribution of 15% identical to the published results [**18**]. The C=O vibrations occur in the region 1750 - 1650 cm^{-1} as indicated in the literature **[19]**. For the title compound, the C=O stretching vibrations were calculated between 1734 and 1657 cm^{-1} with their corresponding PED contributions of 65% and 20%. The calculated values of C–N stretching vibrations are 1319 (24%), 1164 (20%), 1123 (19%), and 592 (20%) cm^{-1}. These vibrations are usually found between 1300–1100 cm^{-1} [**20**]. The C=N stretching vibration bands are responsible for the vibrational modes in the range of 1650 and 1550 cm^{-1}. For TMTh, these vibrations are computed at 1657 cm^{-1} and obtained experimentally at 1624 cm^{-1}. The strong C–S stretching vibrations were identified using B3LYP functional at 955 and 633 cm^{-1}. The vibrations values at 1103 (53%) and 885 cm^{-1} (43%) present symmetric and asymmetric H-C-S bending. The same values indicate that there are H-C-S-C torsion vibrations with PED contribution of 26% and 18%. Furthermore, 565 (22%) and 92 cm^{-1} (21%) present H-C-S-C torsion vibrations confirming the existence of thiazolidinone moiety. Other improvements are shown at 827 (10%), 765 (17%) and 503 cm^{-1} (15%) indicating the N-C-S bending vibrations and conform the over large region at 1035-245 cm^{-1} for aliphatic and aromatic molecules [**21-23**].

Table V .3 Measured and calculated frequencies (cm^{-1}), IR intensity (km/mol) and probable assignments based on PED for TMTh

No.	experimental	B3LYP/6-311G(d.p)			Assignments with PED>10%
		Unscaled	Scaled	I_{IR}	
84	3081	3211	3087	5.38	νCH (59%) Ar ring +γHCH(22%)Ar ring
83	3077	3202	3078	4.28	νCH (64%) Ar ring +νCH (12%) Ar ring +νCH (16%) Ar ring
82		3192	3068	6.54	νCH$_{asy}$ (43%) Ar ring +γHCN (16%) Ar ring
81	3054	3187	3064	7.9	νCH (10%) Ar ring +νCHasy (28%) Ar ring +νCH (11%) Ar ring +νCH (15%) Ar ring
80		3134	3013	25.45	νCH (10%) +νCH (57%) + νCHasy (24%)
79		3126	3006	0.4	νCH (45%) Th ring +νCH (54%) Th ring
78		3111	2990	42.6	νCHasy (40%) +γHCH asy (12%)
77		3108	2988	26.73	νCH (13%) + νCHasy (12%) Ar ring+νCHasy (22%) +νCHasy (10%) +γHCC (13%)
76		3105	2985	16.14	νCH (36%) +νCH (20%) +νCH asy(10%)+νCH (13%)
75		3103	2983	76.01	νCHasy (10%) +νCH (14%) +νCH (31%)
74		3095	2975	4.24	νCH (10%) +νCHasy (10%) +νCH (36%)
73		3093	2974	2.73	νCH (15%) +νCH (22%)
72		3078	2959	11.79	νCH (99%) Th ring
71	2950	3061	2942	39.53	νCHasy (41%) +νCH (20%) +νCHasy (38%)
70		3037	2920	26.87	νCHasy (17%) +νCHasy (11%)
69		3030	2913	23.3	νCH (19%) +νCH (11%) +γHCH asy (10%)
68		3028	2910	17.11	νCH (22%) +νCHasy (12%) +νCH (35%)
67	1830	3002	2886	54.79	νCH (12%) +νCH (42%) +νCH (38%)
66	1755	1803	1734	158.88	νOC (65%) Th ring +νNCasy (19%) Th ring
65	1624	1724	1657	763.12	νOC (20%) Th ring +νNC (19%) Th ring +νNCasy(42%) Th ring +νNCasy (10%)
64		1655	1591	54.41	ν CC (14%) Ar ring +γCHC (20%) Ar ring+γCHC (19%) Ar ring
63	1568	1624	1561	14.41	νCH (26%) Ar ring +γCCH (12%) Ar ring
62	1494	1545	1486	193.68	γCHCasy (18%) Ar ring +γCHC (20%) Ar ring+γHCCasy(11%) Ar ring
61	1475	1520	1461	6.48	γHCCasy(13%)+τHCCC(17%)
60		1506	1448	46.77	γHCH (81%)
59		1503	1445	5.62	γHCH (13%) +τHCHCasy (20%) +τHCHC (30%)
58		1501	1443	4.05	γHCHasy (16%) +γHCC (10%) +τHCHC(25%)
57		1492	1435	8.34	γHCH (69%) +τHCHO (17%)
56		1489	1431	0.2	γHCCasy (11%) +γHCHasy (18%) +τHCCC (22%)
55		1488	1431	0.51	γHCHasy (22%) +OUT CCCH asy (19%)
54		1479	1422	17.17	γHCHasy (13%) +τHCHOasy (25%) +τHCHO (36%)
53	1419	1476	1419	0.85	γHCH (19%) +γHCCasy (10%) +τHCHC(23%)

52		1462	1405	6.04	γHCH (89%) Th ring
51		1451	1395	0.54	νCHasy (10%) Ar ring +γCCHasy (12%) Ar ring +γCCC (16%) Ar ring +γHCCasy (10%) Ar ring
50	1363	1429	1373	13.59	γHCHasy (12%) + γHCH (10%) +γHCHasy (14%)
49		1399	1345	12.44	γHCH (17%) + γHCCasy (16%) +γHCH (24%) +τHCHCasy (10%)
48	1326	1398	1344	9.64	νCH (18) +νCH (14%) +γHCHasy (16%)
47	1299	1372	1319	160.53	νNC (11%) +νNCasy (24%) Th ring
46	1288	1338	1286	97.06	νCHasy (11%) + νCHasy (17%) Ar ring +νCHasy (15%) Ar ring
45		1327	1276	0.57	νCH (10%) Ar ring +γCHC (11%) Ar ring +γCCHasy (12%) Ar ring +γCHCasy (10%) Ar ring +γHCC (12%) Ar ring
44	1251	1281	1231	314.97	νOC (42%) Ar ring
43		1269	1220	33.57	νCC (14%) +νNCasy (12%) Th ring + τHCHC (13%)
42	1214	1252	1204	13.52	τHCSCasy (76%) Th ring
41		1242	1194	10.34	νCH (20%) +τHCCCasy(17%)
40	1187	1241	1193	15.05	νCCasy (10%) +γCHC (13%)
39		1211	1164	213.53	νNCasy (20%) Th ring
38		1206	1159	10.48	γHCH (10%) +τHCHO (40%) +τHCHO (10%)
37		1193	1147	25.94	γCCH (11%) Ar ring +γHCH (15%) Ar ring
36		1171	1126	1.73	νOH (18%) +γCHOasy (36%) +τHCHOasy (29%)
35		1169	1123	117.76	νNC (19%) Th ring +γHCN asy (10%) Ar ring
34		1147	1103	0.41	γHCS asy (53%) Th ring+ τHCSC (26%) Th ring
33	1083	1130	1086	10.03	γCCH (31%) Ar ring +γCCC asy (10%) Ar ring +γHCCasy (11%) Ar ring
32	1038	1063	1022	52.27	νOH (53%) +γCHO (15%)
31		1051	1011	7.4	τHCCC (12%)
30	1001	1047	1006	0.63	νCCasy (31%) Ar ring +νCC (24%) Ar ring
29	990	1029	989	1.61	νCC (31%) Th ring
28		993	955	8.37	νCH (10%) +τHCHCasy (11%) +τHCSCasy (13%) Th ring
27		963	926	0.01	τHCCC (18%) Ar ring +τCCHC (40%) Ar ring +OUT CCCH (15%) Ar ring
26	915	960	923	0.73	νCHasy (11%) + γHCC (17%) +γHCH (10%) +τHCCCasy (12%)
25		942	906	1.87	τHCHC (10%) Ar ring +τHCCC asy(10%) Ar ring +τCCHC (44%) Ar ring
24	896	922	887	0.76	νCC (29%)
23		921	885	4.24	νCH (10%) + νCHasy (10%) + νCH asy(10%) +γHCHasy (13%)
22		921	885	2.74	γHCS (43%) Th ring +OUT OCNC asy (14%) Th ring +τ HCSC (18%) Th ring + OUT CCCN asy (11%) Th ring
21		906	871	24.18	νNC (26%)
20	821	860	827	33.38	νCC (12%) Ar ring +γNCS (10%) Th ring
19		838	805	31.24	τHCCC (20%) Ar ring +τOCHC (14%) Ar ring
18		812	781	2.04	τHCCC (13%) Ar ring +τOCHCasy (13%) Ar ring +τCCHCasy (13%) Ar ring +τCCHCasy (10%) Ar ring + OUT CCCH (30%) Ar ring
17	747	796	765	9.63	νCH asy (11%) +γCCNasy (23%) Th ring +γ CNC (10%) Th ring+γNCS (17%) Th ring
16	739	780	750	1.47	γCCN asy (16%) Th ring +γ NCN (17%) Th ring
15	691	750	721	0.44	ν CC (14%) + ν CC (15%)

14	672	728	700	5.74	τ HCHC (23%) Ar ring
13	653	658	633	2.95	ν CC asy (18%) Ar ring +γ CCC (24%) Ar ring
12		623	599	21.78	ν NC asy (13%)
11		616	592	10.67	ν NC (20%) Th ring +γ CNC (10%) Th ring +γ CCN asy (11%)
10		609	585	5.36	OUT OCNC (44%) Th ring +OUT CCCNasy (27%) Th ring
9	560	588	565	0.21	τ CNCN (11%) Th ring + τ HCSC asy (22%) Th ring + OUT OCNC (20%) Th ring +OUT SNNC asy (23%) Th ring
8	541	545	523	39.74	ν NC (10%)
7		525	505	9.4	τHCHC (11%) Ar ring +τHCHCasy (15%) Ar ring
6	515	523	503	16.88	νNCasy (10%) +γ CCN (10%) Th ring +γNCS (15%) Th ring
5		492	473	4.44	γNCH asy (22%) + τCNCN asy (11%) Th ring
4		473	455	4.41	γOCH (10%)Ar ring +γ HOC asy (11%) Ar ring
3		455	438	9.13	γOCC (15%) Th ring
2		430	413	0.03	OUT CCCCasy (88%) Ar ring
1		408	392	0.58	γHCNasy (18%) Ar ring +OUT OCNC (12%) Th ring +OUT CCNCasy (21%)

ν: stretching(elongation); sy: symmetric; asy: asymmetric; β: in plane bending; γ: out-of-plane bending. ω: wagging; τ: twisting; δ: bending; ρ: rocking; vibrational modes are based on potential energy distribution (PED) and only contributions over 10% are given; scaled frequencies are in unit of cm^{-1}; I_{IR} infrared intensities are in unit of km mol^{-1}.Th Ring: Thiazolic ring (N1-C8-C9-C1-0S1); Arring : Aromatic ring (C2-C3-C4-C5-C6-C7).

V.2.2.2. ^{1}H and ^{13}C-NMR chemical shifts

To perform the NMR spectroscopic analysis, the ^{1}H and ^{13}C isotropic chemical shifts can be calculated using the DFT along with the GIAO methods. In this work, the theoretical ^{1}H and ^{13}C NMR isotropic chemical shifts (ppm) are computed using chloroform as solvent and the corresponding results are summarized in Table 4 together with the experimental chemical shifts that were measured in the same solvent. The experimental ^{1}H and ^{13}C NMR spectra are given in Figure S4 (a,b) as supplementary materials. According to the architecture of the title compound, the ^{1}H isotropic chemical shifts are measured in the range 1.20–7.11 ppm and the corresponding chemical shifts are calculated between 0.79 and 7.36 ppm. Usually, aromatic protons have chemical shifts between 6.00 and 8.00 ppm [24], which is the case for the title compound. Indeed, the observed signals for H3 and H7 are 6.95 ppm, and for H4 and H6 are 7.08 and 7.11 ppm, respectively. The corresponding calculated values are 7.36 ppm for H3 and H7, and 7.21 ppm for H4 and H6 related to previous findings [2**5**]. The methylene protons of the thiazolidinone ring present a singlet signal at 4.10 ppm (3.77 ppm with DFT). The methyl protons of C12, C13 and C14 atoms have a single experimental chemical shift value (1.20 ppm), and the corresponding theoretical values are in the range 0.79−1.89 ppm. For the methyl protons attached to C1, the experimental chemical shift value is about 3.77 ppm and the calculated values are 3.62 and 4.10 ppm. These values are different from the previous methyl protons due to the directly linked electronegative oxygen atom. As can be seen from the above results, the difference between the experimental and theoretical values can be explained by the effect of the electronic environment of the considered atom.

To identify the carbon atoms present in the title molecule, the ^{13}C NMR remains the most suitable technique. The ^{13}C NMR chemical shifts for TMTh were obtained experimentally and theoretically. As can be seen in Table 4, the structure of TMTh contains 14 carbon atoms where all their chemical shifts are reported. It is well known that aromatic carbon atoms typically have ^{13}C NMR chemical shifts above 100 ppm [26]. As a result, the experimental and theoretical chemical shifts of aromatic carbons for TMTh have values greater than 100 ppm which shows the good quality of the recorded ^{13}C NMR data. The heterocyclic ring carbons show resonance values at 158.90 (experimental) and 156.05 (theoretical) for C8 atom, and 171.04 (experimental) and 175.94 (theoretical) for C10 atom. These two values are greater than the resonance of the other carbons due to the electronegativity of neighboring atoms (O, S and N). For the four methyl moieties of TMTh, the corresponding ^{13}C-NMR signals appeared at 55.69 (C1) and 29.59 ppm (C12, C13 and C14), and the calcultated values are 60.99, 26.91 and 26.32 ppm, as can be seen in

Table 4. The C9 atom of the methylene group shows experimental signal at 33.44 ppm and theoretical signal at 37.24 ppm. Referring to the above results, good consistency can be observed by comparing experimental and theoretical chemical shifts.

Table V. 4 Experimental and calculated ^{1}H and ^{13}C NMR chemical shifts (ppm) for TMTh

^{1}H	Experimental	B3LYP/6–311G(d.p)
H1A	3.77	4.10
H1B, H1C	3.77	3.62
H3, H7	6.95	7.36
H4	7.08	7.21
H6	7.11	7.21
H9A, H9B	4.10	3.77
H12A	1.20	0.79
H12B, H12C	1.20	1.15
H13A, H13C, H14A, H14C	1.20	0.92
H13B, H14B	1.20	1.89
^{13}C	Experimental	B3LYP/6–311G(d.p)
C1	55.69	60.99
C2	147.19	146.30
C3, C7	129.17	129.65
C4	114.20	118.04
C5	130.03	132.89
C6	114.20	116.04
C8	158.90	156.05
C9	33.44	37.24
C10	171.04	175.94
C11	54.33	60.82
C12	29.59	26.91
C13, C14	29.59	26.32

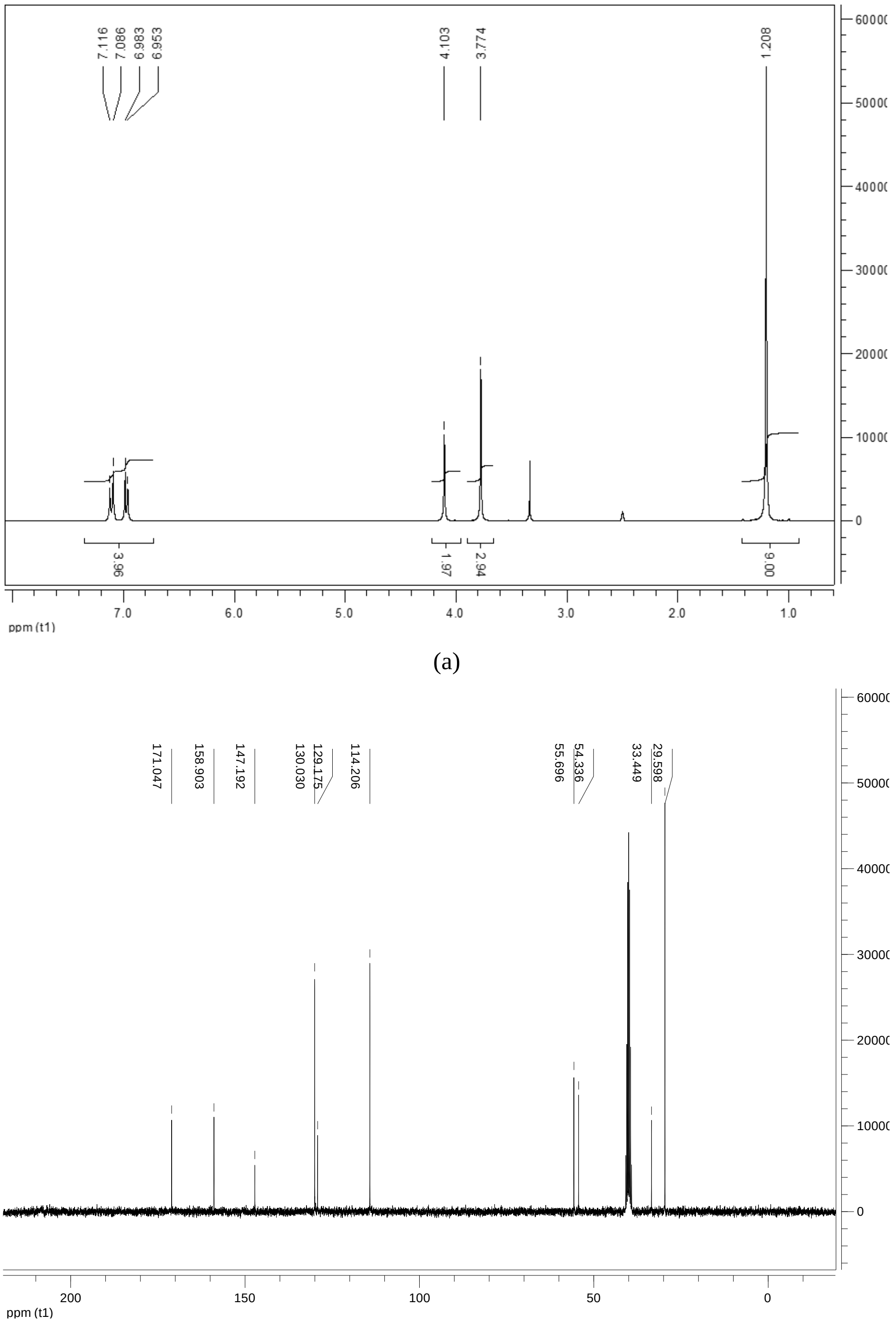

(a)

(b)

FigureV.2. Experimental NMR spectra ^{1}H (a) and ^{13}C (b) for TMTh

V.2.2.3. Absorption effect and frontier molecular orbitals (FMOs)

In the 1950s, K. Fukui developed the frontier orbital theory, which attempts to explain the regioselectivity seen in reactions involving aromatic compounds. Since then, it has been extended to all π and σ systems. According to Fukui's original theory, electrons from the nucleophiles' highest occupied molecular orbital (HOMO) are primarily responsible for charge transfer in a reaction between an electrophile and a nucleophile. Selectivity and reactivity can be explained by this electronic density, which is a frontier. Since then, the theory has been expanded to include all systems π and σ.

In the present work, the absorption effect was investigated using UV-Visible spectroscopy that remains the most important technique for studying conjugated molecules as well as electron delocalization in molecular structures. As long as the molecular structure has delocalization, the wavelength of maximum absorption shifts increases [**27**]. Figure S5 displays the experimental and theoretical UV-Visible spectra of the TMTh molecule. The experimental spectrum was recorded using an absolute ethanol solvent at room temperature, while the theoretical spectrum was calculated by TD-DFT/B3LYP method with 6-311G(d,p) basis set. The theoretical calculations were carried out to determine the excited states in the title compound structure. The vertical excitation energies, oscillator strength (*f*) and wavelength are calculated in gas phase using the same level of theory. The corresponding results are depicted in Table 5. The strong transitions were reported at 4.9810 eV (248.92 nm) with oscillator strength f = 0.0345 and 5.0018 eV (247.88 nm) with oscillator strength f = 0.0152. The calculated absorption wavelength with a maximum value corresponds to the electronic transition from HOMO to LUMO and having a contribution around 62%. As can be seen in Figure S5, the significant absorption peak at 250 nm correlates to the observed spectral peak at 248.9 nm. A strong $\pi \rightarrow \pi^*$ transition with a high attenuation coefficient in the UV-Visible range is expected due to the molecular structure. The maximum UV-Vis absorption wavelength in the spectrum is due to the influence of $\pi \rightarrow \pi^*$ electronic transition. The transition excitation energies are in good agreement with the experimental measurements.

On the other hand, the study of FMOs, known as the HOMO and LUMO, is conducted to better understand the reactivity and kinetic stability as well as the molecular bioactivity. The HOMO (highest occupied molecular orbital) and LUMO (lowest unoccupied molecular orbital) parameters are critical in quantum chemistry calculations for electronic studies [**28**]. The HOMO energy defines the capacity to donate an electron, the LUMO energy characterizes the ability to acquire an electron, and the gap between the two characterizes the molecule's chemical stability. Furthermore, the HOMO energy is proportional to the ionization potential, whereas the LUMO energy is proportional to electron affinity. The overlapping of these orbitals can produce the charge transfer **[29]**. The FMOs of the title compound are determined and the corresponding surfaces are depicted in Figure 3. As can be seen in this figure, the methoxyphenyl groupment is mostly dominated by the molecular orbitals HOMO-1, LUMO, and LUMO+1, whereas the HOMO orbital is entirely located on the thiazolidinone and tert-butylimino fragments, demonstrating the possibility of charge transfer between the methoxyphenyl and the thiazolidinone groups.

The difference in energy between HOMO and LUMO is calculated to be 2.67 eV, emphasizes the kinetic stability of the molecule under consideration. On the other hand, the molecular orbitals composition can be displayed by the total density of states (TDOS) [**30**]. Figure S6 shows the DOS diagram forTMTh. The red and green lines show the virtual and occupied orbitals. From the DOS diagram, it is evident that the donor (thiazole ring) and acceptor (phenyl ring) groups have a simultaneous effect on electron delocalization.

Table V. 5 Experimental and theoretical electronic transitions, oscillator strength and major/minor contributions for TMTh.

Electronic transitions	Exp.λ_{max} (nm)	TD-DFT/B3LYP-6311G(d, p)			
		λ_{cal} (nm)	Energy (eV)	Oscillator strength (f)	Assignments (major contributions ≥ 10%)
S0-S1	250	248.92	4.9810	0.0345	H→L(62%)+H→L+1(12%)
S0-S2		247.88	5.0018	0.0152	H→L+1(60%)+H-2→L(14%) +H→L(11%)
S0-S3		240.07	5.1644	0.0099	H-2→L (39%)+H-2→L+1(23%) +H→L(14%)+H→L+1(12%)
S0-S4		232.76	5.3267	0.0877	H→L+2(31%)+ H-1→L+2(23%) +H-1→L(18%) +H-1→L+3(13%)
S0-S5		228.98	5.4147	0.1555	H→L+2(36%)+ H-1→L+2(19%) +H-1→L +3(17%)
S0-S6		227.48	5.4503	0.0644	H-1→L(52%)+H-1→L+1 (29%)
S0-S7		222.74	5.5664	0.0401	H-5→L(29%)+H-2→L+2(15%) +H-2→L+1(14%)+H-5→L+1(13%)
S0-S8		219.59	5.6462	0.0077	H-1→L+1(43%)+ H-1→L(20%) +H-1→L+2(14%)
S0-S9		218.63	5.6710	0.0631	H-2→L+1(35%)+ H-2→L(33%)
S0-S10		214.02	5.7931	0.0191	H-2→L+2(55%)+ H→L+3(11%)

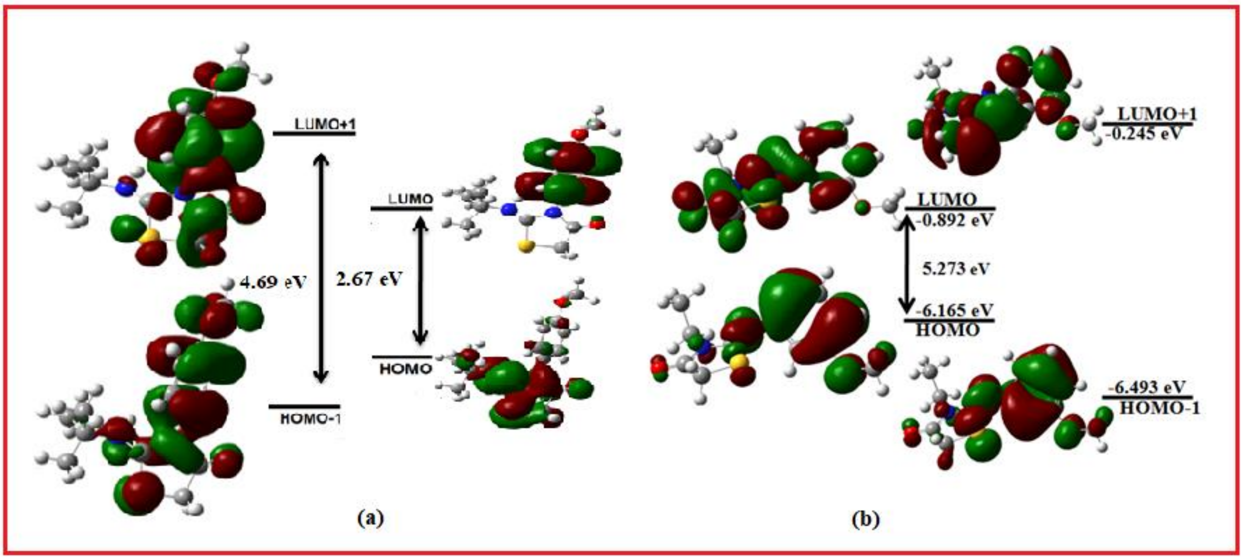

Figure. V. 2. Theoretical frontier molecular orbitals for EMTh and TMTh.

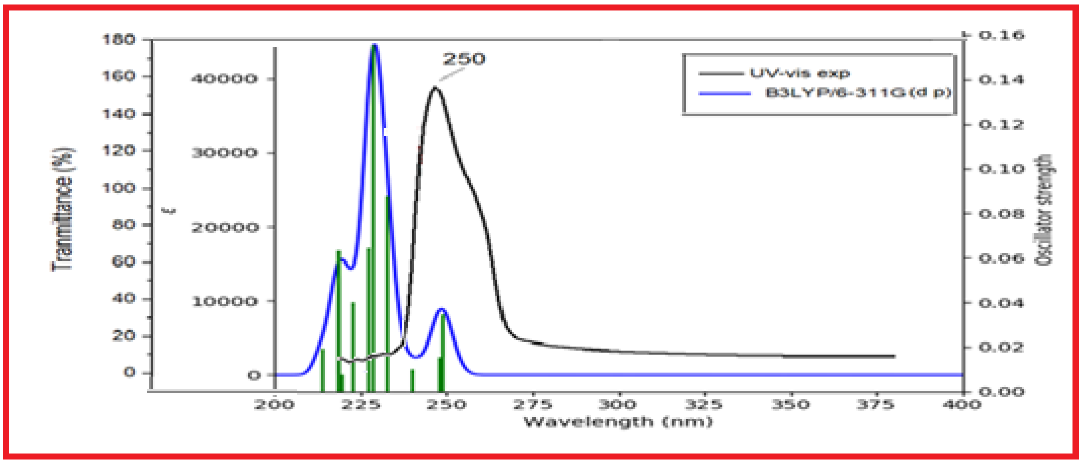

Figure V.3. Superposition of the experimental UV-Visible spectrum with the theoretical TMTh spectrum.

V.3. Conclusion

The study investigates the structural properties of the compound (Z)-3-N-(ethyl)-2-N'-(3-methoxyphenyl imino) thiazolidine-4-one using electron spectroscopy. It comprehensively examines the compound's fundamental frequencies by analyzing second derivatives and conducting Density Functional Theory (DFT) calculations at the B3LYP/6-311G(d,p) level in the gas phase. The acquired infrared (IR) spectra exhibit substantial conformity with scaled fundamentals, specifically highlighting carbon-hydrogen oscillations inside the aromatic ring. The bands of C=O and C=N vibrations that result from "- bonding" are noticeable. The vibrations of the thiazolidine ring and C-S bonds are also examined, revealing a remarkable agreement between the theoretical and experimental results. Furthermore, the utilisation of isotropic shielding values and chloroform as a solvent in 1H and 13C Nuclear Magnetic Resonance (NMR) calculations allows for precise estimates of chemical shifts. The study looks more closely at the Frontier Molecular Orbitals (FMOs), especially the Highest Occupied Molecular Orbitals (HOMOs) and Lowest Unoccupied Molecular Orbitals (LUMOs), to find out how stable the molecules are and how they react with other chemicals. The work specifically focuses on the use of UV-visible spectroscopy to examine the absorption phenomenon, which is essential for understanding conjugated molecules and the dispersion of electrons. Collectively, the investigations provide a thorough comprehension of the compound's structural, spectroscopic, and electrical properties, which can lead to valuable insights regarding its potential bioactivity and reactivity.

References

[1] A.D. Becke, Density-functional thermochemistry. III. The role of exact exchange, J. Chem. Phys. 98 (7) (1993) 5648–5652, https://doi.org/10.1063/1.464913.

[2] R.D. Johnson III, NIST computational chemistry comparison and benchmark database, NIST Stand. Ref. Database Number 101, Release 18 (2016). http ://cccbdb.nist.gov/.

[3] K. Wolinski, J.F. Hinton, P. Pulay, Efficient implementation of the gaugeindependent atomic orbital method for NMR chemical shift calculations, J. Am. Chem. Soc. 112 (1990) 8251–8260

[4] O. ¨ Tamer, N. Dege, G. Demirtas ̧, D. Avcı, Y. Atalay, M. Macit, S. S ̧ ahin, Crystal structure and spectroscopic characterization of (E)-2-(((4-bromo-2- (trifluoromethoxy)phenyl) imino)methyl)-4-nitrophenol: a combined experimental and computational study, J. Mol. Struct. 1063 (2014) 295–306, https://doi.org/ 10.1016/j.molstruc.2014.01.079.

[5] S. P. V. Chamundeeswari, E. R. J. J. Samuel, N. Sundaraganesan, Eur. J. Chem. 2011, 2, 136–145. DOI: 10.5155/eurjchem.2.2.136-145.169

[6] A. Eşme, S. Güneşdoğdu Sağdınç, Spectrochim. Acta A Mol. Biomol. Spectrosc. 2018, 188, 443–455, https://doi.org/10.1016/j.saa.2017.07.034

[7] G. Muhammad, A. Muhammad, A. M. Khalid, J. Mol. Struct. 2018, 1160, 129–141, https://doi.org/10.1016/j.molstruc.2018.01.100

[8] P. K. Murthy, G. Krishnaswamy, S. Armaković, S. J. Armaković, P. A.Suchetan, N. R. Desai, V. Suneetha, R. Sreenivasa Rao, G. Bhargavi, D. B. Arunakumar, J. Mol. Struct. 2018, 1162, 81–95, https://doi.org/10.1016/j.molstruc.2018.02.081

[9] A. Teimouri, A. N. Chermahini, M. D. Emami, Arkivoc 2008, 8, 172–187. 32. H. Dammak, A. Yangui, S. Triki, Y. A. H. Feki, J. Lumin. 2015, 161, 214–220, https://doi.org/10.1016/j.jlumin.2015.01.010

[10] M. Silverstein, G. C. Basseleer, C. Moril, Spectrometric Identification of Organic Compounds, Wiley, New York, 1981.

[12] S. Muthu, J. U. Maheswari, T. Sundius, Spectrochim. Acta A Mol. Biomol. Spectrosc. 2013, 108, 307–318, https://doi.org/10.1016/j.saa.2013.02.022.

[13] S. Muthu, J. U. Maheswari, T. Sundius, Spectrochim. Acta A Mol. Biomol. Spectrosc. 2013, 108, 307–318, https://doi.org/10.1016/j.saa.2013.02.022

[14] G. Socrates, Infrared Characteristic Group Frequencies, Wiley Inter Science Publication, 1980.

[15] G. Varsanyi, Vibrational Spectra of Benzene Derivates, Academic Press, New York, 1969.

[16] K. Toubal, N. Boukabcha, Ö. Tamer, N. Benhalima, S. Altürk, D. Avcı, A. Chouaih, Y. Atalay, A. Djafri, F. Hamzaoui, J. Mol. Struct. 2017, 1147, 569–581.

[17] J.B. Foresman, Ae. Frisch, Exploring chemistry with electronic structure methods, Gaussian, (1996).

[18] O. Kourat, A. Djafri, N. Benhalima, Y. Megrouss, N.E.H. Belkafouf, R. Rahmani, J.- C. Daran, A. Djafri, A. Chouaih, Synthesis, crystal structure, Hirshfeld surface analysis, spectral characterization, reduced density gradient and nonlinear optical investigation on (E)-N'-(4-nitrobenzylidene)-2-(quinolin-8-yloxy) acetohydrazide monohydrate: a combined experimental and DFT approach, J. Mol. Struct. 1222 (2020) 1–15, https://doi.org/10.1016/j.molstruc.2020.128952.

[19] S. Jabeen, T.J. Dines, S.A. Leharne, R. Withnall, B.Z. Chowdhry, A vibrational spectroscopic investigation of rhodanine and its derivatives in the solid state, J. Raman Spectrosc. 41 (2010) 1306–1317.

[20] F. Chain, E. Romano, P. Leyton, C. Paipa, C.A.N. Catalan, M.A. Fortuna, S. A. Brandan, An experimental study of the structural and vibrational properties of sesquiterpene lactone cnicin using FT-IR, FT-Raman, UV–visible and NMR spectroscopies, J. Mol. Struct. (2014) 160–169, 1065-1066.

[21] S. Sharma, H. Sharma, S. Sharma, S. Paul, V.K. Gupta, N. Boukabcha, A. Chouaih, Triflic acid functionalized carbon@Silica composite: synthesis and applications in organic synthesis; DFT studies of indeno[1,2-b]indole, ChemistrySelect 5 (7) (2020) 2201–2213, https://doi.org/10.1002/slct.201904727.

[22] V. Crasta, V. Ravindrachary, S. Lakshmi, S.N. Pramod, M.A. Shridar, J. Shashidhara Prasad, Growth, characterization and crystal structure analysis of 1-(4- chlorophenyl)-3-(4-chlorophenyl)-2-propen-1-one, J. Cryst. Growth 275 (1–2) (2005) e329–e335, https://doi.org/10.1016/j.jcrysgro.2004.10.110.

[23] H. Booth, R.M. Silverstein, G.C. Bassler, T.C. Morrill, Spectrometric Identification of Organic Compounds, Wiley, Chichester, 1991.

[24] W. Meng, G. Jin-Ju, W. Zhong-Bo, W. Zun-Yao, Raman FT-IR, N.M.R. spectra, molecular geometry, vibrational assignments, Ab initio and density functional theory calculations for diethyl phthalate, Chin. J. Struct. Chem. 32 (2013) 890–902.

[25] N.E.H. Belkafouf, F. Triki-Baara, A. Altomare, R. Rizzi, A. Chouaih, A. Djafri, F. Hamzaoui, Synthesis, PXRD structural determination, Hirshfeld surface analysis, and DFT/TD-DFT investigation of 3N-ethyl-2N'-(2-ethylphenylimino) thiazolidin4-one, J. Mol. Struct. 1189 (2019) 8–20, https://doi.org/10.1016/j. molstruc.2019.04.028.

[26] A. Ramalingam, A.R. Guerroudj, S. Sambandam, A. Kumar, R. Krishnamoorthy, N. Boukabcha, A. Chouaih, M. Elayaperumal, Synthesis, vibrational spectra, Hirshfeld surface analysis, DFT calculations, and in silico ADMET study of 3-(2- chloroethyl)-2,6-bis(4-

fluorophenyl)piperidin-4-one: a potent anti-Alzheimer agent, J. Mol. Struct. 1269 (2022), 133845, https://doi.org/10.1016/j. molstruc.2022.133845.

[27] F. Rouessac, A. Rouessac, Chemical Analysis: Modern Instrumentation Methods and Techniques, Wiley, New Jersey, 2013, 2nd Edition.

[28] S. Kumar, A. Radha, M. Kour, R. Kumar, A. Chouaih, S. K.Pandey, DFT studies of disubstituted diphenyldithiophosphates of nickel(II): structural and some spectral parameters, J. Mol. Struct. 1185 (2019) 212–218, https://doi.org/10.1016/j. molstruc.2019.02.105.

[29] A. Kohler, ¨ H. B¨ assler, Electronic Processes in Organic Semiconductors, Wiley-VCH Verlag, Weinheim, 2015, https://doi.org/10.1002/9783527685172.

[30] N.M. O’boyle, A.L. Tenderholt, K.M. Langner, CCLIB: a library for packageindependent computational chemistry algorithms, J. Comput. Chem. 29 (5) (2008) 839–845, https://doi.org/10.1002/jcc.20823.

Chapter VI

Molecular Dynamics Simulation and structure – activity relationship

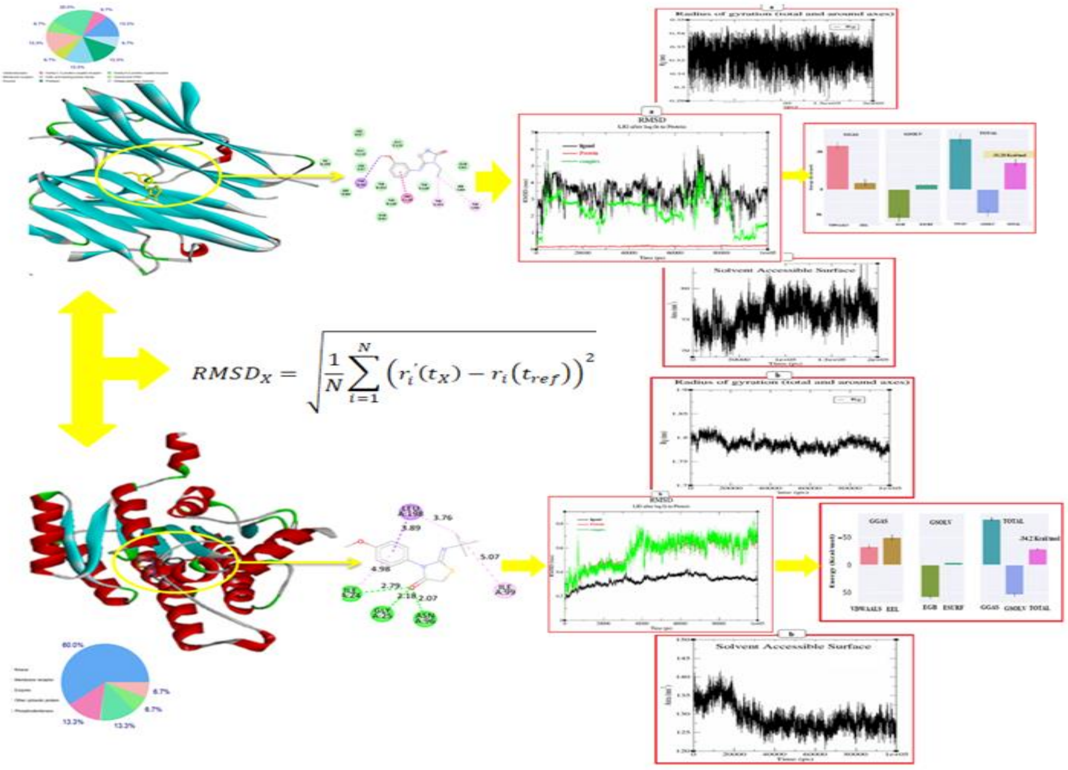

VI.1. Introduction

The study originated ground-state calculations of the title molecule using the Gaussian 09 software, utilizing Density Functional Theory (DFT) with B3LYP functional and a 6–311 G (d, p) basis set. This well-acknowledged mechanism for predicting attributes of organic compounds facilitated the optimization of the molecule's shape. The analysis incorporated the Molecular Electrostatic Surface (MEP) and Global Chemical Reactivity Descriptors (GCRD) characteristics, which encompassed electronegativity, chemical potential, chemical hardness, chemical softness, electrophilicity, and nucleophilicity indices. The electron affinity and ionization potential were computed, yielding valuable information on the chemical reactivity and structural stability. In addition, the compound's dipole moment, polarizability, and first and second-order hyperpolarizabilities were measured to investigate its non-linear optical properties. In addition, the study utilized PASS analysis to forecast the biological activity of the title chemical by identifying possible receptors and evaluating likely activity and inactivity. The process of molecular docking, which is an essential technique in the field of drug development, was performed using AutoDockVina. This allowed for the prediction of the binding affinity and interaction energy between the ligand and receptor. The drug-likeness characteristics were assessed using Lipinski's rule of five, while the SwissADME server gave information on pharmacokinetic and physicochemical aspects. Ultimately, GROMACS 2021 was utilized to conduct Molecular Dynamics (MD) simulation, which allowed for the estimation of binding energies and evaluation of biological activity based on metrics such as RMSD, Rg, RMSF, SASA, and MM-PBSA. This holistic approach improves our comprehension of the structural, kinetic, and biological features of the chemical under investigation.

VI.2. Computational details

VI. 2.1. Molecular properties

The ground-state calculations were performed using the Gaussian 09 package program **[1]**, and the output files were visualized via Gauss View 5 software **[2]**. The title molecule's ground state underwent geometry optimization by DFT with B3LYP functional and 6–311 G (d, p) basis set. This level of theory is commonly used to predict organic compounds' properties, reproducing the experimental geometric parameters **[3–7]**. The molecular electrostatic surface (MEP) was investigated and visualized. At the same time, the Global chemical reactivity descriptors (GCRD) parameters are a good indication to highlight the relationship between chemical reactivity and the strength of the structure. As mentioned in the literature, The GRCD parameters, such as electronegativity (χ), chemical potential (P), chemical hardness (η), chemical softness (s), and the electrophilicity (ω) and nucleophilicity (□) indices, can be obtained from the following equations [8]:

$\eta = \frac{1}{2}(E_{LUMO} - E_{HOMO})$; $\mu = -\left(\frac{I+A}{2}\right)$; $S = \frac{1}{2\eta}$; $\chi = \left(\frac{I+A}{2}\right)$; $\omega = \frac{\mu^2}{2\eta}$.

The electron affinity (A) and ionization potential (I) can be evaluated as $A = -E_{LUMO}$ and $I = -E_{HOMO}$.

We calculated the dipole moment (μ), polarizability (α), and both the first and second-order hyperpolarizabilities (β and γ) of the title chemical to get greater insight into its NLO feature. With the help of the x, y, and z components defined by the following equations [9] using the B3LYP functional, the magnitudes of the μ, α, β, and γ tensors were determined in both static and dynamic regimes.

$$\mu = (\mu_x^2 + \mu_y^2 + \mu_Z^2)^{\frac{1}{2}}; \alpha = \frac{1}{3}(\alpha_{xx} + \alpha_{yy} + \alpha_{zz}); \beta_{\|} = (\beta_x^2 + \beta_y^2 + \beta_z^2)^{\frac{1}{2}}$$

For the first order hyperpolarizability estimation, the detailed relation is as follows:

$$\beta_{\|} = \left[(\beta_{xxx} + \beta_{xyy} + \beta_{xzz})^2 + (\beta_{yyy} + \beta_{yzz} + \beta_{yxx})^2 + (\beta_{zzz} + \beta_{zxx} + \beta_{zyy})^2\right]^{\frac{1}{2}}$$

The Kleinmann hypothesis **[10]** was used to calculate the second-order hyperpolarizability (γ) via the following equation:

$$\gamma = \frac{1}{5}(\gamma_{xxxx} + \gamma_{yyyy} + \gamma_{zzzz} + 2\gamma_{xxyy} + 2\gamma_{xxzz} + 2\gamma_{yyzz})$$

The calculated values have been converted into electrostatic units (esu) (for α; 1 au = 0.1482 10^{-24}esu, for β; 1 au = 8.6393 10^{-33}esu).

VI.2.2. *PASS analysis*

The title compound's biological activity was predicted using the Pass online software. (http://www.way2drug.com/passonline). While the most appropriate receptors for the ligand are predicted [11]. A compound's potential activity (Pa) and probable inactivity (Pi) are identified by the PASS result spectrum [12]. In this case, the terms "probable activity" (Pa) and "probable inactivity" (Pi) are used to establish the outcomes. When Pa is greater than Pi (Pa > Pi) and Pa is equal to or greater than 0.5 (Pa ≥ 0.5), it suggests that the compound is likely to exhibit the predicted activity.

VI. 2.3. Molecular docking

Molecular docking is a commonly used computational approach in drug discovery and pharmaceutical research. It involves predicting the binding affinity and interaction energy between a receptor and a ligand. Molecular docking is used to see ligand-protein interaction sites through AutoDockVina**[13]**. AutoDock Tools **[14]** was performed to prepare the target protein. The docked pose was displayed using Discovery Studio software**[15]** using the PyMol [16].

VI.2.4. Pharmacokinetic and physicochemical properties

To evaluate the drug-likeness parameters of HTBH, Lipinski's rule of five was applied, which is a widely used method in such studies **[17]**. The properties of Lipinski's rule of five were obtained using the SwissADME server (http://www.swissadme.ch)**[18]**.

VI.2.5. Molecular dynamics (MD) simulation

To perform the MD simulation, the GROMACS 2021 program was employed **[19]**. The protein and ligand were docked before the simulation with AutoDockvina software to identify the optimal binding conformation as the initial complex structure for molecular dynamics simulation. The RMSD, Rg, RMSF, SASA and MM-PBSA parameters were evaluated to predict the binding energies and consequently the biological activity of the title compound.

VI.3. Visualization and discussion of the results for EMTh

VI.3.1. Chemical reactivity

Computing the electronic energy of a molecular system enables the construction of the potential energy surface associated with a chemical reaction using quantum chemical techniques, regardless of whether they are based on the wave function or the theory of functional density. The development of Hückel's theory[20-23] in 1931 marked the beginning of theoretical modeling of reactivity. Two widely used chemists' theories are frontier orbital theory [24, 25]and generalization Klopman and Salem [26, 27], which derive from molecular orbital theory. These models focus on energy interaction between two chemical partners that approach each other and disrupt [28-30]. These models have led to the definition of various reactivity indices, which will be presented in this chapter.

The calculated values of GCRD parameters for the title molecule are summarized in Table 1.

It is important to note that these expressions do not account for the orbital relaxation that happens when an electron is transferred or received by the system. Furthermore, the Koopmans [31] approximation is not as accurate as Hartree-Fock orbitals in light of the definition of Kohn-Sham orbitals.

The charge transfer inside the molecule is shown by the chemical hardness (η) value of 2.636 eV. The global electrophilicity index (ω) in Table 1 confirms the molecule's electrophilic behavior with a larger value of 2.361 eV. Conversely, the chemical potential (μ) value of -3.528 eV explains the chemical stability of the title molecule.

Table VI.1. Calculated energy values of the EMTh compound by B3LYP/6-311G(d,p) method

Parameters	Calculated energies
E_{HOMO}	–6.165
E_{LUMO}	–0.892
Energy gap (ΔE)	5.273
Ionization potential (I)	6. 165
Electron affinity (A)	0.892
Electronegativity (χ)	3.528
Chemical potential (μ)	–3.528
Chemical hardness (η)	2.636
Chemical softness (s)	0.189
Electrophilicity index (ω)	2.361

VI.3.2. Molecular Electrostatic Potential

The total charge distribution (electron + proton) surrounding the molecule at that point produces a net electrostatic effect, which is indicated by the molecular electrostatic potential (MEP) [32]. In addition, the MEP surface is useful for studying biological recognition processes, hydrogen bonding interactions, and the reactivity of a wide range of chemical systems [33, 34]. It also aids in the visual comprehension of the molecule's relative polarity. The molecules' size, shape, charge density, and reactive sites are predicted by an electron density isosurface mapped with an electrostatic potential surface. Different colours correspond to the various electrostatic potential values at the surface: red denotes the most electronegative potential, blue denotes the most positive potential, and green denotes the most positive potential.

The positioning of positive and negative charges in a crystal allows scientists to define several highly intriguing physical characteristics, including the molecular electrostatic potential (MEP) [35]. These days, X-ray diffraction and quantum chemistry are used to determine both theoretical and experimental MEP surfaces [36–39]. The title compound's total density (TD) was used to compute the MEP surrounding the title molecule; Figure 8 shows the two maps, TD and MEP. The graphic illustrates the relationship between the partial charges and electronegativity of oxygen atoms O1 and O2 and the negative MEP. The largest positive region—the point of choice for a nucleophilic attack—is indicated by the blue colour in Figure 8B. The MEP plot's colour scheme is based on its ability to show the positive, negative, and neutral electrostatic potential areas along with the size and structure of molecules (Figure 8). The MEP shows the correlation between these physicochemical characteristics and the molecular structure [40–44]. It is possible to determine the molecular dipole moment among them. Figure 9 shows the direction of the molecular dipole moment for the molecule mentioned above.

Following examination of the compound's electrostatic potential map (EMTh):

The region surrounding the oxygen atom (O1) and the sulphur atom (S2) is the primary focus of the red and yellow colours that define the negative molecular zones. These areas show the lowest electrostatic potential values, where electronic density predominates. We infer that these areas are electrophilically reactive from this.

- ➔ The colour blue designates the positive molecular regions, primarily found on hydrogen atoms connected to methyl and ethyl groups and benzene cycles. These areas, where the electron density is a minority, correspond to the highest electrostatic potential values. We infer that these regions are nucleophilically reactive from this.
- ➔ The green colour expresses the neutral region of electrostatic potential in the EMTh molecular structure. Negative and positive densities, concerning the EMTh compound's electronic potential, fall between -4.686 10-2 and +4.686 10-2u.a. The potential molecule electronics are depicted in Figure IV.1.

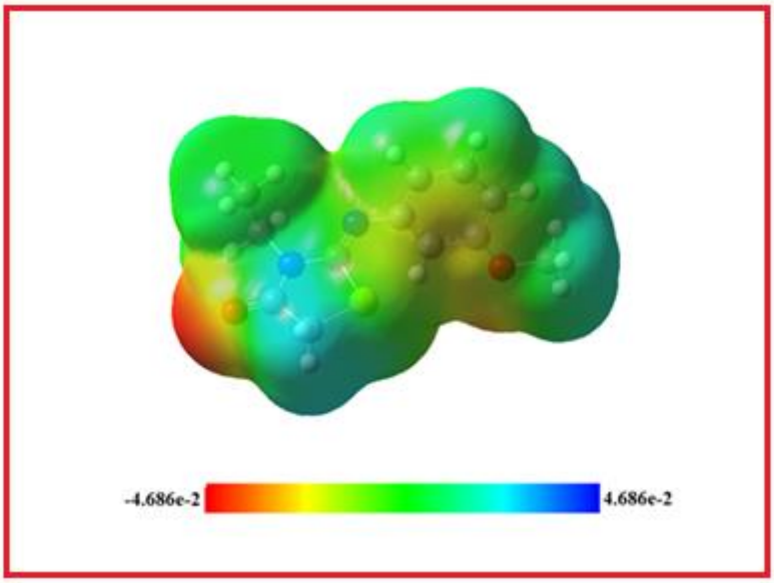

Figure VI. 1. MEP plots for (Z)-3-N-(ethyl)-2-N'-(3-methoxyphenyl imino) thiazolidine-4-one (A) Total electron density, (B) MEP surface

VI.3.3. NLO effect

Non-linear optics (NLO) has opened up new possibilities for exploring the fundamental characteristics of materials, notably in their crystalline state. The non-linear interactions of light with materials are the subject of this area of optics, which means that the reaction of the material is not proportional to the intensity of the incident light. This phenomenon becomes very intriguing and beneficial in a variety of technological disciplines, including data storage, optoelectronics, medicine, and telecommunications.

Organic materials in particular have special properties that make them useful in non-linear optical applications. A pivotal feature is their rapid and vital non-linear reactions, which are frequently ascribed to the existence of delocalized "π" electrons. Included in the molecular structure, these electrons have unrestricted mobility across several atomic nuclei. This delocalization leads to greater asymmetric polarizability between donor and acceptor groups inside the material. The organic molecules' nonlinear optical (NLO) susceptibilities arising from the passage of p electrons from the donor to the acceptor cloud are the main focus of this investigation. Apart from these benefits, low-temperature stability and a propensity to easily relax to random orientation are two more NLO drawbacks of organic molecules [45]. Additionally, new fields with altered phase, frequency, amplitude, or other propagation parameters from the original field are produced by electromagnetic fields interacting with different mediums [46].

The field of nonlinear optics (NLO), which is characterized as the interaction of high-intensity light with matter, is vital to several applications [47, 48], including optoelectronics, data storage, medicine, telecommunications, and optical signal processing [49, 50]. The existence of donor and acceptor groups defines the optical nonlinearity of conjugated organic compounds. Total molecule dipole moment, polarizability, and initial hyperpolarizability values are 2.46 Debye, 2.40×10^{-23}esu, and 2.38×10^{-30}esu, respectively, and are shown in Table VI.2. The estimated polarizability (α) value (using the B3LYP functional) is 2.40× 10-23esu, which is considered quite good when compared to earlier studies. It has been reported that urea and pNA have polarizability values of 0.13×10^{-24}esu and 15.5×10^{-24}esu, respectively [51–53]. Research indicates that the second hyperpolarizability (η) value of the title molecule is 13.22×10^{-36} esu.

The existence of the thiazole moiety and aromatic ring, which function as donors and acceptors in the structure, is confirmed by the large computed value of γ. extending the bridge length between the electron donor and acceptor groups can improve a molecule's NLO characteristics. We present the site-isolation concept, which suggests that NLO effects can be enhanced by efficiently isolating electron-rich and electron-deficient locations inside a molecule. The idea behind this is that longer bridges cause these groups to be more geographically separated from one another. As a spacer, the longer bridge reduces electrical interactions, increases the separation between the donating and accepting groups, and lessens the cancellation of the NLO effect [54]. For NLO materials, the molecule is suggested as a viable candidate by reducing the HOMO-LUMO energy gap. Additionally, the dynamic hyperpolarizabilities were evaluated because observed data are nearly invariably produced at incident optical fields. To limit resonance enhancements, the predicted value for these attributes is ω = 911.3 nm. The electro-optical pockets effect (EOPE) was represented by β||z (−ω; ω, 0), the quadratic electro-optical (dc-Kerr effect) by γ (-ω; ω,0,0), and the dc-SHG by γ (−2ω;ω,ω,0). The second-harmonic generation (SHG) was represented by β||z (−2ω; ω, ω. Dynamic polarizability α (-ω, ω) disperses effects as seen in Table 4 and is predicted to be 2.44 $\times 10^{-23}$esu.Furthermore, it was found that the values of β||z(-w,w,0), β||z (−2ω; ω, ω), γ (-ω;ω,0,0), and γ (−2ω;ω,ω,0) were 2.55 $\times 10^{-30}$, 2.92$\times 10^{-30}$, 14.77$\times 10^{-36}$, and 18.82 $\times 10^{-36}$esu, respectively.

Table VI.2. Molecular dipole moment **(**μ), polarizability (α), and first and second hyperpolarizabilities (β and γ) values for EMTH obtained by B3LYP/6-311G (d. p) levels

Dipole moment			
μ_x	0.000000		
My	0.000000		
Mz	2.46286		
μ (Debye)	2.46286		
Components	Polarizability (0,0)	Polarizability (-w,w) w = 911.3 nm	
α_{xx}	133.172	135.098	
α_{yy}	145.323	147.75	
α_{zz}	207.510	212.004	
‹α› (a.u)	154.76	158.56	
Δα	138.41	144.78	
1 a.u	1.62×10^{-25}	1.64×10^{-25}	
‹α›	2.29×10^{-23}	2.35×10^{-23}	
Δα(esu)×10^{-24}	24	24.4	
Components	First order hyper-polarizability (0,0,0)	First order hyperpolarizability (-w,w,0) w = 911.3 nm	First order hyperpolarizability (-2w,w,w) w = 911.3 nm
β_{xxx}	-151.044	-162.993	-190.635
β_{yxx}	-60.3857	-8.94559	-10.4274
β_{zxx}	73.5446	-64.8259	-78.2693
β_{xyx}	-	-	-126807
β_{yyx}	-	-	-77.5186
β_{zyx}	0.759886	1.09167	-5.67370
β_{xyy}	-7.59347	-65.4535	-75.9652
β_{yyy}	-248.856	-270.914	-325.878
β_{zyy}	-105.444	-112.909	-161.140
β_{xzx}	-	-	(-77.4149
β_{yzx}	-	-	(-1.22827
β_{zzx}	-	-	84.4512
β_{xzy}	-	-	1.97332
β_{yzy}	-	-	-142.966
β_{zzy}	-	-	130.332
β_{xzz}	-0.60.4808	79.3075	100.090
β_{yzz}	115.764	-112.909	145.860
β_{zzz}	581.602	624.325	722.167
β_x	(-413.654	-452.049	-533.916
β_y	-422.055	-470.000	-606.899
β_z	1247.03	1330.30	1486.33
‹β› (a.u)	275.995	296.307	338.382
1 a.u		2.55986	8.64×10^{-33}
‹β›(esu)×10^{-30}	2.38438	2.55986	2.92336

Table VI.2. (Continued)

Components	Second order hyper-polarizability (0,0,0,0)	Second order hyperpolarizability (-w,w,0,0);w = 911.3nm	Second order hyperpolarizability (-2w,w,w,0);w 911.3nm
γ_{xxxx}	9666.44	10467.4	12213.2
γ_{xxyy}	3173.13	3531.13	4278.16
γ_{yyyy}	20870.8	23615.4	10336.3
γ_{xxzz}	7468.47	8389.16	30882.1
γ_{yyzz}	14647.3	16828.7	21688.2
γ_{zzzz}	50212.5	55968.6	71250.3
$\langle\gamma\rangle$(esu) $\times 10^{-36}$	13.2292	14.7727	18.8237

VI.3.4. Molecular docking

Using molecular docking analysis and prediction of activity spectra for substances (PASS), the biological activity of the generated compound is examined. The prediction findings indicated that the drug may have an inhibitory impact on the protein known to inhibit proteasome ATPase, as Table 5 illustrates. The present study selected this protein because of its high Pa value (Pa=0.757). The literature supports the selection of this protein [12]. This target protein's crystal structure (PDB ID: 2AZ5) was found in the RCSB protein data library [55]. Tumour necrosis factor-alpha's protein crystal structure is 2AZ5 [56]. TNF-α is a cytokine that plays a crucial function in the inflammatory process and tumour growth [57].

Using the Discovery Studio program, polar hydrogens were added to the purified protein after inhibitors, additional ligands, and water molecules were removed [58]. Using the Auto Dock Vina program, the molecular docking simulations between the protein 2AZ5 and the title molecule were examined [59]. The following was found to be the protein's active site: grid box dimensions: 40 x 40 x 40 A^3; centers of x, y, and z: -13.687, 71.607, and 27.007, respectively; distances between points: 1.0 Å. The binding free energy (ΔG) was used to rank and list the docked conformations. The nine distinct ligand conformations that have been examined inside the 2AZ5 protein receptor are displayed in Table 6. With the binding energy system (ligand-protein) of -6.3 kcal/mol in mode No. 1, the optimal docking posture was identified [60]. The program Discovery Studio was used to visualize the docking findings. The intramolecular contacts (a-3D form, b-2D form, and c-the best score docking posture of the title chemical) that link the structure to the 2AZ5 protein are depicted in Figure 12. The molecule (Z)-3-N-(Ethyl) in its lowest energy pose Figure 12c depicted -2-N'-(3-Methoxyphenyl Imino) Thiazolidine-4-one in the protein binding site. Table 7 displays the many kinds of intermolecular interactions that can happen between the ligand and the TNF-α protein residue. According to the docking data, two typical hydrogen bond contacts were established between the O atom of the title molecule's thiazolidinone (TYR C: 151) and the -OH group in LEU C: 120 and the N2 atom of the imine group of the title molecule. With N___H•••N notation, the distances for these interactions were found to be 3.76 Å, and with O___H•••O one, they were found to be 3.17 Å. Similarly, at 3.49 Å and 4.65 Å values of distance, respectively, two carbon-hydrogen bond contacts were established between atom C of group CH2 in the title molecule and atom O of the residue SER C: 60 and O atom of the residue GLN C: 61. Furthermore, four hydrophobic contacts were noted, including two π-Alkyl interactions at a distance of 4.98 Å and 5.02 Å between the carbon atom of the ethyl group in the title molecule and TYR C: 59 and TYR C: 151. amide-π stacking interaction developed between the ring aromatic of the title molecule and LEU C: 120 at 4.03 Å value of distance, and π-sigma interaction between the aromatic ring of residue TYR D: 59 at a distance of 3.71 Å. It was discovered that the inhibitor-receptor complex interaction that was theoretically estimated produced a highly effective outcome; so, the chemical we created, the title compound, has a good inhibitory capability.

Table VI. 3. PASS prediction results of the EMTh compound

Pa	**Pi**	**Activity**
0,757	0,008	Proteasome ATPase inhibitor
0,749	0,010	Muramoyl tetrapeptidecarboxypeptidase inhibitor
0,696	0,009	Insulysin inhibitor
0,664	0,004	PfA-M1 aminopeptidase inhibitor
0,638	0,037	Fusarinine-C ornithinesterase inhibitor
0,610	0,016	Spermidine dehydrogenase inhibitor
0,643	0,092	Gluconate 2-dehydrogenase (acceptor) inhibitor
0,579	0,030	Gastrin inhibitor
0,550	0,045	Electron-transferring flavoprotein dehydrogenase inhibitor
0,542	0,041	2-Hydroxyquinoline 8-monooxygenase inhibitor

Table VI.4. AutoDock Vina results of the binding affinity and RMSD values of different poses in 2AZ5 inhibitor of (Z)-3-ethyl-2-((3-methoxyphenyl)imino)thiazolidin-4-one

Mode	Affinity (kcal/mol)	RMSD l.b	RMSD u.b.
1	-6.3	0.000	0.000
2	-6.2	20.099	21.475
3	-6.0	20.060	21.042
4	-6.0	1.198	2.182
5	-5.9	2.459	5.294
6	-5.9	18.483	19.504
7	-5.9	20.099	21.467
8	-5.9	2.911	3.788
9	-5.9	19.779	21.465

Table VI.5. Distances. Types and location of intermolecular interactions formed from the residues of the TNF-α protein (PDB ID: 2AZ5) and the molecule (Z)-3-ethyl-2-((3-methoxyphenyl)imino)thiazolidin-4-one

Protein	Residues	Atom/group of compound	Category	Types	Distance (Å)
PDB(ID : 2AZ5)	C:LEU120	N5	Hydrogen Bond	Conventional Hydrogen Bond	3,76581
	C:TYR151	O6	Hydrogen Bond	Conventional Hydrogen Bond	3,1706
	C:SER60	C8	Hydrogen Bond	CarbonHydrogen Bond	3,49411
	C:GLN61	C8	Hydrogen Bond	CarbonHydrogen Bond	4,65342
	D:TYR59	C17	Hydrophobic	Pi-Sigma	3,71415
	C:LEU120	aromatic ring	Hydrophobic	Amide-Pi Stacked	4,03445
	C:TYR59	C9	Hydrophobic	Pi-Alkyl	4,98901
	C:TYR151	C9	Hydrophobic	Pi-Alkyl	5,02071

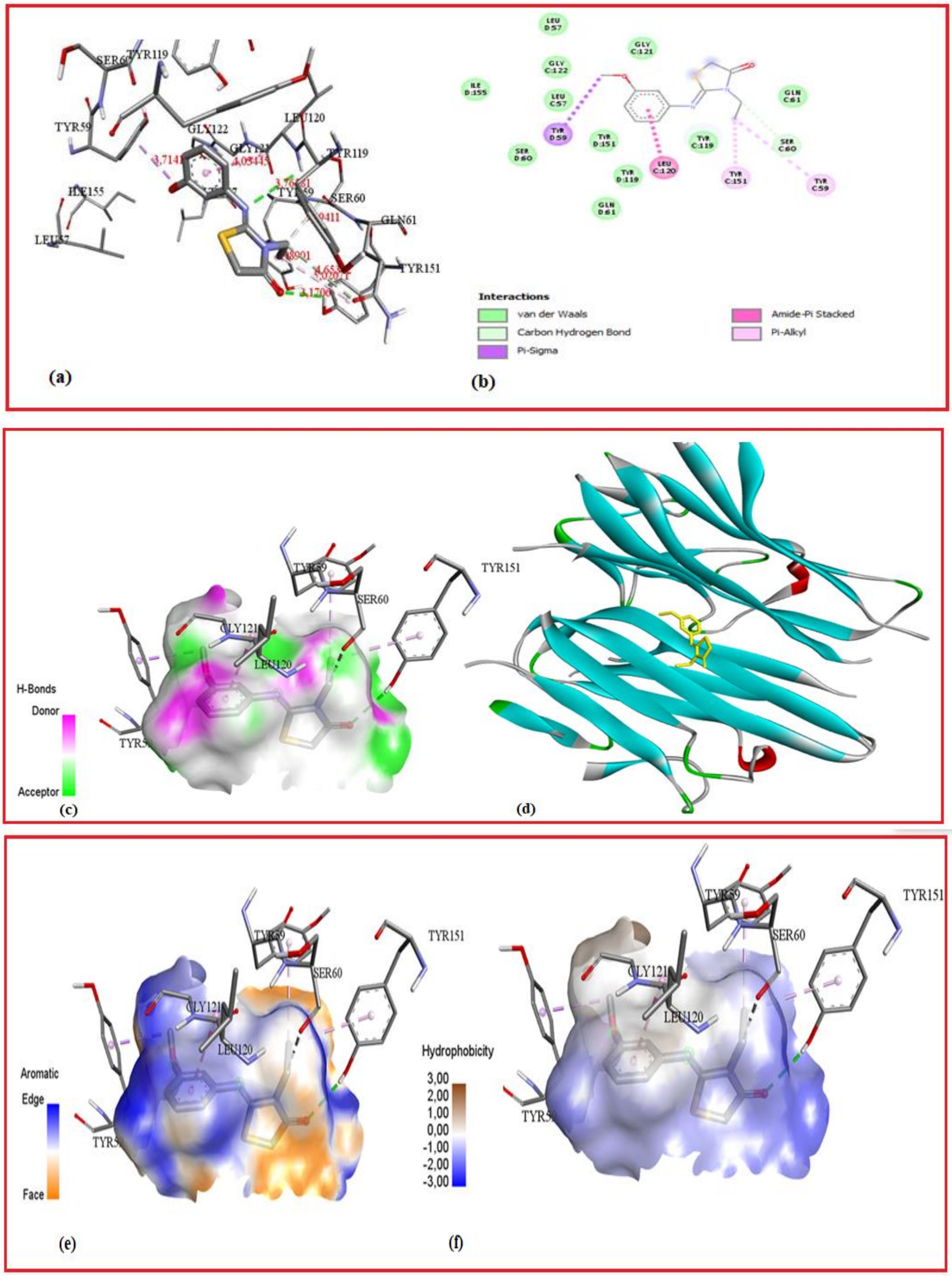

Figure VI.2. (a), Intramolecular interactions that connect the structure to the 2AZ5 protein, (b) 2D form of the 5U9P protein (c) interaction between the active site residues of the protein and ligand. (d) 3D ribbon structure of receptor/5U9P protein, and (e), (f)3D form intermolecular interactions connecting the structure

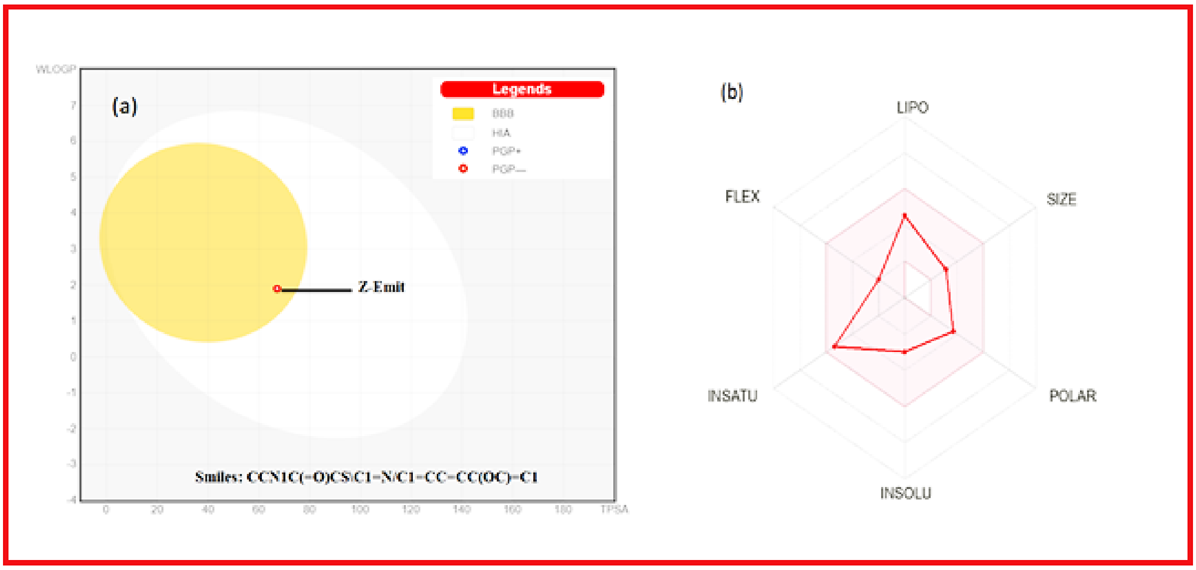

Figure VI. 3. (a) EMTh blood brain barrier (BBB) permeability [BOILED-EGG], and (b) EMTh oral bioavailability radar

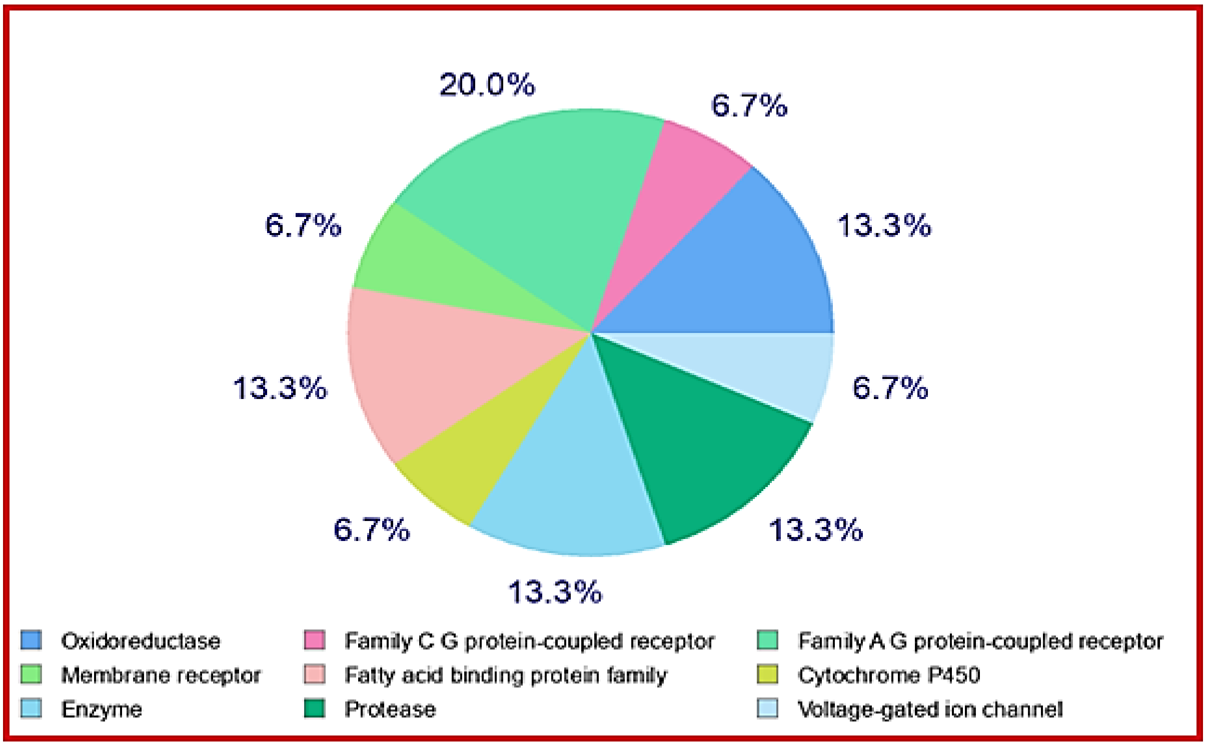

Figure VI.4. Druggability predictions of the title compound

Table VI.6. Physicochemical and pharmacokinetic properties for EMTh

Physicochemical Properties	
Formula	$C_{12}H_{14}N_2O_2S$
Molecularweight	250.32 g/mol
Numberheavyatoms	17
Numberaromaticheavyatoms	6
Fraction Csp^3	0.33
Numberrotatable bonds	3
Numberhydrogen bond acceptors	3
Numberhydrogen bond donors	0
Molarrefractivity	73.86
TPSA	67.20 Å^2
Lipophilicity	
Consensus LogP$_{o/w}$	2.16
Water Solubility	
LogS	-3.48
Solubility	0.821E-01 mg/ml
Pharmacokinetics	
GI absorption	High
BBB permeant	Yes
P-GP substrate	No
CYP1A2 inhibitor	Yes
CYP2C19 inhibitor	Yes
CYP2C9 inhibitor	No
CYP2D6 inhibitor	No
CYP3A4 inhibitor	No
LogK$_p$ (skin permeation)	(-6.10 cm/s
Drug-likeness	
Lipinski	Yes (0 violation)
Ghose	Yes
Veber	Yes
Egan	Yes
Muegge	Yes
Bioavailability score	0.55
MedicinalChemistry	
PAINS	0 alert
Brenk	1 alert: imine_1
Leadlikeness	Yes
Syntheticaccessibilty	3.30(from 1 (very easy) to 10 (very difficult))

VI.4. Visualization and discussion of the results for TMTh

VI.4.1. Reactivity descriptors

The global chemical reactivity descriptors (GCRDs) linked to molecular modelling are regarded as crucial instruments for establishing a relationship between the stability and structure of a material [61]. The literature suggests that two parameters that influence the stability of organic molecules are their softness and chemical hardness [62]. The electronic interactions between molecule components are explained by the GCRD variables.

The calculated values of the GCRD parameters for the substance in question were compiled in Table 6. The determined value of chemical potential (P) is 5.850 eV, indicating chemical stability for the compound under consideration. Additionally, the chemical hardness (η) is around 1.336 eV, indicating favourable charge transport inside the molecule. Furthermore, the negative value of the chemical potential confirms the structural stability of the title compound **[63]**. As can be seen from Table 6 and in comparison to the nucleophilicity index value (0.078 eV^{-1}), the electrophilicity index (ω) has a very significant value of 12.801 eV, which explains the molecule's electrophilic behavior and is consistent with previous findings **[64].** The GCRD parameters are also fundamental for defining the bio-reactivity of molecular systems **[65]**.

Table VI.7. GCRD calculated values of TMTh by B3LYP/6-311G(d,p)

Parameters	Calculated energies (eV)
E_{HOMO}	–7.186
E_{LUMO}	–4.513
E_{HOMO-1}	–8.462
E_{LUMO+1}	–3.769
Energie gap (ΔE)	2.673
Ionisation potential (I)	7.186
Electron affinity (A)	4.513
Electronegativity (χ)	5.850
Chemical potential (P)	–5.850
Chemical hardness (η)	1.336
Chemical softness (s)	0.3741
Electrophilicity index (ω)	12.801
Nucleophilicity index (ε) (eV^{-1})	0.078

VI.4.2. MEP analysis

Molecular electrostatic potential (MEP) has always been considered crucial in the investigation of intermolecular interactions and the localization of nucleophilic and electrophilic attack regions in molecular systems **[66, 67]**. The relationship between the MEP distribution and a molecule's electron density is also widely recognized **[68]**. The molecular electrostatic potential, V(r), at a specific position r(x,y,z) is defined as the electrostatic interaction between the electrical charge generated by the molecule's nuclei and electrons and a proton at r. The following equation was used to calculate the V(r) values for the system being studied:

$$V(r) = \sum_{A} \frac{Z_A}{(R_A - r)} - \int \frac{\rho_{total}(r')}{|r' - r|} dr'$$

Where Z_A is the charge of nucleus A located at R_A, ρ(r') is the electronic density of the molecule, and r' is the dummy atom position. The common colour scheme used to describe the MEP map was widely reported in which the negatively and positively charged regions are coloured in red and blue, respectively **[69]**. On the other hand, due to the higher concentration of electronic density, the nucleophilic sites of the molecule are displayed as red. Reciprocally, electron-deficient regions are displayed in blue. Based on the optimized structure of TMTh, the MEP surface was computed theoretically (Figure 7). According to the MEP map in Figure 7, the most negative region associated with the strongest repulsion is around the carbonyl group and the positive regions associated with the strongest attraction are located on the hydrogen atoms of the molecule. Therefore, it may be inferred that electronegative atoms are the most common sites for nucleophilic attack, whereas hydrogen atoms are the most common locations for an electrophilic attack.

Following examination of the compound's electrostatic potential map (EMTh2):

The region surrounding the oxygen atom (O1) and the sulphur atom (S2) is the primary focus of the red and yellow colours that define the negative molecular zones. These areas show the lowest electrostatic potential values, where electronic density predominates. We infer that these areas are electrophilically reactive from this.

The colour blue designates the positive molecular regions, primarily found on hydrogen atoms connected to methyl and ethyl groups and benzene cycles. These areas, where the electron density is a minority, correspond to the highest electrostatic potential values. We infer that these regions are nucleophilically reactive from this.

The green colour expresses the neutral region of electrostatic potential in the TMTh molecular structure. Negative and positive densities, concerning the TMTh compound's electronic potential, fall between -5.662 10-2 and +5.662 10-2u.a. The potential TMTh molecule electronics are depicted in Figure IV.14.

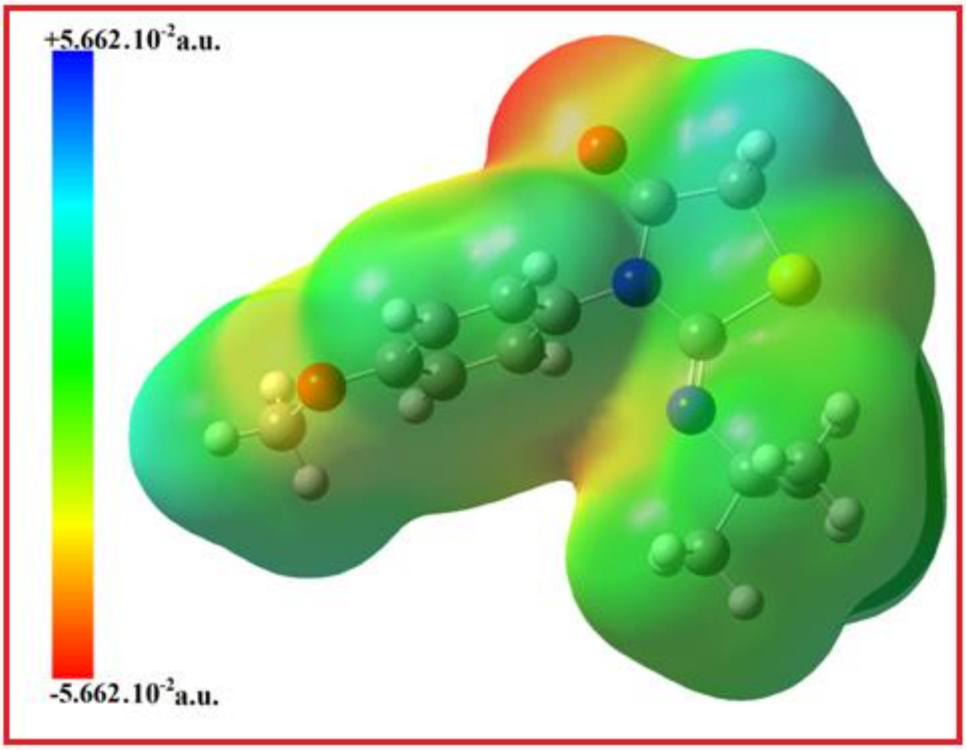

Figure VI. 5. MEP picture for the TMTh compound calculated at B3LYP/6-311G(d,p) level of theory

VI.4.3. NLO effect

Emerging technologies such as signal processing and telecommunications might benefit greatly from the so-called nonlinear optical (NLO) effect, which results from unique phases arising from novel fields created by the interaction of electromagnetic forces in different mediums [70–71].

Table 7 reports the corresponding findings of the NLO properties calculation for the title chemical utilizing the DFT/B3LYP technique with 6-311 G(d,p) basis set.

It is commonly known that increased dipole moment, polarizability, and hyperpolarizabilities are strongly correlated with NLO characteristics.

The dipole moment calculated from B3LYP/6-311G(d,p) is equal to 0.56 D, respectively, which are in the range of values for most similar organic compounds reported in the literature **[72, 73]**and close to that of the urea (3.73 Debye) considered as the organic NLO active typical molecule. The calculated polarizability values are 28.77 × 10^{-24} esu predicted. For the hyperpolarizability, several studies have shown that the first-order hyperpolarizability value is related to the HOMO-LUMO energy gap and the second-order hyperpolarizability value reveals the delocalization of electrons and substantial charge transfer through the π-conjugation **[74]**. The calculated first-order hyperpolarizabilities for TMTh are about 2.91× 10^{-30}esu, which is approximately 15 to 25 times that of urea (0.197 × 10^{-30} esu). The dominant component contributing to this value is β_{xxx}. The second-order hyperpolarizability (γ) values for the title molecule are about 16.29 × 10^{-36} esu as obtained by B3LYP functional, revealing that the title molecule could be regarded as a conventional molecule for optoelectronic and NLO applications. In addition, as observed data are almost always created at incoming optical fields, the dynamic hyperpolarizabilities were assessed. ω = 911.3 nm is the expected value for these features, which limits resonance improvements. The quadratic electro-optical (dc-Kerr effect) was represented by γ (-ω; ω,0,0), the dc-SHG by γ (−2ω;ω,ω,0), and the electro-optical pockets effect (EOPE) by β||z (−ω; ω, 0). The symbol for the second harmonic generation (SHG) was β||z (−2ω; ω, ω). Table 4 illustrates how dynamic polarizability α (-ω, ω) disperses effects. It is estimated to be 29.20 ×10-24esu. Moreover, the values of β||z(-w,w,0), β||z (−2ω; ω, ω), γ (-ω;ω,0,0), and γ (−2ω;ω,ω,0) were discovered to be 3.11 ×10-30, 3.54 ×10-30, 17.84 ×10-36, and 21.50 ×10-36 esu, respectively. Moreover, the values of α, β and γ showed that TMTh may be considered for linear optics applications.

Table VI.8 Molecular dipole moment **(**μ), polarizability (α), and first and second hyperpolarizabilities (β and γ) values for TMTh obtained by B3LYP/6-311G (d. p) levels

Parameters	**B3LYP**		
Dipole moment			
μ_x	0.558		
μ_y	0.028		
μ_z	-0.004		
μ (D)	**0.56**		
Polarizability	**α(0;0)**	**α(-w;w) w= 911.3nm:**	
α_{xx}	235.625	153.921	
α_{xy}	9.729	(-2.21256	
α_{yy}	194.69	196.627	
α_{zx}	-0.011	(-0.447996	
α_{zy}	0.019	0.7.78939	
α_{zz}	152.12	0.240.743	
α (au)	194.145	197.097	
α × 10^{-24} (esu)	**28.77**	29.2068	
First-orderhyperpolarizability	**β(0;0;0)**	**β(-w;w.0) w= 911.3nm:**	**β(-2w;w.w) w= 911.3nm:**
β_{xxx}	390.927	1.82441	2.21666
β_{xxy}	-110.724	(-10.5875	(-9.26910
β_{yxy}	192.772	(-7.32964	(-12.4141
β_{yyy}	139.345	0.118.671	149.772
β_{xxz}	-0.018	(-24.6663	5.92418
β_{yxz}	-0.062	(-12.5321	(-13.5150
β_{yyz}	-0.064	222.864	(-122.598
β_{zxz}	-22.613	5.68286	(-25.7279
β_{zyz}	-12.5891	(-117.016	241.146
β_{zzz}	-50.951	403.841	469.364
$\beta_{\|\|}$ (au)	336.789	360.962	410.534
$\beta_{\|\|}$ × 10^{-30} (esu)	**2.91**	3.11843	3.54669
Second-orderhyperpolarizability	**γ(0;0;0;0)**	**γ(-w;w.0.0) w= 911.3nm:**	**γ(-2w;w.w.0) w= 911.3nm:**
γ_{xxxx}	75037.8	10888.4	11914.3
γ_{yyyy}	24359.9	27412.1	33031.7
γ_{zzzz}	10 207,000	83638.7	103 865,000
γ_{xxyy}	16823.9	4479.93	5202.24
γ_{xxzz}	5116.11	5558.67	6112.59
γ_{yyzz}	4077.06	17780.2	21115.5
<γ> (au)	32327.9	35420.7	42689.3
<γ> × 10^{-36} (esu)	**16.29**	17.8403	21.5013

VI.4.4. Biological activity

VI.4.4.1. PASS and molecular docking analysis

Molecular docking is the dominating computational technique adopted for estimating the binding affinity and interaction energy of a receptor-ligand pair. The online PASS system defines the protein (target) as the accurate and dependable receptor for the ligand. This program predicts more than 300 pharmacological effects, metabolic pathways, and specific toxicities based on the structural formula of a drug [75]. A relationship between the predicted results of the biological activity and their corresponding probability values is shown in Table 8. Results are obtained when comparing Pa ≡ Pi and Pa ⪈ 0.5, utilizing likely activity (Pa) and probable inactivity (Pi). The protein gluconate 2 dehydrogenase (acceptor) protein, identified as 5U9P in the Protein Data Bank (PDB), has been found to potentially be inhibited by the specific chemical mentioned in the PASS research [76, 77]. This protein was chosen for the current study for its high Pa value (Pa = 0.698). Gluconate 2 dehydrogenase is an oxidoreductase enzyme that plays a role in both the pentose phosphate and ketogluconate pathways. Furthermore, the assessment also accounts for the binding energy magnitude of the target protein. A negative binding energy [78] indicates a robust docking capability. In this work, several binding sites between the ligand (TMTh) and the target protein (PDB ID: 5U9P) were determined.

Table 9 presents the binding affinities and their corresponding root-mean-square deviation (RMSD) values for several poses associated with different PDB IDs. These poses involve the studied ligand positioned within the gluconate 2 dehydrogenase (acceptor) protein. The most favourable conformation for molecular docking, as determined by the lowest binding energy and RMSD scores of 2.0, is the docked conformation. This conformation is considered to be the optimal posture for molecular docking [79]. Mode No. 1 achieved the usual docking position with binding energy (ligand-protein) of -6 kcal/mol, which is in excellent agreement with data reported in the literature [80]. Table 10 presents an overview of the intermolecular interactions between a molecule and protein residues with specific PDB IDs, such as PDB ID: 5U9P. The table includes information on the distances, types, and locations of these interactions. The specific receptor for TMTh is a protein. The ligand being studied exhibited interactions with the amino acid residues ILE24, GLY25, and ASN96, which constitute the receptor-binding sites of the 5U9P protein. The distances from the residues to the O2 atom of the thiazolidinone ring are 2.79, 2.18, and 2.07 Å, respectively. The representation of this interaction may be shown in Figure S8. In addition, the π-sigma bond link between LEU198's methyl group and the core of the benzene ring was found in 5U9P, with a distance of 3.89 Å. Figure 8 illustrates the relevant three-dimensional intermolecular interactions between the TMTh ligand and the protein, as observed in several PDB IDs. Mode No. 1 successfully reached the prescribed docking sites with a binding energy (ligand-protein) of -6 kcal/mol which closely matches the results documented in the literature [81]. Based on docking studies, TMTh has anticancer activity, indicating that it might be recognized as a potent inhibitor of the gluconate-2-dehydrogenase protein.

TableVI. 9. PASS prediction for the activity spectrum of the TMTh compound. Pa represents probability to be active and Pi represents probability to be inactive. Pa > Pi and Pa > 0.500

Pa	Pi	Activity
0.698	0.057	Gluconate 2-dehydrogenase (acceptor) inhibitor
0.651	0.080	Aspulvinonedimethylallyltransferase inhibitor
0.571	0.002	MAP kinase kinasekinase inhibitor
0.554	0.073	Phosphatase inhibitor
0.532	0.099	Acrocylindropepsin inhibitor
0.532	0.099	Chymosin inhibitor
0.532	0.099	Saccharopepsin inhibitor
0.511	0.046	Insulysin inhibitor
0.515	0.052	Thioredoxin inhibitor
0.506	0.041	Antianginal

TableVI.10. Binding affinity and RMSD values of different poses in the 5U9P inhibitor of TMTh by Auto Dock Vina

Mode	Affinity (kcal/mol)	Distance from best mode (Å)	
		RMSD l.b.	RMSD u.b.
1	-6.0	0	0
2	-5.4	19.296	21.196
3	-5.2	6.655	9.26
4	-5.1	18.789	19.957
5	-4.9	7.423	10.102
6	-4.9	18.135	20.195
7	-4.8	11.242	13.661
8	-4.8	17.876	19.893
9	-4.8	8.08	10.892

Table VI. 11. Distance types and location of intermolecular interactions formed from the residues of the protein gluconate 2-dehydrogenase (PDB ID: 5U9P) and TMTh

Protein	Ligand	Residue	Atom/moiety	Category	Types	Distance (Å)	Affinity (kcal/mol)
Gluconate 5-dehydrogenase (PDB ID : 5U9P)	TMTh	A: ILE24	O2 atom	Hydrogen Bond	conventional hydrogen bond	2.79	-6
		A:GLY25	O2 atom	Hydrogen Bond	conventional hydrogen bond	2.18	
		A:ASN96	O2 atom	Hydrogen Bond	conventional hydrogen bond	2.07	
		A:LEU198	C_6H_4 ring	Mixed Pi/Alkyl-Hydrophobic	π-Sigma	3.89	
		A:ILE99	methyl group	Alkyl – Hydrophobic	Alkyl	5.07	
		A:LEU198	methyl group	Alkyl – Hydrophobic	Alkyl	3.76	
		A:ILE24	C_6H_4 ring	Mixed Pi/Alkyl-Hydrophobic	π-Alkyl	4.98	

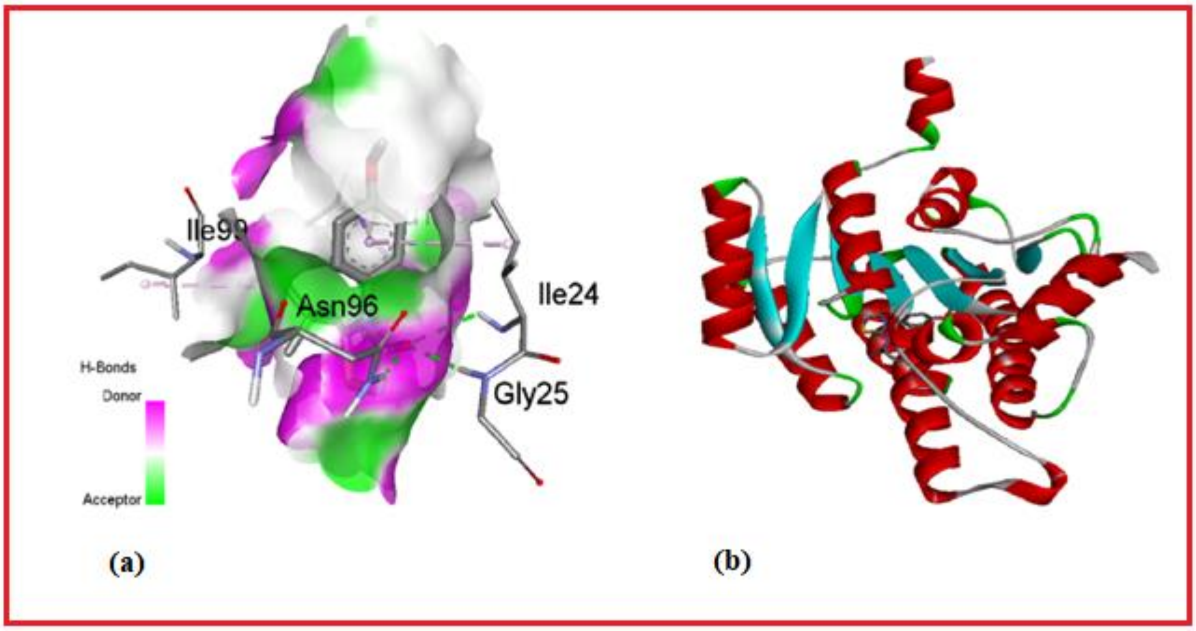

Figure VI.6. (a) 3D ribbon structure of receptor/5U9P protein, (b) interaction between the active site residues of the protein and ligand

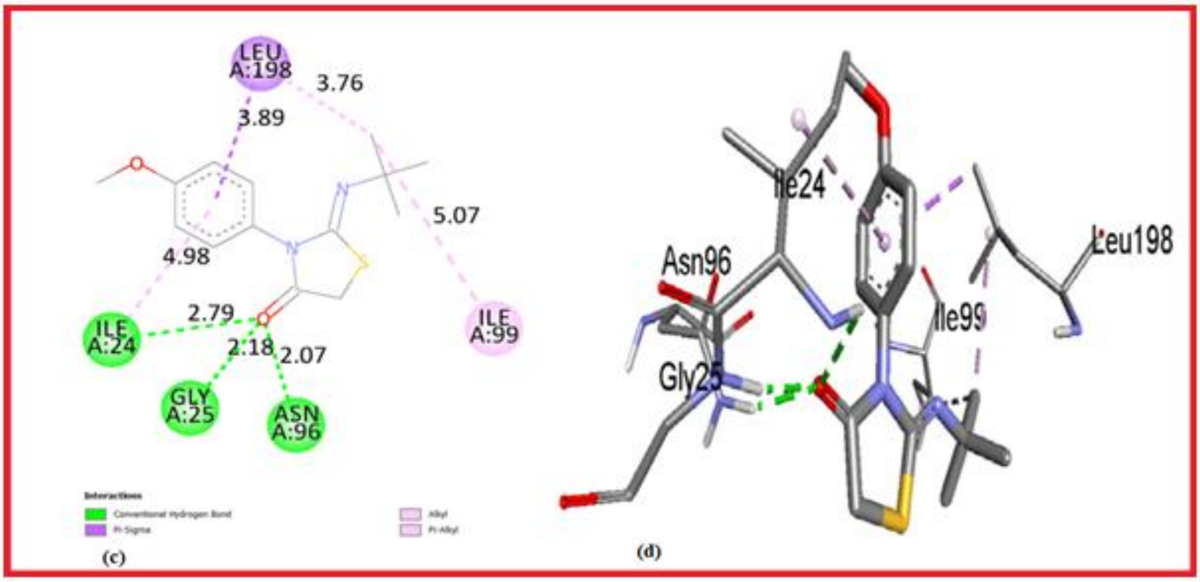

Figure VI.7. (a) 2D form of the 5U9P protein ,and (b) 3D form intermolecular interactions connecting the structure

VI.4.4.2. In silico ADMET investigation

The ADMET study has thoroughly investigated the biological properties of organic substances, including their absorption, distribution, metabolism, excretion, and toxicity. An ADMET study was performed on the title molecule, and the corresponding pharmacokinetic and physicochemical results are summarized in Table 11. The drug-likeness characteristics of TMTh were determined using Lipinski's rule of five, a commonly used method in such investigations **[82]**. The specific results may be seen in Table S2. The SwissADME server was employed to assess the characteristics of Lipinski's rule of five.

The results confirm good bioavailability of the title chemical by showing compliance with Lipinski's rule of five. In addition, we employed rule-based filters developed by Lipinski, Ghose, Veber, and Egan to evaluate the anticipated drug-likeness metrics. Adhering to the specific criteria established in prior studies, particularly for medications taken by mouth, is of utmost importance in this situation **[83**, **84]**.

Figures 10 depicts the bioavailability radar and the BOILED-EGG model for TMTh. The position of the red dot in Figure 9 indicates positive blood-brain barrier (BBB) penetration and gastrointestinal (GI) absorption characteristics, although a negative P-GP impact is seen. The Total Polar Surface Area (TPSA) is a crucial factor in determining the favourable Blood-Brain Barrier (BBB) outcome. The compound's TPSA value of 67.20 Å2 is within the suitable range for this domain.

Based on the data provided in Table S2, the title compound has a noteworthy skin permeation parameter (Log Kp = -5.97 cm/s), increased gastrointestinal absorption, and positive blood-brain barrier permeability. Consequently, the title compound shows promise as a strong therapeutic candidate with the capacity to cross the blood-brain barrier **[85]**. Typically, a TPSA value lower than 90 Å2 is necessary for the penetration of the blood-brain barrier. Ultimately, the drug-likeness investigation substantiates the classification of the examined molecule as a promising candidate for an effective oral medication. Based on the data shown in Figure 10, the title chemical is expected to have inhibitory effects on kinase protein (60%), membrane receptor (13.3%), enzyme (13.3%), phosphodiesterase (6.7%), and other cytosolic proteins (6.7%).

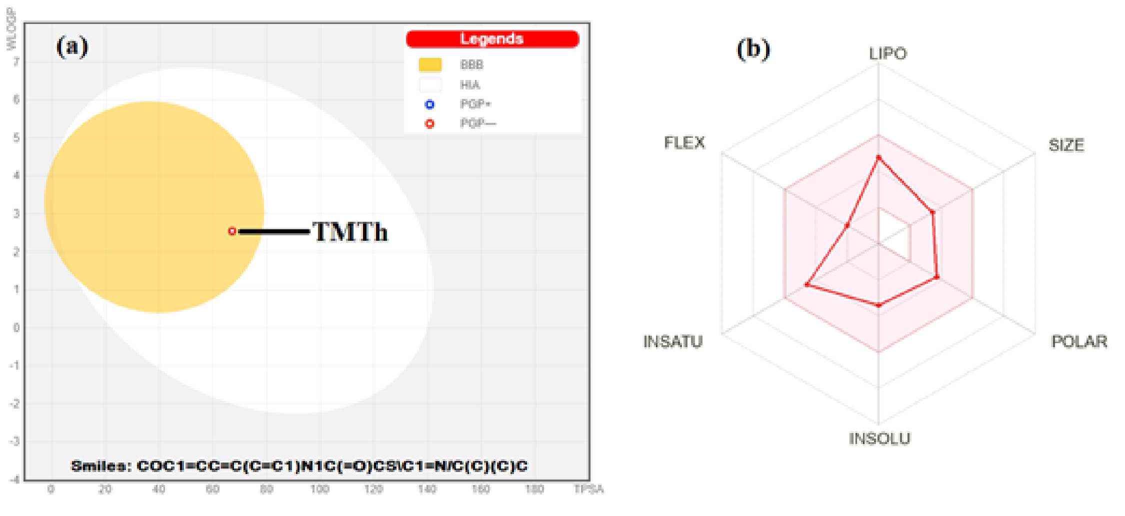

Figure VI. 8. (a) TMTh blood brain barrier (BBB) permeability [BOILED-EGG], and (b) TMTh oral bioavailability radar

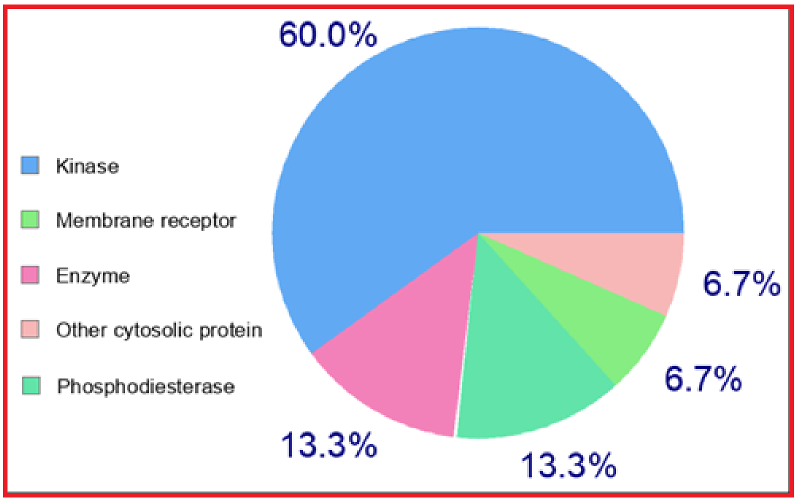

Figure VI.9. Druggability predictions of the title compound

Table VI.12. Physicochemical and pharmacokinetic properties for TMTh

Physicochemical Properties	
Formula	C14H18N2O2S
Molecularweight	278.37 g/mol
Numberheavyatoms	19
Numberaromaticheavyatoms	6
Fraction Csp^3	0.43
Numberrotatable bonds	3
Numberhydrogen bond acceptors	3
Numberhydrogen bond donors	0
Molarrefractivity	83.51
TPSA	67.20 $Å^2$
Lipophilicity	
Consensus $LogP_{o/w}$	2.64
Water Solubility	
LogS	-3.40
Solubility	1.12×E-01 mg/ml
Pharmacokinetics	
GI absorption	High
BBB permeant	Yes
P-GP substrate	No
CYP1A2 inhibitor	Yes
CYP2C19 inhibitor	Yes
CYP2C9 inhibitor	Yes
CYP2D6 inhibitor	No
CYP3A4 inhibitor	No
$LogK_p$ (skin permeation)	-5.97 cm/s
Drug-likeness	
Lipinski	Yes (0 violation)
Ghose	Yes
Veber	Yes
Egan	Yes
Muegge	Yes
Bioavailability score	0.55
MedicinalChemistry	
PAINS	0 alert
Brenk	1 alert: imine_1
Leadlikeness	Yes
Syntheticaccessibilty	3.20 (from 1 (very easy) to 10 (very difficult))

VI.5. Molecular Dynamics (MD) Simulation

Molecular dynamics (MD) simulation is a computer method that is essential for studying the complex behaviours of biomolecules, such as proteins and ligands, at the atomic scale. This work utilized molecular dynamics (MD) simulation to evaluate the efficacy of ligand binding on protein structures. The simulation was performed using the GROMACS 2022 program [86], and the protein topology was constructed using the CHARMM36 force field. The system was solvated using the TIP3P water model and achieved neutralization by introducing Na+ and Cl^- ions [87]. The PDB IDs were used as the starting point for the simulation, which aimed to examine the stability of ligands in the protein's binding site. The simulation lasted for 100 nanoseconds, with a temperature of around 299 K and pressure coupling set at roughly 1.26 bar. Throughout this duration, the system was intricately crafted to maximize energy efficiency. The energy minimization process utilized the steepest descent technique, while position restraint was implemented with NVT (100 ps) and NPT (100 ps) ensembles. The Berendsen thermostat and the Parrinello-Rahman barostat were applied to stabilize temperature and pressure, respectively [88, 89].

The simulation trajectory demonstrated that the ligand, which was originally docked, remained stable within the protein's binding site with very slight conformational alterations. The graphical program XMGRACE v5.1.19 was utilized for thorough data examination [90]. In addition, GROMACS 2022 was used to determine important parameters such as root mean square deviation (RMSD), root mean square fluctuation (RMSF), radius of gyration (Rg), the number of hydrogen bonds established between the protein and the ligand, and interaction energy. These new properties give us important information about the stability and dynamics of the protein-ligand complex. They also suggest possible ways to improve ligand binding in the context of developing new medicines.

VI.5.1. The root means square deviation (RMSD):

The Root Mean Square Deviation (RMSD) technique is employed to compute the average displacement of atoms in a particular frame with respect to a reference frame. The computation is executed for every frame along the trajectory, where the root mean square deviation (RMSD) for frame x is determined using the following formula:

$$RMSD_X = \sqrt{\frac{1}{N}\sum_{i=1}^{N}\left(r_i'(t_X) - r_i\left(t_{ref}\right)\right)^2}$$

Where r' is the position of the selected atoms in frame x after superimposing on the reference frame, where frame x is recorded at timet_X; N is the number of atoms in the atom selection; and

t_{ref} is the reference time (usually the first frame is used as the reference and it is regarded as time t=0). This procedure is iterated for each frame in the simulation track.

The picture displays the progression of RMSD when applied to proteins, with the left Y-axis representing the values. Before calculating the root mean square deviation (RMSD), the protein frames are aligned using the reference frame backbone. This alignment allows for a better understanding of the structural conformation changes. The assessment of Root Mean Square Deviation (RMSD) helps ascertain the equilibrium state of the simulation, where oscillations observed towards the end of the run suggest the presence of a thermal average structure. Changes within the 1-3 Å range are appropriate for small, globular proteins, but bigger changes indicate substantial structural adjustments throughout the simulation. Convergence is essential, as evidenced by the stabilized RMSD values, which indicate equilibration.

The ligand RMSD (root mean square deviation) measures the stability of ligands about the protein and its binding pocket. The 'Lig fit Prot' and 'Lig fit Lig' values in the figure indicate the ligand's root-mean-square deviation (RMSD) after aligning it with the reference protein backbone and measuring it only on the reference conformation. This RMSD measurement captures the ligand's internal oscillations.

The given data depicts the root mean square deviation (RMSD) in figure of the TNF-α protein (PDB ID: 2AZ5) and the molecule (Z)-3-ethyl-2-((3-methoxyphenyl)imino)thiazolidin-4-one throughout a 100 nanosecond simulation period, respectively. The root mean square deviations (RMSDs) for the 2AZ5 (apo form) and 2AZ5-ZEMIT complex, measured from 0 to 100 ns, are 1.27 nm and 6.20 nm, respectively. Significantly, the 2AZ5- ZEMIT complex achieves equilibrium from 10 to 70 nanoseconds, demonstrating its relative stability throughout the experiment. The ligand EMTh demonstrates different mean root mean square deviations (RMSD) for a duration of 100 ns, indicating that it remains at the binding site of 2AZ5 without notable dispersion.

RMSD is a critical metric for assessing differences between conformations. Higher RMSD values indicate greater variability. The provided data presents the RMSD values for the 5U9P protein and the 5U9P-TMTh complex over a 50 nanoseconds simulation period. The RMSD values for the 5U9P (apo form) and 5U9P-TMTh complex, measured from 0 to 100 ns, are 0.27 nm and 0.20 nm, respectively. Importantly, the 5U9P-TMTh complex reaches equilibrium within 30 nanoseconds, demonstrating its relative stability throughout the experiment. The ligand TMTh maintains a mean RMSD of 0.03 nm throughout 100 ns, indicating its consistent presence at the binding site of 7XA2 without significant dispersion.

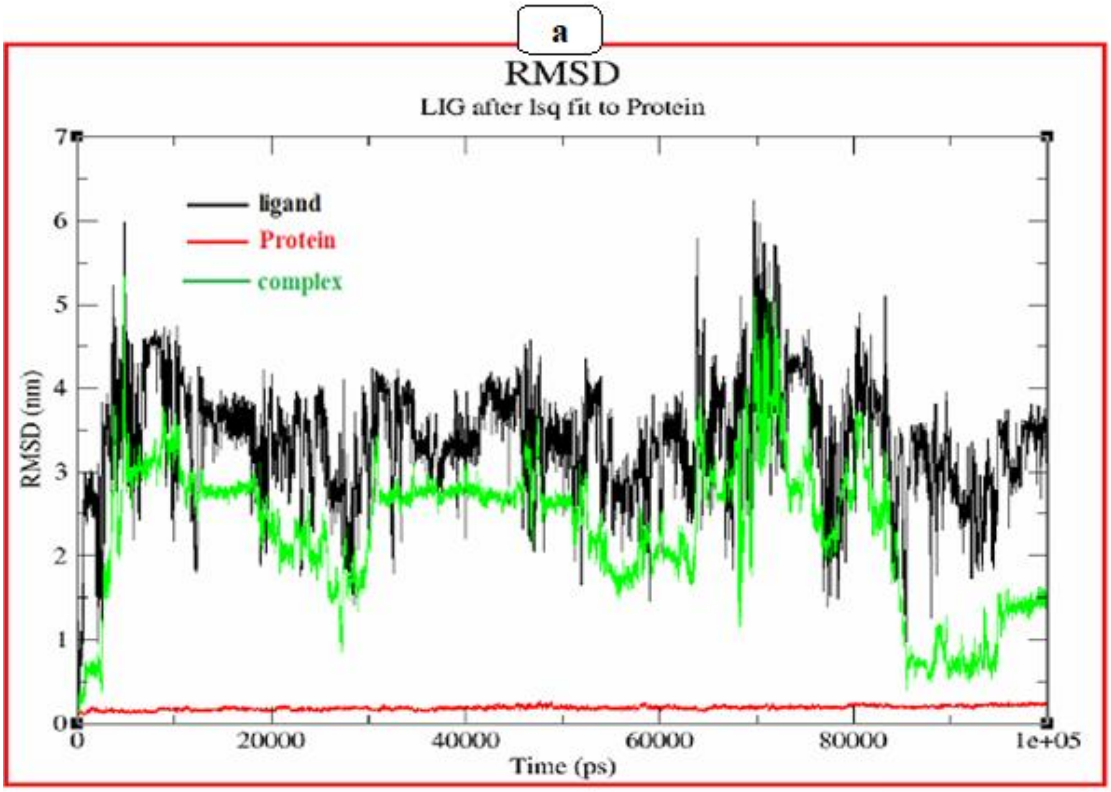

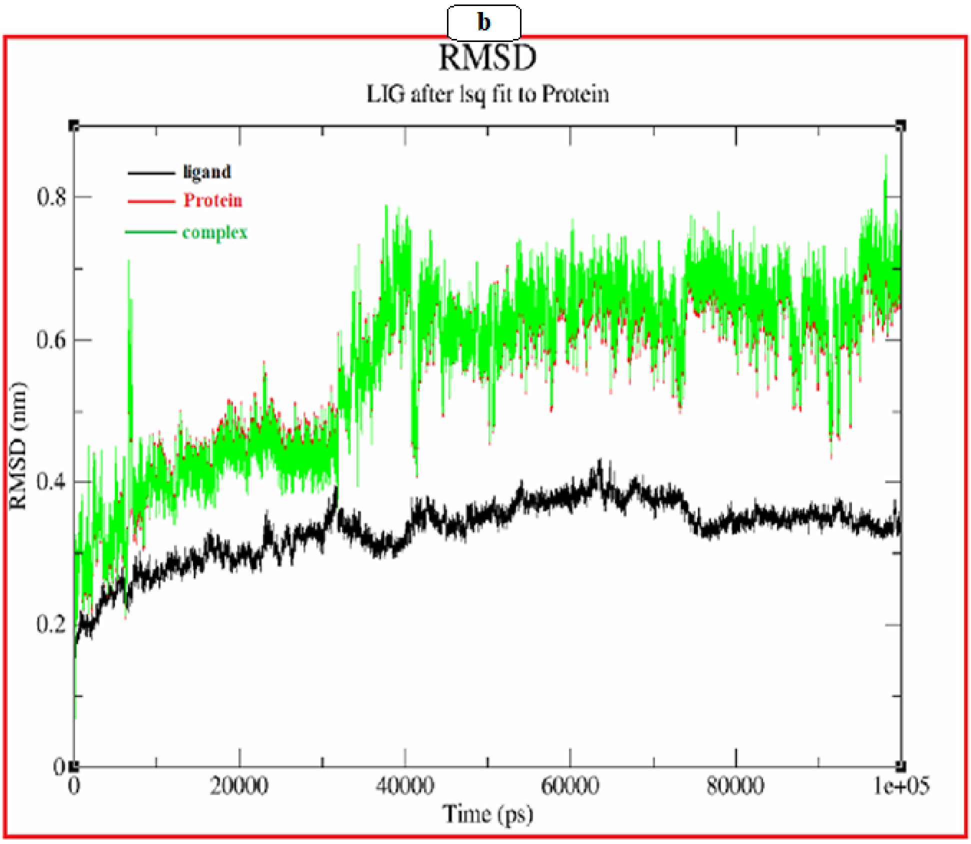

Figure VI. 10.MD simulation trajectories at 100 ns. a. RMSD EMTh complex and b. RMSD TMTh complex, over the time of simulation Red: Protein, black: Protein-HTBH complex, green: ligand.

VI.5.2. The Ligand Root Mean Square Fluctuation (L-RMSF)

The Ligand Root Mean Square Fluctuation (L-RMSF) is a valuable tool for assessing variations in the locations of atoms inside the ligand. The root mean square fluctuation (RMSF) for atom i is calculated using the formula:

$$RMSF_i = \sqrt{\frac{1}{T}\sum_{t=1}^{T}\left(r_i'(t) - r_i\left(t_{ref}\right)\right)^2}$$

Where T represents the total number of time steps, $r_i'(t)$ denotes the position of atom i at time t, and $r_i\left(t_{ref}\right)$ represents the reference position of atom i.

The RMSF is calculated over a trajectory time T. The reference time t ref, typically the first frame, is considered as the zero point of time. r represents the position of atom i in the reference frame at time t ref, while r' represents the position of atom i at time t after being superimposed on the reference frame. The ligand's root mean square fluctuation (RMSF) provides a breakdown of the fluctuations of each atom in the ligand, which corresponds to the two-dimensional structure displayed in the top panel. The root mean square fluctuation (RMSF) of the ligand might provide valuable information on the interaction between ligand fragments and the protein, as well as their contribution to the binding event's entropy. The 'Fit Ligand on Protein' line in the bottom panel displays the ligand variations relative to the protein. The protein-ligand complex is initially aligned based on the protein backbone, and then, the root mean square fluctuation (RMSF) of the ligand is calculated specifically for its heavy atoms.

RMSF, or root mean square fluctuation, quantifies the average variance of protein residues within a specific time interval. The protein's flexibility or stiffness in various regions is revealed by this information [91, 92]. Lower root mean square fluctuation (RMSF) levels indicate greater rigidity or stability in certain areas, whereas larger values indicate significant fluctuations. Figure 8C displays the root mean square fluctuation (RMSF) plot of the protein and ligand. The study reveals that the docked 2AZ5 exhibits distinct minor changes at different residue levels. The interaction between the ligand and the binding pocket location of 2AZ5 leads to a protein structure that is more stable, exhibiting less mobility and flexibility and this is not appearing for 7XA2 protein due to the movement of this protein inside the critical box.

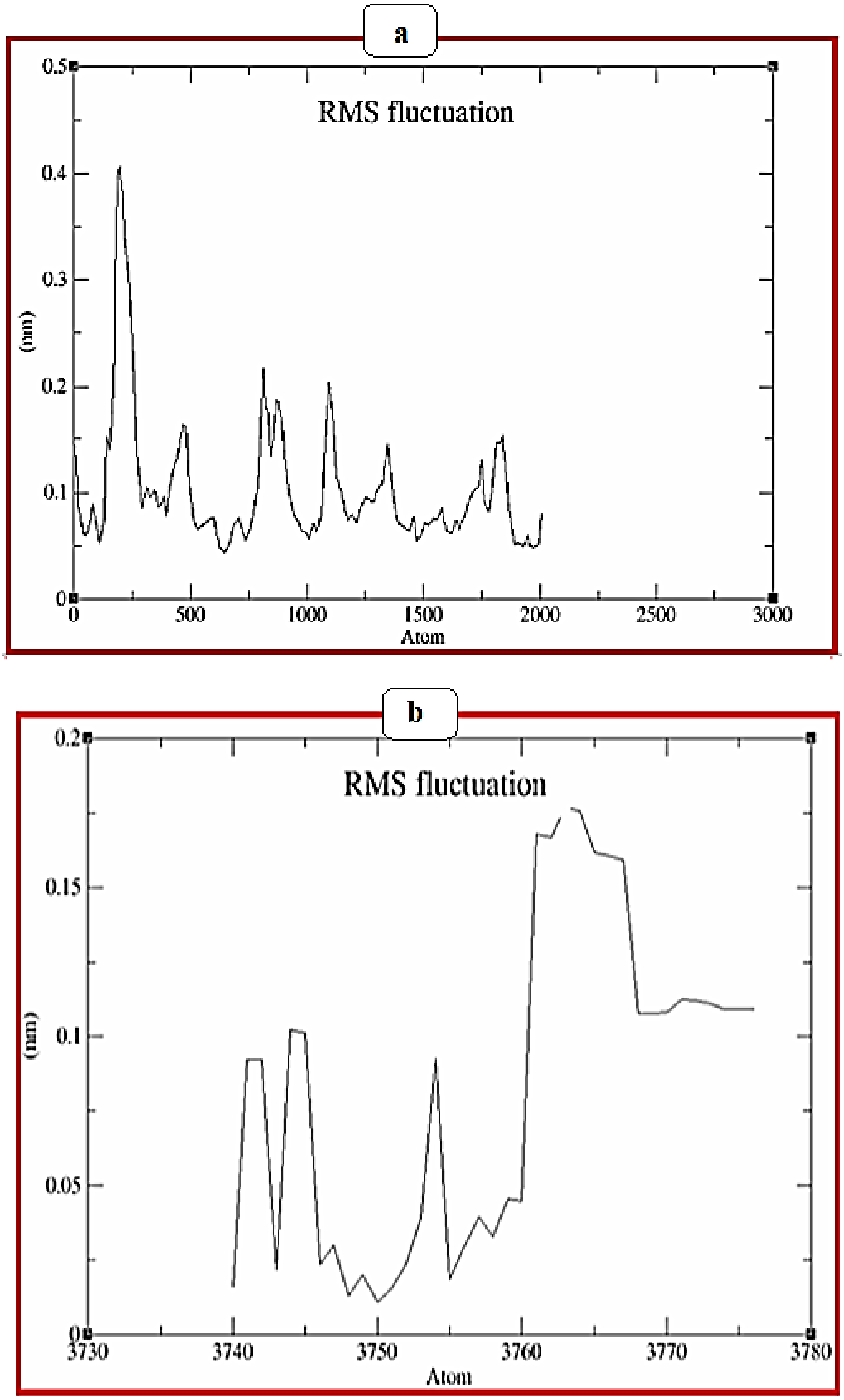

FigureVI.11.MD simulation trajectories at 100 ns. a. RMSF EMTHligand and b. RMSF TMTh ligand, over the time of simulation

VI.5.3. The radius of gyration (Rg)

The radius of gyration (Rg) is an important measure that provides valuable information on the structural density of a protein complex and the distribution of mass around its central point. In the field of molecular dynamics (MD) research, the parameter Rg is shown to be beneficial, especially for evaluating the effectiveness of protein-ligand interactions [93].

Rg plays a crucial role in measuring the degree to which mass is distributed within the complex. A higher Rg number implies a less condensed structure, which may lead to a potential reduction in stability. During the early 1500 picoseconds of the MD analysis, there is a noticeable and considerable increase in the Rg. After the initial phase of growth, the Rg values reach a stable state, oscillating between 0.29 and 0.34 nanometers, as seen in Figure 8B. In the early 19000 picoseconds of the MD analysis, there is a noticeable and considerable stabilization in the Rg at 1.8 nm. After the initial stable phase, the Rg values decrease to a stable state, oscillating between 1.77 and 1.82 nanometers, as seen in Figure 8B.

The observed stabilization in Rg values suggests a shift towards a more uniform and steady structure of the protein complex. These stable ranges of values indicate an evenly distributed mass around the center, indicating a condition of structural equilibrium. Using Rg as a structural parameter provides vital insights into the dynamic behaviour of the protein complex over time, improving our knowledge of its stability and conformational changes during the molecular dynamics simulation.

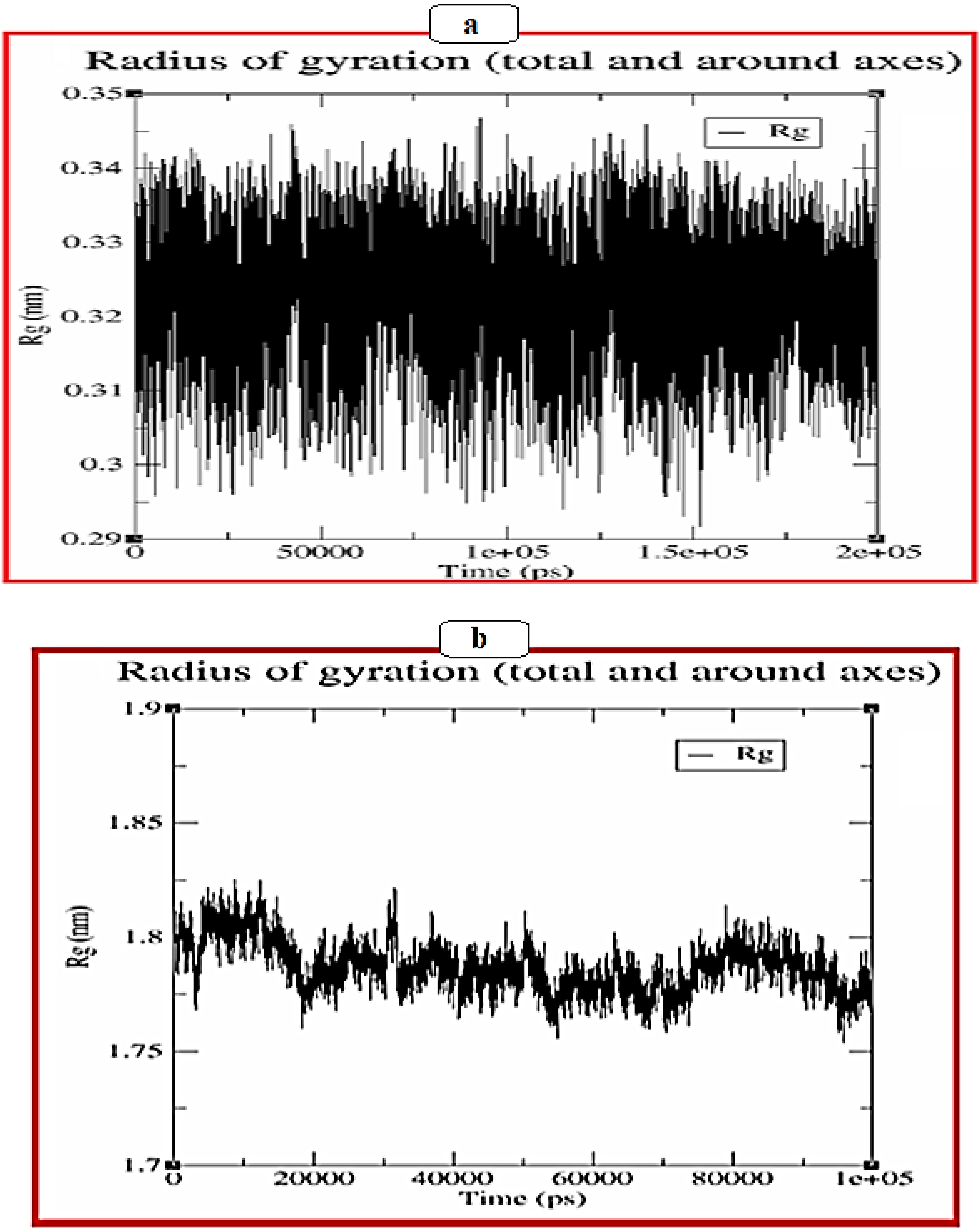

FigureVI.12. MD simulation trajectories at 100 ns. a. Rg EMTh ligand and b. Rg TMTh ligand, over the time of simulation

VI.5.4. The solvent accessible surface area (SASA)

The examined solvent-accessible surface area (SASA) of both the protein and the complex is represented in Figure 8D. The graph provides significant insights into the behaviour of the complex when compared to the protein form.

The graph shows that the complex continually displays a consistent deviation and consistently maintains a lower average value of solvent accessibility during the whole simulation period, in comparison to the protein form [94]. The observed trend in SASA values indicates that the compound exhibits increased stability. Furthermore, the decreased average solvent accessibility indicates that the complex maintains a denser structure throughout the simulation.

The SASA analysis yields significant insights into the intricate dynamics of the complex and its interaction with the solvent environment. The complex's stability and compactness, as evidenced by its decreased average solvent accessibility, provide important insights into its structural integrity over the simulation period. The findings are crucial for comprehending the molecular dynamics and interactions of the system being researched, hence aiding in a full characterization of the protein-ligand complex under inquiry.

VI.5.5. The Poisson-Boltzmann equation and molecular mechanics (MM-PBSA)

Under the context of the complex's environmental circumstances, a thorough assessment of binding energy is performed with increased accuracy using the Poisson-Boltzmann equation and molecular mechanics (MM-PBSA), surpassing the level of detail attained by docking approaches. The energy landscape, as outlined in Table 9 via the MM-PBSA investigation, offers a thorough summary of different energetic constituents.

The protein-ligand interaction involving 2AZ5- ZEMIT has a binding energy of -31.2 kJ/mol (figure 16), the van der Waals energy is precisely determined to be -50.39 kJ/mol, which supports and strengthens the conclusions drawn from the molecular docking analysis. Unlike the docking results, which do not provide a clear indication of electrostatic interactions, the MM-PBSA analysis accurately measures the electrostatic energy as -2.60 kJ/mol (table 12). This difference highlights the increased prediction precision of energy levels attainable with MM-PBSA analysis.

More specifically, the primary molecule being examined demonstrates energies of 27.61, -5.80, and -52.99 kJ/mol for polar solvation, nonpolar solvation energy, and solvation energies, respectively. These detailed energy calculations provide insight into the complex interplay of forces that regulate the molecular interactions inside the system. The integration of MM-PBSA techniques enhances the accuracy and dependability of the acquired results by providing a more detailed comprehension of the thermodynamics and energy involved in the protein-ligand complex.

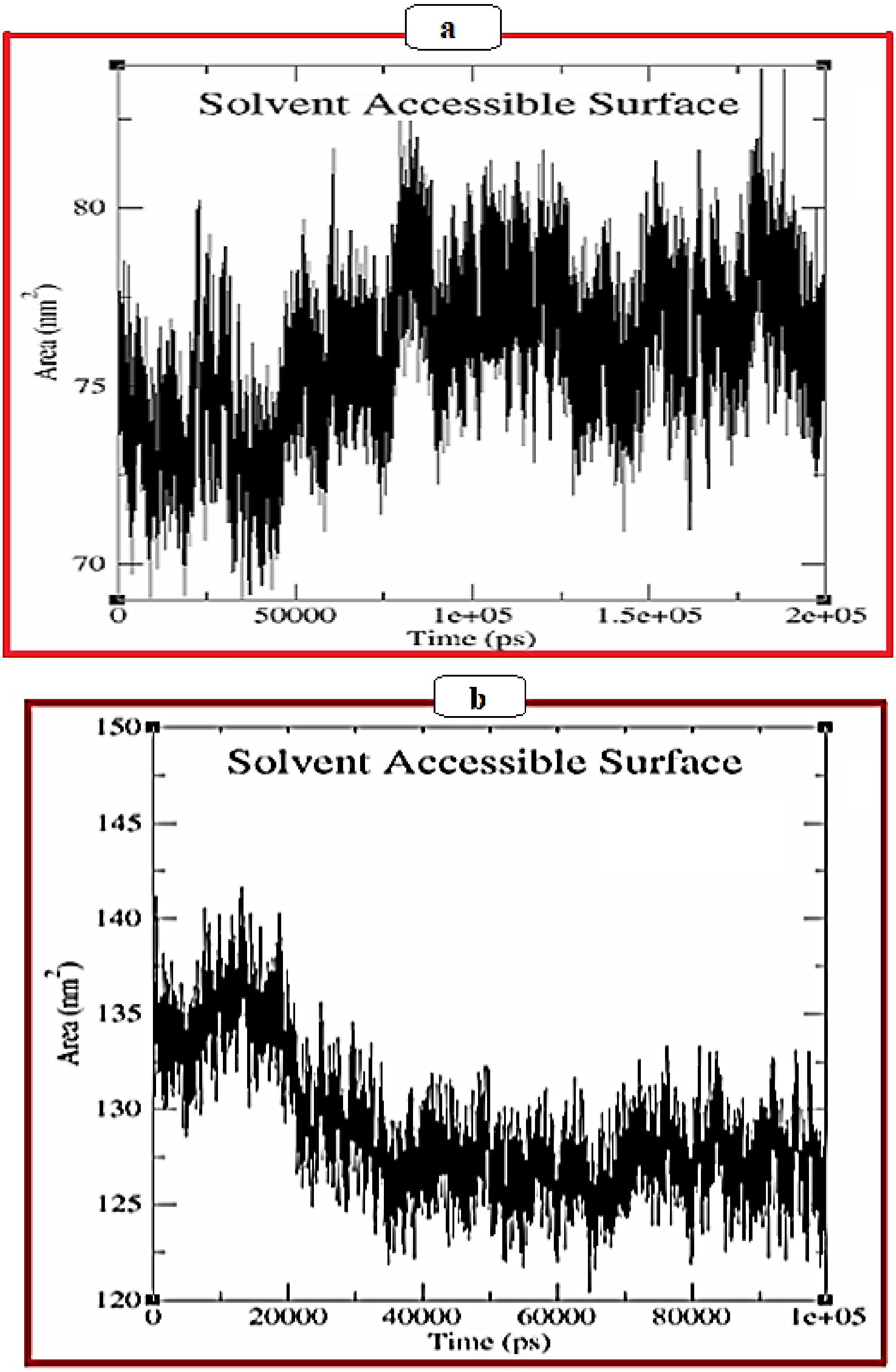

FigureVI.13. MD simulation trajectories at 100 ns. a. SASA for complex 1 , and a. SASA for complex 2 over the time of simulation.

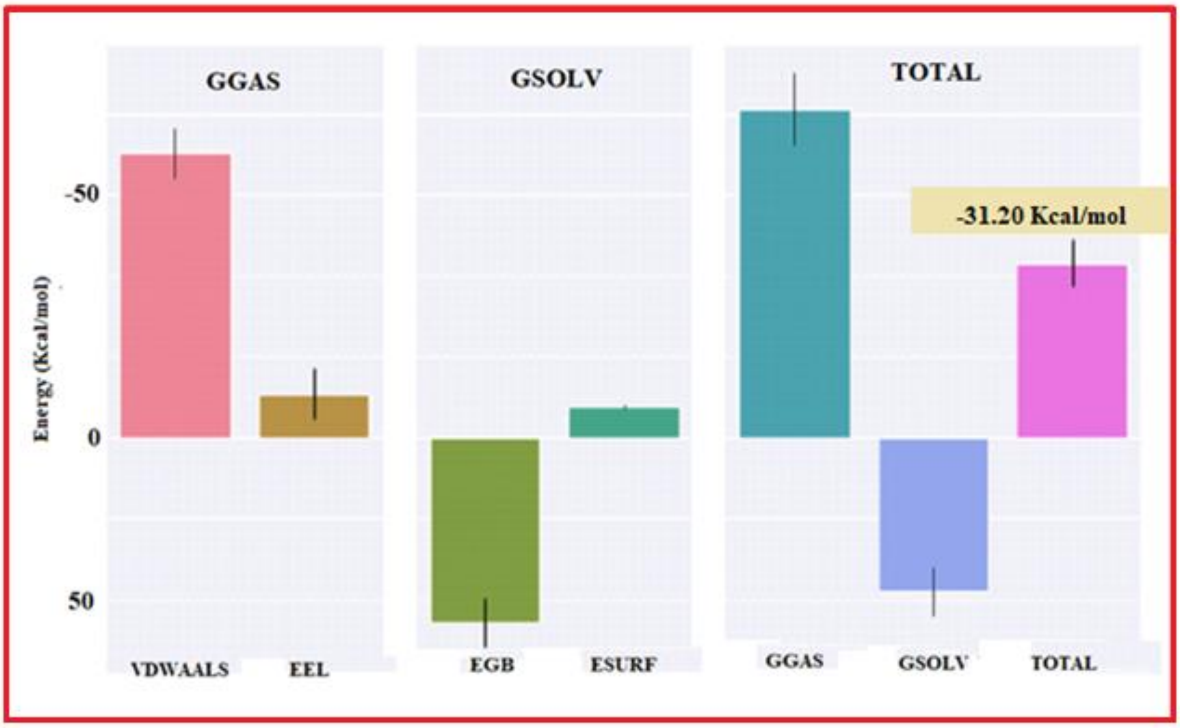

FigureVI.14. Binding energy of the complex 2AZ5- EMTh calculated by MM-PBSA

Table VI.13. Binding energy and other energies values of the 2AZ5- EMTh complex

Type of energy	**Value (kJ/mol)**
van der Waals energy	-50.39
Electrostatic energy	-2.60
Polar solvation energy	27.61
Nonpolar solvation energy	-5.80
solvation energy	-52.99
Binding energy	-31.20
Temperature	298.15 K

The protein-ligand interaction in the 5U9P-TMTh complex has a binding energy of -34.2 kJ/mol (figure 17) . The van der Waals energy is accurately measured to be -55.23 kJ/mol, providing more evidence that confirms and reinforces the findings derived from the molecular docking research. The docking data do not offer a definitive indication of electrostatic interactions, but the MM-PBSA analysis provides an exact measurement of the electrostatic energy as -2.85 kJ/mol (Figure 17). The disparity emphasizes the enhanced accuracy in predicting energy levels achievable using MM-PBSA analysis.

To be more precise, the main molecule under investigation exhibits energies of 30.26, -6.35, and 58.08 kJ/mol for polar solvation, nonpolar solvation energy, and solvation energies, respectively (table 13). The meticulous energy calculations offer a profound understanding of the intricate dynamics of the forces that govern the molecular interactions inside the system. The use of MM-PBSA methods improves the precision and reliability of the obtained results by offering a more comprehensive understanding of the thermodynamics and energetics associated with the protein-ligand complex.

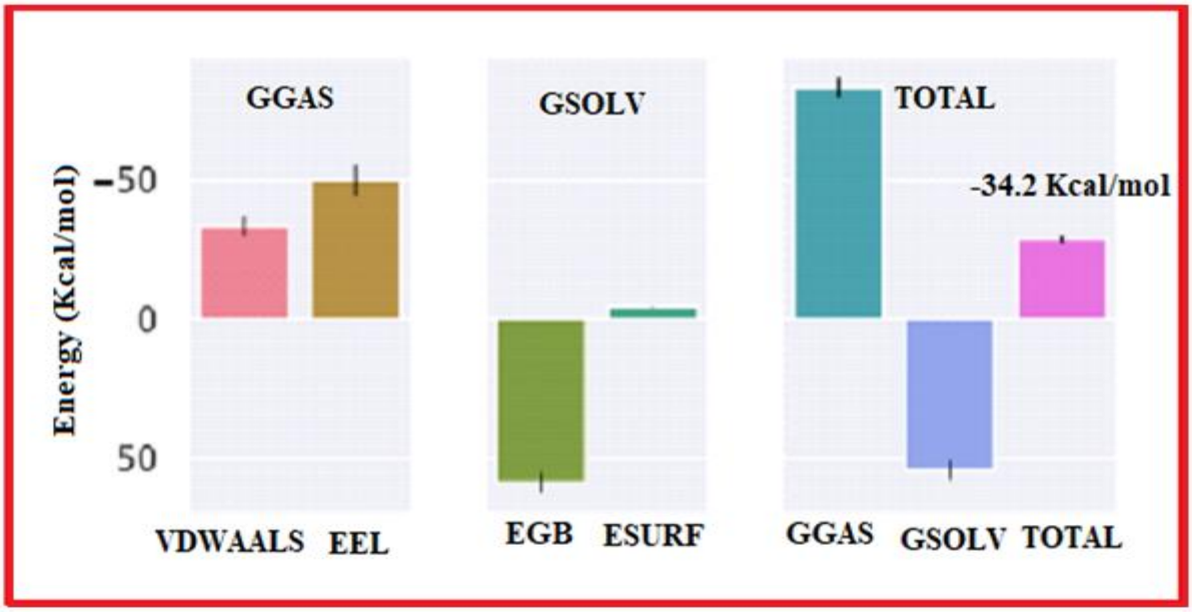

FigureVI.15. Binding energy of the complex 5U9P-TMTh calculated by MM-PBSA

TableVI.14. Binding energy and other energies values of the 5U9P-TMTh complex

Type of energy	**Value (kJ/mol)**
van der Waals energy	-55.23
Electrostatic energy	-2.85
Polar solvation energy	30.26
Nonpolar solvation energy	-6.35
solvation energy	58.08
Binding energy	-34.2
Temperature	298.15 K

VI.6. Conclusion

The molecular docking investigation revealed the medicinal potential of the title chemical, emphasizing its highest binding affinity at the TNF-α receptor protein (PDB ID: 2AZ5). This research not only improves our understanding of the structural properties of the synthesized chemical, but also suggests promising potential in the realm of medicinal chemistry. An investigation was conducted on the nonlinear optical (NLO) phenomenon of TMTh, employing the DFT approach with B3LYP functional for calculations. The latter anticipated more advantageous nonlinear optical (NLO) characteristics, indicating possible uses in optoelectronics. The biological activity of TMTh was evaluated using in silico molecular docking methods, indicating its potential as an inhibitor of the gluconate-2-dehydrogenase protein. The ADMET findings and drug-likeness analysis suggest that TMTh has the potential to be a good candidate for an orally active medication.

The work utilizes Molecular Dynamics (MD) simulation, specifically employing the GROMACS 2022 program with CHARMM36 force field, to assess the effectiveness of ligand binding on protein structures. The simulation, utilizing PDB ID 4ZA2, specifically examines the stability of TMTh within the protein's binding site. It spans duration of 100 nanoseconds at a temperature of 299 K and a pressure of 1.26 bar. The analysis involves the examination of many parameters, including Root Mean Square Deviation (RMSD), Root Mean Square Fluctuation (RMSF), Radius of Gyration (Rg), and Solvent Accessible Surface Area (SASA). The stability of the ligand inside the protein binding site is verified with minimal changes in shape. The RMSD and RMSF studies indicate that the system has reached equilibrium and that the ligand is undergoing internal oscillations. Rg denotes a protein complex structure that is stable, whereas SASA demonstrates the enhanced stability and more compact structure of the complex in comparison to the individual protein. The study employs the Poisson-Boltzmann equation and molecular mechanics (MM-PBSA) to thoroughly evaluate the binding energy, resulting in a more precise and comprehensive comprehension of the thermodynamics and energetics associated with the protein-ligand complex. This approach supports and strengthens the conclusions drawn from molecular docking analyses.

References

[1] M.J. Frisch, G.W. Trucks, H.B. Schlegel, G.E. Scuseria, M.A. Robb, J.R. Cheeseman, G. Scalmani, V. Barone, B. Mennucci, G.A. Petersson, H. Nakatsuji, M. Caricato, X. Li, H.P. Hratchian, A.F. Izmaylov, J. Bloino, G. Zheng, J.L. Sonnenberg, M. Hada, M. Ehara, K. Toyota, R. Fukuda, J. Hasegawa, M. Ishida, T. Nakajima, Y. Honda, O. Kitao, H. Nakai, T. Vreven, J.A. Montgomery, J.E. Peralta, F. Ogliaro, M. Bearpark, J.J. Heyd, E. Brothers, K.N. Kudin, V.N. Staroverov, R. Kobayashi, J. Normand, K. Raghavachari, A. Rendell, J.C. Burant, S.S. Iyengar, J. Tomasi, M. Cossi, N. Rega, J.M. Millam, M. Klene, J.E. Knox, J.B. Cross, V. Bakken, C. Adamo, J. Jaramillo, R. Gomperts, R.E. Stratmann, O. Yazyev, A.J. Austin, R. Cammi, C. Pomelli, J.W. Ochterski, R.L. Martin, K. Morokuma, V.G. Zakrzewski, G.A. Voth, P. Salvador, J.J. Dannenberg, S. Dapprich, A.D. Daniels, Ö. Farkas, J.B. Foresman, J.V. Ortiz, J. Cioslowski, D.J. Fox, Gaussian 09, Revision D.01, Gaussian Inc., Wallingford CT, 2009.

[2] E. Frisch, H.P. Hratchian, R.D. Dennington, T.A. Keith, John Millam, B. Nielsen, A.J. Holder, J. Hiscocks, Gaussian, Syntheses, Structural Elucidation, Thermal Properties, Theoretical Quantum Chemical Studies (DFT) and Biological Studies of BarbituriceHydrazone Complexes Inc. GaussView version 5.0.8, 2009.

[3] S. Bibi, M. Khan, S. ur-Rehman, M. Yaseen, S. Muhammad, R. Nadeem, N. Jahan, S. Noreen, Misbah, Investigation analysis of optoelectronic and structural properties of cis- and trans-structures of azo dyes: density functional theory study, J. Phys. Org. Chem. 34 (2021) -4183. https://doi.org/10.1002/poc.4183

[4] S. Yahiaoui, A. Moliterni, N. Corriero, C. Cuocci, K. Toubal, A. Chouaih, A. Djafri, F. Hamzaoui, 2-thioxo- 3N-(2-methoxyphenyl) -5 [4'-methyl -3'N -(2'-methoxyphenyl) thiazol-2'(3'H)-ylidene] thiazolidin-4-one: synthesis,characterization, X-ray single crystal structure investigation and quantumchemical calculations, J. Mol. Struct. 1177 186–192(2019).https://doi.org/10.1016/j.molstruc.2018.09.052.

[5] S. Demir, A.O. Sario˘glu, S. Güler, N. Dege, M. S¨onmez, Synthesis, crystal structureanalysis, spectral IR, NMR UV-Vis investigations, NBO and NLO of 2-benzoyl-N-(4-chlorophenyl)-3-oxo-3-phenylpropanamide with use of X-ray diffractionsstudies along with DFT calculations, J. Mol. Struct. 1118, 316–324 (2016). https://doi.org/10.1016/j.molstruc.2016.04.042.

[6] M. Azayez, S. Chetioui, Y. Megrouss, N. Boukabcha, A. Djedouani, A. R. Guerroudj, N. MeddahAraibi, A. Chouaih, Experimental and theoretical spectroscopic characterization, Hirshfield surface analysis, TD-DFT calculation, and nonlinear optical properties of (E)-1-

[(2,4,6tribromophenyl)diazenyl]-naphthalen-2-ol azo dye, J. Mol. Struct. 1261, 132887 (2022). https://doi.org/10.1016/j.molstruc.2022.132887

[7] Ž.B. Milanovic´, Z.S. Markovic´, D.S. Dimic´, O.R. Klisuric´, I.D. Radojevic´, D.S. Šeklic´, M.N. Živanovic´, J.D. Markovic´, M. Radulovic´, E.H. Avdovic´, Synthesis, structural characterization, biological activity and molecular docking study of 4,7-dihydroxycoumarin modified by aminophenol derivatives, ComptesRendus. Chim. 24, 215–232(2021). https://doi.org/10.5802/crchim.68

[8] M. Azayez, S. Chetioui, Y. Megrouss, N. Boukabcha, A. Djedouani, A.R. Guerroudj, N. Meddah Araibi, A. Chouaih, Experimental and theoretical spectroscopic characterization, Hirshfield surface analysis, TD-DFT calculation, and nonlinear optical properties of (E)-1-[(2,4,6tribromophenyl)diazenyl]-naphthalen-2-ol azo dye, J. Mol. Struct. 1261 (2022), 132887, https://doi.org/10.1016/j

[9] R. Rahmani, N. Boukabcha, A. Chouaih, F. Hamzaoui, S. Goumri-Said, On the molecular structure, vibrational spectra, HOMO-LUMO, molecular electrostatic potential, UV–Vis, first order hyperpolarizability, and thermodynamic investigations of 3-(4-chlorophenyl)-1-(1yridine-3-yl) prop-2-en-1-one by quantum chemistry calculations, J. Mol. Struct. 1155 (2018) 484–495, https://doi.org/ 10.1016/j.molstruc.2017.11.033.

[10] M. Drissi, N. Benhalima, Y. Megrouss, R. Rahmani, A. Chouaih, F. Hamzaoui, Theoretical and experimental electrostatic potential around the m-nitrophenol molecule, Molecules 20 (2015) 4042–4054, https://doi.org/10.3390/ molecules20034042.

[11] PASS Online prediction. http://www.way2drug.com/passonline/.

[12] P. P. Shinoj Kumar, G. Krishnaswamy, N. R. Desai, S. Sreenivasa, and D. B. Aruna Kumar, Chem. Data Collect. 31, 100617 (2021). https://doi.org/10.1016/j.cdc.2020.100617

[13] O. Trott, A.J. Olson, AutoDockVina: improving the speed and accuracy of docking with a new scoring function, efficient optimization, and multithreading, J. Comput. Chem. NA-NA(2009), https://doi.org/10.1002/jcc.21334

[14] G.M. Morris, R. Huey, W. Lindstrom, M.F. Sanner, R.K. Belew, D.S. Goodsell, A.J. Olson, AutoDock4 and AutoDockTools4: automated docking with selective receptor flexibility, J. Comput. Chem. 30, 2785–2791(2009), https://doi.org/10.1002/jcc. 21256

[15] DassaultSystemes BIOVIA: Discovery studio visualizer 21.1.0.20298 (2020). 2021.

[16] W. L. Delano, ThePyMOL molecular graphics development component, Version 1.8, Schrodinger, LLC, New York, NY, USA, (2015).

[17] C.A. Lipinski, Lead- and drug-like compounds: the rule-of-five revolution, Drug Discovery Today: Technologies 1, 337–341 (2004). https://doi.org/10.1016/j.ddtec.2004.11.007

[18] A. Daina, O. Michielin, V. Zoete, SwissADME: a free web tool to evaluate pharmacokinetics, drug-likeness and medicinal chemistry friendliness of small molecules, Sci. Rep., 7 (2017), p. 42717.

[19] H. Bekker, H.J.C. Berendsen, E.J. Dijkstra, S. Achterop, R. van Drunen, D. van der Spoel, A. Sijbers, H. Keegstra, M.K.R. Renardus, Gromacs: A parallel computer for molecular dynamics simulations. In Physics Computing 92, Proceedings of the 4th International Conference, Prague, Czech Republic, 24–28 August 1992; de Groot, R.A., Nadrchal, J., Eds.; World Scientific: Singapore, 1993; pp. 252–256.

[20] E. Hückel, « Quantentheoretische Beiträge zum Benzolproblem. I. Die Elektronenkonfiguration des Benzols und verwandter Verbindungen », Zeits. f. Physik 1931, 70, 204-286.

[21] E. Hückel, « Quantentheoretische Beiträge zum Benzolproblem. II. Quantentheorie der induzierten Polaritäten », Zeits. f. Physik 1931, 72, 310-337.

[22] E. Hückel, « Quantentheoretische Beiträge zum Problem der aromatischen und ungesättigten Verbindungen III », Zeits. f. Physik 1932, 76, 628-648.

[23] L. Pauling et G. W. Wheland, « The nature of the chemical bond. V. The Quantum-Mechanical Calculation of the Resonance Energy of Benzene and Naphthalene and the Hydrocarbon Free Radicals », J. Chem. Phys. 1933, 1, 362-374.

[24] K. Fukui, T. Yonezawa et H. Shingu, « A Molecular Orbital Theory of Reactivity in Aromatic Hydrocarbons », J. Chem. Phys. 1952, 20, 722-725.

[25] K. Fukui, T. Yonezawa, C. Nagata et H. Shingu, « Molecular Orbital Theory of Orientation in Aromatic, Heteroaromatic and Other Conjugated Molecules », J. Chem. Phys. 1954, 22, 1433-1442.

[26] G. Klopman, « Chemical Reactivity and the Concept of Charge- and Frontier-ControlledReactions », J. Am. Chem. Soc. 1968, 90, 223-234.

[27] L. Salem, « Intermolecular Orbital Theory of the Interaction between Conjugated Systems. I. General Theory », J. Am. Chem. Soc. 1968, 90, 543-552.

[28] R. G. Parr et W. Yang, « Density-Functional Theory of the Electronic Structure of Molecules », Annu. Rev. Phys. Chem. 1995, 46, 701-728.

[29] P. Geerlings, F. De Proft et W. Langenaeker, « Conceptual Density Functional Theory », Chem.Rev. 2003, 103, 1793-1873.

[30] H. Chermette, « Chemical Reactivity Indexes in Density Functional Theory », J. Comp. Chem. 1999, 20, 129-154.

[31] T. Koopmans, « Uber die zuordnung von wellen funktionen und eigenwerten zu den einzelnen

elektronen eines atom », Physica 1934, 1, 104-113

[32] PThul , V.P Gupta , V.J Ram , P Tandon , Spectrochim. Acta, 75 (2010) 251–260.

[33] P Politzer, J.S Murray, D.L Beveridge, R Lavery (Eds.), Theoretical Biochemistry and Molecular Biophysics: A Comprehensive Survey, Protein Adenine Press, Schenectady, New York, 2 (1991).

[34] P Politzer ,J Murray, Theor. Chem. Acc., 108(2002)134– 142.

[35] R. Rahmani, N. Boukabcha, A. Chouaih, F. Hamzaoui, S. Goumri, J. Mol. Struct. 2018,1155, 484–495. DOI:. org/10.1016/j.molstruc.2017.11.033

[36] H. Benaissi, M. Drissi, S. Yahiaoui, Y. Megrouss, A. Chouaih, F. Hamzaoui, J. Optoelectron. Biomed. M. 2018, 10, 73–82

[37] N. Boukabcha, A. Feddag, R. Rahmani, A. Chouaih, F. Hamzaoui, J. Optoelectron. Adv. M. 2018, 20, 140–148

[38] N. Boubegra, Y. Megrouss, N. Boukabcha, A. Chouaih, F. Hamzaoui, Rasayan. J. Chem. 2016, 9, 751–761.

[39] M. Drissi, N. Benhalima, Y. Megrouss, R. Rahmani, A. Chouaih, F. Hamzaoui, Molecules 2015, 20, 4042–4045. DOI: 10.3390/molecules 20034042

[40] J. S. Murray, K. Sen, Molecular Electrostatic Potentials, Concepts and 399 Applications, Elsevier, Amsterdam, 1996.

[41] E. Scrocco, J. Tomasi, in: P. Lowdin (Ed) Advances in Quantum Chemistry, Academic Press, New York. 1978. 402.

[42] F. J. Luque, M. Orozco, P. K. Bhadane, S. R. Gadre, J. Phys. Chem. 1993, 97, 9380–9384. DOI: org/10.1021/j100139a021

[43] J. Sponer, P. Hobza, Int. J. Quant. Chem. 1996, 57, 959–970. DOI: org/10.1002/(SICI)1097-461X(1996)57:53.0.CO;2-S

[44] M. Govindarajan, M. Karabacak, Spectrochim. Acta A Mol. Biomol. Spectrosc. 2012, 96, 421–435. DOI: org/10.1016/j. saa.2012.05.067

[45] A. Karakaş , A. Elmali, H. Ünver, H. Kara, Y. Yahsi, Z. Naturforsch. Synthesis, Structure, Spectroscopic Studies And Ab-Initio Calculations On First Hyperpolarizabilities Of N,N'- Bis(2-Hydroxy-1-Naphthylmethylidene)- 1-Methyl-1,2-Diaminoethane-N,N',O,O'- Copper(Ii).B 61, 968, (2006). https://doi.org/10.1515/znb-2006-0807

[46] R. Rajkumar, A. Kamaraj, S. Bharanidharan, H. Saleem, K. Krishnasamy, Synthesis, spectral characterization, single crystal X-ray diffraction and DFT studies of 4-((2,4,5-triphenyl-1H-imidazole-1- yl)methyl) pyridine derivatives, J. Mol. Struct. 1084, 74-81 (2015). https://doi.org/10.1016/j.molstruc.2014.10.035

[47] H. Moghanian, A. Mobinikhaledi, R. Monjezi, Synthesis, spectroscopy (vibrational, NMR and UV-vis) studies, HOMO-LUMO and NBO analysis of 8- formyl-7-hydroxy-4-

methylcoumarin by ab initio calculations, J. Mol. Struct. 1052, 135-145(2013). https://doi.org/10.1016/j.molstruc.2013.08.043

[48] S. Yahiaoui, A. Moliterni, N. Corriero, C. Cuocci, K. Toubal, A. Chouaih, A. Djafri, F. Hamzaoui, 2-thioxo- 3N-(2-methoxyphenyl) -5 [4'-methyl -3'N -(2'-methoxyphenyl) thiazol-2'(3'H)-ylidene] thiazolidin-4-one: synthesis,characterization, X-ray single crystal structure investigation and quantumchemical calculations, J. Mol. Struct. 1177 186–192(2019).https://doi.org/10.1016/j.molstruc.2018.09.052.

[49] S. Demir, A.O. Sario˘glu, S. Güler, N. Dege, M. S¨onmez, Synthesis, crystal structureanalysis, spectral IR, NMR UV-Vis investigations, NBO and NLO of 2-benzoyl-N-(4-chlorophenyl)-3-oxo-3-phenylpropanamide with use of X-ray diffractionsstudies along with DFT calculations, J. Mol. Struct. 1118, 316–324 (2016). https://doi.org/10.1016/j.molstruc.2016.04.042.

[50] M. Azayez, S. Chetioui, Y. Megrouss, N. Boukabcha, A. Djedouani, A. R. Guerroudj, N. MeddahAraibi, A. Chouaih, Experimental and theoretical spectroscopic characterization, Hirshfield surface analysis, TD-DFT calculation, and nonlinear optical properties of (E)-1-[(2,4,6tribromophenyl)diazenyl]-naphthalen-2-ol azo dye, J. Mol. Struct. 1261, 132887 (2022). https://doi.org/10.1016/j.molstruc.2022.132887

[51] Ž.B. Milanovic´, Z.S. Markovic´, D.S. Dimic´, O.R. Klisuric´, I.D. Radojevic´, D.S. Šeklic´, M.N. Živanovic´, J.D. Markovic´, M. Radulovic´, E.H. Avdovic´, Synthesis, structural characterization, biological activity and molecular docking study of 4,7-dihydroxycoumarin modified by aminophenol derivatives, ComptesRendus. Chim. 24, 215–232(2021). https://doi.org/10.5802/crchim.68

[52]C. Adant, M. Dupuis, J. L. Bredas, Ab initio study of the nonlinear optical properties of urea: Electron correlation and dispersion effects. Int. J. Quantum Chem. 56, 497–507 (1995). https://doi.org/10.1002/qua.560560853

[53] L.T. Cheng, W. Tam, S.H. Stevenson, G.R. Meredith, G. Rikken, S.R. Marder, Experimental investigations of organic molecular nonlinear optical polarizabilities.1. Methods and results on benzene and stilbene derivatives, J. Phys. Chem. 95 (1991) 10631-10643. https://doi.org/10.1021/j100179a026

[53] P. Kaatz, E.A. Donley, D.P. Shelton, A comparison of molecular hyperpolarizabilities from gas and liquid phase measurements, J. Chem. Phys. 108, 849–856 (1998) . https://doi.org/10.1063/1.475448

[54] Y. Liu, Y. Yuan, X. Tian, J. Yuan, J. Sun. High first-hyperpolarizabilities of thiobarbituric acid derivative-based donorπ-acceptor nonlinear optical-phores: Multiple theoretical

investigations of substituents and conjugated bridges effect. Int J Quantum Chem. (2020), e26176. https://doi.org/10.1002/qua.26176

[55] R. P. D. Bank, RCSB PDB: Homepage. https://www.rcsb.org/.

[56] H. T. Idriss and J. H. Naismith, J. Micro. Res. Tech. 50, 184 (2000). https://doi.org/10.1002/1097-0029(20000801)50:33.0.CO;2-H

[57] O. T. P. Kim, M. D. Le, H. X. Trinh, and H. V. Nong, Biophys. Physicobiol. 13, 173 (2016). https://doi.org/10.2142/biophysico.13.0_173

[58] Accelrys Software Inc., Discovery Studio Modeling Environment, Releases 3.5 (Accelrys Discovery Studio, San Diego, 2012).

[59] O. Trott and A. J. Olson, J. Comput. Chem. 31, 455 (2010). https://doi.org/10.1002/jcc.21334

[60] R. S. Shinde, V. H. Masand, and M. K. Patil, Indian J. Pharm. Sci. 81, 851 (2019). https://doi.org/10.36468/pharmaceutical-sciences.579

[61] S. Alturk, N. Boukabcha, N. Benhalima, O. Tamer, A. Chouaih, D. Avcı, Y. Atalay, F. Hamzaoui, Conformational, spectroscopic and nonlinear optical investigations on 1-(4-chlorophenyl)-3-(4-chlorophenyl)-2-propen-1-one: a DFT study, Indian J. Phys. 91 (5) (2017) 501–511, https://doi.org/10.1007/s12648-016-0945-3.

[62] N.M. O'boyle, A.L. Tenderholt, K.M. Langner, CCLIB: a library for packageindependent computational chemistry algorithms, J. Comput. Chem. 29 (5) (2008) 839–845, https://doi.org/10.1002/jcc.20823.

[63] S. S¸ ahin, N. Dege, (E)-N-(3-chlorophenyl)-1-(5-nitro-2-(piperidin-1-yl)phenyl) methanimine: X-ray, DFT, ADMET, Boiled-Egg Model, druggability, bioavailabilty, and human cyclophilin D (CypD) inhibitory activity, J. Mol. Struct. 1250 (2) (2022), 131744, https://doi.org/10.1016/j.molstruc.2021.131744.

[64] M.R. Albayati, S. Kansız, N. Dege, S. Kaya, R. Marzouki, H. Lgaz, R. Salghi, I.H. Ali, M.M. Alghamdi, I.-M. Chung, Synthesis, crystal structure, Hirshfeld surface analysis and DFT calculations of 2-[(2,3-dimethyl phenyl) amino]-N'-[(E)-thiophen -2-ylmethylidene] benzohydrazide, J. Mol. Struct. 1205 (2020), 127654, https:// doi.org/10.1016/j.molstruc.2019.127654.

[65] R. Parthasarathi, V. Subramanian, D.R. Royb, P.K. Chattaraj, Electrophilicity index as a possible descriptor of biological activity, Bioorg. Med. Chem. 12 (2004) 5533–5543, https://doi.org/10.1016/j.bmc.2004.08.013.

[66] D.A. Kleinman, Nonlinear dielectric polarization in optical media, Phys. Rev. 126 (6) (1962) 1977–1979, https://doi.org/10.1103/physrev.126.1977.

[67] N. Boukabcha, A. Feddag, R. Rahmani, A. Chouaih, F. Hamzaoui, Molecular structure, multipolar charge density study and nonlinear optical properties of 4- methyl-N-[(5-nitrothiophen-2-

ylmethylidene)] aniline, J. Optoelectron. Adv. M. 20 (3–4) (2018) 140–148.

[68] S. Kansız, A. Tolan, H. ˙ Içbudak, N. Dege, Synthesis, crystallographic structure, theoretical calculations, spectral and thermal properties of trans-diaquabis(trans-4- aminoantipyrine)cobalt(II) acesulfamate, J. Mol. Struct. 1190 (2019) 102–115. doi.org/10.1016/j.molstruc.2019.04.058.

[69] N. Dege, N. S¸ enyüz, H. Batı, N. Günay, D. Avcı, O. ¨ Tamer, Y. Atalay, The synthesis, characterization and theoretical study on nicotinic acid [1-(2,3-dihydroxyphenyl) methylidene]hydrazide, Spectrochim. Acta Part A: Mol. Biomol. Spectrosc. 120 (2014) 323–331, https://doi.org/10.1016/j.saa.2013.10.030.

[70] V.M. Geskin, C. Lambert, J.-L. Br´edas, Origin of high second- and third-order nonlinear optical response in ammonio/borato diphenylpolyene zwitterions: the remarkable role of polarized aromatic groups, J. Am. Chem. Soc. 125 (50) (2003) 15651–15658, https://doi.org/10.1021/ja035862p.

[71] N. Boukabcha, A. Direm, M. Drissi, Y. Megrouss, N. Khelloul, N. Dege, M. Tuna, A. Chouaih, Synthesis, structural determination, hirshfeld surface analysis, 3D energy frameworks, electronic and (static, dynamic) NLO properties of oNitroacetanilide (o-NAA): a combined experimental and quantum chemical study, Inorg. Chem. Commun. 133 (2021), 108884, https://doi.org/10.1016/j.inoche.2021.108884.

[72] V.S. Naik, P.S. Patil, N.B. Gummagol, Q.A. Wong, C.K. Quah, H.S. Jayanna, Structural, linear optical, second and third-order nonlinear optical properties of two halogenated chalcone derivatives containing thiophene moiety, Chem. Phys. Lett. 761 (2020), 138051, https://doi.org/10.1016/j.cplett.2020.138051.

[73] P. Kaatz, E.A. Donley, D.P. Shelton, A comparison of molecular hyperpolarizabilities from gas and liquid phase measurements, J. Chem. Phys. 108 (3) (1998) 849–856, https://doi.org/10.1063/1.475448.

[74] N. Benhalima, N. Boukabcha, O. ¨ Tamer, A. Chouaih, D. Avcı, Y. Atalay, F. Hamzaoui, Solvent effects on molecular structure, vibrational frequencies, and NLO properties of N-(2,3-dichlorophenyl)-2-nitrobenzene–sulfonamide: a density functional theory study, Braz, J. Phys. 46 (2016) 371–383, https://doi.org/ 10.1007/s13538-016-0419-2.

[75] V.V. Poroikov, D.A. Filimonov, W.-D. Ihlenfeldt, T.A. Gloriozova, A.A. Lagunin, Y. V. Borodina, M.C. Nicklaus, PASS biological activity spectrum predictions in the enhanced open NCI database browser, J. Chem. Inf. Comput. Sci. 43 (1) (2003) 228–236, https://doi.org/10.1021/ci020048r.

[76] A. Lagunin, A. Stepanchikova, D. Filimonov, V. Poroikov, PASS: prediction of activity spectra for biologically active substances, J. Bioinform. 16 (2000) 747–748, https://doi.org/10.1093/bioinformatics/16.8.747.

[77] R.P.D. Bank, RCSB PDB: homepage, 2020. https://www.rcsb.org/.

[78] K. Matsushita, E. Shinagawa, & M. Ameyama. [31]d-Gluconate dehydrogenase from bacteria, 2-keto-d-gluconate-yielding, membrane-bound. Carbohydrate Metabolism - Part D, 187–193, (1982). doi:10.1016/s0076-6879(82)89033-2.

[79] W.L. Delano, The PyMOL Molecular Graphics Development Component, Version 1.8,

Schrodinger, LLC, New York, NY, USA, 2015.

[80] M. Gür, S. Yerlikaya, N. S¸ ener, S. Ozkınalı, ¨ M.C. Baloglu, H. Gokçe, ¨ Y. Celik Altunoglu, S. Demir, ˙ I. S¸ ener, Antiproliferative-antimicrobial properties and structural analysis of newly synthesized Schiff bases derived from some 1,3,4- thiadiazole compounds, J. Mol. Struct. 1219 (2020), 128570, https://doi.org/ 10.1016/j.molstruc.2020.128570.

[81] S. Fazil, S. M, Y.S. Mary, Y.S. Mary, V. Chandramohan, N. Kumar, C. Van Alsenoy, Structural (SC-XRD), spectroscopic, DFT, MD investigations and molecular docking studies of a hydrazone derivative, Chem. Data Collect. 100588 (2020), https://doi. org/10.1016/j.cdc.2020.100588.

[82] C.A. Lipinski, Lead- and drug-like compounds: the rule-of-five revolution, Drug Discov. Today: Technol. 1 (2004) 337–341.

[83] M.H.M. Belhachemi, A. Benmohammed, H. Saiah, N. Boukabcha, M. Saidj, N. Dege, A. Djafri, A. Chouaih, Synthesis, structural determination, molecular docking and biological activity of 1-(4-fluorobenzyl)-5-bromolindolin-2,3-dione, J. Mol. Struct. 1265 (2022), 133342, https://doi.org/10.1016/j.molstruc.2022.133342.

[84] S. Yahiaoui, Y. Megrouss, N. Boukabcha, N.E.H. Belkafouf, N. Khelloul, R. Rahmani, N. Boubegra, A. Chouaih, Structural characterization, molecular docking assessment, drug-likeness study and DFT investigation of 2-(2-{1,2- dibromo-2-[3-(4-chloro-phenyl)-[1,2,4] oxadiazol-5-yl]-2-fluoro-ethyl1}-phenyl)- methyl 3-methoxy-acrylic ester, J. Indian Chem. Soc. 99 (2022), 100745, https:// doi.org/10.1016/j.jics.2022.100745.

[85] S.A. Hitchcock, L.D. Pennington, Structure-brain exposure relationships, J. Med. Chem 49 (26) (2006) 7559–7583, https://doi.org/10.1021/jm060642i.

[86] Bekker, H.; Berendsen, H.J.C.; Dijkstra, E.J.; Achterop, S.; van Drunen, R.; van der Spoel, D.; Sijbers, A.; Keegstra, H.; Renardus, M.K.R. Gromacs: A parallel computer for molecular dynamics simulations. In Physics Computing 92, Proceedings of the 4th International Conference, Prague, Czech Republic, 24–28 August 1992; de Groot, R.A., Nadrchal, J., Eds.; World Scientific: Singapore, 1993; pp. 252–256

[87] Jorgensen, W.L.; Chandrasekhar, J.; Madura, J.D. Comparison of simple potential functions for simulating liquid water. J. Chem. Phys. 1983, 79, 926–935. [CrossRef]

[88] Berendsen HJC, Postma JP, Gunsteren WFV, DiNola A, Haak JR (1984) Molecular dynamics with coupling to an external bath. J Chem Phys 81:3684–90

[89] Berendsen HJC, Grigera JR, Straatsma TP (1987) The missing term in effective pair potentials. J Phys Chem 91:6269–71

[90] P. J. Turner. XMGRACE, Version 5.1. 19. Center for Coastal and Land-Margin Research, Oregon Graduate Institute of Science and Technology, Beaverton, OR 2 (2005).

[91] L. Martínez, Automatic identification of mobile and rigid substructures in molecular dynamics simulations and fractional structural fluctuation analysis. *PloS one*, 10(3), e0119264.

(2015). https://doi.org/10.1371/journal.pone.0119264

[92] B. Pandey, P. Sharma, Structural insights into impact of Y134F mutation and discovery of novel fungicidal compounds against CYP51 in Pucciniatriticina, J. Cell. Biochem. 119: 2588-2603(2010). https://doi.org/10.1002/jcb.26422.

[93] S. Khan, F.I. Khan, T. Mohammad, P. Khan, G.M. Hasan, K.A. Lobb, A. Islam, F. Ahmad, M.I. Hassan, Exploring molecular insights into the interaction mechanism of cholesterol derivatives with the Mce4A: a combined spectroscopic and molecular dynamic simulation studies, Int. J. Biol. Macromol. 111: 548-560. (2018) https://doi.org/10.1016/j.ijbiomac.2017.12.160.

[94] J.S. Al-Otaibi, R.A. Costa, E.V. Costa, V.L. Tananta, Y. S. Mary · Y. S. Mary, Insights into solvation, chemical reactivity, structural, vibrational and anti-hypertensive properties of a thiazolopyrimidine derivative by DFT and MD simulations. Struct Chem. **33**, 1271–1283 (2022), https://doi.org/10.1007/s11224-022-01931-1

The research into thiazolic derivatives, including rhodanine, thiazoline, and iminothiazolidinone, has illuminated profound insights into their molecular structures and functional characteristics. Employing a multidisciplinary approach integrating X-ray diffraction, spectroscopic techniques, molecular modeling, and quantum mechanical approximations, scientists have deciphered the intricate relationship between molecular structure and properties. This endeavor holds significant promise for advancing materials science and pharmacology by uncovering novel thiazolic structures and their potential applications.

In light of this, the research work in this thesis focused on structural determination and spectral characterization of two novel thiazole derivatives: (Z)-3-N-(ethyl)-2-N’-((3-methoxyphenyl)imino)thiazolidine-4-one (EMTh) and (Z)-2N-(tert-butylimino)-3N’-(4-methoxyphenyl) thiazolidin-4-one (TMTh). As a result of this effort, we have successfully determined the precise structures of EMTh and TMTh through a combination of X-ray crystallography, spectroscopy and quantum chemistry based theoretical calculations.

The initial objective was to elucidate the structures using infrared spectroscopy and nuclear magnetic resonance (^{1}H and ^{13}C). Subsequent detailed structural analyses were employed to investigate the molecular, electronic, and optoelectronic properties of both materials. Single crystal X-ray crystallography, conducted at low temperatures with an automatic kappa CCD diffractometer, yielded high-resolution data. The results were structurally resolved and refined using the Shelxs and Shelxl programs. Molecular geometries, characterized by bond lengths, valence angles, and torsion angles, were compared between experimental and theoretical results, demonstrating a satisfactory agreement. In case of EMTh the crystal structure analysis revealed a non-planar molecular configuration with a notable 86.0° dihedral angle between the benzene and thiazolidinone rings. The crystal's molecular arrangement was controlled by C-H•••O and C-H•••N hydrogen bonds, leading to a unique three-dimensional packing pattern. For compound TMTh the monoclinic crystal structure containing eight molecules in the unit cell was determined.

Analysis of inter- and intramolecular interactions through Hirshfeld surface analysis highlighted weak hydrogen bonds responsible for crystal stacking.

The investigation extended to vibrational modes, UV-Visible spectrum, and charge transfer dynamics using TD-DFT/B3LYP/6–311G (d,p), revealing strong π→π* electronic transitions. Frontier Molecular Orbitals (FMOs) energies provided chemical reactivity descriptors, emphasizing the electrophilic behavior of TMTh. Electron localization features were explored through ELF and LOL isosurface distributions, indicating significant electron localization on covalent bonds.

The electron density distribution was thoroughly examined, allowing for the characterization of atomic and molecular interactions, as well as the determination of molecular properties such as dipole moment and electrostatic potential.

Finally, nonlinear optical properties were evaluated, revealing that both compounds, EMTh and TMTh, could be considered promising candidates for material development due to their high hyperpolarizability (β) values.

The two compounds were also tested for their biological activity using the known theoretical approach “molecular docking”. The investigation terminated with Molecular Dynamics (MD) simulations by employing GROMACS 2022 with CHARMM36 force field. by employing GROMACS 2022 with CHARMM36 force field. A rigorous assessment of the effectiveness of ligand binding on protein structures was performed. The thorough examination of parameters such as RMSD, RMSF, Rg, and SASA has provided a comprehensive evaluation of the stability and structural changes within the protein-ligand complex, supported by the Poisson-Boltzmann equation and molecular mechanics (MM-PBSA).The molecular docking investigation has highlighted the medicinal potential of the title chemicals, suggesting promising applications in medicinal chemistry. Particularly, in silico molecular docking methods suggest its potential as an inhibitor of the gluconate-2-dehydrogenase protein. The ADMET findings and drug-likeness analysis further emphasize TMTh's potential as an orally active medication.

In summary, this comprehensive research, spanning experimental validations and computational simulations, not only advances our understanding of thiazolic cycles but also showcases the potential for transformative applications across diverse scientific domains. The interdisciplinary nature of this work serves as a model for future research endeavors, emphasizing the collaborative synergy between experimental and theoretical approaches, ultimately contributing to the innovative development of molecular sciences.

SCIENTIFIC PRODUCTION

1. Publications

1. **F.Z. Boudjenane**, F. Triki-Baara, N. Boukabcha, N.E.H. Belkafouf, N. Dege, M. Saidj, N. Khelloul, A. Djafri, A. Chouaih, Synthesis, crystallographic and spectroscopic investigation, chemical reactivity, hyperpolarizabilities and in silico molecular docking study of (Z)-2N-(tert-butylimino)-3N'-(4-methoxyphenyl) thiazolidin-4- one, **Journal of Molecular Structure** 135620 (**2023**), https://doi.org/10.1016/j. molstruc.2023.135620.

2. **F. Z. Boudjenane**, Z. D. Benyahlou, M.H. M. Belhachemi, N. Boukabcha, Ö. Tamer, S. Yahiaoui, Y. Atalay, E. Tarcan, A. Chouaih, A theoretical investigation on hirshfeld surface, IR., UV–Vis, 1H and 13C NMR spectra, nonlinear optical properties, and in silico molecular docking of an organometallic compound: Dibromobis(l-proline)zinc(II), **Journal of Computational and Theoretical Chemistry**, 114345, (**2023**), https://doi.org/10.1016/j.comptc.2023.114345.

3. C. Tabti, A. Benmohammed, N. Boukabcha, N. Dege, A. Djafri, **F. Z. Boudjenane**, A. Chouaih, A. Djafri, Synthesis, Structural Characterization and Theoretical NLO Activity of N-(4-Acetyl-5-(4-(Nitro) Phenyl)-4,5-Dihydro-1,3,4-Thiadiazol-2-yl)-N-Phenyl Acetamide, Polycyclic Aromatic Compounds, 2158882, (**2022**), https://doi.org/10.1080/10406638.2022.2158882

2. Communications

1. **October 2020**: 1ER SEMINAIRE NATIONAL DES SCIENCES D'INTERFACES CHIMIE-BIOLOGIE (1ER SNSI C-B), SOUK-AHRAS, ALGERIA

O: "Crystal structure determination by x-ray diffraction and DFT quantum chemical investigation of new organic compound for biological application" by **Boudjenane Fatima Zohra,** Boukabcha Nourdine, Chouaih Abdelkader

2. **April 21-22, 2021**: 1ST INTERNATIONAL CONFERENCE ON SUSTAINABLE ENERGY AND ADVANCED MATERIALS IC-SEAM'21, OUARGLA, ALGERIA.

O: "Crystal structure determination by x-ray diffraction and theoretical calculations of new thiazolic semiconductor compound" by **Fatima Zohra Boudjenane,** Nourdine Boukabcha, Abdelkader Chouaih

3. **May 16-20, 2021:** THE 2ED SYMPOSIUM ON MATERIALS CHEMISTRY, BOUMERDES-ALGERIA

P: "X-ray determinations and DFT calculation of new organic compound" by Ahlam Roufieda Guerroudj, Boukabcha Nourdine, **Boudjenane Fatima Zohra**, Chouaih Abdelkader

SCIENTIFIC PRODUCTION

4. **May 20, 2021:** JOURNÉE NATIONALE D'ÉTUDE DU GÉNIE DES PROCÉDÉS, MOSTAGANEM, ALGERIA

O: "Crystal structure determination by x-ray diffraction and theoretical calculations of new thiazolic semiconductor compound" by **fatima zohra boudjenane**, nourdine boukabcha, abdelkader Chouaih

5. **September 17-18, 2021:** SEMINAIRE INTERNATIONAL SUR LES SCIENCES DE LA MATIERE (PHYSIQUE ET CHIMIE)

O: "Synthesis and characterisation of anion exchange in layered double hydroxide based on Zn and Cr" by **boudjenane. F. Z,** Chouaih. A, bahmani. A, bel kafouf. N, boukabcha N

6. **September 29, 2021:** 1ST INTERNATIONAL CONFERENCE ON COMPUTATIONAL & APPLIED PHYSICS ICCAP2021, BLIDA, ALGERIA.

O: "Synthesis and characterisation of layered double hydroxide based on Zn and Cr used for anion exchange" by **boudjenane . f z,** Chouaih. A, bahmani. a, belakfouf. n, boukabcha n, megrouss. y

7. **September 29-30, 2021:** POLYMER & MEDITERRANEAN INTERNATIONAL CONFERENCE 2021, BEJAIA-ALGERIA.

O: "DFT quantum chemical method for thiazolidinone derivative synthesis, x-ray structure determination, and related physical properties" by **boudjenane fatima zohra**, Chouaih Abdelkader, mergous youcef, djafri ayada, boukebcha nourdine, bouldiab yasmine, belkaouf nour el houda

O: "The prediction of structural, electronic, magnetic and elastic properties of a new half-heusler alloy: first principles calculations" by bouldiab yasmine, terkhi sabria, sefir yamina, **boudjenane fatima zohra**, bendahma Fatima

8. **November 1-3, 2021:** 1ST INTERNATIONAL CONFERENCE ON APPLIED ENGINEERING AND NATURAL SCIENCES ICAENS 2021, KONYA-TURKEY

O: "First principal investigation of half-metallic ferromagnetism in Cr based half-Heusler compound" by Y. Bouldiab, S. Terkhi, Z. Aziz , M. A. Boudjeltia**, F. Z. Boudjenane,**

O: "Thermal effect on reliability and efficiency of 5nm DG-FinFET Transistors" by Nassima Bourahla, **Fatima Zohra Boudjenane**

O: "A theoretical study of the synthesized (Z)-3-N-(ethyl)-2-N'-((3-methoxyphenyl)imino)thiazolidine-4-one and its NLO properties, molecular docking analysis" by **Boudjenane Fatima Zohra**

9. **December 4-5, 2021:** 1ERE CONFERENCE NATIONAL SUR LA PHYSIQUE DES MATERIAUX ET LEURS APPLICATIONS (CNPMA'2021) USTHB, ALGER, ALGERIA.

P: "Synthèse, analyse du spectre vibrationnel, réactivité chimique et docking moléculaire d'un dérivé de la thiazolidinone" by **boudjenane fatima zohra**, Chouaih Abdelkader, boukebcha nourdine, bouldiab yasmine, bourahla nassima

P: « Etude ab-initio des propriétés structurales, électroniques, et magnétiques d'un matériau demi-Heusler (XYZ) pour des applications spintroniques », by Y. Bouldiab, S. Terkhi, Z. Aziz, M. A. Boudjaltia, **F.Z.Boudjenane**, Y. Sefir,

SCIENTIFIC PRODUCTION

10. **December 11-12, 2021:** INTERNATIONAL PALANDOKEN SCIENTIFIC STUDIES CONGRESS ISARC, ERZURUM, Turkey

O: "Synthesis and X-ray structure determination of thiazolidinone derivative" by **boudjenane fatima zohra**

O30: "Synthesis, characterization and anion exchange of a layered double hydroxide based on Zn and Cr" by **boudjenane fatima zohra**

11. **February 07-09, 2022:** THE FIRST INTERNATIONAL SEMINAR ON MATERIALS SYNTHESIS AND ENVIRONMENTAL MONITORING, OUARGLA, ALGERIA.

O: "Study of layered double hydroxide based on Zn and Cr employed in anion exchange using x-ray diffraction and infrared spectroscopy" by **boudjenane fatima zohra**, Chouaih Abdelkader, bahmani abdallah, boukabcha nouredine

12. **October 26-27, 2022:** THE 1ST INTERNATIONAL CONFERENCE ON RENEWABLE MATERIALS AND ENERGIES ICRME2022, OUARGLA, ALGERIA.

O: "Anion exchange, x-ray diffraction, infrared spectroscopy of a novel layered double hydroxide" by **BOUDJENANE Fatima Zohra**, BAHMANI Abdellah, BOURAHLA Nassima, CHOUAIH Abdelkader, BOUKABCHA Nouredine

13. **December 10-13, 2022:** 1ST INTERNATIONAL CONFERENCE ON SCIENTIFIC AND ACADEMIC RESEARCH, KONYA, TURKEY.

O: "ELF isosurface study and NLO activity of a synthesized organic Molecule" by **Fatima Z Boudjenane**

O: "The study of an organic molecule's ELF isosurface and NLO activity by DFT methods" by **Fatima Z Boudjenane**

O: "Experimental and Theoretical Structural Determination, Intermolecular Charge Transfer, MEP And Nonlinear Optics Application For An Organic Molecule" by Zohra Douaa Benyahlou, belhachemi mortada, kheira hammou, **boudjenane Fatima zohra**

14. **December 20 - 23, 2022:** 1ST INTERNATIONAL CONFERENCE ON ENGINEERING, NATURAL AND SOCIAL SCIENCES ICENSOS 2022, KONYA, TURKEY.

O: "The study of an organic molecule's ELF isosurface and NLO activity by DFT methods" by **Fatima Z Boudjenane**

15. **March 14-16, 2023:** THE 2ND INTERNATIONAL CONFERENCE ON SCIENTIFIC AND ACADEMIC RESEARCH, Konya, Turkey.

O: "NLO characteristics of tridentate ONO organic ligands in molybdenum push-pull coordination" by **Fatima Zohra Boudjenane**

O: "The performance and investigation of the electronic and structural properties of the thiazolidinone molecule" by **Fatima Zohra Boudjenane**

O: "X-ray diffraction and infrared spectroscopy analysis of the synthesized LDH based on Cr and Zn" by **Fatima Zohra Boudjenane**

O: "Spectral, modeling and biological studies on a novel organic compound" by **Fatima Zohra Boudjenane**

O: "Analysis of Received Power Characteristics of Commercial Photodiodes in Indoor Los Channel Visible Light Communication" by **BOUDJENANE Fatima Zohra**

SCIENTIFIC PRODUCTION

16. **March 23-24, 2023:** The 3rd INTERNATIONAL BLACK SEA MODERN SCIENTIFIC RESEARCH CONGRESS, SAMSUN, TURKEY

O: "FROM RESEARCH TO REALITY: advancements and opportunities in visible light communication for wireless networks" by **Fatima Zohra Boudjenane**

17. **April 18-20, 2023:** THE 1ST INTERNATIONAL CONFERENCE ON SCIENTIFIC AND INNOVATIVE STUDIES ICSIS 2023, KONYA, TURKEY.

O: "Performance Analysis of Low-Cost Visible Light Communication Systems" by **Fatima Zohra Boudjenane**

O: "Advantages of Visible Light Communication in Smart Cities" by **Fatima Zohra Boudjenane**

O: "Design and Implementation of a Low-Cost Visible Light Communication System for Smart Homes" by **Fatima Zohra Boudjenane**

18. **August 16-18, 2023:** 1ST INTERNATIONAL CONFERENCE ON RECENT AND INNOVATIVE RESULTS IN ENGINEERING AND TECHNOLOGY, KONYA, TURKEY.

O: "Synthesis, and Molecular modeling of the (Z)-2N-(tert-butylimino)-3N'-(4-methoxyphenyl) thiazolidin-4-one (TMTh) compound" by **Fatima Zohra Boudjenane**

O: "Comparative study of water quality" by **Fatima Zohra Boudjenane**

O: "Drug design, molecular docking, in silico ADMET investigation of a new thiazolidinone derivative" by **Fatima Zohra Boudjenane**

O: "In silico SwissADME, lazar investigation of a new organic compound" by **Fatima Zohra Boudjenane**

O: "Biological activity prediction and electrostatic properties determination of a thiazole derivative" by Megrouss Youcef, Salem Yahiaoui, **Fatima Zohra Boudjenane**

19. **July 29-31, 2023:** 1ST INTERNATIONAL CONFERENCE ON MODERN AND ADVANCED RESEARCH, KONYA, TURKEY.

O: "NLO characteristics of tridentate ONO organic ligands in molybdenum push-pull coordination" by **Fatima Zohra Boudjenane**

O: "Synthesis, crystallographic and spectroscopic investigation, and in silico molecular docking study of (Z)-2N-(tert-butylimino)-3N’-(4-methoxyphenyl) thiazolidin-4-one" by **Fatima Zohra Boudjenane**

O: "Quantum chemical study of an NLO candidate 1(Z)-2N-(tert-butylimino)-3N’-(4-methoxyphenyl) thiazolidin-4-one" by **Fatima Zohra Boudjenane**

O: "DFT study and structure determination of a new thiazolidinone derivative" by **Fatima Zohra Boudjenane**

20. **December 25-26, 2023:** THE 3RD INTERNATIONAL CONFERENCE ON SCIENTIFIC AND ACADEMIC RESEARCH, KONYA, TURKEY.

O: "Theoretical Investigation of the Compound C14H8N2OS2's Properties" by **Fatima Zohra Boudjenane**

Workshop:

- **F.Z. Boudjennane,** "Structural resolution by X-ray diffraction on single crystal and powder + Piloting of a single crystal diffractometer at a distance", 06 and 7 November 2022, the Abbes Laghrour Khenchela University.

Journal of Molecular Structure 1287 (2023) 135620

Contents lists available at ScienceDirect

Journal of Molecular Structure

journal homepage: www.elsevier.com/locate/molstr

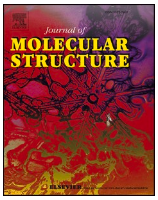

Synthesis, crystallographic and spectroscopic investigation, chemical reactivity, hyperpolarizabilities and in silico molecular docking study of (Z)-2N-(tert-butylimino)-3N’-(4-methoxyphenyl) thiazolidin-4-one

Fatima Zohra Boudjenane [a], Fayssal Triki-Baara [b], Nourdine Boukabcha [a,c], Nour El Houda Belkafouf [a], Necmi Dege [d], Merzouk Saidj [a], Nawel Khelloul [a,e], Ayada Djafri [b], Abdelkader Chouaih [a,*]

[a] *Laboratory of Technology and Solid Properties (LTPS), Abdelhamid Ibn Badis University of Mostaganem, Mostaganem 27000, Algeria*
[b] *Laboratory of Organic Applied Synthesis (LSOA), Department of Chemistry, Faculty of Sciences, University of Oran 1, Ahmed Ben Bella, Oran 31000, Algeria*
[c] *Chemistry Department, Faculty of Exact Sciences and Informatic, Hassiba Benbouali University, Chlef 02000, Algeria*
[d] *Department of Physics, Ondokuz Mayis University Samsun, Samsun 54187, Turkey*
[e] *Faculty of Sciences and Technology, Mustapha Stambouli University of Mascara, B.P.763, Mascara 29000, Algeria*

ARTICLE INFO

Keywords:
Thiazolidinones
DFT
ELF – LOL
HOMO – LUMO
NLO
Molecular docking

ABSTRACT

This study presents the results related to the synthesis of (Z)-2N-(tert-butylimino)-3N’-(4-methoxyphenyl) thiazolidin-4-one (TMTh) and its characterization by X-ray diffraction and spectroscopic techniques. The compound was characterized by 1H and 13C NMR and FT-IR spectroscopy. According to the single-crystal X-ray diffraction (SC-XRD) analysis, the title compound belongs to the centrosymmetric I2/a space group of the monoclinic system with 8 molecules in the unit cell. Using density functional theory (DFT) at the B3LYP/6-311 G (d,p) level, the optimized structure of TMTh was predicted. The structure was described by the geometric parameters confirming a good consistency between experimental and theoretical structural results. The identification of weak interactions and their contributions, including the C – H···O and C – H···S hydrogen bonds, and van der Waals (vdW) interactions, which are necessary for maintaining the crystal packing, were also addressed by the use of Hirshfeld surface (HS) and RDG analyses. From the HS, the major contribution with 56.3% is due to H···H contacts. To obtain and identify the vibration frequencies and their assignments, the PED (Potential Energy Distribution) analysis of the title compound was carried out. The results were then confirmed and compared to the experimental FT-IR spectral data. The ^{1}H and ^{13}CNMR chemical shifts were also calculated to compare and complement the experimental results. To highlight the compound’s absorption behavior, the electronic transitions are assigned according to the time-dependent density functional theory (TD-DFT) outcomes and confirmed the electronic circular dichroism (ECD) spectrum. The experimental and theoretical UV–vis spectra are also provided suggesting a strong $\pi \rightarrow \pi^*$ transition at 250 nm. Charge transfer inside the molecule was considered using the frontier molecular orbitals (FMOs) investigations, and ELF, LOL, and MEP distribution maps were also investigated. The HOMO and LUMO energies were used to estimate the chemical reactivity descriptors and the corresponding energy gap is 2.67 eV. The nonlinear optical (NLO) activity of the compound has been analyzed, and the corresponding properties have been evaluated. The most important first and second order hyperpolarizabilities calculated with BPV86 functional were found to be 5.58×10^{-30} esu and 26.01×10^{-36} esu, respectively The present study deals also with the in silico ADMET study using molecular docking and the SwissADME web tool to determine the physicochemical and pharmacokinetic properties. The biological activity was performed against the gluconate 2-dehydrogenase protein with 5U9P, 4HP8, 4Z9X, 1VL8, 4IBO and 3O03 receptors.

---

* Corresponding author.
E-mail address: abdelkader.chouaih@univ-mosta.dz (A. Chouaih).

https://doi.org/10.1016/j.molstruc.2023.135620
Received 7 January 2023; Received in revised form 18 April 2023; Accepted 19 April 2023

1. Introduction

Heterocycles are ring compounds that contain carbon as well as other elements such as oxygen, nitrogen, and sulfur. These heterocyclic materials are used in optoelectronic devices such as photovoltaic and solar cells, and organic light emitting diodes (OLEDs) [1,2]. Heterocyclic structures are also found in a variety of potentially conducting polymers, optically nonlinear polymers, and biomaterials [3]. Among them, thiazolidinones and their derivatives are significant nonlinear optical (NLO) materials that already have piqued the interest of researchers due to their wide range of applications and high NLO efficiency. Several thiazolidinone-based compounds have been experimentally and theoretically studied for their NLO applications [4]. Moreover, it is well known that the material's NLO behavior is highly dependent on its own three-dimensional geometry. On the other hand, the thiazolidinone derivatives with extended π-conjugation, in particular, exhibit improved second order NLO properties [5,6]. Many of these compounds have been synthesized and studied for their spectroscopic properties and biological activity [7–9]. The compounds bearing thiazolidinone moiety have been reported in the literature for their antibacterial, anticancer, anti-inflammatory and antiviral activities [10–13]. In addition, thiazolidinones have been considered as pharmacologically active scaffold due to their wide range of reported biological activities. Literature reveals that a spectrum of biological activities are exhibited by thiazolidinone heterocyclic ring system [14,15]. Furthermore, the introduction of substituents on NH group of thiazolidinone has been an important and widely used strategy to modify thiazolidinone analogues for the potential clinical drugs [16].

This study introduces the synthesis of (Z)−2N-(tert-butylimino)−3N'-(4-methoxyphenyl) thiazolidin-4-one (TMTh) and its (1H, 13C)-NMR; UV–Vis and FTIR spectroscopic features. The spectroscopic properties were also determined with in-depth theoretical calculations. To illustrate the various interactions and provide quantitative data on the contribution of each intermolecular interaction in the crystal packing, Hirshfeld surface analysis and fingerprint plots were performed. In the present study, we investigated other molecular properties of the title compound, such as HOMO-LUMO orbitals, global reactivity descriptors, and molecular electrostatic potential, in addition to charge transfer within this molecule. The molecular electrostatic potential surface was analyzed, and the NLO activity of the molecule was also evaluated including the dipole moment (μ), polarizability (α), first-order hyperpolarizability (β), and second-order hyperpolarizability. Moreover, the prediction of activity spectra for substances (PASS) and the molecular docking have been studied to undertake a more in-depth inquiry and give additional information, particularly in establishing the biological activity of the chemical under investigation.

2. Experimental and computational details

2.1. *Synthesis and characterization*

2.1.1. *Synthesis of (Z)−2N-(tert-butylimino)−3N'-(4-methoxyphenyl) thiazolidin-4-one*

In ethanol with acetic acid, a solution of 1-tert-butyl-3-(4-methoxyphenyl) thiourea and ethyl bromoacetate was prepared as shown in Scheme 1. At room temperature, the mixture was stirred for 6 h. Slow evaporation was used to recrystallize (Z)−2N-(tert-butylimino)−3N'-(4-methoxyphenyl) thiazolidin-4-one (TMTh) crystals from ethanol. Simple crystallization procedure was used to purify the title compound. Finally, the precipitated solid was filtered, washed with water and recrystallized to give the target compound.

2.1.2. *Characterization of (Z)−2N-(tert-butylimino)−3N'-(4-methoxyphenyl) thiazolidin-4-one*

Experimental techniques (including FT-IR, NMR, and UV–Vis) were used to characterize TMTh. On a Perkin-Elmer FT-IR spectrometer, the IR spectrum of a KBr pellet was recorded in the range 400−4000 cm^{-1}. The measured wavenumbers are reported in cm^{-1}. In DMSO-d_6 solvent at 25 °C, the ^1H and ^{13}C NMR spectra were measured using a Bruker AC-500 MHz spectrometer. Relative to TMS, which serves as an internal standard, chemical shifts are reported as δ (ppm). Electronic UV–Vis spectrum was recorded using a Shimadzu UV-2900 Pc-spectrophotometer in the range from 200 to 700 nm in chloroform solution.

2.1.3. *Spectral data*

Yield 68% m.p. 110 °C. IR (KBr.νcm^{-1}): 2981 ($CH2_{thia}$); 1719 (C = O); 1622 (C = N); 1389 ($N—C_{thia}$); 786.815 ($C\text{-}S\text{-}C_{thia}$). ^{1}HNMR (500 MHz, DMSO-d6.δ ppm. J (Hz)): 1.20 (s. 9H. CH_3); 3.77(s. 3H. $O—CH_3$); 4.10 (s. 2H. $CH_{2\ thia}$); 6.95–6.98 (m. 2H. H_{arom}); 7.08–7.11 (m. 2H. H_{arom}). ^{13}CNMR (125 MHz, DMSO-d6): 171.04 (C = O); 158.90(C = N); 147.19; 130.03; 129.17; 114.20; 55.69(O—CH3); 54.33; 33.44 ($CH_{2\ Thia}$); 29.59.

2.2. *X-ray crystallography and data collection*

Brown colored crystals were selected for the present crystallographic study. X-ray diffraction experiment was performed on a STOE IPDS II single crystal diffractometer and the data were collected using monochromated MoKα radiation (λ = 0.71073 Å) at ambient temperature. These data are used for solving and refining the structure. The structure was solved and refined using the Shelxs [17] and Shelxl [18] programs, respectively. Direct methods were used to solve the structure. The anisotropic refinement of all non-hydrogen atoms was carried out using all reflections with $I > 2\sigma$ (I). Geometric analysis and crystal structure visualization were carried out using Mercury [19] and ORTEP [20] softwares. The X-ray measurement conditions, crystallographic data and refinement details are summarized in Table 1.

2.3. *Computational methodology*

By examining their structures and chemical characteristics, computational approaches are an excellent method for designing molecules. In this case, the theoretically optimized geometry of the title molecule in the gas phase was performed using the Gaussian 09 software [21]. The output files were visualized via the GaussView 5.0.8 software [22]. The structural properties of TMTh were determined by applying Becke's three-parameter hybrid functional (B3) for the exchange part and the Lee-Yang Parr(LYP) correlation function with 6–311G(d. p) basis set

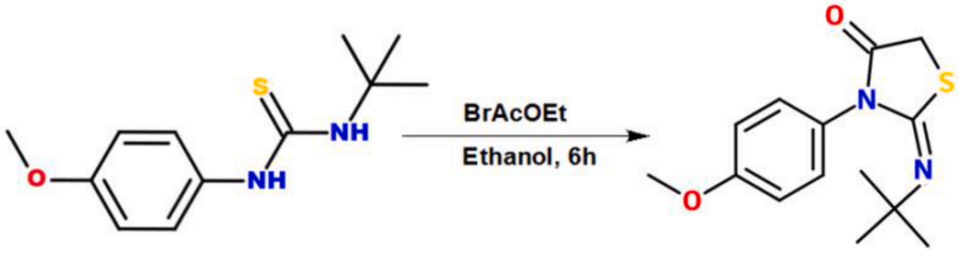

Scheme 1. Synthesis chemical pathway for TMTh.

Table 1
Experimental conditions and crystallographic details for TMTh.

Chemical formula	$C_{14}H_{18}N_2O_2S$
M (g/mol)	277.35
Crystal system. space group	Monoclinic, I2/a
Temperature (K)	296
a, b, c (Å)	13.6185 (6), 5.7532 (2), 37.1790 (17)
β(°)	91.349 (4)
V (Å ^{3})	2912.2 (2)
Z	8
Radiation type	Mo Kα
μ (mm^{-1})	0.222
Crystal size (mm)	0.220 × 0.203 × 0.190
Diffractometer	STOE IPDS 2
Absorption correction	X-RED32; Stoe & Cie. 2002
No. of measured reflections	19,866
No. of independent reflections	3225
No. of observed [$I > 2\sigma(I)$] reflections	2169
h, k, l	−17→17, −7→7, −47→47
R$_{int}$	0.015
(sin θ/λ) $_{max}$ ($Å^{-1}$)	0.727
R[$F^2 > 2(F^2)$], w*R*(F^2), S	0.046, 0.134, 1.032
No. of parameters	172
No. of restraints	0
H-atom treatment	H-atom parameters constrained
Δρ$_{max}$. Δρ$_{min}$ (e $Å^{-3}$)	0.38, −0.29

[23,24]. Using the same calculation level, the vibrational frequencies of the title molecule in the gas phase were computed. To get results that were in the best accord with the experimental data, the scale factor was applied. For B3LYP/6–311G(d,p), the scaling factor with the standard value of 0.9679 was used [25]. Additionally, the potential energy distribution was investigated by the VEDA 4 software for the assignments of the vibrational modes [26]. The electronic spectrum, absorption wavelengths and oscillator strengths of the title compound were calculated using the TD-DFT method based on the previously optimized structure [27]. The energies of molecular orbitals and related parameters such as electronegativity, chemical hardness and softness were calculated at the same level of theory. The molecular electrostatic potential was theoretically investigated to highlight the nucleophilic and electrophilic zones in the molecule along with the electron localization function and localized orbital locator distributions. Additionally, the electric dipole moment (μ), mean polarizability (α), anisotropy of the polarizability (Δα), total first-order static hyperpolarizability (β) and the second-order static hyperpolarizability (γ) were computed in order to evaluate the nonlinear optical properties of TMTh.

3. Results and discussion

3.1. Structure description

Fig 1 displays the X-ray crystallographic structure of the title compound along with its optimized molecular geometry. Table 2 provides some experimental and computed bond lengths and angles. The full list of geometric parameters is provided in the supporting information. The above results show that the title compound crystallizes in the I2/a space group of the monoclinic system. The optimized geometrical parameters of TMTh were calculated at the same level of theory. From Table 2, the C10−O2 bond has a typical double bond nature. The experimental results for the two C − S bond lengths, namely C8−S1 and C9−S1, are in the normal range of $C^{(Sp3)}$−*S* single bond [1.81 Å] [28, 29]. All C − N bonds exhibit conventional single bond character except C8−N2 bond. The N1−C10 bond is somewhat shorter than the other C − N single bond [30,31]. The molecular structure is made up of two planar moieties, one with the methoxyphenyl group and the other with the tert-butylimino-thiazolidin-4-one group. The corresponding dihedral angle between the two planes is around 68°

3.2. Crystal packing, HS and RDG analyses

3.2.1. Intermolecular H-bonds

By examining the crystal packing of the title compound, some intermolecular interactions have been identified. In similar reported structures containing thiazole moiety, the crystal packing is mainly based on short contacts and weak π–π interactions [32,33]. A sequence of weak C − H···O hydrogen bonds (Table 3) link the molecules in a three-dimensional framework in the crystal packing of the title compound, and some of them are depicted by dashed lines as illustrated in Figure S1. The electronegative O2 atom is involved in the main interactions and form hydrogen bonds with H3 and H1C atoms as can be seen in Table 3. Furthermore, the C1 and C3 atoms, connected to the precedent H atoms, act as donors while O2 as acceptor. The shortest H-bonds are given by C3−H3···O2 and C1−H1C···O2 which have values

Table 2
Selected bond lengths (Å) and angles (°) by X-ray diffraction and theoretical calculations for TMTh.

Bond lengths	X-ray	DFT	Bond angles	X-ray	DFT
C8−S1	1.784(2)	1.823	C8−S1−C9	93.68(9)	92.67
C9−S1	1.790(3)	1.827	C2−O1−C1	118.17(19)	117.65
O1−C2	1.362(2)	1.368	C10−N1−C8	117.96(16)	111.64
O1−C1	1.415(3)	1.429	C10−N1−C5	118.97(16)	120.42
C10−O2	1.205(3)	1.218	C8−N1−C5	123.04(15)	121.13
N1−C5	1.437(2)	1.439	N1−C10−C9	111.99(19)	111.64
N1−C8	1.411(3)	1.422	C6−C5−C4	120.57(18)	119.88
N1−C10	1.379(3)	1.396	C6−C5−N1	119.58(18)	119.77
N2−C8	1.252(3)	1.265	C4−C5−N1	119.73(18)	120.32
N2−C11	1.482(3)	1.477	N2−C8−N1	120.92(17)	121.17
C10−C9	1.501(3)	1.524	N2−C8−S1	130.84(16)	129.93
C11−C13	1.524(3)	1.544	N1−C8−S1	108.24(13)	108.88
C11−C14	1.517(4)	1.544	O1−C2−C7	124.51(19)	124.68
C11−C12	1.520(3)	1.542	O1−C2−C3	115.27(19)	115.67

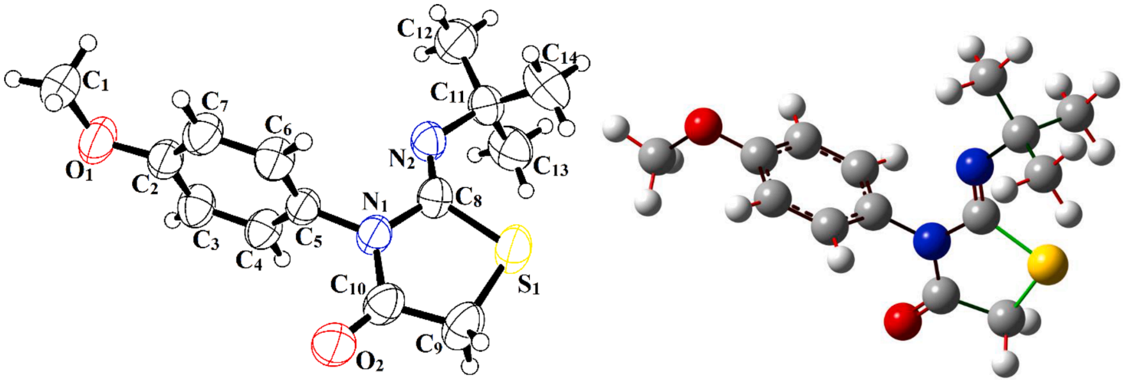

Fig. 1. Molecular structure of TMTh (left) X-ray structure, (right) optimized structure using B3LYP/6-311G(d,p).

Table 3
The possible hydrogen bonds for TMTh.

D − *H*···A	*D* − *H* (Å)	*D* − *A* (Å)	H···A (Å)	*D* − *H*···A (Å)	Equivalent positions
C3−H3···O2	1.08	3.396	2.488	163.98	x,−1/2,−y−1,+z
C1−H1C···O2	1.08	3.425	2.598	119.7	−x,+y + 1/2,-z + 1/2

of 2.488 and 2.598 Å, respectively. As shown in Figure S1, π–π stacking interactions are present in the crystal packing and the centroid-to-centroid distance between the thiazole and benzene ring of neighbouring molecule being 4.262 Å.

3.2.2. Hirshfeld surface analysis

The Hirshfeld surface (HS) analysis is one of the crucial methods for the investigation of intermolecular interactions. Using the HS outputs, we can explore the molecular interactions in the crystalline environment. The following equation describes the d_{norm} (normalized connection distance), which is calculated from the atoms' *de, di,* and van der Waals radii (r_i^{vdw} and r_e^{vdw}):

$$d_{norm} = \frac{\left(d_i - r_i^{vdw}\right)}{r_i^{vdw}} + \frac{\left(d_e - r_e^{vdw}\right)}{r_e^{vdw}}$$

where de and di stand for, respectively, the internal and external distances from the site to the closest nucleus. The 3D-HS map and their related 2D-fingerprint plots were obtained using the CrystalExplorer21 software [34]. The red regions represent shorter contacts with negative d_{norm} value and blue regions represent longer contacts with positive d_{norm} value. The white regions represent van der Waals contacts with zero d_{norm} value [35]. As shown in Fig 2, the HS of the title compound was mapped with color scale from −0.150 to 1.849 Å and the shape-index from −1.0 to 1.0 Å. In Fig 2(a) the dark-red regions indicate the short interatomic contacts. These red spots indicate the presence of C–H···O and C − H···S hydrogen bonds. The shape index surface for the title molecule is highlighted in Fig 2(b) showing the presence of red and blue triangles that are related to π–π stacking interactions. As illustrated in Fig 2(c), the C3−H3···O2 intermolecular interactions are displayed by dashed lines. For the 2D-fingerprint plots of Figure S2, the most important contributions were represented. As can be seen, the major contribution to the surface with 56.3% is due to H···H contacts. The H···O/O···H contacts which are attributed to the C–H···O interactions occur as two sharp symmetric spikes with a contribution of 16.9% to the HS. The presence of these spikes is characteristic of strong hydrogen bonds. The C–H/H–C interactions presented by two symmetrical wings on the left and right sides with a percentage 12.7%. The C···H/H···C interactions are presented by two symmetrical wings on the left and right sides with a contribution of 12.7%. On the other hand, the S···H/H···S and N···H/H···N intercontacts contribute with 6.6 and 3.2% to the HS, respectively.

3.2.3. RDG analysis

In recent times, noncovalent interactions, particularly H-bond, steric effect, and van der Waals interactions can be revealed by applying reduced density gradient (RDG) analysis [36]. As is well known, RDG is a theoretical method for describing a molecular system that is based on the electron density and its derivatives. The noncovalent interactions are considered as weak interactions and are very useful to understand the behavior of molecules towards their activities [37,38]. The areas of these interactions and their graphical representation are provided using the RDG analysis and its variants. The following equation yields the RDG values:

$$RDG\ (r) = \frac{1}{2(3\pi r^2)^{1/3}} \frac{|\nabla\rho(r)|}{\rho(r)^{4/3}}$$

where $\rho(\mathbf{r})$ is the electron density and $\nabla\rho(\mathbf{r})$ is the gradient of $\rho(\mathbf{r})$ at the point r. The RDG assessment utilizing the Multiwfn [39] and VMD softwares [40] is reported in Fig 3 along with the 2D scatter plot and 3D isosurface densities of TMTh. The graphical depiction of ρ(r) versus sign (λ2)ρ, in which the second eigenvalue corresponds to the electron density, provides a useful indication of the nature and strength of interactions. Sign(λ2)ρ is used to reveal the nature of interactions by their value and sign. Sign(λ2)ρ > 0, sign(λ2)ρ < 0 and sign(λ2)ρ ≈ 0 are related to the repulsive, attractive, and van der Waals (VDW) interactions, respectively. As shown in Fig 3, the dominating green and brown bicolored flat regions showed that the exclusion and attraction effects coexisted in the molecular structure under investigation. On the other hand, the center of the thiazole and benzene rings displayed red spindle shapes that were related to the steric effect. Thus, it can be concluded that the scatter graph significantly helps in identifying the presence of intermolecular interactions throughout the surface map.

3.3. Spectral analysis

3.3.1. Vibrational spectra analysis

It is well known that infrared spectroscopy is a very powerful tool for identifying functional groups in a molecular system. To achieve this identification, the VEDA program was used giving the total PED assignments. The results of the PED analysis are gathered in Table S2 along with the experimental frequencies where a scaling factor of 0.96 was applied [41]. A comparison of the theoretical and experimental FT-IR spectra for TMTh is shown in Figure S3. The C–H stretching vibrations of the aromatic ring for TMTh were calculated and are located in the range of 3087–3064 cm^{-1} [42]. The same vibrations have experimental values between 3081 and 3054 cm^{-1}. As shown in Table S1, the calculated stretching vibrations of CH_2 and CH_3 functional groups are expected to be in the range 3013−2886 cm^{-1} [43,44]. The bands between

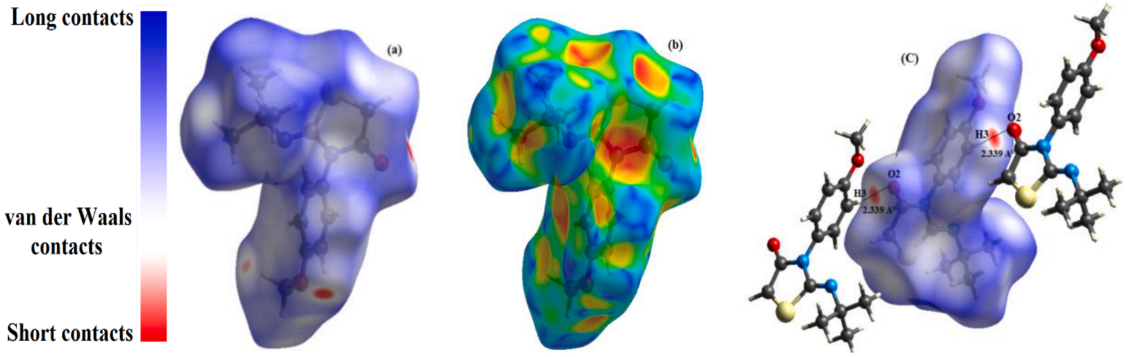

Fig. 2. Hirshfeld surfaces for visualizing the intermolecular contacts of the title compound: (a) d_{norm} Hirshfeld surface, (b) shape index and (c) d_{norm} selected intermolecular contacts.

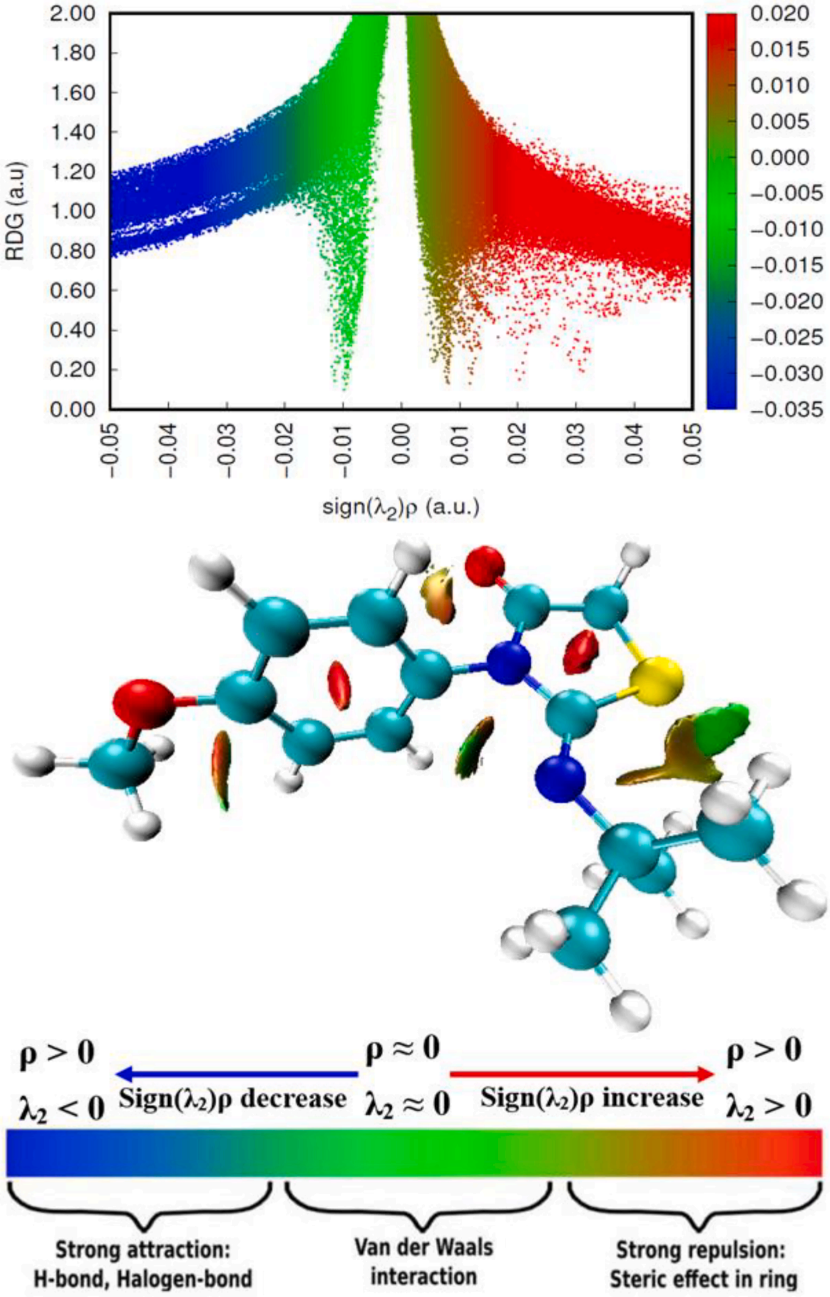

Fig. 3. RDG graph and scatter map of TMTh.

1503 and 1488 cm^{-1} were assigned to the deformation modes for the CH_3 group. The stretching vibration of the aromatic C − C in TMTh appeared at 1591 cm^{-1} with a PED contribution of 15% that can be found to be similar to the results published in the literature [45]. For the title compound, the C = O stretching vibrations were calculated between 1734 and 1657 cm^{-1} with their corresponding PED contributions of 65% and 20% [46]. The calculated values of C − N stretching vibrations are 1319 (24%), 1164 (20%), 1123 (19%), and 592 (20%) cm^{-1} [47]. The C = N stretching vibrations are computed at 1657 cm^{-1} and obtained experimentally at 1624 cm^{-1}. The strong C − S stretching vibrations were identified theoretically at 955 and 633 cm^{-1}. The vibrations values at 1103 (53%) and 885 cm^{-1} (43%) present symmetric and asymmetric H—C-S bending. The same values indicate that there are H—C-S-C torsion vibrations with PED contribution of 26% and 18%. Furthermore, 565 (22%) and 92 cm^{-1} (21%) present H—C-S-C torsion vibrations confirming the existence of thiazolidinone moiety.

3.3.2. ^{1H} and ^{13}CNMR chemical shifts

In this work, the theoretical ^{1}H and ^{13}C NMR isotropic chemical shifts (ppm) are computed with the GIAO method [48] using chloroform as solvent and the corresponding results are summarized in Table 4 together with the experimental chemical shifts that were measured in the same solvent. The experimental ^{1}H and ^{13}C NMR spectra are given in Figure S4 (a,b) as supplementary materials. The ^{1}H isotropic chemical shifts are measured in the range 1.20–7.11 ppm and the corresponding chemical shifts are calculated between 0.79 and 7.36 ppm. The observed signals for H3 and H7 are 6.95 ppm, and for H4 and H6 are 7.08 and 7.11 ppm, respectively [49]. The corresponding calculated values are 7.36 ppm for H3 and H7, and 7.21 ppm for H4 and H6 [50]. The methylene protons of the thiazolidinone ring present a singlet signal at 4.10 ppm (3.77 ppm with DFT). The methyl protons of C12, C13 and C14 atoms have a single experimental chemical shift value (1.20 ppm), and the corresponding theoretical values are in the range 0.79−1.89 ppm.

Table 4
Experimental and calculated ^{1}H and ^{13}C NMR chemical shifts (ppm) for TMTh.

^{1}H	Experimental	B3LYP/6–311G(d.p)
H1A	3.77	4.10
H1B, H1C	3.77	3.62
H3, H7	6.95	7.36
H4	7.08	7.21
H6	7.11	7.21
H9A, H9B	4.10	3.77
H12A	1.20	0.79
H12B, H12C	1.20	1.15
H13A, H13C, H14A, H14C	1.20	0.92
H13B, H14B	1.20	1.89
^{13}C	Experimental	B3LYP/6–311G(d.p)
C1	55.69	60.99
C2	147.19	146.30
C3, C7	129.17	129.65
C4	114.20	118.04
C5	130.03	132.89
C6	114.20	116.04
C8	158.90	156.05
C9	33.44	37.24
C10	171.04	175.94
C11	54.33	60.82
C12	29.59	26.91
C13, C14	29.59	26.32

For the methyl protons attached to C1, the experimental chemical shift value is about 3.77 ppm and the calculated values are 3.62 and 4.10 ppm.

The ^{13}C NMR chemical shifts for TMTh were obtained experimentally and theoretically. As can be seen in Table 4, the experimental and theoretical chemical shifts of aromatic carbons for TMTh have values greater than 100 ppm which shows the good quality of the recorded ^{13}C NMR data [51]. The heterocyclic ring carbons show resonance values at 158.90 (experimental) and 156.05 (theoretical) for C8 atom, and 171.04 (experimental) and 175.94 (theoretical) for C10 atom. These two values are greater than the resonance of the other carbons due to the electronegativity of neighboring atoms (O, S and N). For the four methyl moieties of TMTh, the corresponding ^{13}CNMR signals appeared at 55.69 (C1) and 29.59 ppm (C12, C13 and C14), and the calcultated values are 60.99, 26.91 and 26.32 ppm, as can be seen in Table 4. The C9 atom of the methylene group shows experimental signal at 33.44 ppm and theoretical signal at 37.24 ppm.

3.3.3. *Absorption effect and frontier molecular orbitals (FMOs)*

In the present work, the absorption effect was investigated using UV–Visible spectroscopy that remains the most important technique for studying conjugated molecules as well as electron delocalization in molecular structures. As long as the molecular structure has delocalization, the wavelength of maximum absorption shifts increases [52]. Figure S5 displays the experimental and theoretical UV–Visible spectra of the TMTh molecule. The experimental spectrum was recorded using an absolute ethanol solvent at room temperature, while the theoretical spectrum was calculated by TD-DFT/B3LYP method with 6–311G(d,p) basis set. The theoretical calculations were carried out to determine the excited states in the title compound structure. The vertical excitation energies, oscillator strength (*f*) and wavelength are calculated in gas phase using the same level of theory. The corresponding results are depicted in Table 5. The strong transitions were reported at 4.9810 eV (248.92 nm) with oscillator strength $f = 0.0345$ and 5.0018 eV (247.88 nm) with oscillator strength $f = 0.0152$. The calculated absorption wavelength with a maximum value corresponds to the electronic transition from HOMO to LUMO and having a contribution around 62%. As can be seen in Figure S5, the significant absorption peak at 250 nm correlates to the observed spectral peak at 248.9 nm. A strong $\pi \rightarrow \pi^*$ transition with a high attenuation coefficient in the UV–Visible range is expected due to the molecular structure. The maximum UV–Vis absorption wavelength in the spectrum is due to the influence of $\pi \rightarrow \pi^*$ electronic transition.

Table 5
Experimental and theoretical electronic transitions, oscillator strength and major/minor contributions for TMTh.

Electronic transitions	Exp.λ_{max} (nm)	TD-DFT/B3LYP-6311G(d, p)			
		λ_{cal} (nm)	Energy (eV)	Oscillator strength (f)	Assignments (major contributions ≥ 10%)
S0-S1	250	248.92	4.9810	0.0345	H→L(62%)+H→L + 1(12%)
S0-S2		247.88	5.0018	0.0152	H→L + 1(60%)+H-2→L(14%)+H→L(11%)
S0-S3		240.07	5.1644	0.0099	H-2→L (39%)+H-2→L + 1(23%)+H→L(14%)+H→L + 1(12%)
S0-S4		232.76	5.3267	0.0877	H→L + 2(31%)+H-1→L + 2(23%)+H-1→L(18%)+H-1→L + 3 (13%)
S0-S5		228.98	5.4147	0.1555	H→L + 2(36%)+H-1→L + 2(19%)+H-1→L + 3 (17%)
S0-S6		227.48	5.4503	0.0644	H-1→L(52%)+H-1→L + 1 (29%)
S0-S7		222.74	5.5664	0.0401	H-5→L(29%)+H-2→L + 2(15%)+H-2→L + 1 (14%)+H-5→L + 1(13%)
S0-S8		219.59	5.6462	0.0077	H-1→L + 1 (43%)+ H-1→L (20%)+H-1→L + 2 (14%)
S0-S9		218.63	5.6710	0.0631	H-2→L + 1 (35%)+ H-2→L (33%)
S0-S10		214.02	5.7931	0.0191	H-2→L + 2 (55%)+ H→L + 3 (11%)

On the other hand, the study of FMOs, known as the HOMO and LUMO, is conducted to better understand the reactivity and kinetic stability as well as the molecular bioactivity. The HOMO (highest occupied molecular orbital) and LUMO (lowest unoccupied molecular orbital) parameters are critical in quantum chemistry calculations for electronic studies [53]. The HOMO energy defines the capacity to donate an electron, the LUMO energy characterizes the ability to acquire an electron, and the gap between the two characterizes the molecule's chemical stability. Furthermore, the HOMO energy is proportional to the ionization potential, whereas the LUMO energy is proportional to electron affinity. The overlapping of these orbitals can produce the charge transfer [54]. The FMOs of the title compound are determined and the corresponding surfaces are depicted in Fig 4. As can be seen in this figure, the methoxyphenyl groupment is mostly dominated by the molecular orbitals HOMO-1, LUMO, and LUMO+1, whereas the HOMO orbital is entirely located on the thiazolidinone and tert-butylimino fragments, demonstrating the possibility of charge transfer between the methoxyphenyl and the thiazolidinone groups. The difference in energy between HOMO and LUMO is calculated to be 2.67 eV, emphasizes the kinetic stability of the molecule under consideration. On the other hand, the molecular orbitals composition can be displayed by the total density of states (TDOS) [55]. Figure S6 shows the DOS diagram for TMTh. The red and green lines show the virtual and occupied orbitals. From the DOS diagram, it is evident that the donor (thiazole ring) and acceptor (phenyl ring) groups have a simultaneous effect on electron

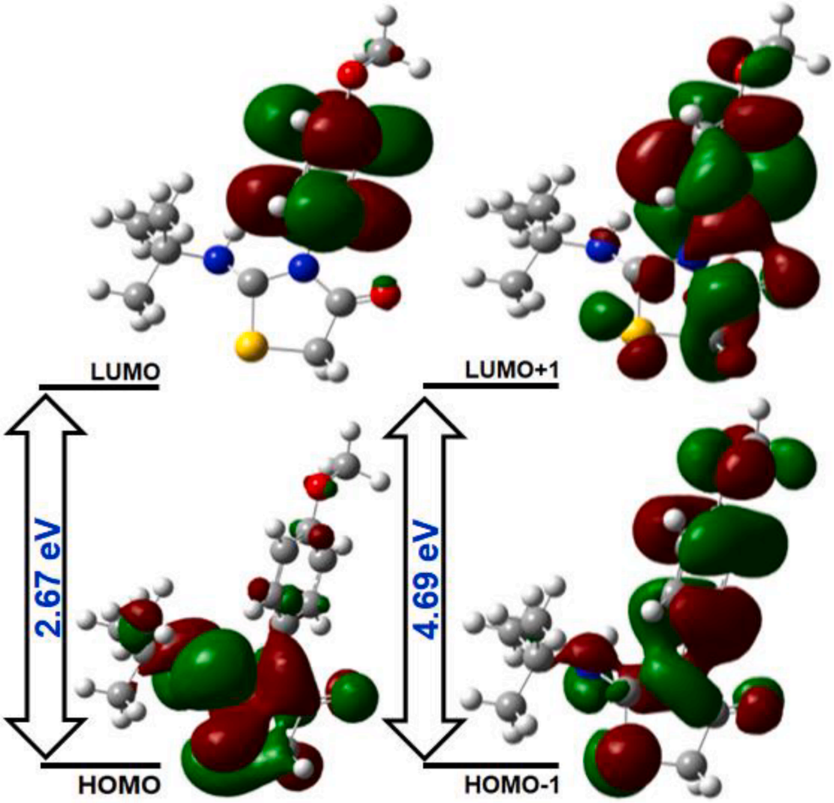

Fig. 4. Theoretical frontier molecular orbitals for TMTh.

delocalization.

3.3.4. Electronic circular dichroism

As is well known, optically active samples such as anisotropic materials and some crystals absorb left-handed and right-handed light from circular polarized light differently. Circular dichroism (CD) is described as the difference in absorbance between left and right handed light. On the other hand, circular dichroism (CD) is also used to determine the chirality or handedness of molecular systems. For small biomolecules, it is very frequently used to ascertain the secondary structure of proteins. In the present work, we investigated electronic circular dichroism (ECD) of TMTh using the TD-DFT method. Fig 5 shows the ECD spectrum for TMTh. As depicted in Fig 5, the spectrum shows three positive peaks at 214, 228, and 249 nm, as well as two negative peaks in 220 and 240 nm. The first peak, or lowest peak in positive phase, is revealed at 214 nm by the S0-S10 (H-2 to $L + 2$) electronic transition (see Table 5), whereas the maximum positive peak, or highest peak in positive phase, is revealed at 228 nm by the electronic transition S0-S5 expressed as (H to $L + 2$) transition. The lower energy bands at 220 and 240 nm, respectively, are produced by the electronic transitions S0-S8 (H-1 to $L + 1$) and S0-S3 (H-1 to L). According to the calculations above, there is consistency between the UV and circular dichroism spectra. The title compound absorbs left-handed light more efficiently than right-handed light, according to the positive peaks, while right-handed light was heavily absorbed in the negative phase, which is in good accordance with proteins that include alpha helices [56,57].

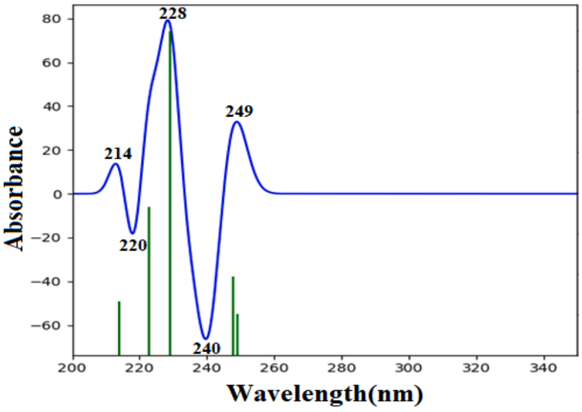

Fig. 5. ECD spectrum of TMTh.

3.4. Reactivity descriptors

The global chemical reactivity descriptors, or GCRDs, associated to the molecular modeling are considered as essential tools for establishing a connection between a material's structure and its stability [58]. According to the literature, chemical hardness and softness are two factors that affect how stable organic molecules are [55]. The GCRD variables explain how molecular components interact electronically. Based on the ionization potential ($IP = -E_{HOMO}$) and the electron affinity ($EA = -E_{LUMO}$), the GRCD parameters including electronegativity (χ), chemical potential (P), chemical hardness (η), chemical softness (s), and electrophilicity (ω) and nucleophilicity (ε) indices can be obtained from the following equation [59]:

$$\chi = \frac{(IP + EA)}{2};\ P = -\frac{(IP + EA)}{2};\ \eta = \frac{(IP - EA)}{2};\ S = \frac{1}{2\eta};\ \omega = \frac{P^2}{2\eta};\ \varepsilon = \frac{1}{\omega}$$

Table 6 summarized the computed values of the GCRD parameters for the title compound. The chemical potential (P) calculated value is −5.850 eV, showing that the title compound is chemically stable, while the chemical hardness (η) is around 1.336 eV, suggesting that charge transfer inside the molecule is favorable. Furthermore, the negative value of the chemical potential confirms the structural stability of the title compound [60]. As can be seen from Table 6 and in comparison to

Table 6

GCRD calculated values of TMTh by B3LYP/6–311G(d,p).

Parameters	Calculated energies (eV)
E_{HOMO}	−7.186
E_{LUMO}	−4.513
E_{HOMO-1}	−8.462
E_{LUMO+1}	−3.769
Energie gap (ΔE)	2.673
Ionization potential (I)	7.186
Electron affinity (A)	4.513
Electronegativity (χ)	5.850
Chemical potential (P)	−5.850
Chemical hardness (η)	1.336
Chemical softness (s)	0.3741
Electrophilicity index (ω)	12.801
Nucleophilicity index (ε) (eV^{-1})	0.078

the nucleophilicity index value (0.078 eV^{-1}), the electrophilicity index (ω) has a very significant value of 12.801 eV, which explains the molecule's electrophilic behavior and is consistent with previous findings [61]. The GCRD parameters are also fundamental for defining the bio-reactivity of molecular systems [62].

3.5. ELF, LOL and MEP distribution

3.5.1. ELF and LOL isosurfaces

Surface analysis provides maps of the electron localization function (ELF) and localized orbital locator (LOL) employing covalent bonds. Both ELF and LOL are based on kinetic energy density and exhibit a high probability of locating an electron pair on the surface of molecules. In contrast to ELF, which is based on electron pair density, LOL is often observed when localized orbitals overlap and produce large gradients of localized orbitals [63,64]. As in Bader's theory, the ELF and LOL functions and their topological studies enable partition of the molecular space into basins of electronic localization instead of atomic basins or regions of charge concentration [37]. The appropriate mathematical model for characterizing chemical bonding is based on topological study of the ELF and LOL functions. The ELF and LOL isosurface 2D maps for the title compound were determined using Multiwfn software. The ELF and LOL figures for TMTh are presented in color shade maps and are shown in Figs 6 and S7, respectively. The ELF maps are plotted in the range 0.0–1.0, while the LOL maps are plotted in the range 0.0–0.8. As can be seen in Fig 6, the covalent regions present between carbon-carbon and carbon-nitrogen atoms is indicated by red color. The blue circles around C, N, O and S nuclei display the electron depletion region between inner shell and valance shell. Therefore, electrons are concentrated in all hydrogen atoms. Furthermore, electrons are concentrated in the phenyl and thiazole rings' interatomic bond areas. The LOL function is considered a popular function for revealing electron localization character. From Figure S7, we can see that the regions with C—C, C—N and C-S covalent bonds, highlighted in red, have high LOL values, indicating high levels of electron localization. On the other hand, the blue circles around the nuclei indicate the areas where the outer and inner shells of the valence region are electron-depleted.

3.5.2. MEP analysis

Molecular electrostatic potential (MEP) has always been considered as crucial in the investigation of intermolecular interactions and the localization of nucleophilic and electrophilic attack regions in molecular systems [65,66]. The relationship between the MEP distribution and a molecule's electron density is also widely recognized [67]. The molecular electrostatic potential, V(r), at a specific position r(x,y,z) is defined as the electrostatic interaction between the electrical charge generated by the molecule's nuclei and electrons and a proton at r. The following equation was used to calculate the V(r) values for the system being studied:

$$V(r) = \sum_A \frac{Z_A}{(R_A - r)} - \int \frac{\rho_{total}(r')}{|r' - r|} dr'$$

Where Z_A is the charge of nucleus A located at R_A, ρ(r') is the electronic density of the molecule, and r' is the dummy atom position. The common color scheme used to describe the MEP map was widely reported in which the negatively and positively charged regions are colored in red and blue, respectively [68]. On the other hand, due to higher concentration of electronic density, the nucleophilic sites of the molecule are displayed as red. Reciprocally, electron-deficient regions are displayed in blue. Based on the optimized structure of TMTh, the MEP surface was computed (Figure S8). According to the MEP map in Figure S8, the most negative region associated with the strongest attraction is around the carbonyl group and the positive regions associated with the strongest repulsion are located on the hydrogen atoms of the molecule. Therefore, it may be inferred that electronegative atoms are the most common sites for nucleophilic attack, whereas hydrogen atoms are the most common locations for an electrophilic attack.

3.6. NLO effect

When electromagnetic forces interact in various media, new fields with distinct phases arise, eventually leading to the so-called nonlinear optical (NLO) effect, which can provide a wide variety of capabilities for

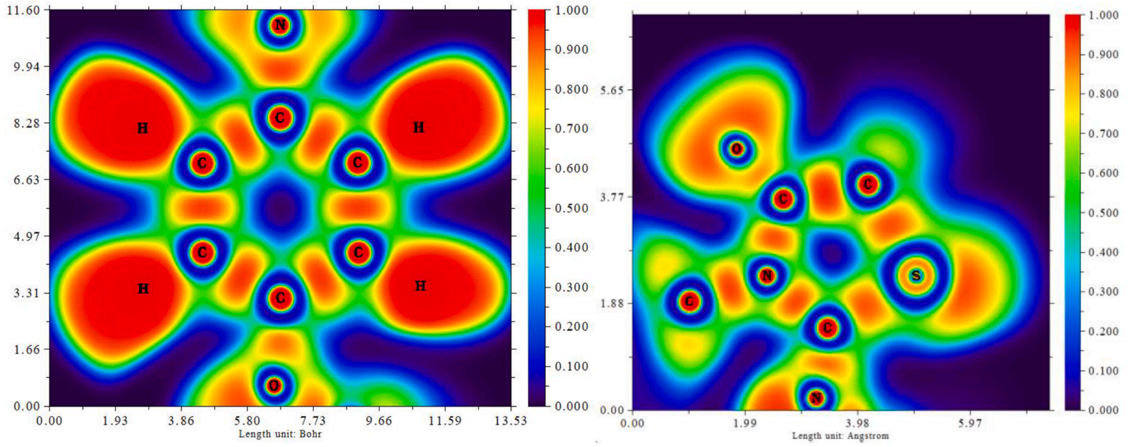

(a)

(b)

Fig. 6. ELF shaded isosurface maps for TMTh, (a) phenyl fragment, (b) thiazole fragment.

emerging technologies like as telecommunications and signal processing [69–71]. To understand more about the title compound's NLO property, we computed dipole moment (μ), polarizability (α), and first and second order hyperpolarizabilities (β and γ). The magnitude of μ, α, β and γ tensors were calculated using the x, y and z components described by the following equations [72]:

$$\mu = \left(\mu_x^2 + \mu_y^2 + \mu_Z^2\right)^{\frac{1}{2}}; = \frac{1}{3}\left(\alpha_{xx} + \alpha_{yy} + \alpha_{zz}\right);\ \beta \parallel = \left(\beta_x^2 + \beta_y^2 + \beta_z^2\right)^{\frac{1}{2}}$$

For the first order hyperpolarizability estimation, the detailed relation is as follows:

$$\beta \parallel = \left[\left(\beta_{xxx} + \beta_{xyy} + \beta_{xzz}\right)^2 + \left(\beta_{yyy} + \beta_{yzz} + \beta_{yxx}\right)^2 + \left(\beta_{zzz} + \beta_{zxx} + \beta_{zyy}\right)^2\right]^{\frac{1}{2}}$$

The Kleinmann hypothesis [65] was used to calculate the second-order hyperpolarizability (γ) via the following equation:

$$\gamma = \frac{1}{5}\left(\gamma_{xxxx} + \gamma_{yyyy} + \gamma_{zzzz} + 2\gamma_{xxyy} + 2\gamma_{xxzz} + 2\gamma_{yyzz}\right)$$

The calculation of the NLO properties for the title compound were carried out and the corresponding results are reported in Table 7.

It is well established that NLO properties are closely related to the higher values of dipole moment, polarizability and hyperpolarizabilities.

The dipole moment calculated by B3LYP and BPV86 functionals are equal to 0.56 and 2.19 D, respectively, which are in the range of values for most similar organic compounds reported in the literature [73,74] Compared to the B3LYP functional, the BPV86 functional gives a better value of the dipole moment. The predicted dipole moment value for the isolated gas phase molecule of TMTh obtained by BPV86 functional is close to that of the urea (3.73 Debye) considered as the organic NLO active typical molecule. The calculated polarizability values are 28.77 × 10^{-24} and 30.17 × 10^{-24} esu predicted using B3LYP and BPV86 functionals, respectively. For the hyperpolarizability, several studies have shown that the first-order hyperpolarizability value is related to the HOMO-LUMO energy gap and the second-order hyperpolarizability value reveals the delocalization of electrons and substantial charge transfer through the π-conjugation [75]. The calculated first-order hyperpolarizabilities for TMTh using B3LYP and BPV86 are about 2.91 × 10^{-30} and 5.58 × 10^{-30} esu, respectively, which are approximately from 15 to 25 times that of urea (0.197 × 10^{-30} esu). The dominant component contributing to this value is β_{xxx}. The second-order hyperpolarizability (γ) values for the title molecule are about 16.29 × 10^{-36} and 26.01 × 10^{-36} esu as obtained by B3LYP and BPV86 functionals, revealing that the title molecule could be regarded as a conventional molecule for optoelectronic and NLO applications. Moreover, the values of α, β and γ showed that TMTh may be considered for linear optics applications.

Table 7

Calculated molecular dipole moment (μ), polarizability (α), and first and second hyperpolarizabilities (β and γ) values for TMTh.

Parameters	B3LYP	BPV86
Dipole moment		
μ_x	0.558	−0.052
μ_y	0.028	−0.765
μ_z	−0.004	−0.393
μ (D)	0.56	2.19
Polarizability		
α_{xx}	235.625	250.102
α_{xy}	9.729	−4.797
α_{yy}	194.69	156.588
α_{zx}	−0.011	−16.585
α_{zy}	0.019	18.557
α_{zz}	152.12	204.073
α (au)	194.145	203.587
α × 10^{-24} (esu)	28.77	30.17
First-order hyperpolarizability		
β_{xxx}	390.927	823.569
β_{xxy}	−110.724	64.674
β_{yxy}	192.772	52.990
β_{yyy}	139.345	−6.301
β_{xxz}	−0.018	60.629
β_{yxz}	−0.062	154.164
β_{yyz}	−0.064	−7.715
β_{zxz}	−22.613	196.296
β_{zyz}	−12.5891	−54.603
β_{zzz}	−50.951	26.426
$\beta_{\|\|}$ (au)	336.789	645.475
$\beta_{\|\|}$ × 10^{-30} (esu)	2.91	5.58
Second-order hyperpolarizability		
γ_{xxxx}	75,037.8	12,784.5
γ_{yyyy}	24,359.9	15,197.8
γ_{zzzz}	10,207.0	29,176.8
γ_{xxyy}	16,823.9	11,468.7
γ_{xxzz}	5116.11	22,799.1
γ_{yyzz}	4077.06	8743.59
⟨γ⟩ (au)	32,327.9	51,648.9
⟨γ⟩ × 10^{-36} (esu)	16.29	26.01

3.7. *Biological activity*

3.7.1. *PASS and molecular docking analysis*

Molecular docking is the most often computational approach used for determining the interaction energy and binding affinity of receptor-ligand complex [76]. The online PASS program, which predicts over 300 pharmacological effects, biochemical mechanisms, and specific toxicities based on a substance's structural formula, defines the protein (target) as the accurate and consistent receptor for the ligand [77]. The predicted results of the biological activity are listed in Table 8 associated with their probability values. Probable activity (Pa) and probable inactivity (Pi) are used to establish the corresponding results with Pa > Pi and Pa ≥ 0.5. According to the PASS study, the title compound may inhibit the gluconate 2-dehydrogenase protein (acceptor) with 5U9P, 4HP8, 4Z9X, 1VL8, 4IBO and 3O03 receptors that can be obtained from the Protein Data Bank (PDB) [78,79]. Because of its high Pa value (Pa = 0.698), this protein was chosen for the present study. The gluconate 2-dehydrogenase is an oxidoreductase enzyme that is involved in the ketogluconate and pentose phosphate pathways. Furthermore, the target protein is chosen based on its binding energy value. A negative binding energy indicates a good docking ability [80]. In this work, binding sites between the ligand (TMTh) and the target proteins were estimated. The Auto dock 4.2.6 program is used to carry out the docking calculations [81] and the PyMol program for visualization [82].

In Table 9, binding affinities for various poses in the 5U9P inhibitor of the investigated ligand that were found within the gluconate 2 dehydrogenase protein (acceptor) are listed along with their root-mean-square deviation (RMSD) values. The binding affinities in the other receptors (4HP8, 4Z9X, 1VL8, 4IBO and 3O03) are given in Table S3. The optimal pose for molecular docking is the docked conformation with the lowest binding energy and RMSD scores of 2.0 [83]. The conventional

Table 8

PASS prediction for the activity spectrum of the title compound. Pa represents probability to be active and Pi represents probability to be inactive. Pa > Pi and Pa > 0.500.

Pa	Pi	Activity
0.698	0.057	Gluconate 2-dehydrogenase (acceptor) inhibitor
0.651	0.080	Aspulvinonedimethylallyltransferase inhibitor
0.571	0.002	MAP kinase kinasekinase inhibitor
0.554	0.073	Phosphatase inhibitor
0.532	0.099	Acrocylindropepsin inhibitor
0.532	0.099	Chymosin inhibitor
0.532	0.099	Saccharopepsin inhibitor
0.511	0.046	Insulysin inhibitor
0.515	0.052	Thioredoxin inhibitor
0.506	0.041	Antianginal

Table 9
Binding affinity and RMSD values of different poses in the 5U9P inhibitor of TMTh by Auto Dock Vina.

Mode	Affinity (kcal/mol)	Distance from best mode (Å)	
		RMSD l.b.	RMSD u.b.
1	−6.0	0	0
2	−5.4	19.296	21.196
3	−5.2	6.655	9.26
4	−5.1	18.789	19.957
5	−4.9	7.423	10.102
6	−4.9	18.135	20.195
7	−4.8	11.242	13.661
8	−4.8	17.876	19.893
9	−4.8	8.08	10.892

docking position was reached in mode No. 1 defined a binding energy (ligand-protein) of −6.0 kcal/mol showing a good satisfactory with literature results [84]. Table 10 provides an overview of the intermolecular interactions between the molecule and the residues of the proteins 5U9P, 4HP8, 4Z9X, 1VL8, 4IBO and 3O03, including their distances, kinds, and locations. The 5U9P, 4HP8, 4Z9X, 1VL8, 4IBO and 3O03 proteins are defined as accurate receptors for TMTh. The intermolecular interactions between the TMTh ligand and all the proteins are shown in figures (S9 to S20). For the 5U9P protein, the docking results show three strong conventional hydrogen bonds. These intermolecular interactions are observed between the O2 atom of the thiazolidinone group and ILE 24, GLY 25 and ASN 96 residues with distances of 2.79, 2.18 and 2.07 Å, respectively. Additionally, Pi-sigma, Alkyl and Pi-Alkyl interactions were also observed between LEU 198, ILE 99 and ILE 24 residues and C_6H_4 and methyl groups. The above cited interactions are shown in Figure S10. The most efficient interactions are those involving O2 atom leading to enhance the binding between the ligand and the 5U9P protein. For the 4HP8 protein, as can be seen in Figure S12, four strong intermolecular interactions are observed between the O2 atom of the thiazolidinone group, and ARG41 and ARG42 residues. The corresponding distances are 2.41 and 2.16 Å for ARG 41, and 2.00 and 2.60 Å for ARG 42. On the other hand, Alkyl and Pi-Alkyl interactions are observed between the C_6H_4 and methyl moieties, and ALA 87, ILE 63, ARG 41 and PHE 65 residues. The docking findings of 4Z9X protein revealed the existence of one efficient interaction between the SER 145 residue and the O2 atom with a distance of 3.23 Å. The other hydrophobic interactions are observed between ILE 143, ILE 21 and PRO 188 residues, and methyl and C_6H_4 groups. As can be seen in Table 10 and Figure S16, TMTh showed hydrophobic interactions with 1VL8 residues (VAL 231 and PHE 232) involving the methyl and C_6H_4 groups. For the 4IBO protein, the docking results showed that TMTh interacts with this protein thtrough two strong conventional hydrogen bonds. These interactions are observed between ARG 109 and TYR 113 residues, and the O2 atom of the thiazolidinone group with the distances 2.35 and 2.55 Å, respectively. In addition, TMTh showed hydrophobic interactions of the methyl C_6H_4 groups with the following residues of 4IBO: ALA67 and ARG109 (Figure S18). For the 3O03 receptor, one hydrogen bond was observed between LEU7 residue and the methyl group with a distance of 3.50 Å. Other hydrophobic interactions were also observed for which TMTh is linked to 3O03 residues (ALA37 and PHE10) with Pi-Alkyl interactions. On the other hand, the studied molecule binds to the PHE 10 residue via Pi-Sigma interaction (Figure S20).

The conventional docking positions were reached in mode No. 1 defined a binding energy (ligand-protein) of −6.0, −5.9, −5.9, −4.8, −4.3, and −5.0 kcal/mol showing a good satisfactory with literature results [84]. The docking results indicate that TMTh possesses antitumor activity, suggesting that the compound TMTh may be strongly recognized as a suitable inhibitor of the gluconate-2-dehydrogenase protein.

3.7.2. In silico ADMET investigation

The biological activity of organic compounds has been widely studied using the absorption, distribution, metabolism, excretion, and toxicity, or ADMET, analysis. The ADMET study was carried out for the title compound and the corresponding pharmacokinetic and physicochemical results are gathered in Table S4. The drug-likeness parameters of TMTh are also reported in Table S4 and were expressed by the Lipinski's rule of five, which is considered the most useful method for this kind of studies [85]. The SwissADME server (www.swis-sadme.ch/index.php) provided the properties of Lipinski's rule five. From the obtained results, the title compound complies well with the Lipinski rule of five indicating a good bioavailability. Furthermore, rule-based filters from Lipinski, Ghose, Veber, and Egan were also used to evaluate the predicted drug-likeness parameters of the title compound. In this context, oral drugs should match the suitable requirements as reported in many previous research works [86,87]. The bioavailability radar and the BOILED-EGG model of TMTh are displayed in Fig. 7. As shown in this figure, based on the position of the red dot for our compound, we can deduce that the BBB penetration and GI absorption parameters are favorable (positive), while the P-GP effect on the molecule is unfavorable (negative). Total Polar Surface Area (TPSA) is the main factor contributing to the favorable BBB result. The TPSA value of our compound is 67.20 Å^2, and it is in the appropriate domain region. According to the results of Table S4, the significant value of the skin permeation parameter (Log Kp = −5.97 cm/s), the higher gastrointestinal (GI) absorption and the positive blood-brain barrier (BBB) permeant suggest that the title compound could be a strong therapeutic candidate and can penetrate the blood-brain barrier. As it is well known, a TPSA of less than 90 Å^2 is typically required for a molecule to penetrate the blood-brain barrier [88]. Consequently, according to the drug-likeness study, the tested compound could be considered as potential active oral drug. For the inhibition activity, as shown in Figure S21, the title compound has been predicted to inhibit kinase protein with the probability of 60%, membrane receptor (13.3%), enzyme (13.3%), phosphodiesterase (6.7%), and other cytosolic protein with the probability of 6.7%.

4. Conclusion

In conclusion of the present paper, the TMTh molecule ((Z)−2N-(tert-butylimino)−3N'-(4-methoxyphenyl) thiazolidin-4-one) was synthesized and its structure was analyzed using SC-XRD and spectroscopic techniques. The experimental measurements were supported and complemented by in-depth theoretical calculations. The structure of TMTh belongs to the space group I2/a of the monoclinic crystal system. In this work, the DFT method with the B3LYP functional and the 6–311G(d,p) basis set have been used to perform the theoretical calculations. The calculated geometrical parameters were found to be consistent with those of the SC-XRD study. The structural investigation showed that the title compound is formed by methoxyphenyl and tert-butylimino-thiazolidin-4-one groups in two different planes with a dihedral angle of 68° The structural study has been completed by identifying the hydrogen bonding using HS, fingerprint, and RDG analyses. It has been found that the main intermolecular interactions are C—H···O and C—H···S which connected molecules into 3D architecture in the crystal packing and the major contributions to the surface are due to H···H contacts with 56.3%. The electrostatic behavior of TMTh was studied and the repulsive, attractive, and van der Waals (VDW) noncovalent interactions were also identified. The theoretical vibrational modes and their assignments were carried out giving a good correlation with the experimental spectroscopic results. The 1H and 13C isotropic chemical shifts were computed using the optimized geometry and the corresponding results were found to be consistent with the experimental chemical shifts except for some values where the differences are explained by the effect of the electronic environment of the considered atom. The theoretical UV–Visible spectrum was calculated by TD-DFT/B3LYP/6–311G(d,p) and compared with the experimental one. This wavelength absorption is associated with the strong $\pi \rightarrow \pi^*$ electronic transition. Furthermore, the electronic

Table 10
Distance types and location of intermolecular interactions formed from the residues of the protein gluconate 2-dehydrogenase and TMTh.

Protein	Ligand	Residue	Atom/ moiety	Category	Types	Distance (Å)	Affinity (kcal/ mol)
Gluconate 5-dehydrogenase (PDB ID : 5U9P)	TMTh	A: ILE24	O2 atom	Hydrogen Bond	conventional hydrogen bond	2.79	−6.0
		A:GLY25	O2 atom	Hydrogen Bond	conventional hydrogen bond	2.18	
		A:ASN96	O2 atom	Hydrogen Bond	conventional hydrogen bond	2.07	
		A:LEU198	C_6H_4 ring	Mixed Pi/Alkyl-Hydrophobic	Pi-Sigma	3.89	
		A:ILE99	methyl group	Alkyl -Hydrophobic	Alkyl	5.07	
		A:LEU198	methyl group	Alkyl -Hydrophobic	Alkyl	3.76	
		A:ILE24	C_6H_4 ring	Mixed Pi/Alkyl-Hydrophobic	Pi-Alkyl	4.98	
Gluconate 5-dehydrogenase (PDB ID : 4HP8)		B: PHE65	methyl group	Hydrophobic	Pi-Alkyl	4.71	−5.9
		B:ILE63	methyl group	Hydrophobic	Alkyl	5.42	
		B:ALA87	methyl group	Hydrophobic	Alkyl	4.16	
		B: ALA87	C_6H_4 ring	Hydrophobic	Pi-Alkyl	4.83	
		B:ARG41	C_6H_4 ring	Hydrophobic	Pi-Alkyl	4.28	
		B: ARG41	O2 atom	Hydrogen Bond	conventional hydrogen bond	2.41	
		B: ARG41	O2 atom	Hydrogen Bond	conventional hydrogen bond	2.16	
		B: ARG42	O2 atom	Hydrogen Bond	conventional hydrogen bond	2.00	
		B: ARG42	O2 atom	Hydrogen Bond	conventional hydrogen bond	2.60	
Gluconate 5-dehydrogenase (PDB ID : 4Z9X)		A: ILE143	methyl group	Hydrophobic	Alkyl	5.29	−5.9
		A:ILE21	methyl group	Hydrophobic	Alkyl	4.33	
		A:ILE21	C_6H_4 ring	Hydrophobic	Pi-Alkyl	5.09	
		A: PRO188	C_6H_4 ring	Hydrophobic	Pi-Alkyl	4.89	
		A:SER145	O2 atom	Hydrogen Bond	conventional hydrogen bond	3.23	
Gluconate 5-dehydrogenase (PDB ID : 1VL8)		A: VAL231	methyl group	Hydrophobic	Alkyl	4.57	−4.8
		A: VAL231	C_6H_4 ring	Hydrophobic	Pi-Alkyl	5.34	
		A:PHE232	methyl group	Hydrophobic	Pi-Alkyl	4.99	
Gluconate 5-dehydrogenase (PDB ID : 4IBO)		A: ALA67	methyl group	Hydrophobic	Alkyl	3.52	−4.3
		A:ARG109	C_6H_4 ring	Hydrophobic	Pi-Alkyl	5.38	
		A: TYR113	O2 atom	Hydrogen Bond	conventional hydrogen bond	2.55	
		A: ARG109	O2 atom	Hydrogen Bond	conventional hydrogen bond	2.35	
Gluconate 5-dehydrogenase (PDB ID : 3O03		A: LEU7	methyl group	Hydrogen Bond	Carbon hydrogen bond	3.50	−5
		A:ALA37	C atom	Hydrophobic	Pi-Alkyl	4.82	
		A:PHE10	methyl group	Hydrophobic	Pi-Alkyl	4.87	
		A: PHE10	methyl group	Hydrophobic	Pi-Sigma	3.76	

circular dichroism provided similar results to the UV–Vis analysis. The HOMO, LUMO, and gap energies were estimated theoretically. The energy gap (DE) value of 2.67 eV, which also indicated the kinetic stability of TMTh, confirmed charge transfer within the molecule. The FMOs energies were used to compute the chemical reactivity descriptors and the results have shown that the title molecule has a very significant electrophilicity index (12.801 eV) suggesting an electrophilic behavior. On the other hand, the ELF and LOL isosurface distribution of TMTh revealed electron localization character and indicated high levels of electron localization on the covalent bonds. The electron density distribution was also confirmed by the MEP map showing that the sites for nucleophilic and electrophilic attacks were located on electronegative and hydrogen atoms, respectively. The NLO effect of TMTh was studied and the corresponding properties were calculated using the DFT method at B3LYP and BPV86 functionnals. The BPV86 functional predicted better values of NLO properties revealing that the title molecule could be used for optoelectronic and NLO applications. Finally, molecular docking tools were used to analyze the biological activity of TMTh, and the findings suggested that the title compound could be a suitable inhibitor of the gluconate-2-dehydrogenase protein. From the in silico ADMET results and according to the drug-likeness study, the title compound could be considered a potential active oral drug.

Supplementary crystallographic data

Crystallographic data for the structure reported in this article have

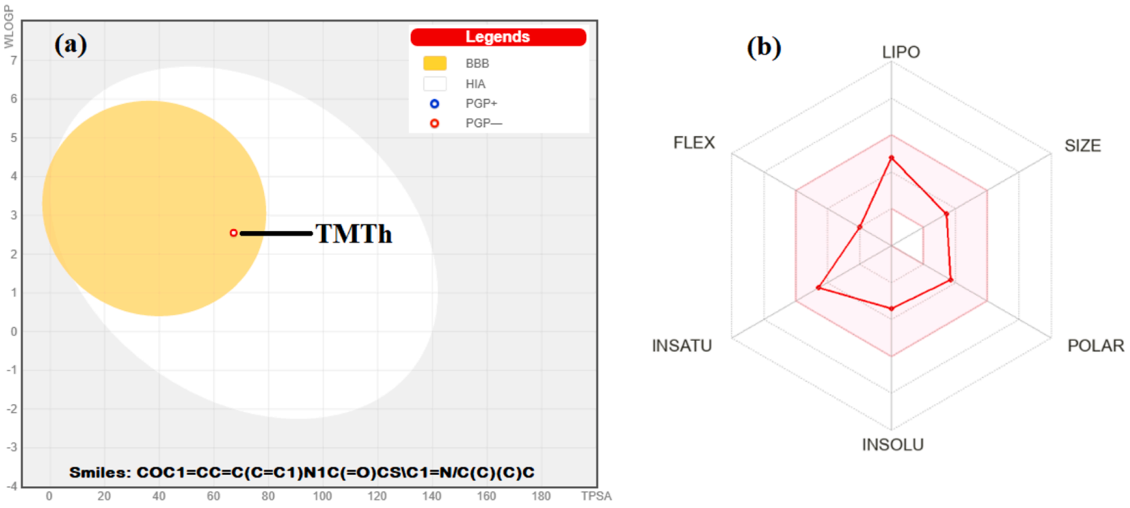

Fig. 7. (a) TMTh blood brain barrier (BBB) permeability [BOILED-EGG], and (b) TMTh oral bioavailability radar.

been deposited with Cambridge Crystallographic Data Center, CCDC 1547696. Copies of this information may be obtained free of charge from the Director, CCDC, 12 Union Road, Cambridge, CBZ IEZ, UK. Facsimile (44) 01223 336 033, E-mail: deposit@ccdc.cam.ac.uk or http://www.ccdc.com.ac.uk/deposit.

Declaration of Competing Interest

The authors declare that they have no known competing financial interests or personal relationships that could have appeared to influence the work reported in this paper.

Data availability

Data will be made available on request.

Acknowledgments

This work was supported by the ministry of higher education and scientific research, the Directorate General for Scientific Research and Technological Development (DG-RSDT), and the Abdelhamid Ibn Badis University of Mostaganem.

CRediT authorship contribution statement

F. Z. Boudjenane: Methodology, Investigation, Writing - review & editing. F. Triki-Baara: Synthesis, Writing - review & editing, Data curation. N. Boukabcha: Methodology, Investigation, Software, Writing - review & editing, Formal analysis. N. E. H. Belkafouf: Investigation, Software, figures preparation. N. Dege: X-ray Data Processing, Structure Determination, CIF validation. M. Saidj: Investigation, Software. N. Khelloul: Software, Writing - review & editing, Formal analysis. A. Djafri: Synthesis, Supervision, Spectroscopic analysis, reviewing. Abdelkader Chouaih: Supervision, Conceptualization, Methodology, review & editing.

Supplementary materials

Supplementary material associated with this article can be found, in the online version, at doi:10.1016/j.molstruc.2023.135620.

References

[1] M. Wei, C. Lin, C. Yang, Y. Kiang, J. Lee, H. Lin, Emission characteristics of organic light-emitting diodes and organic thin-films with planar and corrugated structures, Int. J. Mol. Sci. 11 (4) (2010) 1527–1545, https://doi.org/10.3390/ijms11041527.

[2] K. Chen, R. Wu, X. Li, W. Liu, Z. Wei, J. Wang, L. Zhou, High-quality all-fluorescent white organic light-emitting diodes obtained by balancing carriers with hole limit layer, Opt. Mater. (Amst) 123 (2022), 111917, https://doi.org/10.1016/j.optmat.2021.111917.

[3] Ed.H.S. Nalwa (Ed.), Handbook of Organic Conductive Molecules and Polymers, Chichester: Wiley-VCH, 1997.

[4] J.K. Salim, Q.M.A. Hassan, A.M. Jassem, H.A. Sultan, A. Muala Dhumad, C. A. Emshary, An efficient ultrasound-assisted CH3COONa catalyzed synthesis of thiazolidinone molecule: theoretical and nonlinear optical evaluations of thiazolidinone-Schiff base derivative, Opt. Mater. (Amst) 133 (2022), 112917, https://doi.org/10.1016/j.optmat.2022.112917.

[5] N. Boukabcha, A. Djafri, Y. Megrouss, Ö. Tamer, D. Avcı, M. Tuna, N. Dege, A. Chouaih, Y. Atalay, A. Djafri, F. Hamzaoui, Synthesis, crystal structure, spectroscopic characterization and nonlinear optical properties of (Z)-N'-(2,4-dinitrobenzylidene)-2-(quinolin-8-yloxy) acetohydrazide, J. Mol. Struct. 1194 (2019) 112–123, https://doi.org/10.1016/j.molstruc.2019.05.074.

[6] A. Djafri, F. Perveen, N. Benhalima, N. Khelloul, R. Rahmani, A. Djafri, A. Chouaih, M.B. Kanoun, S. Goumri-Said, Experimental spectral characterization, Hirshfeld surface analysis, DFT/TD-DFT calculations and docking studies of (2Z,5Z)-5-(4-nitrobenzylidene)-3-N(2-methoxyphenyl)-2-N'(2-methoxyphenylimino) thiazolidin-4-one, Heliyon 6 (2020) 15, https://doi.org/10.1016/j.heliyon.2020.e05754, e057542:1-e057542.

[7] R. Rahmani, F. Perveen, N. Benhalima, A. Djafri, N. Khelloul, A. Chouaih, A. Djafri, M.B. Kanoun, S. Goumri-Said, FTIR, NMR and UV–Visible Spectral Investigations, Theoretical Calculations, Topological Analysis, Chemical Stablity, and Molecular Docking Study on Novel Bioactive Compound: The 5-(5-Nitro Furan-2-Ylmethylen), 3-N-(2-Methoxy Phenyl),2-N'-(2-Methoxyphenyl) Imino Thiazolidin-4-One, Polycyclic Aromatic Compounds, 2022, https://doi.org/10.1080/10406638.2022.2094971.

[8] R. Rahmani, A. Djafri, A. Chouaih, A. Djafri, F. Hamzaoui, A.M. Krallafa, Molecular structure, FT-IR, NMR (13C/1H), UV–Vis spectroscopy and DFT calculations on (2Z, 5Z)-3-N(4-methoxy phenyl)-2-N'(4- methoxy phenyl imino)-5-((E)-3-(2-nitrophenyl)allylidene) thiazolidin-4-one, S. Afr, J. Chem 72 (2019) 176–188. https://hdl.handle.net/10520/EJC-17c4a8c444.

[9] S. Yahiaoui, A. Moliterni, N. Corriero, C. Cuocci, K. Toubal, A. Chouaih, A. Djafri, F. Hamzaoui, 2-thioxo- 3N-(2-methoxyphenyl) -5 [4'-methyl -3'N -(2'-methoxyphenyl) thiazol-2'(3'H)-ylidene] thiazolidin-4-one: synthesis, characterization, X-ray single crystal structure investigation and quantum chemical calculations, J. Mol. Struct. 1177 (2019) 186–192, https://doi.org/10.1016/j.molstruc.2018.09.052.

[10] N.C. Desai, H.K. Mehta, A.M. Jethawa, J.D. Monapara, V.M. Khedkar, B.P. Dave, Design, synthesis, antimicrobial evaluation, and in-silico studies of some 4-thiazolidinone hybrids bearing coumarin and pyridine moieties, J. Heterocycl. Chem. 59 (12) (2022) 2177–2189, https://doi.org/10.1002/jhet.4550R.

[11] S. Khan, H. Ullah, F. Rahim, M. Nawaz, R. Hussain, L. Rasheed, Synthesis, in vitro α-amylase, α-glucosidase activities and molecular docking study of new benzimidazole bearing thiazolidinone derivatives, J. Mol. Struct. 1269 (2022), 133812, https://doi.org/10.1016/j.molstruc.2022.133812.

[12] R. Manda, R. Venkata Nadh, T.L. Viveka, G. Angajala, V. Aruna, New benzylidene festooned thiazolidinone-coumarin molecular hybrids targeting human breast adenocarcinoma cells: design, synthesis, sar, molecular modelling and biological evaluation as CDK2 inhibitors, J. Mol. Struc. (2023), 135453, https://doi.org/10.1016/j.molstruc.2023.135453.

[13] M. Abdalla, S. Gomha, M. Abd El-Aziz, N. Serag, Synthesis and evaluation of some novel thiazoles and 1,3-thiazines as potent agents against the rabies virus, Turk. J. Chem. 40 (2016) 441–453, https://doi.org/10.3906/kim-1506-13.

[14] C.F. Hu, P.L. Zhang, Y.F. Sui, J.S. Lv, M.F. Ansari, N. Battini, S. Li, C.H. Zhou, R. X. Geng, Ethylenic conjugated coumarin thiazolidinediones as new efficient antimicrobial modulators against clinical methicillin-resistant Staphylococcus aureus, Bioorg. Chem. 94 (2020), 103434, https://doi.org/10.1016/j.bioorg.2019.103434.

[15] G. Angajala, V. Aruna, P. Pavan kumar, P.G. Reddy, Biocatalytic one pot three component approach: facile synthesis, characterization, molecular modelling and hypoglycemic studies of new thiazolidinedione festooned quinoline analogues catalyzed by alkaline protease from Aspergillus niger, Bioorg. Chem. 119 (2022), 105533.

[16] T. Tomašić, N. Zidar, M.M. Premru, D. Kikelj, L.P. Mašič, Synthesis and antibacterial activity of 5-ylidenethiazolidin-4-ones and 5-benzylidene-4,6-pyrimidinediones, Eur. J. Med. Chem. 45 (2010) 1667–1672, https://doi.org/10.1016/j.ejmech.2009.12.030.

[17] G.M. Sheldrick, A short history of SHELX, Acta Cryst A 64 (2008) 112–122.

[18] G.M. Sheldrick, Crystal structure refinement with SHELXL, Acta Cryst A 71 (2015) 3–8.

[19] C.F. Macrae, P.R. Edgington, P. McCabe, E. Pidcock, G.P. Shields, R. Taylor, M. Towler, Mercury: visualisation and analysis of crystal structures, J. Appl. Cryst. 39 (2006) 453–457.

[20] L.J. Farrugia, ORTEP-3 for windows - a version of ORTEP-III with a graphical user interface (GUI), J. Appl. Crystallogr. 30 (1997) 565, https://doi.org/10.1107/S0021889897003117.

[21] M.J. Frisch, G.W. Trucks, H.B. Schlegel, G.E. Scuseria, M.A. Robb, J.R. Cheeseman, G. Scalmani, V. Barone, B. Mennucci, G.A. Petersson, H. Nakatsuji, M. Caricato, X. Li, H.P. Hratchian, A.F. Izmaylov, J. Bloino, G. Zheng, J.L. Sonnenberg, M. Hada, M. Ehara, K. Toyota, R. Fukuda, J. Hasegawa, M. Ishida, T. Nakajima, Y. Honda, O. Kitao, H. Nakai, T. Vreven, J.A. Montgomery Jr., J.E. Peralta, F. Ogliaro, M. Bearpark, J.J. Heyd, E. Brothers, K.N. Kudin, V.N. Staroverov, R. Kobayashi, J. Normand, K. Raghavachari, A. Rendell, J.C. Burant, S.S. Iyengar, J. Tomasi, M. Cossi, N. Rega, J.M. Millam, M. Klene, J.E. Knox, J.B. Cross, V. Bakken, C. Adamo, J. Jaramillo, R. Gomperts, R.E. Stratmann, O. Yazyev, A.J. Austin, R. Cammi, C. Pomelli, J.W. Ochterski, R.L. Martin, K. Morokuma, V.G. Zakrzewski, G.A. Voth, P. Salvador, J.J. Dannenberg, S. Dapprich, A.D. Daniels, E.O. Farkas, J. B. Foresman, J.V. Ortiz, J. Cioslowski, D.J. Fox, Gaussian 09, Revision A.02, Gaussian Inc, Wallingford, CT, 2009.

[22] R.D. Dennington, T.A. Keith, J.M. Millam, GaussView 5.0.8, Gaussian Inc., 2008.

[23] A.D. Becke, Density-functional thermochemistry. III. The role of exact exchange, J. Chem. Phys. 98 (7) (1993) 5648–5652, https://doi.org/10.1063/1.464913.

[24] C. Lee, W. Yang, R.G. Parr, Development of the Colle-Salvetti correlation-energy formula into a functional of the electron density, Phys. Rev. B 37 (2) (1993) 785–789, https://doi.org/10.1103/physrevb.37.785.

[25] R.D. Johnson III, NIST computational chemistry comparison and benchmark database, NIST Stand. Ref. Database Number 101, Release 18 (2016). http://cccbdb.nist.gov/.

[26] M.H. Jamroz, Vibrational Energy Distribution Analysis VEDA4, Warsaw, 2004, 2010.

[27] Ö. Tamer, N. Dege, G. Demirtaş, D. Avcı, Y. Atalay, M. Macit, S. Şahin, Crystal structure and spectroscopic characterization of (E)-2-(((4-bromo-2-(trifluoromethoxy)phenyl) imino)methyl)-4-nitrophenol: a combined experimental and computational study, J. Mol. Struct. 1063 (2014) 295–306, https://doi.org/10.1016/j.molstruc.2014.01.079.

[28] A.J.C. Wilson, International Tables for Crystallography, Kluwer, Dordrecht, 1995 vol C.

[29] R. Gupta, R.P. Chaudhary, X-ray, NMR and DFT studies on benzo[*h*]thiazolo[2,3-*b*] quinazoline derivatives, J. Mol. Struct. 1049 (2013) 189–197.

[30] K. Toubal, N. Boukabcha, Ö. Tamer, N. Benhalima, S. Altürk, D. Avcı, A. Chouaih, Y. Atalay, A. Djafri, F. Hamzaoui, Spectroscopic (FT-IR, 1H and 13C NMR) characterization and density functional theory calculations for (Z)-5-(4-nitrobenzyliden) -3- N(2-ethoxyphenyl) -2-thioxo - thiazolidin-4-one (ARNO), J. Mol. Struct. 1147 (2017) 569–581, https://doi.org/10.1016/j.molstruc.2017.06.102.

[31] M. Boulakoud, K. Toubal, S. Yahiaoui, G. Chita, A. Chouaih, A. Djafri, F. Hamzaoui, molecular structure investigation of z-3n(2-ethoxyphenyl)-2-n′(2-ethoxyphenyl)-imino-thiazolidin-4-one by ab initio, DFT and X-ray diffraction methods, J. Struct. Chem 56 (7) (2015) 1373–1378, https://doi.org/10.1134/S0022476615070197.

[32] A. Djafri, A. Chouaih, J.C. Daran, A. Djafri, F. Hamzaoui, Crystal and molecular structure of (2Z, 5Z)-3-(2-methoxyphenyl)-2-[(2-*methoxyphenyl*) *imino*]-5-(4-nitrobenzylidene) thiazolidin-4-one, Acta Cryst. E 73 (2017) 511–514, https://doi.org/10.1107/S2056989017003218.

[33] Y. Megrouss, F. Triki-Baara, N. Boukabcha, A. Chouaih, A. Hatzidimitriou, A. Djafri, F. Hamzaoui, Synthesis, X-ray structure determination and related physical properties of thiazolidinone derivative by DFT quantum chemical method, Acta Chim. Slov. 66 (2019) 490–500, https://doi.org/10.17344/acsi.2019.5066.

[34] P.R. Spackman, M.J. Turner, J.J. McKinnon, S.K. Wolff, D.J. Grimwood, D. Jayatilaka, M.A. Spackman, CrystalExplorer: a program for Hirshfeld surface analysis, visualization and quantitative analysis of molecular crystals, J. Appl. Cryst. 54 (2021) 1006–1011, https://doi.org/10.1107/S1600576721002910.

[35] N. Khelloul, K. Toubal, N. Benhalima, R. Rahmani, A. Chouaih, A. Djafri, F. Hamzaoui, Crystal structure, Hirshfeld surface analysis and computational studies of thiazolidin-4-one derivative: (Z)-5-(4-chlorobenzylidene)-3-(2-ethoxyphenyl)-2-thioxothiazolidin-4-one, Acta Chim. Slov. 63 (2016) 619–626, https://doi.org/10.17344/acsi.2016.2362.

[36] E.R. Johnson, S. Keinan, P. Mori-Sanchez, J. Contreras-Garcia, A.J. Cohen, W. Yang, Revealing noncovalent interactions, J. Am. Chem. Soc. 132 (2010) 6498–6506.

[37] O. Noureddine, N. Issaoui, M. Medimagh, O. Al-Dossary, H. Marouani, Quantum chemical studies on molecular structure, AIM, ELF, RDG and antiviral activities of hybrid hydroxychloroquine in the treatment of COVID-19: molecular docking and DFT calculations, J. King Saud Univ. Sci. 33 (2021), 101334, https://doi.org/10.1016/j.jksus.2020.101334.

[38] C. Chiter, A. Bouchama, T.N. Mouas, H. Allal, M. Yahiaoui, I. Warad, A. Zarrouk, A. Djedouani, Synthesis, crystal structure, spectroscopic and hirshfeld surface analysis, NCI-RDG, DFT computations and antibacterial activity of new asymmetrical azines, J. Mol. Struct. 1217 (2020), 128376, https://doi.org/10.1016/j.molstruc.2020.128376.

[39] T. Lu, F. Chen, Multiwfn: a multifunctional wavefunction analyzer, J. Comput. Chem. 33 (2012) 580–592.

[40] E. Runge, E.K.U. Gross, Density-functional theory for time-dependent systems, Phys. Rev. Lett. 52 (12) (1984) 997–1000.

[41] J.B. Foresman, Ae. Frisch, Exploring chemistry with electronic structure methods, Gaussian, (1996).

[42] O. Kourat, A. Djafri, N. Benhalima, Y. Megrouss, N.E.H. Belkafouf, R. Rahmani, J.-C. Daran, A. Djafri, A. Chouaih, Synthesis, crystal structure, Hirshfeld surface analysis, spectral characterization, reduced density gradient and nonlinear optical investigation on (E)-N'-(4-nitrobenzylidene)-2-(quinolin-8-yloxy) acetohydrazide monohydrate: a combined experimental and DFT approach, J. Mol. Struct. 1222 (2020) 1–15, https://doi.org/10.1016/j.molstruc.2020.128952.

[43] S. Jabeen, T.J. Dines, S.A. Leharne, R. Withnall, B.Z. Chowdhry, A vibrational spectroscopic investigation of rhodanine and its derivatives in the solid state, J. Raman Spectrosc. 41 (2010) 1306–1317.

[44] F. Chain, E. Romano, P. Leyton, C. Paipa, C.A.N. Catalan, M.A. Fortuna, S. A. Brandan, An experimental study of the structural and vibrational properties of sesquiterpene lactone cnicin using FT-IR, FT-Raman, UV–visible and NMR spectroscopies, J. Mol. Struct. (2014) 160–169, 1065-1066.

[45] S. Sharma, H. Sharma, S. Sharma, S. Paul, V.K. Gupta, N. Boukabcha, A. Chouaih, Triflic acid functionalized carbon@Silica composite: synthesis and applications in organic synthesis; DFT studies of indeno[1,2-*b*]indole, ChemistrySelect 5 (7) (2020) 2201–2213, https://doi.org/10.1002/slct.201904727.

[46] V. Crasta, V. Ravindrachary, S. Lakshmi, S.N. Pramod, M.A. Shridar, J. Shashidhara Prasad, Growth, characterization and crystal structure analysis of 1-(4-chlorophenyl)-3-(4-chlorophenyl)-2-propen-1-one, J. Cryst. Growth 275 (1–2) (2005) e329–e335, https://doi.org/10.1016/j.jcrysgro.2004.10.110.

[47] H. Booth, R.M. Silverstein, G.C. Bassler, T.C. Morrill, Spectrometric Identification of Organic Compounds, Wiley, Chichester, 1991.

[48] K. Wolinski, J.F. Hinton, P. Pulay, Efficient implementation of the gauge-independent atomic orbital method for NMR chemical shift calculations, J. Am. Chem. Soc. 112 (1990) 8251–8260.

[49] W. Meng, G. Jin-Ju, W. Zhong-Bo, W. Zun-Yao, Raman FT-IR, N.M.R. spectra, molecular geometry, vibrational assignments, Ab initio and density functional theory calculations for diethyl phthalate, Chin. J. Struct. Chem. 32 (2013) 890–902.

[50] N.E.H. Belkafouf, F. Triki-Baara, A. Altomare, R. Rizzi, A. Chouaih, A. Djafri, F. Hamzaoui, Synthesis, PXRD structural determination, Hirshfeld surface analysis, and DFT/TD-DFT investigation of 3N-ethyl-2N'-(2-ethylphenylimino) thiazolidin-4-one, J. Mol. Struct. 1189 (2019) 8–20, https://doi.org/10.1016/j.molstruc.2019.04.028.

[51] A. Ramalingam, A.R. Guerroudj, S. Sambandam, A. Kumar, R. Krishnamoorthy, N. Boukabcha, A. Chouaih, M. Elayaperumal, Synthesis, vibrational spectra, Hirshfeld surface analysis, DFT calculations, and in silico ADMET study of 3-(2-chloroethyl)-2,6-bis(4-fluorophenyl)piperidin-4-one: a potent anti-Alzheimer agent, J. Mol. Struct. 1269 (2022), 133845, https://doi.org/10.1016/j.molstruc.2022.133845.

[52] F. Rouessac, A. Rouessac, Chemical Analysis: Modern Instrumentation Methods and Techniques, Wiley, New Jersey, 2013, 2nd Edition.

[53] S. Kumar, A. Radha, M. Kour, R. Kumar, A. Chouaih, S. K.Pandey, DFT studies of disubstituted diphenyldithiophosphates of nickel(II): structural and some spectral parameters, J. Mol. Struct. 1185 (2019) 212–218, https://doi.org/10.1016/j.molstruc.2019.02.105.

[54] A. Köhler, H. Bässler, Electronic Processes in Organic Semiconductors, Wiley-VCH Verlag, Weinheim, 2015, https://doi.org/10.1002/9783527685172.

[55] N.M. O'boyle, A.L. Tenderholt, K.M. Langner, CCLIB: a library for package-independent computational chemistry algorithms, J. Comput. Chem. 29 (5) (2008) 839–845, https://doi.org/10.1002/jcc.20823.

[56] N. Özdemir, B. Eren, M. Dinçer, Y. Bekdemir, Experimental andab initiocomputational studies on 4-(1H-benzo[*d*]22midazole-2-yl)-N,N-dimethylaniline, Mol. Phys. 108 (1) (2010) 13–24, https://doi.org/10.1080/00268970903476688.

[57] P. Politzer, J.S. Murray, T. Clark, Halogen bonding and other σ-hole interactions: a perspective, Phys. Chem. Chem. Phys. 15 (27) (2013) 11178, https://doi.org/10.1039/c3cp00054k.

[58] S. Alturk, N. Boukabcha, N. Benhalima, O. Tamer, A. Chouaih, D. Avcı, Y. Atalay, F. Hamzaoui, Conformational, spectroscopic and nonlinear optical investigations on 1-(4-chlorophenyl)-3-(4-chlorophenyl)-2-propen-1-one: a DFT study, Indian J. Phys. 91 (5) (2017) 501–511, https://doi.org/10.1007/s12648-016-0945-3.

[59] M. Azayez, S. Chetioui, Y. Megrouss, N. Boukabcha, A. Djedouani, A.R. Guerroudj, N. Meddah Araibi, A. Chouaih, Experimental and theoretical spectroscopic characterization, Hirshfeld surface analysis, TD-DFT calculation, and nonlinear optical properties of (E)-1-[(2,4,6*tribromophenyl*)*diazenyl*]-naphthalen-2-ol azo dye,

J. Mol. Struct. 1261 (2022), 132887, https://doi.org/10.1016/j.molstruc.2022.132887.

[60] S. Şahin, N. Dege, (E)-N-(3-chlorophenyl)-1-(5-nitro-2-(piperidin-1-yl)phenyl) methanimine: X-ray, DFT, ADMET, Boiled-Egg Model, druggability, bioavailabilty, and human cyclophilin D (CypD) inhibitory activity, J. Mol. Struct. 1250 (2) (2022), 131744, https://doi.org/10.1016/j.molstruc.2021.131744.

[61] M.R. Albayati, S. Kansız, N. Dege, S. Kaya, R. Marzouki, H. Lgaz, R. Salghi, I.H. Ali, M.M. Alghamdi, I.-M. Chung, Synthesis, crystal structure, Hirshfeld surface analysis and DFT calculations of 2-[(2,3-*dimethyl phenyl*) *amino*]-N'-[(E)-thiophen -2-ylmethylidene] benzohydrazide, J. Mol. Struct. 1205 (2020), 127654, https://doi.org/10.1016/j.molstruc.2019.127654.

[62] R. Parthasarathi, V. Subramanian, D.R. Royb, P.K. Chattaraj, Electrophilicity index as a possible descriptor of biological activity, Bioorg. Med. Chem. 12 (2004) 5533–5543, https://doi.org/10.1016/j.bmc.2004.08.013.

[63] B. Silvi, A. Savin, Classification of chemical bonds based on topological analysis of electron localization functions, Nature 371 (1994) 683–686, https://doi.org/10.1038/371683a0.

[64] H. Jacobsen, Localized-orbital locator (LOL) profiles of transition-metal hydride and dihydrogen complexes, Can. J. Chem. 87 (2009) 695–973, https://doi.org/10.1139/V09-060.

[65] D.A. Kleinman, Nonlinear dielectric polarization in optical media, Phys. Rev. 126 (6) (1962) 1977–1979, https://doi.org/10.1103/physrev.126.1977.

[66] N. Boukabcha, A. Feddag, R. Rahmani, A. Chouaih, F. Hamzaoui, Molecular structure, multipolar charge density study and nonlinear optical properties of 4-methyl-N-[(5-nitrothiophen-2-ylmethylidene)] aniline, J. Optoelectron. Adv. M. 20 (3–4) (2018) 140–148.

[67] M. Drissi, N. Benhalima, Y. Megrouss, R. Rahmani, A. Chouaih, F. Hamzaoui, Theoretical and experimental electrostatic potential around the m-nitrophenol molecule, Molecules 20 (2015) 4042–4054, https://doi.org/10.3390/molecules20034042.

[68] S. Kansız, A. Tolan, H. İçbudak, N. Dege, Synthesis, crystallographic structure, theoretical calculations, spectral and thermal properties of trans-diaquabis(trans-4-aminoantipyrine)cobalt(II) acesulfamate, J. Mol. Struct. 1190 (2019) 102–115. doi.org/10.1016/j.molstruc.2019.04.058.

[69] N. Dege, N. Şenyüz, H. Batı, N. Günay, D. Avcı, Ö. Tamer, Y. Atalay, The synthesis, characterization and theoretical study on nicotinic acid [1-(2,3-dihydroxyphenyl) methylidene]hydrazide, Spectrochim. Acta Part A: Mol. Biomol. Spectrosc. 120 (2014) 323–331, https://doi.org/10.1016/j.saa.2013.10.030.

[70] V.M. Geskin, C. Lambert, J.-L. Brédas, Origin of high second- and third-order nonlinear optical response in ammonio/borato diphenylpolyene zwitterions: the remarkable role of polarized aromatic groups, J. Am. Chem. Soc. 125 (50) (2003) 15651–15658, https://doi.org/10.1021/ja035862p.

[71] R. Rahmani, N. Boukabcha, A. Chouaih, F. Hamzaoui, S. Goumri-Said, On the molecular structure, vibrational spectra, HOMO-LUMO, molecular electrostatic potential, UV–Vis, first order hyperpolarizability, and thermodynamic investigations of 3-(4-chlorophenyl)-1-(1yridine-3-yl) prop-2-en-1-one by quantum chemistry calculations, J. Mol. Struct. 1155 (2018) 484–495, https://doi.org/10.1016/j.molstruc.2017.11.033.

[72] N. Boukabcha, A. Direm, M. Drissi, Y. Megrouss, N. Khelloul, N. Dege, M. Tuna, A. Chouaih, Synthesis, structural determination, hirshfeld surface analysis, 3D energy frameworks, electronic and (static, dynamic) NLO properties of o-Nitroacetanilide (o-NAA): a combined experimental and quantum chemical study, Inorg. Chem. Commun. 133 (2021), 108884, https://doi.org/10.1016/j.inoche.2021.108884.

[73] V.S. Naik, P.S. Patil, N.B. Gummagol, Q.A. Wong, C.K. Quah, H.S. Jayanna, Structural, linear optical, second and third-order nonlinear optical properties of two halogenated chalcone derivatives containing thiophene moiety, Chem. Phys. Lett. 761 (2020), 138051, https://doi.org/10.1016/j.cplett.2020.138051.

[74] P. Kaatz, E.A. Donley, D.P. Shelton, A comparison of molecular hyperpolarizabilities from gas and liquid phase measurements, J. Chem. Phys. 108 (3) (1998) 849–856, https://doi.org/10.1063/1.475448.

[75] N. Benhalima, N. Boukabcha, Ö. Tamer, A. Chouaih, D. Avcı, Y. Atalay, F. Hamzaoui, Solvent effects on molecular structure, vibrational frequencies, and NLO properties of N-(2,3-dichlorophenyl)-2-nitrobenzene–sulfonamide: a density functional theory study, Braz, J. Phys. 46 (2016) 371–383, https://doi.org/10.1007/s13538-016-0419-2.

[76] V.V. Poroikov, D.A. Filimonov, W.-D. Ihlenfeldt, T.A. Gloriozova, A.A. Lagunin, Y. V. Borodina, M.C. Nicklaus, PASS biological activity spectrum predictions in the enhanced open NCI database browser, J. Chem. Inf. Comput. Sci. 43 (1) (2003) 228–236, https://doi.org/10.1021/ci020048r.

[77] A. Lagunin, A. Stepanchikova, D. Filimonov, V. Poroikov, PASS: prediction of activity spectra for biologically active substances, J. Bioinform. 16 (2000) 747–748, https://doi.org/10.1093/bioinformatics/16.8.747.

[78] R.P.D. Bank, RCSB PDB: homepage, 2020. https://www.rcsb.org/.

[79] K. Matsushita, E. Shinagawa, & M. Ameyama. [31]d-Gluconate dehydrogenase from bacteria, 2-keto-d-gluconate-yielding, membrane-bound. Carbohydrate Metabolism - Part D, 187–193, (1982). doi:10.1016/s0076-6879(82)89033-2.

[80] M. Saidj, A. Djafri, R. Rahmani, N.E.H. Belkafouf, N. Boukabcha, A. Djafri, A. Chouaih, Molecular structure, experimental and theoretical vibrational spectroscopy, (HOMO-LUMO, NBO) investigation, (RDG, AIM) analysis, (MEP, NLO) study and molecular docking of Ethyl-2-{[4-Ethyl-5-(Quinolin-8-yloxyMethyl)-4H-1,2,4-Triazol-3-yl] Sulfanyl} acetate, Polycycl. Aromat. Compd (2022) 1–25, https://doi.org/10.1080/10406638.2022.2039238.

[81] G.M. Morris, AutoDock Version 4.2 - User Guide, AutoDock Version 4.2 -, User Guid. 1–49 (2010).

[82] W.L. Delano, The PyMOL Molecular Graphics Development Component, Version 1.8, Schrodinger, LLC, New York, NY, USA, 2015.

[83] M. Gür, S. Yerlikaya, N. Şener, S. Özkınalı, M.C. Baloglu, H. Gökçe, Y. Celik Altunoglu, S. Demir, İ. Şener, Antiproliferative-antimicrobial properties and structural analysis of newly synthesized Schiff bases derived from some 1,3,4-thiadiazole compounds, J. Mol. Struct. 1219 (2020), 128570, https://doi.org/10.1016/j.molstruc.2020.128570.

[84] S. Fazil, S. M, Y.S. Mary, Y.S. Mary, V. Chandramohan, N. Kumar, C. Van Alsenoy, Structural (SC-XRD), spectroscopic, DFT, MD investigations and molecular docking studies of a hydrazone derivative, Chem. Data Collect. 100588 (2020), https://doi.org/10.1016/j.cdc.2020.100588.

[85] C.A. Lipinski, Lead- and drug-like compounds: the rule-of-five revolution, Drug Discov. Today: Technol. 1 (2004) 337–341.

[86] M.H.M. Belhachemi, A. Benmohammed, H. Saiah, N. Boukabcha, M. Saidj, N. Dege, A. Djafri, A. Chouaih, Synthesis, structural determination, molecular docking and biological activity of 1-(4-fluorobenzyl)-5-bromolindolin-2,3-dione, J. Mol. Struct. 1265 (2022), 133342, https://doi.org/10.1016/j.molstruc.2022.133342.

[87] S. Yahiaoui, Y. Megrouss, N. Boukabcha, N.E.H. Belkafouf, N. Khelloul, R. Rahmani, N. Boubegra, A. Chouaih, Structural characterization, molecular docking assessment, drug-likeness study and DFT investigation of 2-(2-{1,2-dibromo-2-[3-(4-chloro-phenyl)-[1,2,4] oxadiazol-5-yl]-2-fluoro-ethyl1}-phenyl)-methyl 3-methoxy-acrylic ester, J. Indian Chem. Soc. 99 (2022), 100745, https://doi.org/10.1016/j.jics.2022.100745.

[88] S.A. Hitchcock, L.D. Pennington, Structure-brain exposure relationships, J. Med. Chem 49 (26) (2006) 7559–7583, https://doi.org/10.1021/jm060642i.